Kinetics of Carbide Precipitation during Laser Beam Welding of Dual-Phase and Martensitic Steels

by

Dulal Chandra Saha

A thesis
presented to the University of Waterloo
in fulfilment of the
thesis requirement for the degree of
Doctor of Philosophy
in
Mechanical and Mechatronics Engineering

Waterloo, Ontario, Canada, 2016

Author's Declaration

I hereby declare that I am the sole author of this thesis. This is a true copy of the thesis, including any required final revisions, as accepted by my examiners.

I understand that my thesis may be made electronically available to the public.

Abstract

In order to ensure a high passenger safety and reduce greenhouse gas emissions, dual-phase (DP) and martensitic steels (MS) are increasingly being used in the automotive industries. However, the main issue in the welding of steels containing a metastable martensite phase is softening, which occurs in the sub-critical heat affected zone (SCHAZ) and deteriorates joint integrity. This work attempts to understand the martensite tempering kinetics involved during high-speed laser beam welding where steels are exposed to the rapid heating and cooling cycles.

Fiber laser welding was performed on DP steel and its dissimilar combination with high strength low alloy (HSLA) steel. Different zones that produced at heat affected zone (HAZ) were characterized with respect to microstructure, micro- and nano-hardness, and tensile testing. Microstructural characterization suggests that the as-received martensite phase decomposes in the SCHAZ and forms various shapes and sizes of carbides, which reduces the local microhardness of the steel and subsequently the sample fractured in this zone during tensile loading.

In addition, the chemical composition and microstructure of DP steel plays an important role in the tempering reaction kinetics. The study conducted on the DP780 steel composed of ferrite, martensite, and bainite microconstituents, exhibited increasing microhardness in the HAZ instead of softening. This phenomenon is referred to as "secondary hardening". Rapid isothermal tempering conducted in a Gleeble simulator also indicated occurrence of secondary hardening at 500°C, as confirmed by plotting the tempered microhardness against the Holloman-Jaffe parameter. The mechanism of secondary hardening in this kind of a steel was unveiled by advanced characterization techniques carried out using transmission electron microscopy (TEM) with high-angle annular dark-field (HAADF) imaging. The experimental results suggested that the cementite (Fe_3C) and TiC phases located in the bainite phase of DP780 steel decomposed upon rapid tempering to form needle-shaped Mo_2C and plate-shaped M_4C_3 carbides giving rise to secondary hardening. In order to investigate the influences of steel microstructure on the martensite tempering kinetics two commercially produced DP980 grade steels were used. The study suggests that the severity of martensite tempering can be avoided by modifying the microstructure of the steels; the DP980 steel produced with a combination

of martensite, ferrite, and a blocky retained austenite phase promotes high tensile strength of the laser welded joint similar to the un-welded material.

Strength of the tempered martensite significantly differed depending on the nature of the tempering mode and heat input. Therefore, tempered martensite obtained from four different tempering modes was investigated. Extensive recovery and reduction of boundary regions was identified on the structure tempered slowly, whereas rapidly tempered structures retained a high density of dislocations and less decomposition of the lath structure.

The study revealed that dislocation density has a prominent effect on the macroscopic strength of the tempered martensite over all other strength contributors. In addition, rapid thermal cycles retained a high density of dislocations after tempering thus improving the tempered martensite strength. Therefore, the combined effect of dislocation density and the rapid thermal cycle was investigated by deforming the martensitic sheets to different levels of plastic deformation and subsequently tempering using conventional furnace tempering and the laser beam welding. It was found that the increased dislocation density due to the plastic deformation caused more nucleation sites for cementite precipitation, short-range carbon diffusion, and shorter growth period of cementite. The morphologies of the cementite were changed from elongated to small quasi-spherical when the sheet was plastically deformed. The deformed and tempered martensite yielded higher microhardness resulting from finer and semicoherent precipitates, a high density of retained dislocation density, and the presence of untempered and partially tempered martensite blocks.

The thermal analysis of martensite tempering carried out using a dilatometer suggests that the carbide precipitation temperature range increases to the higher tempering temperature when the sheet was subjected to rapid thermal cycles. Finally, a microstructural based model was applied to predict the yield strength and microhardness of the tempered martensite by incorporating the effects of heating rate, tempering temperature, and time. Experimental and modelling results suggest that the faster tempering mode in combination with a very short tempering duration provides the highest tempered martensite strength.

Acknowledgements

It is my privilege to express my gratitude and respect to all of the people who mentored, guided, inspired and helped me during my 4 years' research work at the University of Waterloo.

Firstly, I would like to express my heartiest gratitude to Prof. Norman Zhou and Prof. Adrian Gerlich for their consistent support, guidance, and the laboratory facilities to carry out this research work. I am extremely thankful to them for providing me the greater freedom with broader vision in the field of materials science.

I am really grateful to Dr. Sashank Nayak, and Dr. Elliot Biro for their invaluable support, suggestion and recommendation. Dr. Nayak has always been helpful and supportive and gave me the best support I required during my initial period of my research. I would like to thank Dr. Biro for his valuable inputs in this research work; the fruitful discussion we had during our occasional meeting will be truly remembered.

I am thankful to Mr. Daniel Westerbaan for his kind cooperation and helping hand in sample preparation and laser welding laboratory organization. Thank you Dan for teaching me the fiber laser welding process and allowing me to share the laser lab facilities. I would like to thank to Dr. Ali Nasiri for training the diode laser welding system and organizing the laser lab.

I would like to take this opportunity to acknowledge my current and previous colleagues at CAMJ including Nathan Lun, Rufus, Boyd Panton, Robert Liang, Tirdad Niknejad, Peng Peng, Andrew Paquegnat, Nei Huang, Jiao Zhen, Pavlo Penner, Jeff Wang, Paola Russo, Meng Sun, Joyce Koo, Nazmul Huda, Yuji Kisaka, Emanuel Santos, Gitanjali Shanbhag, Arshad Harooni, Melisa Hatat, Abdelbaset, Stephen Peterkin and many more.

I would like to thank Dr. Levente Balogh from the Department of Mechanical and Materials Engineering, Queen's University, for the dislocation density measurements from the Synchrotron data, and Dr. Yuquan Ding from the Mechanical and Mechatronics Engineering Department, University of Waterloo for his kind cooperation with the nanoindentation study.

The financial support from the Natural Sciences and Engineering Research Council (NSERC), ArcelorMittal Dofasco, and Auto21 are highly appreciated.

Dedicated to

The memory of my father
Badal Chandra Saha

To my loving family
In Bangladesh

To my lovely, beautiful wife
Sonali Saha

Table of Contents

List of Figures

List of Tables

List of Abbreviations

Abbreviations	Designations
AHSS	Advanced high strength steel
LWBs	Laser welded blanks
TWBs	Tailor welded blanks
FLW	Fiber laser welding
DLW	Diode laser welding
BM	Base metal
HAZ	Heat affected zone
FZ	Fusion zone
ICHAZ	Intercritical heat affected zone
SCHAZ	Subcritical heat affected zone
UCHAZ	Upper critical heat affected zone
TM	Tempered martensite
UTM/PTM	Untempered martensite or partially tempered martensite
PDM	Partially decomposed martensite
DM	Decomposed martensite
DB	Decomposed bainite
RA	Retained austenite phase
YS	Yield strength
LYS	Lower yield strength
UYS	Upper yield strength
UTS	Ultimate tensile strength
M_s	Martensite starts temperature
M_f	Martensite finishes temperature
CCT	Continuous cooling transformation diagram
TTT	Time-temperature-transformation diagram
SEM	Scanning electron microscopy
TEM	Transmission electron microscopy

Abbreviations	Designations
STEM	Scanning transmission electron microscopy
HAADF	High-angle annular dark field
SAD	Selected area diffraction
FIB	Focused ion beam
EBSD	Electron backscattered diffraction
IPF	Inverse pole figure
XRD	X-ray diffraction
EDX/EDS	Energy-dispersive X-ray spectroscopy
EELS	Electron energy loss spectroscopy
HRTEM	High-resolution transmission electron microscopy
FFT	Fast Fourier Transformation
IFFT	Inverse Fourier Filtered Transformation
BC	Band contrast
KAM	Kernel average misorientation
APT	Atom probe tomography
TTP	Time-temperature-precipitation diagram
H-J	Hollomon-Jaffe
CHT	Continuous heating transformation
ECD	Equivalent circular diameter
FHT	Furnace heat treated
GHT	Gleeble heat treated
TP	Tempering parameter
OR	Orientation relationship
PAGB	Prior austenite grain boundary
DSC	Differential scanning calorimetry
JMAK	Johnson-Mehl-Avrami-Kolmgorov

List of Symbols

Symbols	Designations
K_s	Thermal conductivity of steel
α_s	Thermal diffusivity of steel
C_p	Specific heat of the solid
v	Welding speed
Φ_0	Incident photon flux
V	Illuminated sample volume
μ	Sample transmission (μ=0.80 for a sample thickness of 0.50 mm and an X-ray energy of 80 keV
r_0	Thomson scattering length (2.82×10^{-15} m)
λ	The photon wavelength (0.155 Å) at E = 80 keV
m_{hkl}	Multiplicity factor
F_{hkl}	The structure factor
L_P	Lorentz factor for the complete powder ring, $L_P=(1/4)\sin(\theta)$
P	Polarisation factor, $P=[1+\cos^2(2\theta)]/2$
exp(-2M)	Debye-Waller factor
C_s	Steel carbon content
C_m	Martensite carbon content
f_m	Volume fraction of martensite
f_b	Volume fraction of bainite
H_v	Vickers microhardness
H_n	Nanohardness
k'	Locking parameter
d	Grain diameter
M	Taylor factor
G	Elastic isotropic shear modulus
ρ	Dislocation density
$<X>_A$	Area weighted average sub-grain size
C_{seg}	Segregated carbon atoms

Symbols	Designations
C_{nom}	Nominal carbon composition of the steel
v_{at}	Atomic volume of iron
a_{seg}	Average distance between the carbon atoms segregated to dislocation
E_r	Effective indentation modulus
R_i	Indenter tip radius
E	Young's modulus
ν	Poisson's ratio
x	diffusion distance
D_{diff}	Diffusivity
σ_{ss}	Solid solution strengthening
σ_{pct}	Precipitation strengthening
σ_{gb}	Grain boundary strengthening
σ_{ρ}	Forest dislocation density strengthening
η	Elastic modulus
δ	Lattice distortion
r	Atomic radius
μ	Shear modulus
d_p	Packet diameter
d_b	Block diameter
D_{γ}	Prior-austenite grain diameter
k_{HP}	Hall-Petch constant
$\rho_{lath,0}$	Dislocation density at as-quenched condition
ε	Lattice strain associated with the carbon redistribution
$d_{Cottrell}$	Thickness of the Cottrell atmosphere
b	Burgers vector
$d_{lath,0}$	Martensite lath width at as-quenched condition
r_p	Mean radius of carbides
f_p	Volume fraction of carbides
l_c	Mean carbon spacing

Symbols	Designations
λ_0	The constant accounted for the diffusion barrier for carbon segregation
R	Molar gas constant
ρ_{lath}	Dislocation density at tempered condition
d_{lath}	Martensite lath width at tempered condition
ε_x	The lattice strain from FCC to the martensitic structure along x direction
ε_y	The lattice strain from FCC to the martensitic structure along y direction
ε_z	The lattice strain from FCC to the martensitic structure along z direction

1 Introduction

1.1 Background

Fuel efficiency, safety, and minimizing environmental impact are key issues for the automotive industry [1, 2], and these can be accomplished with the use of advanced high strength steel (AHSS) as a result of its high strength and good formability. AHSS are produced by precisely controlling the cooling rate from austenite or austenite-ferrite phase to obtain desired microstructures. AHSS comprises various grades of steel, which are categorized based on their microstructure, chemistry, and mechanical properties, including dual-phase (DP), transformation induced plasticity (TRIP), twinning induced plasticity (TWIP), complex phase (CP), and martensitic steel (MS). A DP steel consists of a soft ferrite matrix with hard martensite islands as a second phase. A TRIP steel is composed of a primarily ferrite matrix with the addition of retained austenite, and martensite or bainite structures. On the other hand, TWIP steel comprises a fully austenitic microstructure. A CP steel contains a small amount of martensite, retained austenite and pearlite within a ferrite/bainite matrix. A MS steel is fully martensitic structure.

Laser welded blanks (LWBs), also known as tailor welded blanks (TWBs), are another way for auto makers to decrease vehicle weight to reduce CO_2 gas emission and increase fuel economy. LWBs are composed of two or more sheets of similar or dissimilar materials, thicknesses and/or coating types welded together, which are formed to fabricate the required three dimensional automotive body parts [3]. The advantages of the LWBs are weight reduction, cost minimization, improved material usage, and scrap reduction with improved part integration. Generally, LWBs are made with mild or interstitial free steels. However, in recent years, the weight reduction ability of LWBs have been increased by employing high strength steels like high strength low alloy (HSLA) steel and AHSS. The dissimilar combination also improves the crash performance of the blanks, since higher strength alloys can be used in the location where crash performance is crucial [4-6].

Initially, the automotive industry relied on CO_2 lasers to produce LWBs; however, recently, fiber laser welding (FLW) has gained popularity because of its several advantages, including lower capital costs, higher plug efficiency, greater flexibility in beam

delivery, higher power density (>10^5 W/cm^2), and narrower beam size, which provides welds with improved properties [7, 8]. In addition, the high-speed welding operation can be performed using FLW, which eventually increases the productivity and reduces production cost. Higher welding speeds are also advantageous in terms of the heat affected zone (HAZ) softening, as high-speed welding process provides a lower heat input; therefore, it reduces the degree of softening and the soften zone width [7, 8].

The HAZ softening associated with martensite tempering, which is a multi-stage process that is generally performed to enhance the ductility and toughness of the quenched steels containing martensite structure. In the first stage of tempering (80-180°C), segregation and redistribution of carbon occurs at lattice defects (dislocations), carbon clusters and transitional carbides, especially ε-carbide ($Fe_{2.4}C$), are formed [9-11]. It should be noted that the transitional carbides typically only precipitate when the carbon content of the steel exceeds 0.2 wt.%. The retained austenite is sometimes present at the interlath region of martensite structure [12], and decomposes into ferrite and cementite between the temperatures of 200-300°C during the second stage of tempering [11]. In the third stage of tempering segregated carbon and transitional carbides transform into stable or metastable carbides such as cementite (Fe_3C), which occurs at higher temperature, in the range of 250-350°C [11].

The martensite tempering process is greatly dependent on tempering temperature and time. Other factors such as heating rate, steel composition, carbon content of martensite, volume fraction of martensite, and defect sites (such as dislocation density) in the matrix also contribute to the carbide precipitation kinetics during tempering. There are numerous welding processes where the heating mode and rate highly vary. For example, FLW forms a keyhole during welding, whereas a DLW applies the conduction mode of welding. Therefore, the heating and cooling rates are completely different between these two modes of welding processes. Thus, if the steel being welded has a martensite phase in its base metal (BM), it will undergo tempering; depending on heating rate or heat input. Hence, it is a matter of concern to optimize the heat input or heating rate to obtain a desired tempering response.

Therefore, the objective of this study is to develop a better understanding of softening kinetics involved during martensite tempering, which will reveal the fundamental issues

associated with welding of martensite containing steels. Knowledge obtained from this study will enable the engineering of thermal cycles in welding to achieve a proper tempering response.

1.2 Aims

The aim of this thesis work is to investigate the following items, which will eventually provide fundamental knowledge in the field of carbide precipitation kinetics during rapid tempering of martensite phase.

1. To develop a detailed understanding of tempering of DP and martensitic steel by correlating carbide precipitation kinetics during high-speed laser welding process with the mechanical properties of welded joint.
2. To reveal the influence of steel chemistry and microstructure on the tempering kinetics of martensite.
3. To determine the influences of various tempering modes such as laser welding, furnace heat treatment, and Gleeble heat treatment on the micro- and nano-scale structural changes of martensite.
4. To correlate carbide shape and size distribution with thermal cycles imposed during rapid tempering of the as-quenched and deformed martensitic steels.
5. To study the structure-properties correlation of the simulated tempered martensite obtained with various heating rates and predict the tempered martensite strength (yield strength and microhardness) by combining all tempering parameters such as temperature, time, and heating rate.

1.3 Thesis outline

The content of this thesis work has been divided into nine Chapters. In Chapter 1, a brief introduction to background, problems, objectives and the scopes of the research work are presented. In-depth literature survey including physical metallurgy of DP and MS steels, phase transformation of martensite, martensite tempering kinetics, and the consequences of tempering on the strength (microhardness and tensile) of martensite are summarized in Chapter 2. In Chapter 3, a detailed information of the studied materials, processes, sample preparation procedures, and advanced characterization methods used in this research work are presented. In Chapter 4, microstructural features of the different zones (FZ and HAZ) produced during the laser beam welding of DP and HSLA steels are evaluated; emphasis was given on the SCHAZ where a reduction of microhardness was detected. In Chapter 5, the effects of two major issues such as steel chemistry, and microstructure on the martensite tempering kinetics of DP steels are investigated. Chapter 6 reports the influences of various tempering modes such as furnace heat treatment, Gleeble heat treatment, laser beam welding on the subtle microstructural changes and its consequences on the micro- and nano-scale mechanical properties of the tempered martensite. Chapter 7 demonstrates the combined effects of plastic deformation and rapid thermal cycles applied by the cold-rolling and the high-speed fiber laser on the carbide precipitation kinetics of fully martensitic steels. Chapter 8 presents the thermal and microstructural correlation of the tempered martensite obtained via tempering in a Gleeble thermomechanical simulator with wide ranges of tempering conditions such as different heating rates, temperature, and time. Finally, Chapter 9 lists the major conclusions and contributions made in this work and provides recommendations for future research.

2 Literature Review

2.1 Dual-phase (DP) steel

DP steels are composed of soft ferrite, hard martensite, and occasionally bainite phase. A combination of soft and hard phases (composite structure) of DP steel provides a balance of strength and ductility compared to other AHSS. DP steels are produced by intercritically annealing process, where a mixture of ferrite and austenite are formed, thus subsequent rapid cooling produces the desired final microstructure [13-15]. The cooling rates and the alloy composition are the two main factors determining the phases in DP steels. This kind of steel can be produced either with a combination of rapid cooling and lean chemistry (only C, Mn and Si) or with a low cooling combined with additional Cr and Mo alloys which are required to delay the pearlitic and bainitic transformations. By delaying these phase transformations allow a high fraction of austenite remain at intercritical annealing temperature range thus produces a desired fraction of martensite during cooling to the room temperature [16]. The ultimate tensile strength (UTS) of DP steels depend on the volume fraction of the hard martensite phase, as the volume fraction of martensite increases the UTS of steel also increases; however, the ductility of this steel decreases. For example, DP600 steel containing 15% martensite has a UTS of about 600 MPa and elongation over 20%; on the other hand, 50% martensite containing DP980 steel has a UTS of 980 MPa but only 14% elongation (Figure 2-1).

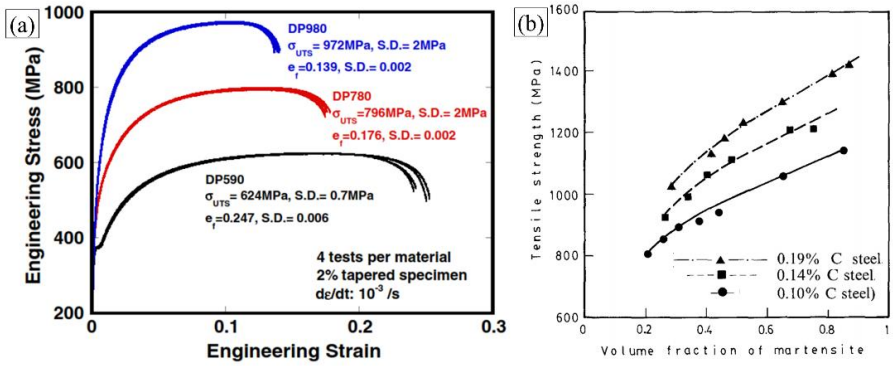

Figure 2-1 (a) Typical engineering stress vs. strain curves of different grades of DP steels [17], and (b) tensile strength of DP steels as a function of martensite volume fraction. Steels were intercritically annealed followed by water quenching [18]

2.2 Martensitic steel

Martensitic steel is composed of nearly 100% martensite phase which is produced by rapidly quenching of the austenite phase to the martensite structure in a run-out table or in the cooling section of the continuous annealing line [16]. Martensitic steel provides the highest tensile strength (YS: 950-1150 MPa, and UTS: 1200-1500 MPa) with low ductility (about 4% of engineering strain) as can be seen in Figure 2-2. The strength of martensitic steel is determined by the carbon content of steel [19]; the greater the steel carbon content the higher the UTS. To increase the ductility of martensitic steel, a tempering treatment is usually applied thus the strength of the martensitic steel is slightly decreased but ductility is increased.

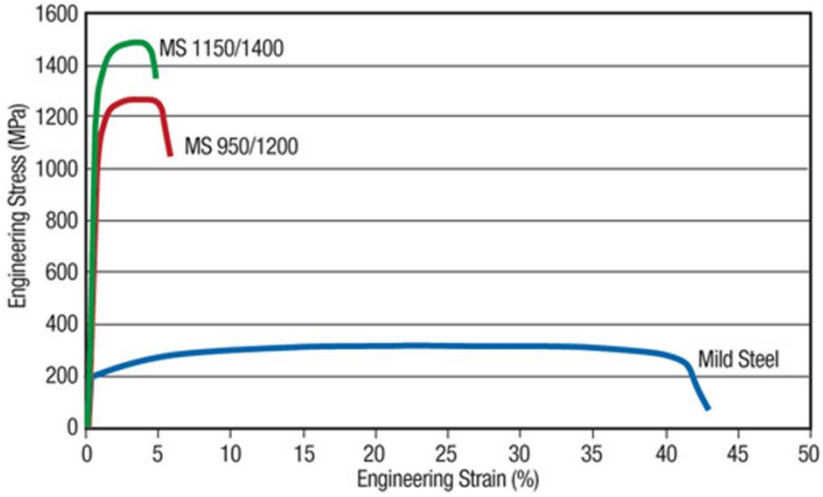

Figure 2-2 Typical engineering stress vs. strain curves of martensitic steels (tensile curve of the mild steel also shown for a comparison) [16]

2.3 Martensite transformation

Martensitic transformation is a diffusionless process which occurs by a Bain strain transformation that is required to change from a FCC crystal to a BCC structure. Martensite plates can grow at a high-speed which approaches to that of the speed of sound in the metal; therefore, the transformation can avoid any kind of diffusion, even that of interstitial atoms. Martensite transformation occurs at a specific temperature called martensite start temperature, M_s, therefore, is referred to as an athermal transformation process. The M_s

temperature, for a specific steel can be calculated using the empirical relationship (equation 2-1) as proposed by Andrews [20] (concentrations in wt.%). During quenching from the austenite phase, martensite starts to nucleate and grow when it reaches the M_s temperature and the transformation reaction is completed at the martensite finish temperature, M_f.

$$Ms\ (°\mathrm{C}) = 539 - 423(\%\mathrm{C}) - 30.4(\%\mathrm{Mn}) - 17.7(\%\mathrm{Ni}) - 12.1(\%\mathrm{Cr}) - 7.5(\%\mathrm{Mo}) \quad (2\text{-}1)$$

The transformed BCC structure in FCC reference frame is highly tetragonal thus considered as BCT cell (Figure 2-3). During transformation, the z-axis ([001]) of BCT phase contracts by an amount of 23% and x- ([100]) and y-axis ([010]) expands by 12%. The carbon atoms trapped in the octahedral sites of BCT cell. The tetragonality of martensite is determined by the amount of carbon present in the octahedral sites (Figure 2-3). The literature data presented in Figure 2-4 shows the relationship between the lattice parameters of lath martensite and the carbon content of steel. The tetragonality (*c/a* ratio) of lath martensite increases above the carbon content of 0.3 wt.%; in the case of the low carbon containing steel (≤0.2 wt.% C), a negligible martensite tetragonality is observed. Carbon mostly, segregates and diffuses into the dislocation lines and lath boundaries during transformation [21].

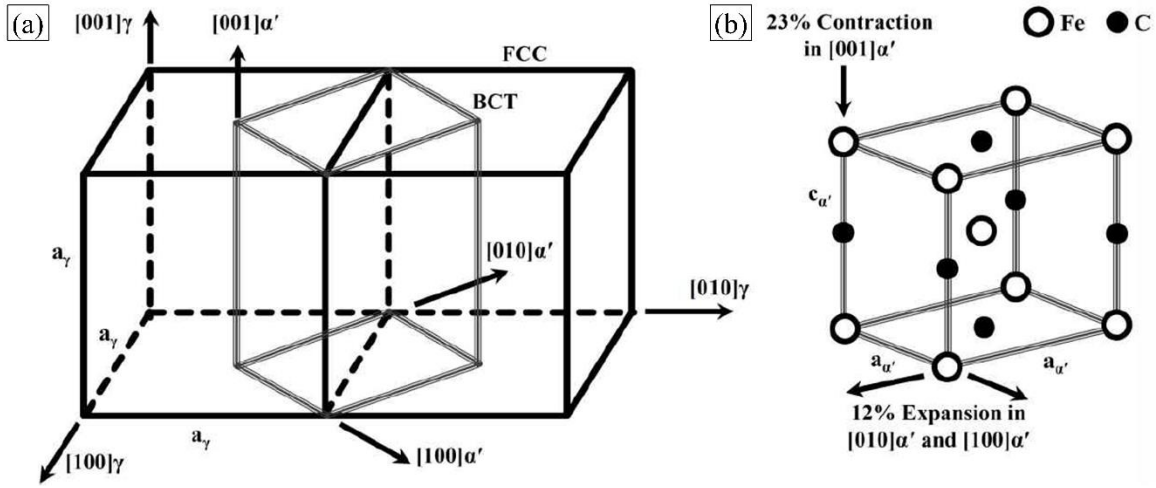

Figure 2-3 (a) The crystal relationship between FCC and BCT structure, and (b) the BCT unit cell after the Bain strain. Figure is reproduced from reference [22]

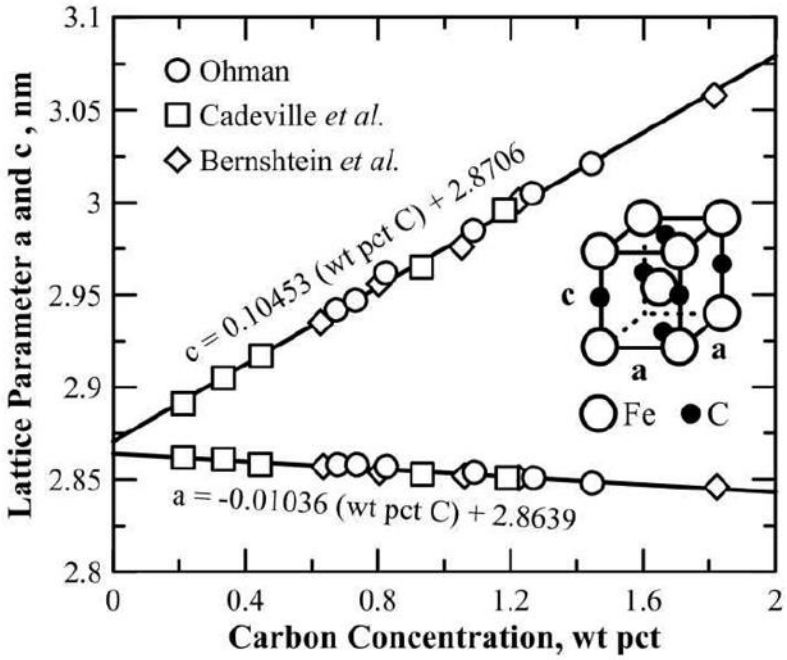

Figure 2-4 Literature data of lattice parameters of Fe-C lath martensite as a function of steel carbon content [23]. Figure is reproduced from reference [22]

Figure 2-5 shows the 3D atom probe tomography carbon maps of a medium carbon (1.31 at.%) containing martensitic steel [12]. Two regions are selected for the carbon line scan, one is corresponding to the retained austenite film at lath boundary (region (c)) and another one is across the dislocation lines (region (d)). Carbon content at retained austenite film shows approximate concentration of 6.0 ± 0.5 at.% with a 4.0 ± 0.5 nm thick layer (Figure 2-5(c)). It was reported that about 8% of total carbon has segregated to the retained austenite film [12]. Carbon atom maps presented in Figure 2-5(a) also shows a fine carbon distribution and carbon depleted matrix region in the martensite matrix. The carbon line scanning across the martensite matrix shown in Figure 2-5(d) which depicts a carbon concentration of 5-6 at.% with a thickness of 5 nm and about 20 nm interval. The formation of 5-6 nm thick layer of carbon rich atoms was reported to be the Cottrell atmospheres at lath boundaries formed by the interstitial carbon atoms around the dislocation lines [12, 24, 25].

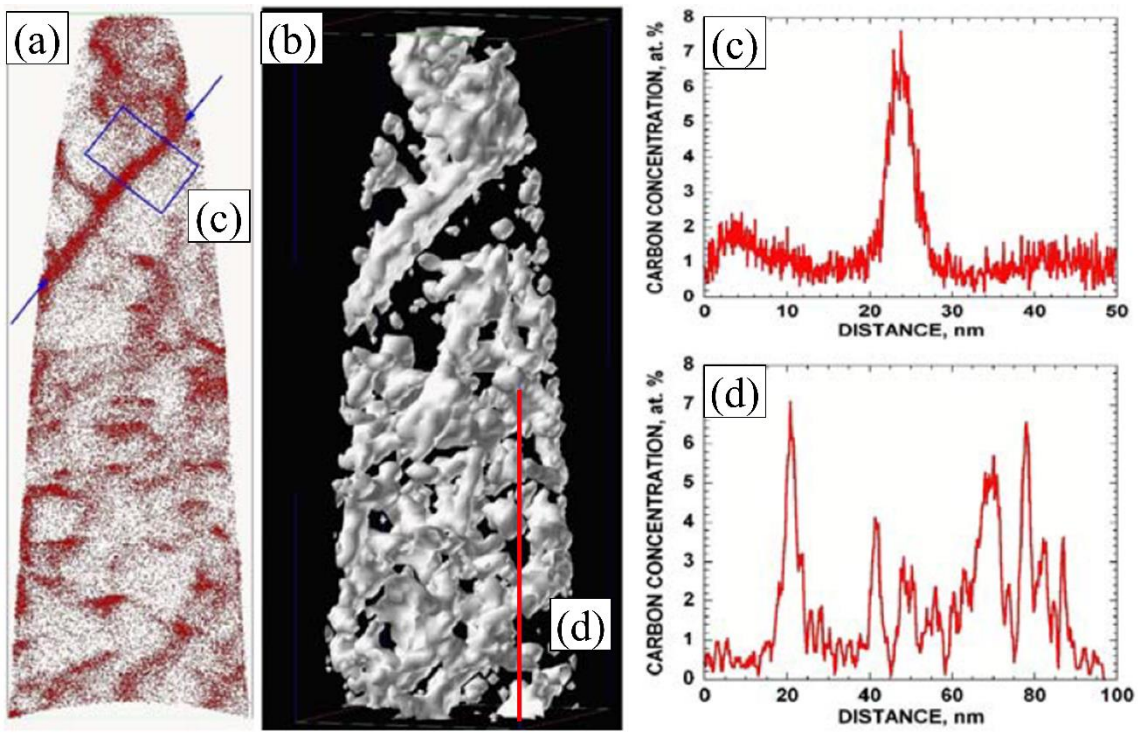

Figure 2-5 3D atom probe tomography analysis of a medium carbon (1.31 at.%) lath martensite showing, (a) carbon maps (region (c) referred to the carbon rich retained austenite film), (b) a distribution of 1.3 at.% carbon isoconcentration surfaces (the vertical line referred to the line scanning line across the martensite matrix, region (d)), (c) carbon line scan profile of region (c) marked in (a), and (d) carbon distribution across the line (d) marked in (b) [12]

2.3.1 Morphology of martensite

The morphology of martensite is highly dependent on the alloy composition and carbon content. Based on the carbon content, martensite forms in the shape of laths, i.e. ruler shaped units, or plates, i.e. lenticular shaped units. It has been reported that martensite forms as a lath in the low and medium carbon steels (< 0.4 wt.% C) (Figure 2-6(a) and (b)), whereas, a lenticular or plate shaped martensite was found in the high carbon containing steels (> 0.6 wt.% C) (Figure 2-6(c) and (d)) [26]. Martensite composed of various sub-units, boundaries, and defects; the prior-γ grain, the largest unit of martensite, is divided into four packets which is subdivided into 6 blocks containing several laths oriented in an identical crystal direction as schematically shown in Figure 2-6(a). Conversely, plate shape

martensite consists of non-parallel martensite units (Figure 2-6(c)). A distinct feature of the plate martensite is that it contains a midrib which is reported to be the first forming unit. The midrib can be completely or partially twinned, or a combination of twinned and untwinned region, which was reported to be highly dislocated (Figure 2-6(d)) [27].

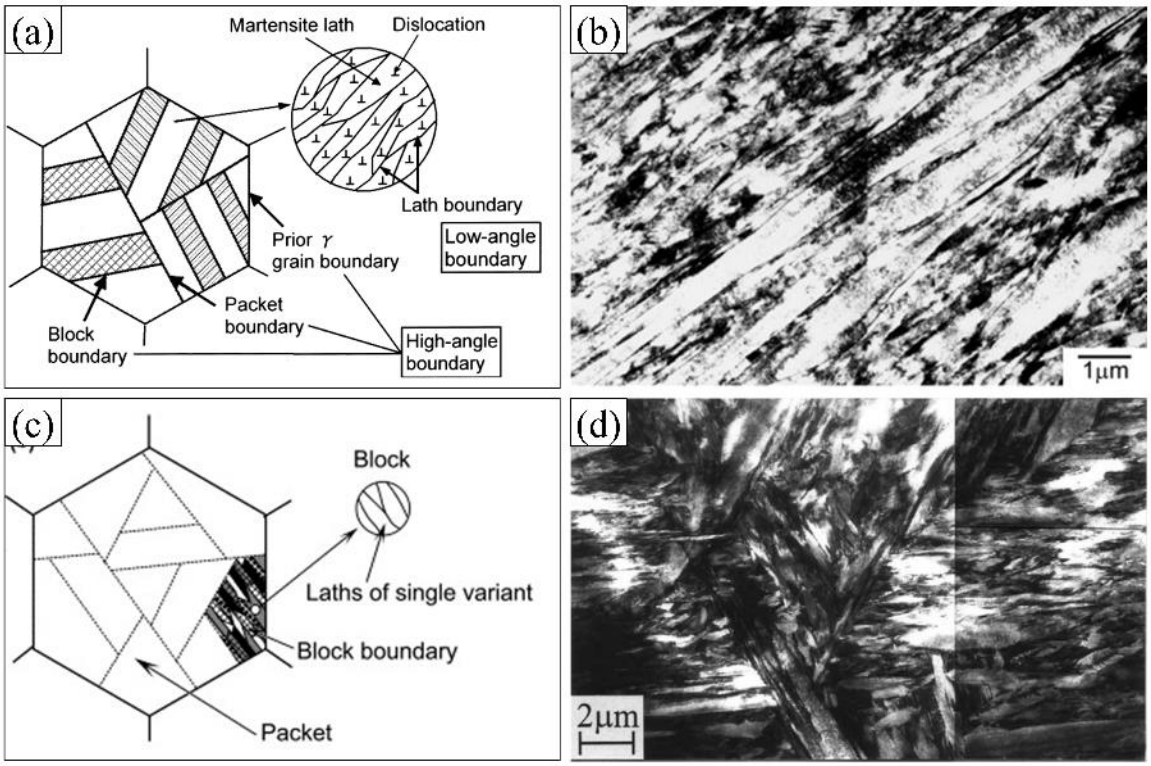

Figure 2-6 (a) Schematic representation of various boundaries and defects sites in a 0.2 wt.% C lath martensite [28], (b) TEM image of lath martensite [29], (c) Schematic of plate martensite in 0.6 wt.% C steel [30], and (d) TEM image of plate martensite [30]

2.3.2 Effect of alloying elements in martensite

Generally, the alloying element lowers the martensite starts (M_s) temperature; however, among the other alloying elements, the interstitial atoms such as C and N_2 has much stronger effect on the transformation temperature. It has been reported that 1 wt.% of C lowers the martensite finish (M_f) temperature by over 300°C (Figure 2-7) [31]. A higher M_s temperature in the low carbon containing steels often leads to the formation of carbides by rearranging carbon atoms themselves, which is usually called autotempering [32-34]. Conversely, the high C containing steels possess lower M_s temperature, therefore,

partitioning of carbon atoms occur at lath boundary leading to a high volume fraction of the retained austenite [35].

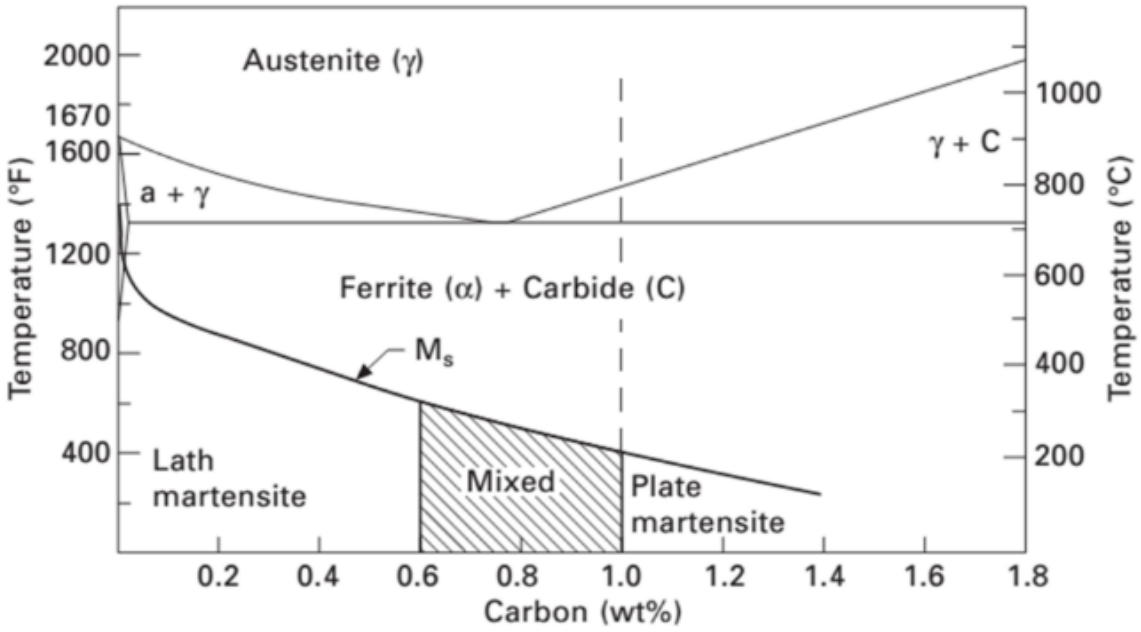

Figure 2-7 M_S temperatures and morphologies of martensite as a function of carbon content superimposed on the iron-carbon diagram [36]

2.3.3 The strength of martensite structure

Although the strength of martensite is largely dependent on the steel C content, there are numerous factors which also alter the strength of martensite, such as substitutional atoms, interstitial solid solutions, dislocations, (i.e. work hardening) fine twins, prior-γ grain size, segregation of carbon atoms, and precipitation of iron carbides. Figure 2-8 shows the relationship between tensile strength and carbon content. As it can be seen that tensile strength of martensite linearly increases with carbon content of steels due to a greater tetragonality and lattice distortion (Figure 2-4), and a high density of dislocation [18, 31, 37]. Refinement of the prior-γ grain size also has a positive effect on the strength of martensite, since the yield strength of martensite varies with the inverse square root of the grain size. In addition to the high-angle boundaries which are prior-γ grain, packet, and block boundaries, the low-angle boundaries such as lath boundaries, acted as an obstacle to the dislocation movement thus contributes to increasing the strength of martensite [38].

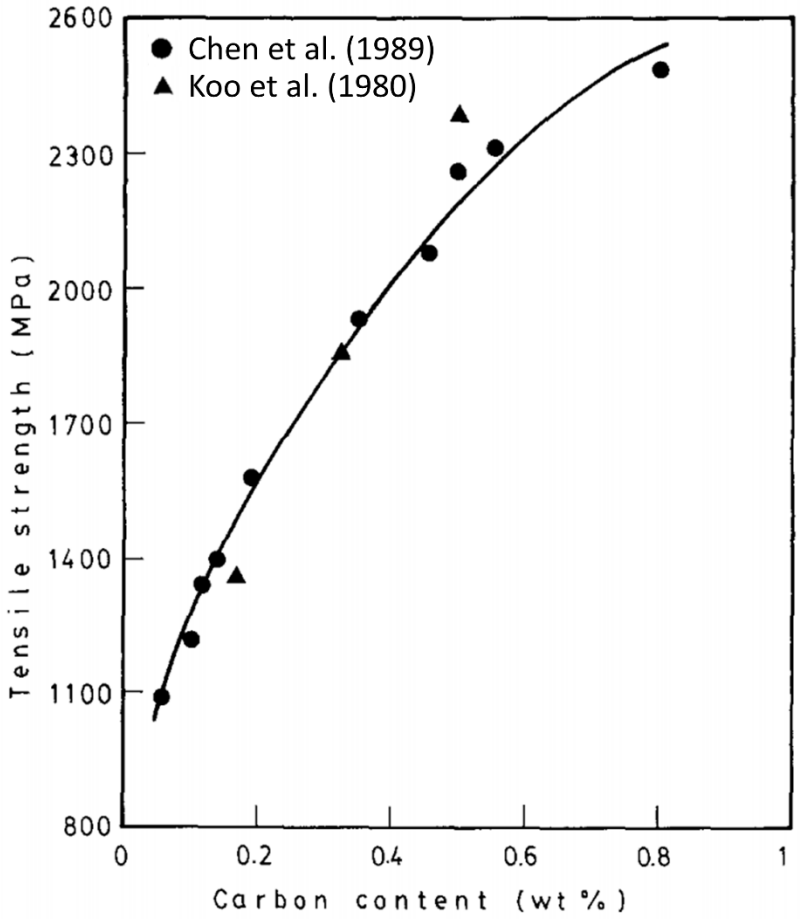

Figure 2-8 Effect of carbon on the tensile strength of martensite. Steels were supercritically annealed and followed by water quenching [18]

The complex composite nature of martensite is considered to be chemically and mechanically inhomogeneous. A local fluctuation of the micro-mechanical response within a single prior-γ grain of lath martensite was reported to be the effect of various boundaries and defect density presence in a lath martensite [39, 40]. Morsdorf et al. [39] demonstrated that the nanoindents located at coarse lath's center (away from boundaries) possesses the lowest nanohardness; on the other, a highest nanohardness was measured at thin lath adjacent to the boundary as shown in Figure 2-9. This phenomenon also supported by He et al. [40], where it was found that the nanoindent located at small martensite block has a higher hardness value compared to the indent at large martensite block.

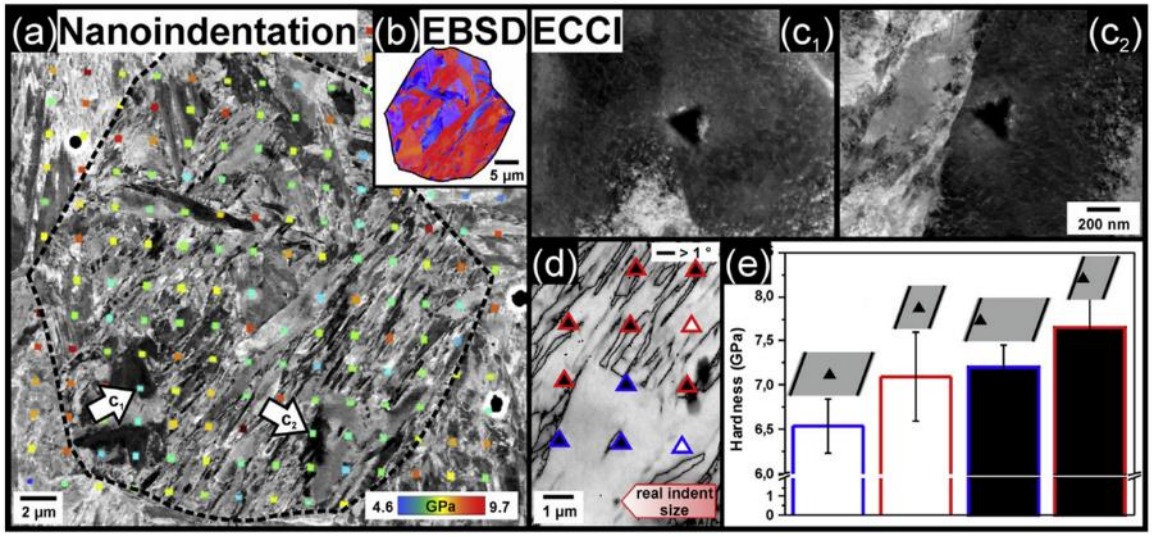

Figure 2-9 (a) Nanohardness maps on a prior-γ grain, (b) IPF map from EBSD analysis, (c) indents either probe the lath interior (c_1) or contain boundary effects (c_2), (d) EBSD maps of the indented area, and (e) averaged nanohardness of coarse and thin laths combined with the effect of boundaries [39]

2.3.4 Dislocation density on lath martensite

It is well known that the lath martensite structure is heavily dislocated; the dislocation density is in the order of 10^{14} to 10^{15} m^{-2} [21, 33]. Dislocation density increases with carbon content due to lattice distortion induced by the interstitial carbon atoms [21, 37]. Figure 2-10 shows the plot of dislocation density as a function of carbon content which indicates a reduction of dislocation density over 0.6 wt.% steel carbon content. The drop of dislocation density in high carbon steel is attributed to the formation of the twinned and plate martensite (Figure 2-7) which possesses lower defect densities compared to the lath martensite.

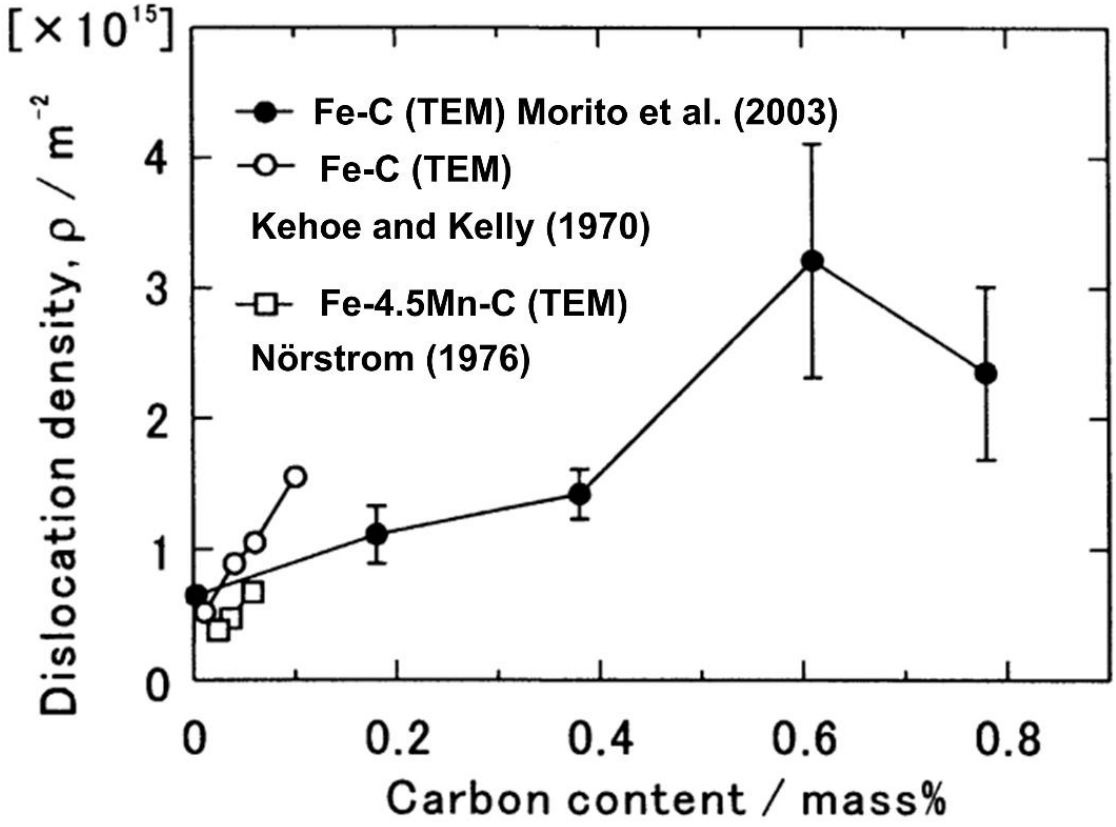

Figure 2-10 Dislocation density in lath martensite as a function of carbon content in Fe-C alloys [37]

2.4 Martensite tempering

The tempering is a process which is generally performed to improve the toughness and ductility of the martensitic steels without compromising a great reduction of hardness and strength. The study on the martensite tempering kinetics has been carried out extensively [41-44] using various instrumental techniques such as resistometry [41], X-ray diffraction (XRD) [42, 44-46], Mössbauer spectroscopy [47-50], electron microscopy [51-53], and atom probe field ion microscopy [54, 55]. Martensite tempering is a multi-stage process through which various carbides (Table 2-1) are formed during heating; four overlapping tempering stages have been reported in the literature.

2.4.1 Precipitation of carbides during tempering

2.4.1.1 The first stage of tempering

During tempering of martensitic steels, the first carbide precipitates as very fine transitional carbide such as ε-carbide with a chemistry of $Fe_{2.4}C$, which is eventually replaced by the more thermodynamically stable carbides such as cementite (Fe_3C) [56-58]. However, ε-carbide formation is limited by the carbon content of steel; this type of carbide does not form during tempering of low carbon containing steel (~ 0.2 wt.% C) [58-61]. The common crystal orientation and the lattice relation of ε-carbide with the ferrite matrix are shown in Table 2-2.

2.4.1.2 The second stage of tempering

In low and medium carbon steels, retained austenite can be found between martensite laths. The retained austenite is known to be highly unstable at higher temperature (below Ac_1), therefore, this phase is likely to decompose into ferrite and cementite at temperature ranges of 200 to 300°C [11]. It has been demonstrated that the small amount of the retained austenite in a medium-carbon steel is stable up to 200°C, and then completely transformed to ferrite and cementite at 300°C.

2.4.1.3 The third stage of tempering

This stage of tempering is associated with replacement of the unstable transitional carbides with the stable cementite (Fe_3C). At much higher tempering temperature, the martensite matrix becomes ferrite by releasing carbon to form Fe_3C. Although the martensite structure becomes ferrite and cementite after tempering, the lath type morphology can be observed as well; therefore, it is referred to tempered martensite. The strength of the tempered martensite depends on the size, shape and distribution of precipitated cementite; the coarser cementite reduces hardness much compared to the finer cementite. It should be noted that second and third stage of tempering occurs simultaneously and in both the cases the product phases are ferrite and cementite (Figure 2-11). The common orientation relationship (OR) between cementite and ferrite are shown in Table 2-2.

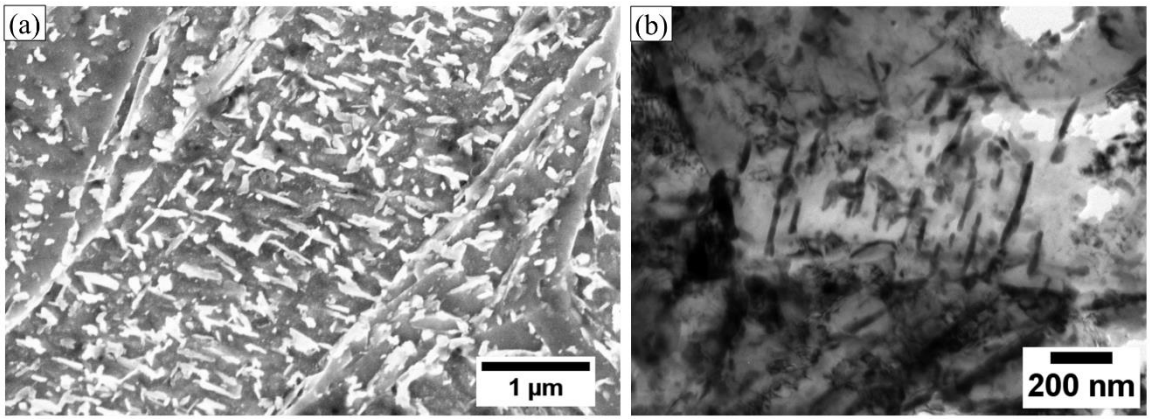

Figure 2-11 (a) Scanning electron microscopy (SEM), and (b) transmission electron microscopy (TEM) micrograph of the tempered martensite with intralath fine cementite plates in 0.23 wt.% C steel tempered at 420°C for 1 s with a heating rate of 1°C/s (unpublished work by Saha et al.)

2.4.1.4 The fourth stage of tempering

This is the last stage of tempering which is associated with the replacement of cementite (Fe_3C) by the formation of alloy carbides at much higher tempering temperature, close to Ac_1 line. Cementite is known to be metastable structure at higher temperature; therefore, at higher temperature the iron atoms of the cementite are substituted by the alloying elements to form alloy carbides. Once alloy carbides are formed, the hardness tends to increase above the as-received material, which is commonly known as *secondary hardening* [61-64]. Figure 2-12 represents the effect of alloying elements on the hardness trends during tempering of alloyed martensitic steels as a function of tempering parameter. Four types of steels marked as class 1 to class 4 are used to identify the tempering responses on the hardness trends. Class 1 steel is a low carbon steel which shows a continuous softening with respect to the tempering parameter. Class 2 steel is alloyed but the lower alloying element than the needed amount to have a notable secondary hardening response. On the other hand, highly alloyed and sufficient carbon containing Class 3 steel shows a secondary hardening peak after tempering at higher temperature. Class 4 steel also contains similar alloying elements as Class 2 but considerably lower carbon content, therefore, secondary hardening was not identified. The transitional elements such as Cr, Mo, W, V,

and Nb are known as strong carbide forming elements, if these elements are present in the steel in a sufficient amount then it provides a secondary hardening effect [61].

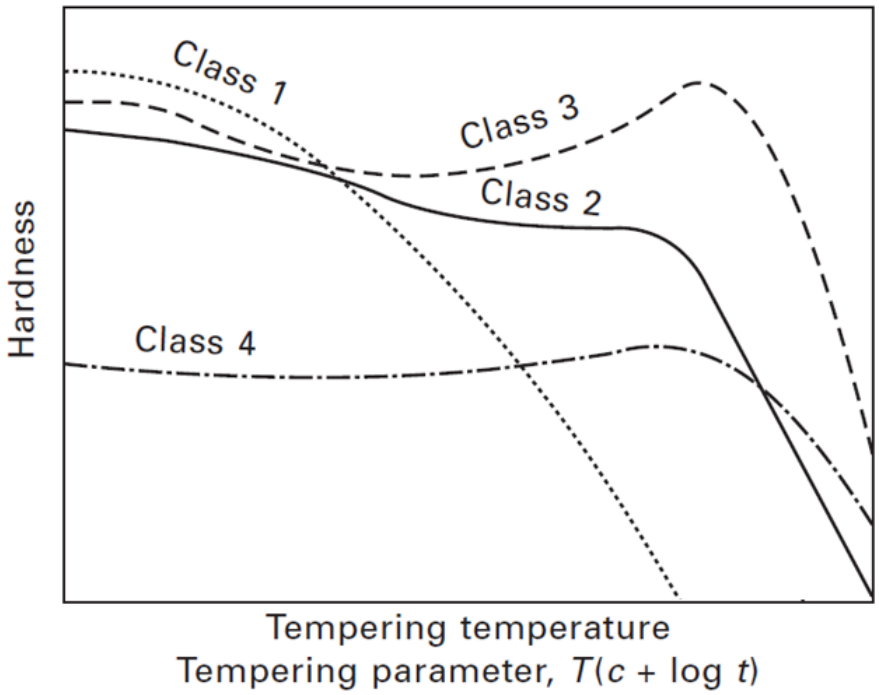

Figure 2-12 Schematic classification of tempering response to alloying, based on changes in hardness, as a function of tempering temperature or parameter [65]

Table 2-1 Crystal structures and lattice parameters of the stable and metastable carbides found in the tempered martensite and bainitic steels [61]

Carbide	Crystal System	Lattice Parameters (Å)		
		a	*b*	*c*
κ	Hexagonal	6.9		4.8
ε	Hexagonal	2.735		4.339
χ	Monoclinic	11.563	3.573	5.058
η	Orthorhombic	4.704	4.318	2.830
Fe_3c, θ	Orthorhombic	4.525	5.087	6.743
M_7C_3	Orthorhombic	4.526	7.010	12.142
$M_{23}C_6$	Cubic	10.624	-	-
M_6C	Cubic	11.082	-	-

Table 2-2 Crystal orientation and lattice relationship of commonly found carbides in tempered martensite

Description	ε-carbide	θ-cementite	References
Chemical composition	$Fe_{2.4}C$	Fe_3C	
Crystal Structure	Hexagonal close packed	Orthorhombic	
Space group	$P6_322$	Pnma	
Orientation relationship		Bagaryatski $(001)_\theta \| \| (211)_\alpha$ $[100]_\theta \| \| [0\bar{1}1]_\alpha$ $[010]_\theta \| \| [1\bar{1}\bar{1}]_\alpha$ Isaichev $(\bar{1}03)_\theta \| \| (110)_\alpha$ $[010]_\theta \| \| [1\bar{1}\bar{1}]_\alpha$ $[311]_\theta$ 0.91° from $[1\bar{1}1]_\alpha$ Pitsch-Petch $(001)_\theta \| \| (5\bar{2}\bar{1})_\alpha$ $[100]_\theta$ 2.6° from $[13\bar{1}]_\alpha$ $[010]_\theta$ 2.6° from $[113]_\alpha$	[66-71]
	Jack $(0001)_\varepsilon \| \| (011)_{\alpha'}$ $(10\bar{1}0)_\varepsilon \| \| (2\bar{1}1)_{\alpha'}$ $(10\bar{1}1)_\varepsilon \| \| (101)_{\alpha'}$		

2.4.2 Effect of heating rate on martensite tempering

The time-temperature-precipitation (TTP) diagram is schematically presented in Figure 2-13 to describe the effect of heating rate on the cementite precipitation. It can be seen that heating rate has a significant effect on the precipitation kinetics. Low heating rate requires a longer tempering time to cementite precipitate whereas the higher heating rate takes less time to start cementite nucleation. It can be noted that a higher heating rate also increases the cementite start temperature compared to the temperature requires for the lower heating rate (Figure 2-13). Another important aspect is that cementite precipitation

is completed within a very short time in the case of the rapid heating rate, which suggests that finer needle-shape cementite precipitates due to the insufficient reaction time. The shorter tempering time also provides partial recovery of martensite lath [72, 73]. In contrast, the slow heating rate requires a longer heating time, therefore, coarser and spheroidized (disc shape) cementite could be expected [28, 72, 73].

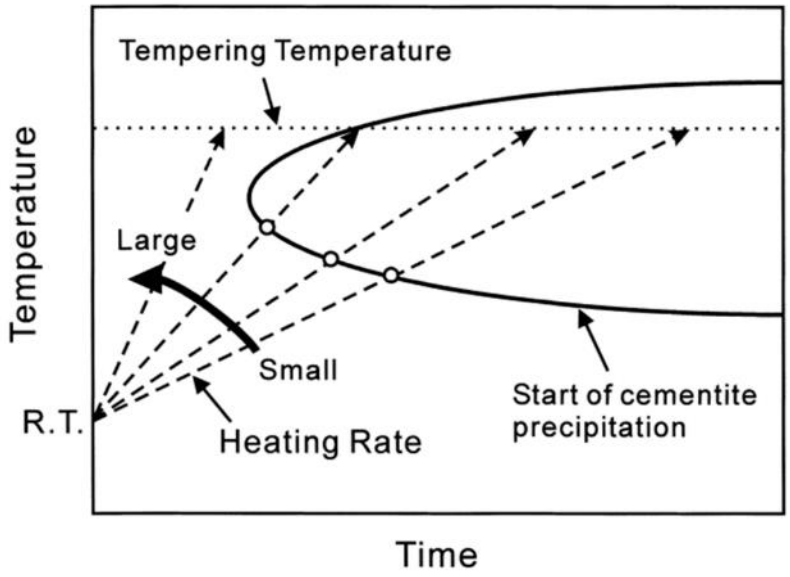

Figure 2-13 Schematic TTP diagram describing the effect of heating rate on cementite precipitation [28]

Figure 2-14 illustrates the effect of heating rate on carbide shape, size and their distribution during tempering of the martensitic steel. When a lath martensite is tempered at normal tempering condition (with atmospheric furnace), coarser cementite is precipitated at lath boundary. As the cementite precipitates by the expense of carbon; therefore, a small amount of carbon as a solid solution can be expected in the intralath region, which suggests it will have a low dislocation density, since dislocations are annihilated by the recovery of the ferrite grains [28, 74-76]. Conversely, in the case of rapid heating and tempering, smaller and finer cementite was reported in the lath boundary and intralath region, which leads to a large amount of solid solution of carbon in the matrix, and a high dislocation density. Finally, the uniform dispersion of the fine cementite provides less softening in the martensite structure under rapid tempering condition [28, 72].

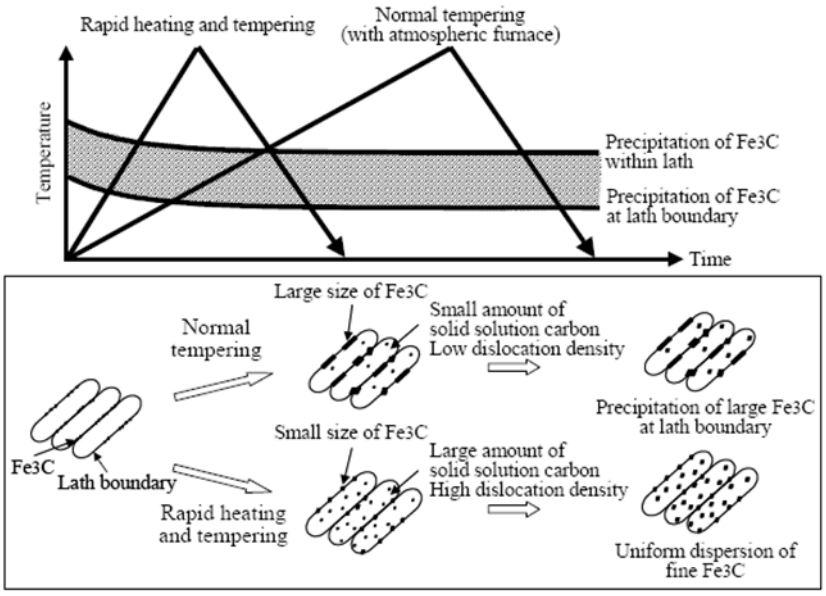

Figure 2-14 Effect of heating rate on carbide refinement during tempering [77]

2.4.3 Hollomon-Jaffe tempering parameter

As the tempering process is influenced by temperature and time, therefore, the tempering cycle was generalized using Hollomon-Jaffe tempering parameter [78], which has been used extensively to predict the tempering response on hardness. Hollomon-Jaffe tempering parameter describes the effect of tempering time and temperature in the isothermal heat treatment process. The Hollomon-Jaffe (H-J) parameter is calculated using equation (2-2) where temperature, time and the effect of carbon content were considered to obtain a wide range of tempering parameter which can be used to predict the hardness of the tempered structure. The main theme of Hollomon-Jaffe tempering parameter is that for a specific material, if H-J parameters are similar for different tempering temperature and time then they would provide a similar degree of tempering response.

$$TP_{H-J} = T[c + \log(t)] \tag{2-2}$$

where, TP_{H-J} is the H-J tempering parameter, T is the temperature (K), c is a material constant related to martensite C content and t is the tempering time (s).

2.5 Microhardness and strength of tempered martensite

2.5.1 Microhardness

As previously discussed in section 2.4.1, there are four sequential and overlapping stages occur during tempering of Fe-C martensitic steels which eventually reduces strength of martensite and increases ductility. At initial stage of tempering, carbon atom segregates into the lattice defects (dislocations) and various boundaries and precipitation of transition carbides occur below 200°C. In this stage, a little change of microhardness (Figure 2-15) is identified due to loss of tetragonality of martensite as carbon atoms diffuse from the octahedral interstitial sites. This stage is followed by the reduction of dislocation density by annihilation and recovery process above 300°C. In addition, the decomposition of retained austenite also observed; nevertheless, a negligible fraction of retained austenite usually existed in a low carbon martensitic steel which has insignificant effect on the microhardness reduction during tempering. Prolong tempering at higher temperature (over 300°C) reduces the microhardness of the sample significantly due to greater recovery and Ostwald ripening of cementite as noted by the large hardness drop in Figure 2-15.

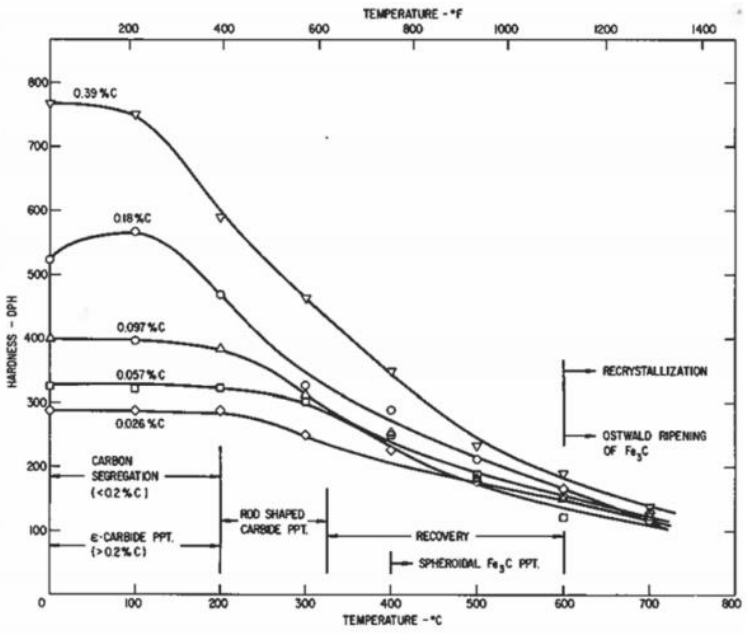

Figure 2-15 Hardness change in Fe-C martensite tempered for 1 hr as a function of tempering temperature [33, 57]

2.5.2 Tensile strength

As-quenched martensite possesses the highest YS and UTS compared to all other steel alloys; however, it has limited toughness owing to the lower strain elongation with rapid work hardening. Since as-quenched sample subjected to tempering, the UTS of the tempered martensite decreased significantly [79-82] due to softer ferrite matrix formed by the migration of carbon atoms from the octahedral lattice sites of martensite. Tempering can favor the elastic limit, Swarr ad Krauss [79] reported that the YS of martensite increases from 700 MPa to 910 MPa while sheet is subjected to tempering at 400°C for 1 min; however, UTS reduces by 450 MPa (from 1500 MPa to 1050 MPa) [79]. Figure 2-16 shows the changes of YS and UTS of tempered martensite as a function of tempering temperature and time [81]. Both strengths decrease continuously with tempering temperature and time suggesting that tempering has identical influences on the YS and UTS. It can be noted that a higher tempering temperature and a longer tempering time significantly affects the strength of the samples. However, tempering temperature has pronounced effect on the strength reduction compared to tempering time as also confirmed by other researchers [80, 82].

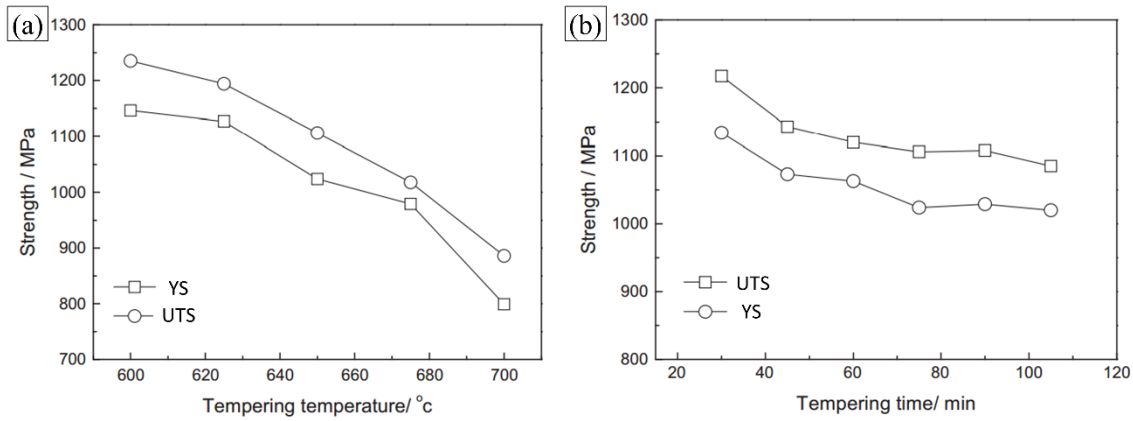

Figure 2-16 The changes of the YS and UTS of 0.25 wt.% C martensitic steel during tempering plotted as function of (a) tempering temperature, and (b) tempering time [81]

2.6 Plastic deformation of as-quenched lath martensite

Plastic strain on the lath martensite deforms the martensite substructure and introduces a high amount of dislocation density as studied by Swarr and Krauss [79]. Figure 2-17(a) shows a TEM micrograph of the autotempered lath martensite prior to deformation; some of the autotempered carbides are highlighted with the dotted circles and the lath boundaries are indicated by the arrows. A uniformly distributed dislocation density can be observed with a magnitude between 10^{10} and 10^{11} cm^{-2}. When the lath martensite undergoes a tensile deformation process, a well-developed dislocation cell structures are observed as shown by large arrows in Figure 2-17(b). A pile-up dislocation is found at the lath boundaries (marked with black arrows in Figure 2-17(b)) which is also observed by Kim et al. [80] where they found a pile-up dislocation at lath boundaries in the region where the sample underwent necking during tensile loading. Lath boundaries are considered to be the low-angle boundaries with a misorientation angle less than 3° thus bypass the dislocation propagation. However, it has also been shown that dislocation pile-up occurs at lath boundaries until a critical stress is reached afterwards dislocation emission occurs [83, 84].

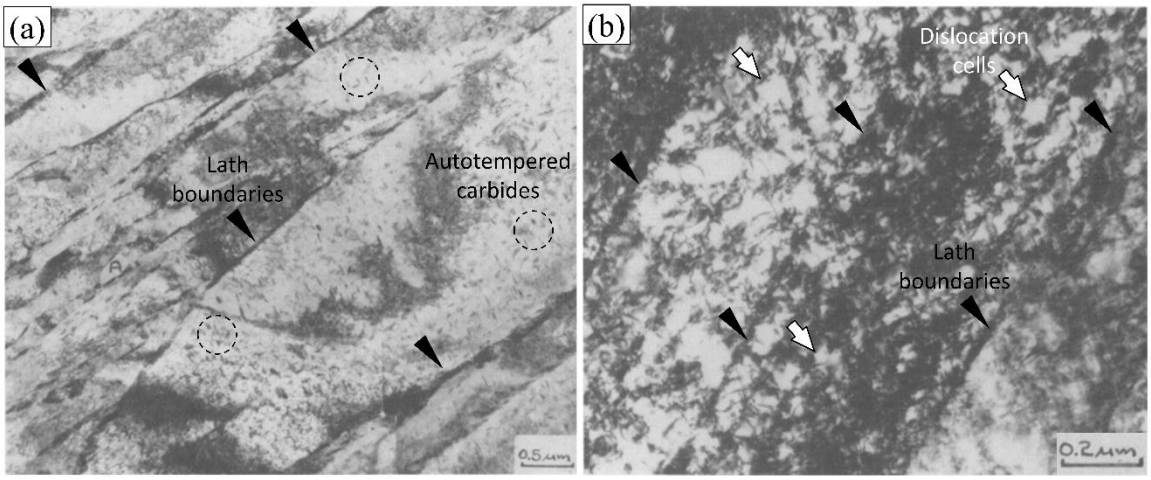

Figure 2-17 (a) Bright-field TEM micrograph of as-quenched autotempered Fe-0.2 wt.% C lath martensite; autotempered carbides are marked with dotted circles and arrows indicate the lath boundaries. (b) TEM micrograph of tensile deformed as-quenched Fe-0.2 wt.% C lath martensite; dislocation cells and lath boundaries are shown by large and small arrows, respectively [79]

Figure 2-18 shows the Vickers microhardness and dislocation density as a function of cold-rolling reduction of ferritic steel [85]. The microhardness of the samples increased with the percentage of cold-rolling reduction as shown in Figure 2-18(a). The material becomes work hardened when subjected to the cold-rolling reduction of the sheet thickness [85]. Cold-rolling reduction also increases the dislocation density in the samples thus strengthened the material by work hardening (Figure 2-18(b)). An abrupt increases of dislocation density is observed below 20% reduction of the sheet thickness afterwards dislocation density remains nearly constant.

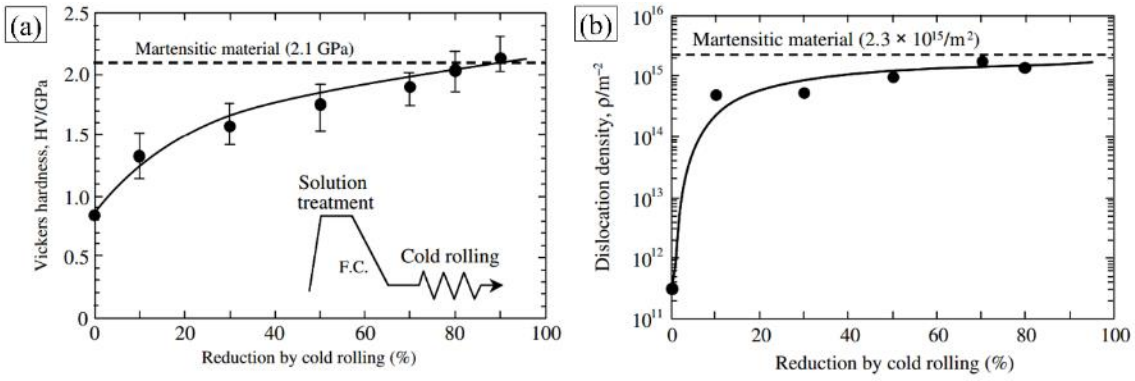

Figure 2-18 (a) The plot of measured Vickers microhardness as a function of cold-rolling reduction of ferritic steel, and (b) dislocation density as a function of the cold-rolling reduction [85]

2.7 Laser beam welding

LASER is an acronym for **L**ight **A**mplification **S**timulated by the **E**mission of **R**adiation [86]. Lasers produce a collimated and coherent beam of light (coherent: waves of one wavelength all in phase). Coherent beam of light of a single wavelength can be focused on a much smaller spot size which amplifies the power density. The laser is a high power density process that provides an unique welding capability to maximize penetration with the minimal heat input. The weld is formed as the intense laser light rapidly hits the material surface (typically in fractions of milliseconds). Based on the power density and the focus spot size, the laser welding can be categorized as: conduction mode, transition "keyhole" mode, and penetration or "keyhole" mode (Figure 2-19(a)). Among the three types of laser welding methods, the keyhole or deep penetration mode welding is the most

widely used form of welding. In this mode, the laser is focused on a workpiece with a narrow beam size which ensures a high power density ($\geq 10^5$ W/cm^2), thus the metal vaporizes and opens up a blind hole in the molten metal pool, and typically known as "keyhole". Vapor pressure inside the "keyhole" holds back the surrounding molten metal and kept this hole open during the process. The metal vapor also re-radiates laser energy into the molten metal along the side wall of the keyhole, thus transfers energy through the entire depth of the keyhole and results a weld with a deeper aspect ratio (depth/width ratio > 1.5).

Conversely, in conduction mode of welding, due to low power density (wider beam), the laser beam interacts with only surface of the materials being welded. The energy is transferred to the atoms at the surface of the materials and heated up atoms which then transfer heat to atom below the surface of the materials. Therefore, the heat transferred as a conduction mode, hence called conduction mode of welding (Figure 2-19(a)). Conduction mode of welding only achievable when low power density with considerably wider beam size is used (Figure 2-19(b)). Another form of laser welding which is called transition "keyhole" welding is produced by a laser with medium power density which results more penetration than the conduction mode due to the creation of "keyhole". However, due to medium energy density, the welds become shallow with a weld aspect ratio of 1.

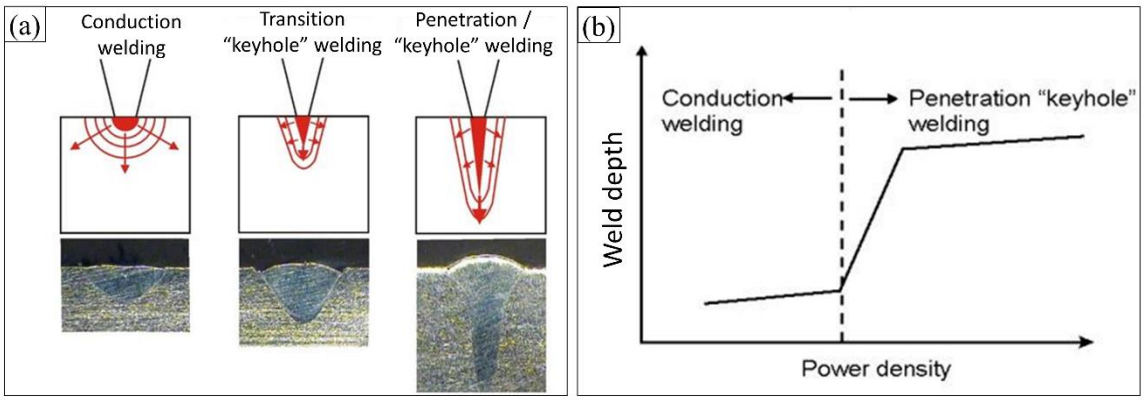

Figure 2-19 (a) A schematic representation of conduction, transition "keyhole", and penetration or "keyhole" welding, and (b) a relationship between laser power density and weld penetration [87]

2.7.1 Thermal cycles in welding

The thermal cycle involved in the welding process can be obtained from the fundamental heat transfer equation. The analytical solution of the heat transfer equation was provided by Rosenthal [88]. In Rosenthal solution, the welding parameters such as welding current, voltage, welding speed, and weld geometry are taken into account to simplify the heat source. 2D analytical Rosenthal model is expressed as:

$$T - T_0 = \frac{Q}{2\pi k_s t}\exp(\frac{-xV}{2\alpha_s})K_0(\frac{rV}{2\alpha_s}) \quad (2\text{-}3)$$

where, T is temperature (K), T_0 is the initial sheet temperature (K), Q is the input power (W), k_s is the thermal conductivity of the material at solid state ($Wm^{-1}K^{-1}$), α_s is the thermal diffusivity of the solid (m^2s^{-1}), $\alpha_s = \frac{k_s}{\rho_s C_p}$; ρ_s is the density of the solid (kgm^{-3}), C_p is the specific heat of the solid ($Jkg^{-1}K^{-1}$), t is the thickness of the sheets (m), V is the welding speed (ms^{-1}), r is the radial distance from the heat source location, given by:

$$r = \sqrt{x^2 + y^2} \quad (2\text{-}4)$$

2.7.2 Phase transformation during laser beam welding

During welding of structural steel by means of a fusion welding process, several zones with different microstructures are formed depending on the imposed thermal cycles. The original microstructure of the as-received material undergoes different microstructure changes which are categorized as the fusion zone (FZ), and heat affected zone (HAZ). Solid state phase transformations occurred adjacent to the FZ, which is referred to the HAZ, and the HAZ areas are sub-divided into various zones depending on the transformation temperature. The tempered zone refers to the zone where temperature lies between 200°C and Ac_1 line, the BM is transformed into different phases and residual stress are relaxed [89]. Approaching the FZ, when temperatures reach between Ac_1 and Ac_3, the microstructure partially transforms into austenite, which upon cooling to room temperature transforms into different phases, this zone is referred to as partially transformed zone. When the temperature exceeds the Ac_3 line, the microstructure completely transforms into austenite; therefore, it refines the microstructure which is defined as the recrystallized zone.

At higher temperature, adjacent to the fusion boundary, the entire austenite phase can grow thus called as the grain growth zone; the entire transformation processes are schematically presented in Figure 2-20.

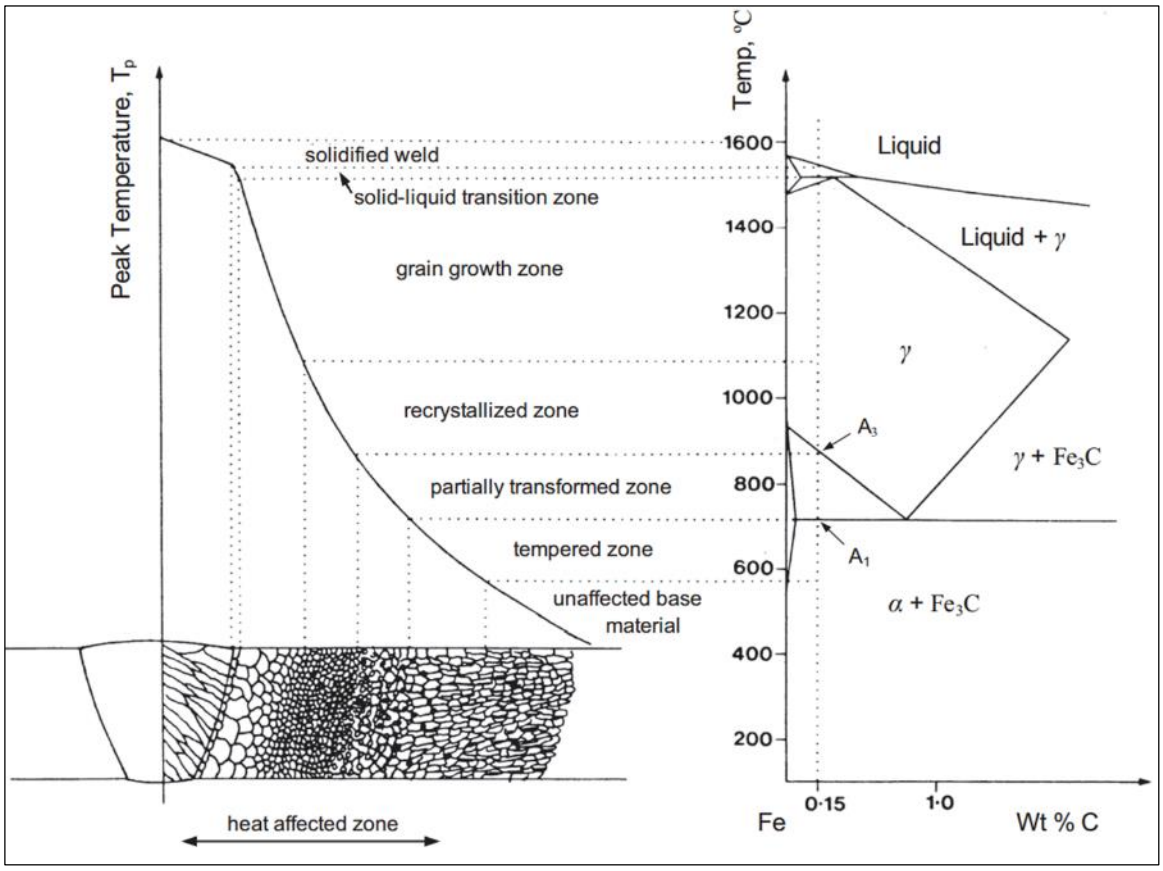

Figure 2-20 A schematic diagram of the various sub-zones of the HAZ approximated corresponding to the 0.15 wt.% C indicated on the Fe-Fe_3C equilibrium diagram [89]

2.8 Summary

Throughout the literature survey on physical metallurgy of steels and kinetics of martensite tempering the following major points can be drawn:

1. The UTS of DP steels depends on the volume fraction of the hard martensite phase, and the martensite carbon content. As the volume fraction and the carbon content of martensite increases the UTS of steel increases; however, the ductility of steel decreases.

2. An atom probe tomography analysis reveals a complete carbon segregation into the dislocation lines at lath boundaries in the form of Cottrell atmosphere or a film-like retained austenite during martensitic transformation. The width of the Cottrell atmosphere was reported to be about 7 nm width.
3. Lath martensite was found to be highly chemically and mechanically heterogeneous thus was considered to be a composite structure of the hard and soft phase. Nanohardness measured at coarse lath center was significantly lower than the one observed in the fine lath at vicinity of the lath boundary.
4. Tempering of martensite reduces the strength (UTS and microhardness) of martensite by forming various carbides, and soft ferrite matrix. The factors such as tempering temperature, tempering time, mode of heating (i.e. heating rate), defect density (i.e. dislocation density), and carbon content of martensite significantly affects the strength of the tempered martensite.

3 Experimental Methodology

3.1 Materials

Different grades of DP and martensitic steels are used in this investigation. The chemical compositions, phase fractions, and the mechanical properties of the materials are provided in Table 3-1, Table 3-2, and Table 3-3, respectively.

Table 3-1 Chemical composition of the investigated steels

Grade / Chemistry	HSLA	DP780 (FMB)	DP980 (Steel A)	DP980 (Steel B)	Martensitic (M220)
C	0.08	0.14	0.15	0.09	0.23
Mn	0.8	1.91	1.5	2.1	0.38
Si	0.5	0.286	0.3	0.3	0.199
Cr	0.0	0.247	0.0	0.2	0.024
Mo	0.0	0.104	0.0	0.3	0.004
Al	0.05	0.026	0.05	0.05	0.062
Ni	0.0	0.02	0.0	0.0	0.013
V	0.0	0.004	0.0	0.0	0.003
Nb	0.0	0.001	0.0	0.02	0.001
Ti	0.0	0.022	0.0	0.03	0.039
CE_N [90]	0.23	0.39	0.41	0.56	0.31

Table 3-2 Microconstituent fractions and the mechanical properties of the materials used in this work

Grade / Microconstituents	HSLA	DP780 (FMB)	DP980 (Steel A)	DP980 (Steel B)	Martensitic (M220)
Martensite (%)	-	24	56	38	100
Bainite (%)	-	13	-	7	-
Retained Austenite (%)	-	-	<1	9	-
Ferrite (%)	100	63	43	46	-

Table 3-3 Mechanical properties of the materials used in this work

Grade / Mechanical Properties	HSLA	DP780 (FMB)	DP980 (Steel A)	DP980 (Steel B)	Martensitic (M220)
Yield Strength, YS (MPa)	401	485	697	618	1340
Ultimate Tensile Strength, UTS (MPa)	548	763	1083	998	1555
Elongation (%)	20	19.23	12.2	14.0	3.3

3.2 Laser beam welding

3.2.1 Diode laser welding

Diode laser welding (DLW) was performed using Nuvonyx 4 kW diode laser system equipped with a six-axis Panasonic robotic arm with a 0.5 × 12 mm rectangular laser beam. A full penetration weld was obtained with a combination of power and speed of 4 kW, and 1.2 m/min, respectively. In order to limit oxidation, helium shielding gas is provided in front of the molten pool with a flow rate of 30 l/min using a 6 mm diameter soft Cu tube.

3.2.2 Fiber laser welding

FLW was conducted in an IPG Photonics Ytterbium Fiber Laser System (YLS-6000-S2) integrated with six-axis Panasonic robotic arm using various laser power and speed as provided in each Chapter separately. The focal length, spot size, and fiber core diameter were 200 mm, 0.6 mm, and 0.3 mm, respectively; detailed description of the laser properties can be found in Table 3-4.

Table 3-4 Fiber laser characteristics used in this study

Laser Type	Laser Source		Laser Head		Beam	Fiber
	Make	Model	Make	Focal Length	Spot Size	Fiber Core
Ytterbium Laser System	IPG Photonics	YLS-6000-S2	Laser Mechanisms	200 mm	0.6 mm Diameter	0.3 mm Diameter

3.3 Heat treatment and tempering

3.3.1 Furnace heat treatment

Isothermal tempering was carried out in a conventional muffle furnace; various peak temperatures were applied with various tempering durations. The heat treated samples were cooled from the peak temperature to room temperature in an air atmosphere.

3.3.2 Dilatometry and Gleeble testing

In order to investigate the effect of heating rate on the precipitation kinetics of martensite tempering, the strain changes during tempering of the samples to 1000°C were examined by dilatometric tests. The experiments were carried out in a DSI Gleeble 3800 thermo-mechanical simulator. The specimens of 20 × 100 × 1.8 mm^3 were heated above the Ac_1 line with heating rates of 0.5°C/s to 500°C/s, and the cooling rate 25°C/s was kept constant. The dimensional changes (transverse width) of the samples were measured using a quartz push rod linear variable differential transformer (LVDT) positioned at the mid-length. The K-type thermocouple (TC) was used to measure the actual temperatures and recorded along with the strain data. To ensure the size of the isothermal zone was sufficient for TEM analysis, a thermal gradient map of the samples during heating and cooling was determined using TC measurements. Four samples (shown in Figure 3-1) where equipped with additional TCs welded at corner and edge points, placed according to the required size for the TEM samples. The thermal gradient results obtained with the fastest heating rate showed a reduction in temperature of less than 2% at edge compared to the central control value. This is considered an acceptable accuracy for the purpose of TEM microstructural analysis. It is noted here that the Gleeble's manufacturer gives only 1% accuracy of the control TC itself. A 10 mm × 10 mm sample was cut from the center of the heated sheets (Figure 3-2) for the Vickers microhardness, SEM, TEM and EBSD analysis. The measured thermal profiles during Gleeble heat treatment are schematically presented in Figure 3-4. The corresponding values of the parameters (heating rates, temperatures, and holding times) can be found in Table 3-5.

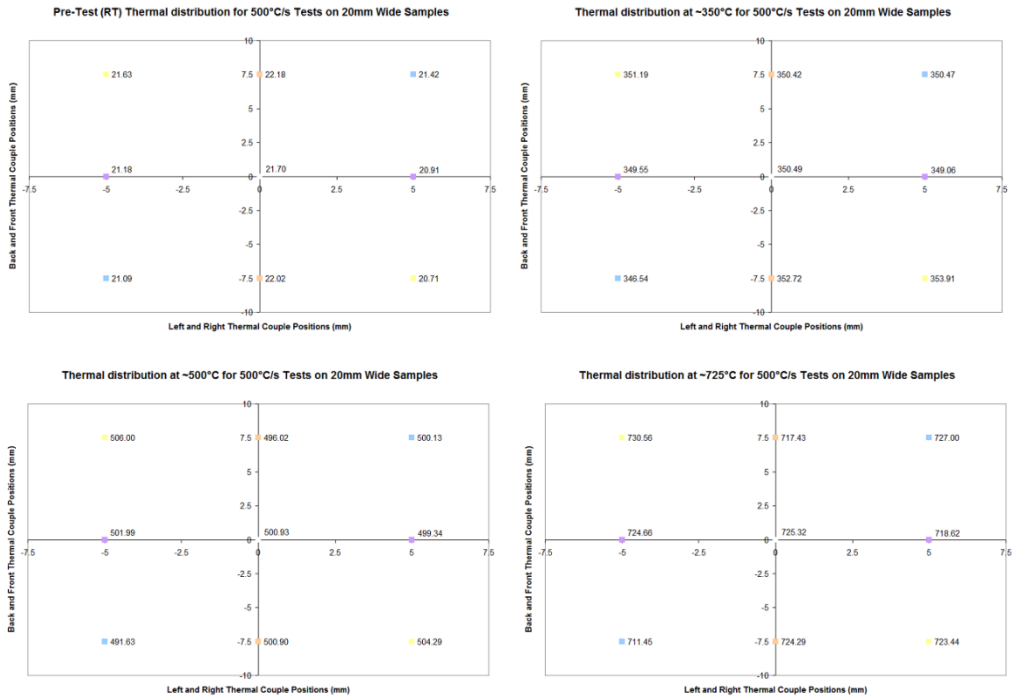

Figure 3-1 Thermal gradient map for 20 mm wide flat strip samples using 500°C/s heating rate

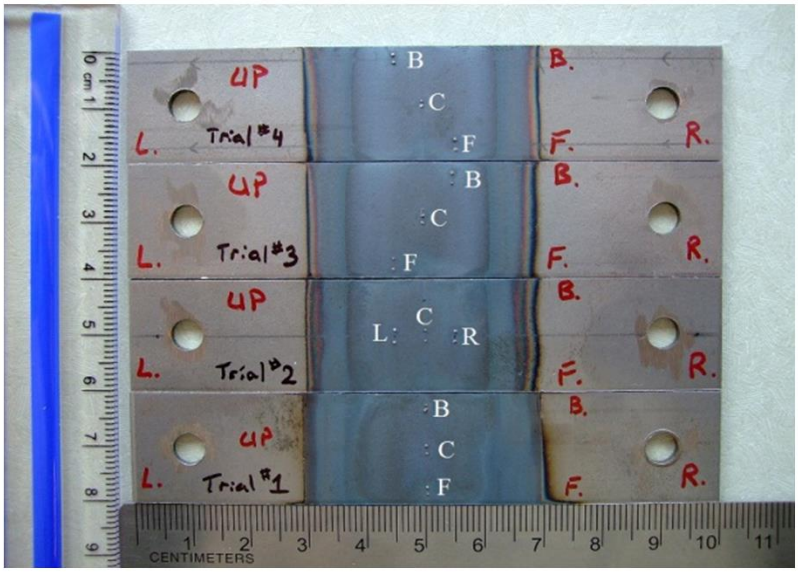

Figure 3-2 Photo of samples used for the thermal gradient mapping

To reduce warping and twisting of the samples during heating and cooling, active force-zeroing was implemented: allowing the left-side grips to move outward during

heating, and inward during cooling (Figure 3-3), until the force reading is brought to zero, accommodating the change in length of the samples.

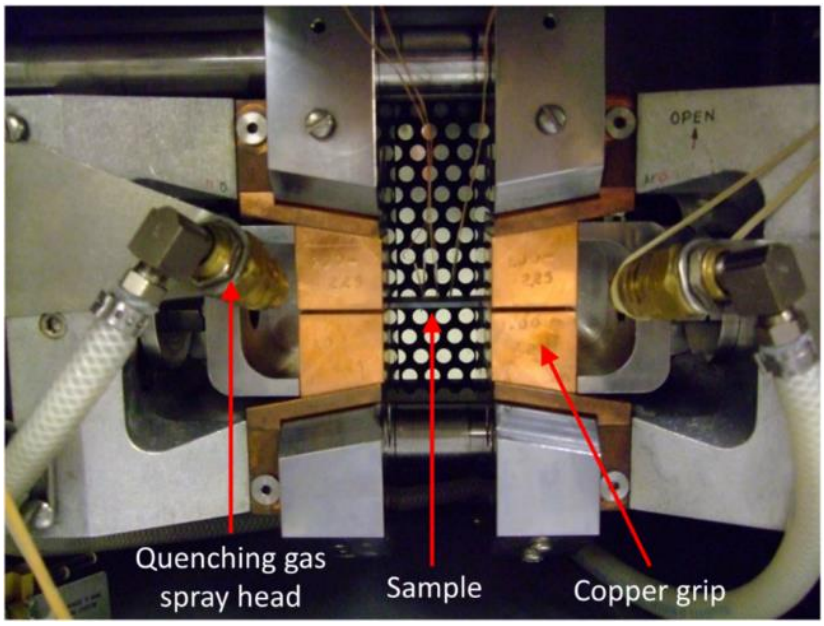

Figure 3-3 Experimental set-up for Gleeble tests showing mounted specimen on Gleeble with thermocouples and argon quenching gas spray heads

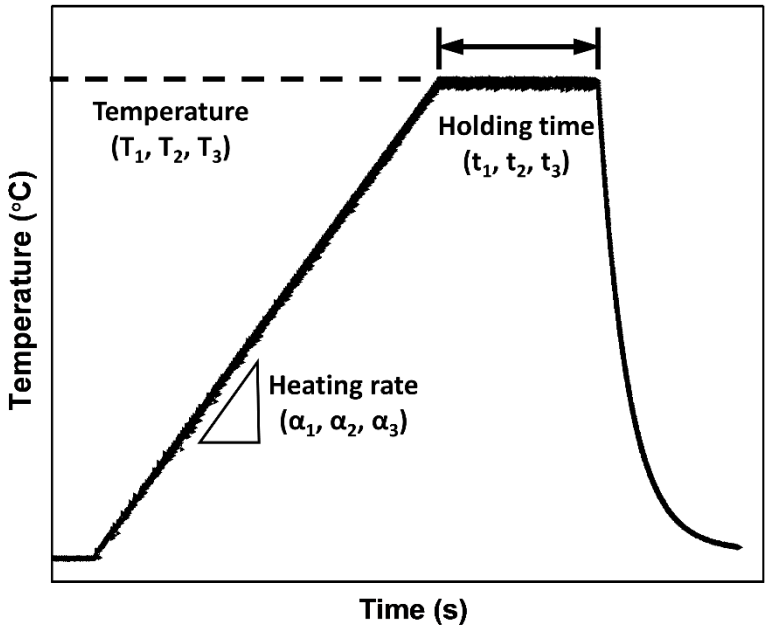

Figure 3-4 Schematic representation of the tempering cycle applied during tempering in a Gleeble thermomechanical simulator

Table 3-5 The list of tempering parameters shown in Figure 3-4

Heating Rate (°C/s)	Temperature (°C)	Holding time (s)		
		t_1	t_2	t_3
	240			
α_1: 1°C/s	330			
	420			
	285			
α_2: 10°C/s	380	1	10	100
	480			
	340			
α_3: 100°C/s	430			
	495			

3.3.2.1 Processing of dilatometry data

The dimensional change of the samples during heating provides an indication of the phase transformation. The specific volume change of the sample is associated with the atomic volume change between the parent and product phase [91]. It can be assumed that isotropic dilatation occurred during phase transformation, and the volume change ($\Delta V = V\text{-}V_0$) with respect to the initial volume (V_0) is a function of relative length change ($\Delta l/l_0$), where l_0, and l are the initial and final length of the samples, and $\Delta l = l\text{-}l_0$.

$$\frac{\Delta V}{V_0} = \left(1 + \frac{\Delta l}{l_0}\right) - 1 \approx 3\frac{\Delta l}{l_0} \qquad (3\text{-}1)$$

Afterward, the lever rule is applied as schematically shown in Figure 3-5 where, phase A is the parent phase and phase B is the product phase. The parameters $x = (\frac{\Delta l}{l_0})_A - \left(\frac{\Delta l}{l_0}\right)_{exp}$, and $y = (\frac{\Delta l}{l_0})_{exp} - \left(\frac{\Delta l}{l_0}\right)_B$ where, $(\frac{\Delta l}{l_0})_A$, and $(\frac{\Delta l}{l_0})_B$ are the theoretical length change of phase A and B, respectively. The fraction of phase A and B can be calculated at temperature T as: $A = \frac{y}{x+y}$, and $B = \frac{x}{x+y}$.

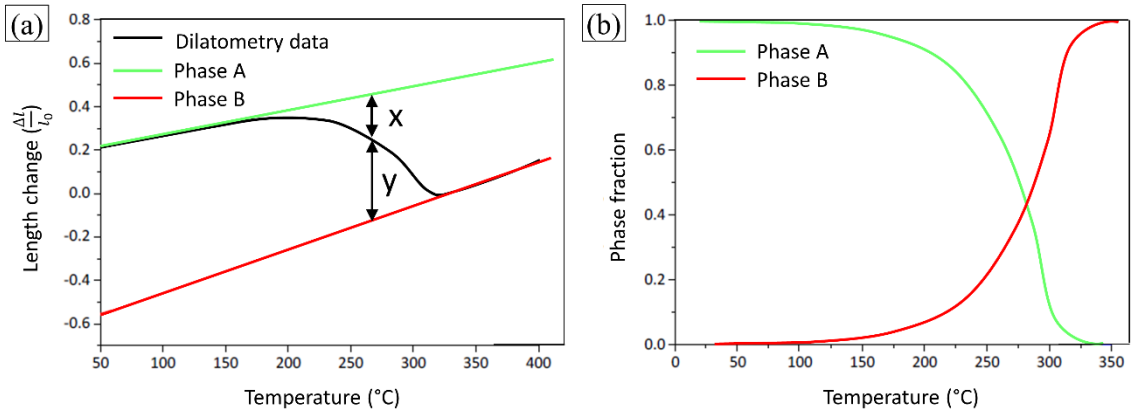

Figure 3-5 Processing of dilatometry data showing, (a) a schematic presentation of the lever rule, and (b) the estimated phase fractions

3.4 Microstructural Characterization

3.4.1 Scanning electron microscopy (SEM)

The samples for the microstructural evolution were prepared using standard metallographic procedures, with final polishing using 1µm diamond media, followed by etching with 2% Nital solution. A JEOL Zeiss Leo 1550 field-emission scanning electron microscope (FE-SEM) was used to characterize the microstructure. The particle size was measured manually with an image analysis software, imageJ, from the several high-resolution FE-SEM images with a magnification of 100,000X; a more than 1,000 particles were measured for each condition. The carbide sizes are presented here are the equivalent circular diameter ($ECD = 2\sqrt{\frac{A}{\pi}}$) of the particles with the equivalent diameter.

3.4.2 Transmission electron microscopy (TEM)

Transmission electron microscopy (TEM) was used to evaluate the microstructure using a JEOL 2010F (Japan Electron Optics Ltd., Tokyo, Japan) electron microscope operated at 200 kV. TEM samples were prepared by using standard twin-jet electropolishing, focused ion beam, and carbon replica extraction methods. For twin-jet electropolishing, the samples were mechanically ground and polished to thin foils with

thickness of 40 to 50 µm, afterward 3 mm disc were punched. The discs were then further thinned in a Struers Tenupol-5 twin-jet electropolishing unit using 10% $HClO_4$ and 90% ethanol containing electrolyte maintained at -45°C with a voltage of 15 V. To prepare the carbon replica samples, a thin carbon film (about 5 nm thickness) was deposited on the surface of the etched (2% Nital solution) samples; then 4% HNO_3 in ethanol solution was used to float the deposited carbon films and collected samples on to the copper grids; detailed description of the carbon replica sample preparation method can be found elsewhere [92].

In order to extract the TEM samples from the narrow SCHAZ, focused ion beam (FIB) method was used. During FIBing the platinum (Pt) coating was deposited on top of the area of interest (i.e. SCHAZ) using the electron beam as shown in Figure 3-6(a); afterward a wedge shape sample was milled from the both sides (Figure 3-6(b)). After final polishing (Figure 3-6(c)) of the wedge, the sample lamella was lifted out with a manipulator inserted and welded to the sample with Pt coating (Figure 3-6(d)).

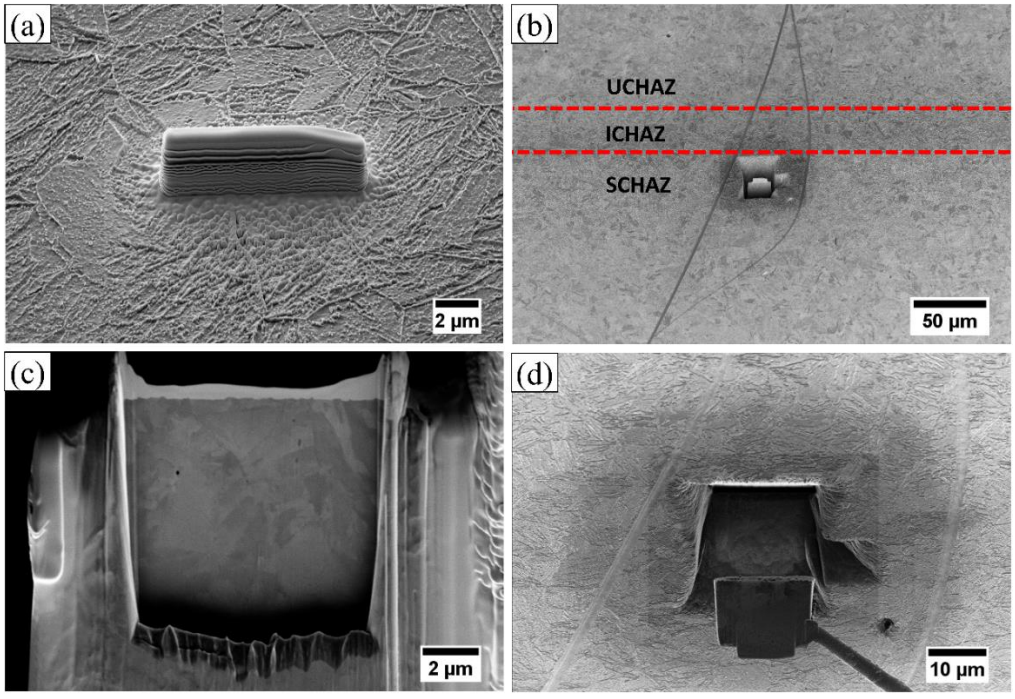

Figure 3-6 FIB method used to extract TEM lamella from the SCHAZ of the fiber laser welded sample showing, (a) platinum (Pt) coating deposited on the area of SCHAZ, (b) cutting and milling of the sample lamella, (c) TEM sample after final milling operation, and (d) extraction of the lamella from the bulk sample using a manipulator

3.4.3 Electron backscattered diffraction (EBSD)

The samples for the EBSD analysis were prepared using mechanical grinding with a series (200 to 4000 grit) of SiC papers and followed by mechanical polishing with 3 μm, 1 μm, and 0.25 μm diamond sprays. For the final sample preparation, a chemo-mechanical polishing was performed using a 0.05μm colloidal silica with Struers MD-Chem polishing cloth for 20-30 mins.

EBSD analysis was performed using JEOL JSM-7000F equipped with a Schottky field emission gun and an EBSD detector. EBSD data was acquired from a 30 × 30 μm area with an acceleration voltage, step size, working distance, and tilt angle condition of 20 keV, 0.05 μm, 15 mm, and 70°, respectively. The post processing of the data was carried out using a commercial software CHANNEL 5 package. By using iterative noise reduction cleaning method, more than 97% indexing rate was obtained. To ensure sharp and relatively noise free, all data were collected with 3 × 3 binning (3 frames background correction).

3.4.4 Synchrotron X-ray diffraction characterization

Synchrotron X-ray measurements were carried out at the 33-ID-D beamline of the Advanced Photon Source (APS) at the Argonne National Laboratory. The experiments at this beamline were conducted in reflection mode. The size of the beam was 2000 μm × 50 μm (vertical cross section) where the 2000 μm side was perpendicular to the plane defined by the direct and diffracted beams. The X-ray photon energy was 11 keV corresponding to a wavelength of λ = 1.12713 Å. The detector was located at a distance of 1406.5 mm from the sample, and a tube filled with He gas along this length was used to avoid air absorption and scattering. The detector was a "Pilatus 100K" with 487 × 195 pixels, with a pixel size of 0.172 mm. The detector was moving with a step size of ~0.133°, and the resulting 600 2D images were integrated by a software at the beamline to create the 1D patterns used for the data analysis. The detector was set to ignore photons with energies <~7-8 keV in order to filter out the Fe fluorescence originating from the steel samples, which significantly lowers the background and improves the quality of the data.

3.4.4.1 Volume fraction of retained austenite

The volume fraction of the retained austenite was estimated from the integrated peaks intensity of ferrite and austenite by the following formulas [93]:

$$f_\gamma = \frac{\frac{1}{N}\sum_{i=1}^{N}\left(\frac{I_{\gamma,i}}{R_{\gamma,i}}\right)}{\frac{1}{N}\sum_{i=1}^{N}\left(\frac{I_{\gamma,i}}{R_{\gamma,i}}\right)+\frac{1}{M}\sum_{i=1}^{M}\left(\frac{I_{\alpha,i}}{R_{\alpha,i}}\right)} \tag{3-2}$$

where, N and M are the number of ferrite and austenite reflection peaks considered, respectively. The subscript i represents the $\{hkl\}$ reflections of the interested spots; ($R_{\alpha,i}$) and ($R_{\gamma,i}$) are the normalization factors of the ferrite and austenite intensities obtained from the intensities of powder diffraction patterns without texture component $I_{th,i}$,

$$R_i = \frac{I_{th,i}}{\Phi_0 V \mu} \tag{3-3}$$

$$I_{th,i} = \Phi_0 r_0^2 \frac{m_{hkl}\lambda^3 |F_{hkl}|^2 V}{v^2} \mu L_P P exp(-2M) \tag{3-4}$$

3.4.5 Differential scanning calorimetry tests

The DSC measurements were performed at the thermophysical property section of the NETZSCH instruments testing laboratory, Burlington, MA, USA, using a NETZSCH model DSC 204 F1. The specific heat is determined by running a baseline and sapphire standard over the temperature range of interest. The sample is then run and the specific heat is calculated by the standard ratio method. Data evaluation is carried out by a comprehensive PC software package allowing computation of peak and onset temperatures, inflection points, partial area integration, specific heat, and transformation energetics.

3.5 Mechanical testing

Mechanical properties of the studied materials were performed using Vickers microhardness, nanoindentation, and tensile testing.

3.5.1 Microhardness tests

Vickers microhardness was measured in a Clemex JS-2000 automated computerized hardness tester under 200 gm (for DP steels) or 1 kg load (for martensitic steel) and 15 s dwell time. Sufficient distance (≥150 μm) was maintained between consecutive indentations to avoid interference from the stain fields developed by the adjacent indents. For the heat treated samples at least 12 indents were made on each sample and the average values are reported here with 95% confidence interval. For hardness measurement across the laser beam welded profiles a high-resolution hardness pattern was used to perform indentation, as shown in Figure 3-7. In order to measure the microhardness in the narrow SCHAZ, additional indents were performed above and below the center indentation line profile.

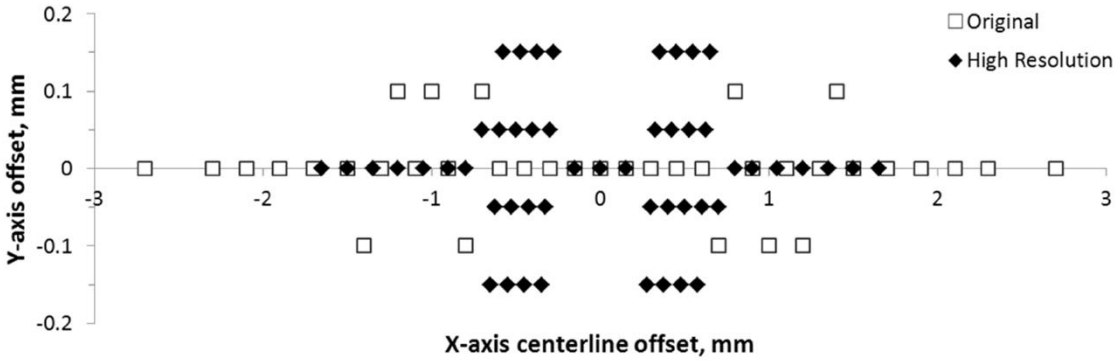

Figure 3-7 The high-resolution indenting pattern used for the microhardness measurement across the welded profiles (reproduced from reference [94])

3.5.2 Nanoindentation tests

The samples used for the nanoindentation study was prepared specially using an additional final polishing in a VibroMet® 2 Vibratory polisher with 0.25 μm colloidal silica for 2 hrs to remove any deformation induced by the prior grinding and polishing steps. Nanoindentation was conducted using a Hysitron Triboindenter TI-900 equipped with a scanning probe microscope in a load control condition with a constant loading rate of 500 μNs^{-1} up to a maximum load of 5000 μN. The hardness values are reported here are the average of 12-16 indents with a 95% confidence interval. A typical loading and unloading curve during indentation with a Berkovich indenter is shown in Figure 3-8(a), where *F*, *h*,

S represents the applied load, displacement, and contact stiffness, respectively. Figure 3-8(b) shows an example of 4 × 4 indented test matrix made on each sample; an additional indent (marked with red arrow in Figure 3-8(b)) was made to identify the sequences of the indents during SEM observation.

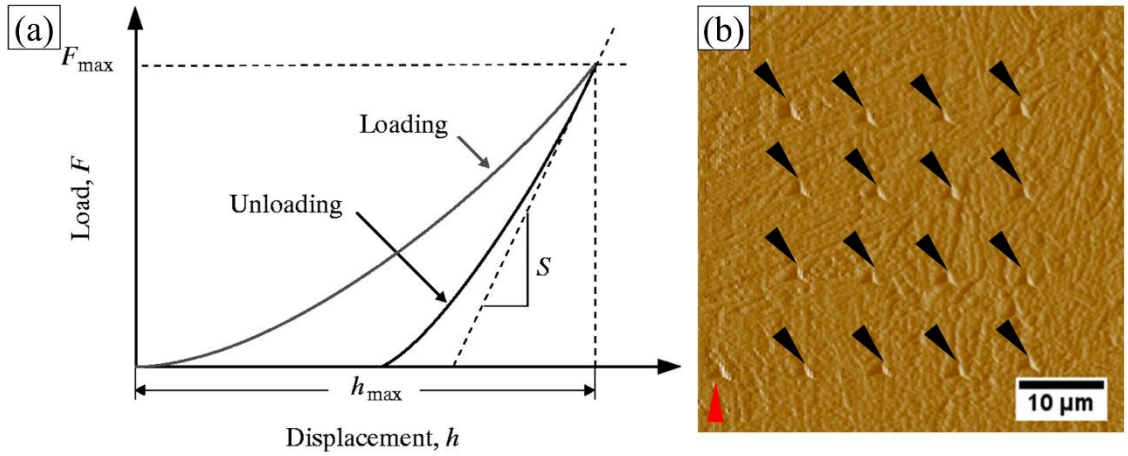

Figure 3-8 (a) A schematic representation of indentation load-displacement curve [95], and (b) a sample 4 × 4 nano-indented test matrix made on a sample

3.5.3 Tensile tests

Uniaxial quasi-static tensile testing was performed using an automated computerized tensile tester with a crosshead speed of 2.54 mm/min. The samples for the tensile testing were prepared according to ASTM: E8 [96] standard. A schematic dimension of the tensile tested sample is shown in Figure 3-9, the welded joint was being at the center of gauge length.

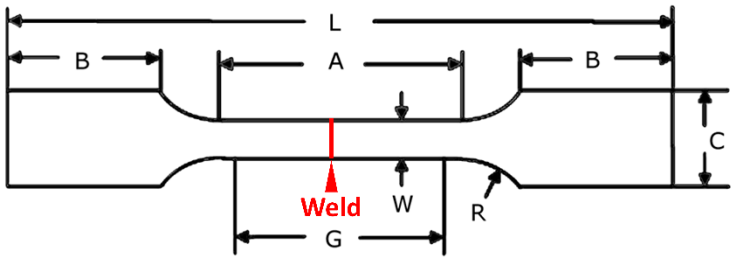

Dimensions in mm	
G- Gauge length	50
W- Width	12.5
R- Radius of fillet	12.5
L- Overall length	200
A- Length of reduced section	57
B- Length of grip section	50
C- Width of grip section	20

Figure 3-9 Schematic representation of the tensile tested samples' geometry [96]

4 Microstructure-properties Correlation of Tempered Martensite in Fiber Laser Welding

4.1 Introduction

In order to understand the tempering kinetics of martensite and its consequence on weld performance, the initial investigation was carried out on a DP980 steel contains about 50% martensite and 50% ferrite and its dissimilar combination with HSLA steel. As the kinetics of martensite tempering is governed by the carbide nucleation, precipitation, and growth processes, these will impart the mechanical properties of the tempered martensite structure. Therefore, the aims of this Chapter are to understanding the tempering kinetics of martensite subjected to a rapid thermal cycle employed using a high-speed fiber laser welding system and its relation to the mechanical performance. The content of this Chapter has been previously published by Saha et al. [97]. This Chapter is divided into two main sections; first, microstructural features of the as-received BM, and the different zones of the HAZ and FZ were evaluated using SEM, and TEM analysis. Emphasis was given to in-depth characterization of the SCHAZ (soften zone). In addition, the weld solidification phenomena, and the effects of chemistry on the solidification microstructure are discussed. Second, the joint performance of the laser welded similar and dissimilar materials were evaluated by performing Vickers microhardness, nanoindentation, and tensile testing. Finally, microstructure-property correlation between the tempered zone and the joint strength were discussed in details.

4.2 Experiments

All experiments were conducted on 1.2 mm thickness of hot dip galvanized DP980 (Steel A) and HSLA steels. The chemistry, and phase fractions and mechanical properties of the steels are shown in Table 3-1, Table 3-2, and Table 3-3, respectively. Welds were made using an IPG Photonics Ytterbium Fiber Laser System, the details of which are listed in Table 3-4. Fiber laser welds were made on butt welding configuration with laser power of

6 kW, welding speed 12, 14, and 16 m/min, and beam focal length of 200 mm on the sheet surface.

4.3 Results

4.3.1 Microstructural analysis

The representative microstructure of the BM of DP980 steel consisted of a ferrite (α, dark regions) and martensite phase (α′, white regions) (Figure 4-1(a)). BM of HSLA steel consisted of a ferrite matrix (α) with carbides (C) distributed inside the grains or along the grain boundaries (Figure 4-1(b)). Figure 4-2 shows the weld profiles of the similar and dissimilar DP980 and HSLA weld. Different microstructural regions in the HAZ of the DP980 side are shown in Figure 4-3.

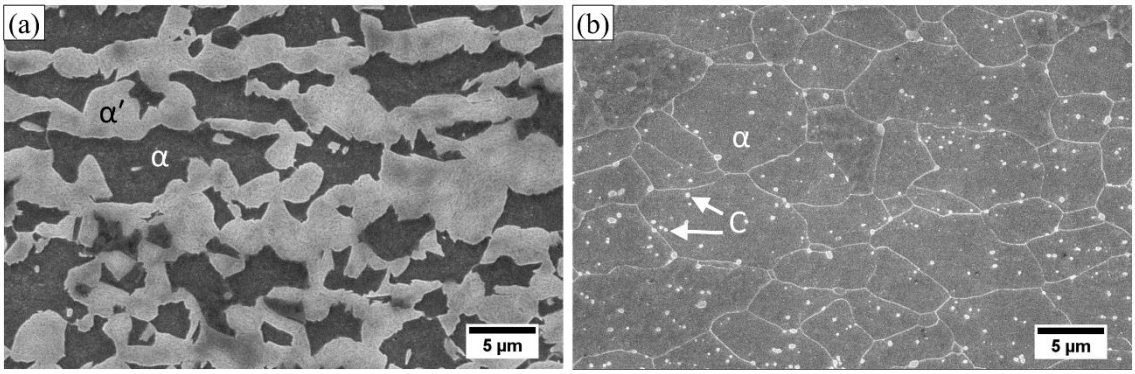

Figure 4-1 Typical SEM microstructures of the as-received materials (a) DP980 (Steel A), and (b) HSLA steel; where α is ferrite, α′ is martensite, and C is carbides

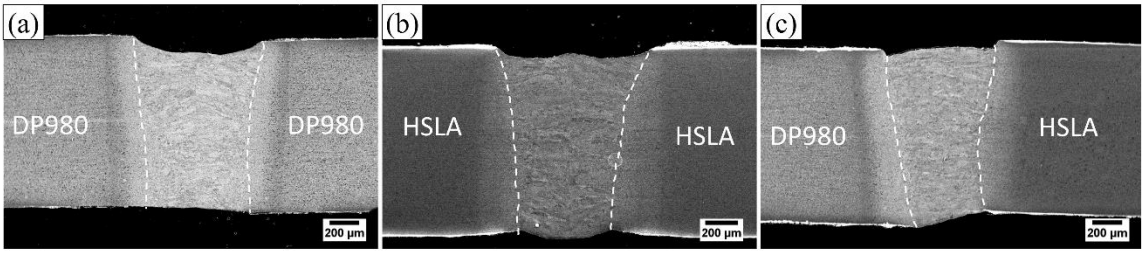

Figure 4-2 SEM micrographs of the full weld profiles for samples welded with a laser power and speed of 6 kW and 16 m/min, (a) DP980-DP980, (b) HSLA-HSLA, and (c) DP980-HSLA

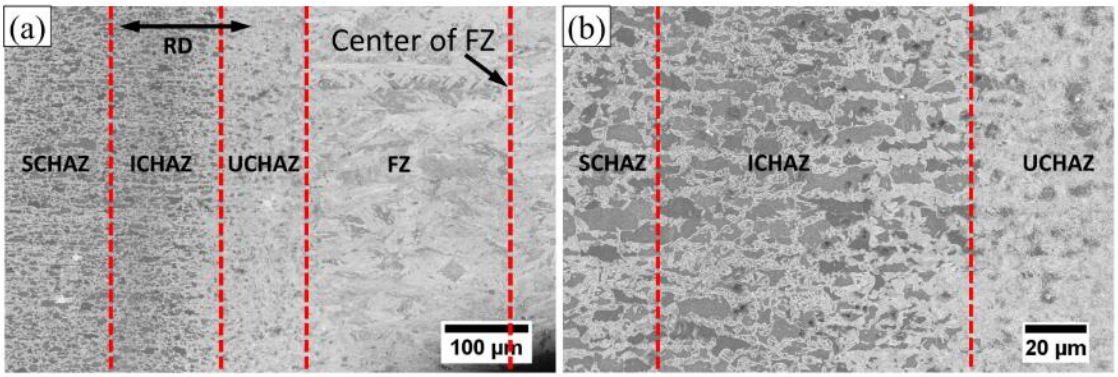

Figure 4-3 SEM micrographs of the HAZ of DP980 side: (a) an overview of the FZ and HAZ, and (b) a magnified view of the HAZ containing uppercritical HAZ (UCHAZ), intercritical HAZ (ICHAZ), and subcritical HAZ (SCHAZ)

4.3.1.1 Intercritical HAZ (ICHAZ)

The ICHAZ temperature is between Ac_1 and Ac_3 line. In this temperature range, the as-received steel partially austenitized which upon cooling transformed to martensite again (marked as "new martensite" represents newly formed martensite), see Figure 4-4(a). It should be noted that the ICHAZ contains a lower martensite fraction compared to the DP980 BM (Figure 4-1(a)); this is attributed to the local incomplete austenitization resulting from the lower austenization temperature just above Ac_1 line.

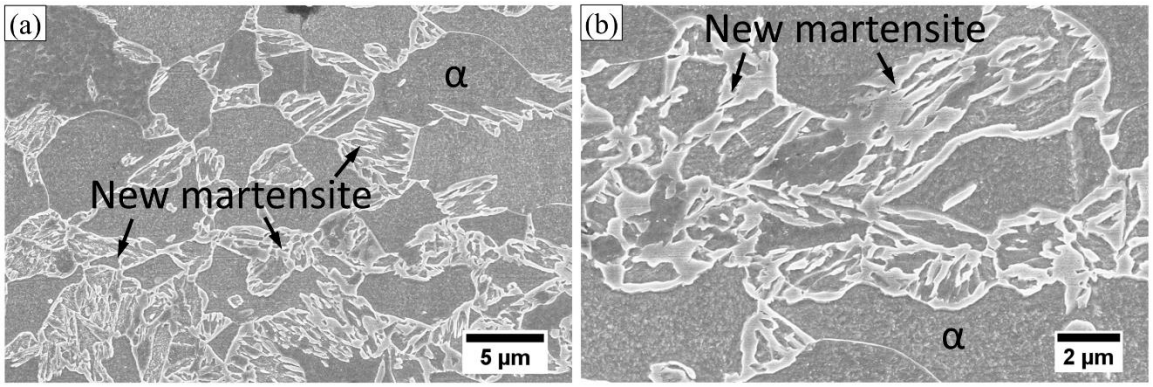

Figure 4-4 SEM micrograph of the ICHAZ (400 µm away from the weld centerline) showing (a) a microstructure combination of the new martensite and ferrite (α), and (b) a magnified view of the new martensite phase

4.3.1.2 Subcritical HAZ (SCHAZ, tempered region at HAZ, soften zone)

During welding, the SCHAZ was exposed to a temperature which is below the Ac_1 line thus the existing metastable martensite phase in the BM of the DP980 steel underwent tempering process and reduced the strength of the zone locally. During tempering, carbon atoms diffused from the carbon supersaturated martensite phase and formed various shapes of carbides such as cementite (Fe_3C). The carbide precipitation kinetics are accelerated by the carbon diffusion at various boundaries; carbon diffusion distance increases with tempering temperature and time. The boundaries (high- and low-angle grain boundaries) and the defect sites (dislocations) present in the martensite phase provide effective nucleation sites for the carbide precipitates. Due to the differences in diffusion energy at these boundaries, the carbide precipitates acquire different a shape, size and number density. The tempered region on the DP980 side of the weld (Figure 4-3), also known as SCHAZ, was observed next to the BM illustrating carbide precipitation at various boundaries (Figure 4-5), which agrees with the literature [7, 8, 72, 98-103]. The shape and size distribution of the precipitated carbides play an important role on the macroscopic strength of the welded joint via precipitation strengthening as explored in the following Chapters.

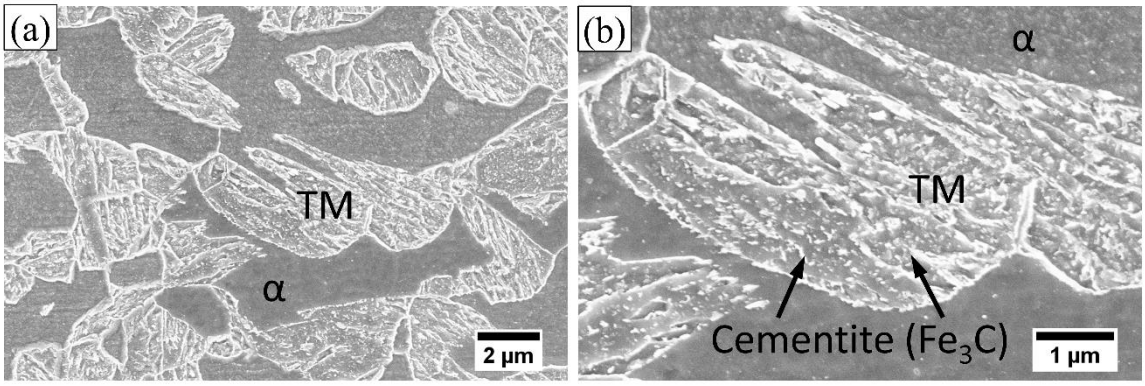

Figure 4-5 SEM micrograph of the SCHAZ (470 µm away from the weld centerline) showing (a) a microstructure combination of tempered martensite (TM) and ferrite (α), and (b) a magnified view of the TM phase with carbide (θ) precipitates on a ferrite matrix

4.4 Mechanical properties

4.4.1 Microhardness

The microhardness profiles for all the welds are compared in Figure 4-6. The microhardness distributions shown in Figure 4-6 are the average of 4-5 indentation line profiles across the welds cross-section. The hardness profile within the FZ of the dissimilar weld was observed to be in-between that of the similar welds; with an increased hardness value on the HSLA side of the FZ compared to the similar HSLA weld; this is also evidence of inadequate mixing. This phenomenon can be attributed to the richer chemistry formed by mixing of the materials resulting in the formation of a higher martensite fraction upon cooling to the room temperature. The composition analysis was carried out by energy-dispersive X-ray spectroscopy (EDX) line scanning to estimate the Mn concentration along the FZ for three kinds of the welded sample. The average Mn concentrations were measured to be (in wt.%) about 1.58, 1.22, and 0.84 for DP980-DP980, HSLA-DP980, and HSLA-HSLA weld, respectively. The estimated Mn concentration also confirmed the presence of the richer chemistry formed by mixing of two dissimilar materials as expected. The FZ hardness of the DP980 weld was observed to be higher when compared to the HSLA weld and dissimilar weld due to the fully martensitic microstructure [98]. It is interesting to note that a hardness reduction was detected in the FZ on the DP980 side just beside the weld centerline; which was attributed to the formation of the softer microstructural phase containing bainite [104]. In addition, the hardness at the centerline of the FZ in the dissimilar weld was closed to that of the similar HSLA weld consisting of bainite and martensite [98]. The hardness in the SCHAZ, which is marked as soft zone (circles) in Figure 4-6, was found to be 50 HV below the hardness of the untempered DP980 steel. Softening in the DP980 steel welds is attributed to martensite tempering, which occurs when the steel is heated between 200°C and its Ac_1 temperature [100, 105, 106]. The minimum hardness of this softened zone varied from 303 to 288 HV, which increased with increasing welding speed, while the FZ also became narrower (800 µm to 600 µm as the welding speed increased from 12 m/min to 16 m/min). However, the FZ width in all the welds, as measured from the hardness profiles, was in the range of 800-900 µm [98].

The width of the HAZ and the FZ is dependent on the welding parameters used and also the welding process [98]. An increased of hardness was detected in the ICHAZ (width: 50-70 μm, indicated with small arrows in Figure 4-6) compared to the SCHAZ due to the newly formed fresh martensite phase resulting from incomplete austenization (Figure 4-4). The volume fraction of martensite in the ICHAZ is clearly lower than the martensite fraction at untempered BM; therefore, microhardness in this zone (ICHAZ, 340 HV) is between the hardness of the BM (358 HV) and SCHAZ (303 HV).

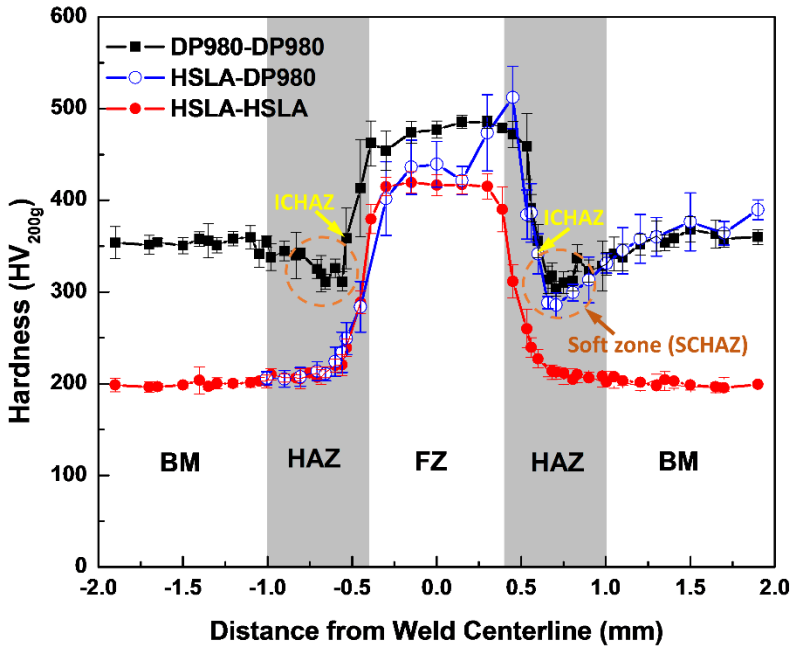

Figure 4-6 Representative hardness profiles across the similar DP980, HSLA, and dissimilar HSLA-DP980 weld. The error bars represent the 95% confidence interval of 5 individual indents

4.4.2 Tensile properties and fractography

The engineering stress vs. engineering strain curves of the BM and the welds of DP980 and HSLA steel are shown in Figure 4-7. At least three tensile samples were tested for each condition. The BM of the DP980 steel exhibits the highest UTS (1097 MPa) and elongation (12.9%) due to the higher fraction of martensite phase; alternatively, the BM shows minimal YS (719 MPa) compared to the welded samples (Table 4-1). Increasing welding speed from 12 m/min to 16 m/min decreased the UTS from 1081 MPa to 1041 MPa;

although YS remained nearly same as that of the BM. It can be noted that the YS of the SCHAZ may increase the YS as the upper yield strength and lower yield strength characteristics return [107, 108]; but due to sample geometry, it was not measured as the BM was yielded first. The mechanical properties of the welded specimens demonstrated a reduction from the BM properties. During tensile testing, it was observed that the fracture occurred in the SCHAZ (Figure 4-8(a)); which can be predicted from the microhardness distribution as hardness value was significantly lower in this zone compared to the other locations (Figure 4-6). Necking was not seen in the BM of the fractured specimen, and the heterogeneity of the sample likely contributed to the decrease in the ductility, with a lower load bearing capacity of the soft zone where fracture occurred. It can be asserted that the ductility of the SCHAZ would be much higher than that of the BM in case of DP980 steel [107, 108]. However, as strain was highly localized in the SCHAZ and not over the entire gauge length, the total elongation across the gauge length appeared to decrease.

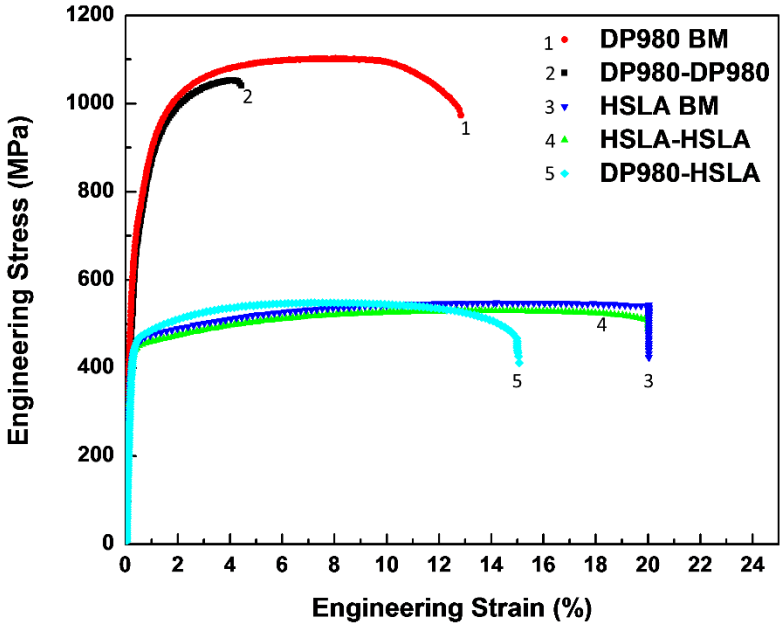

Figure 4-7 Representative engineering stress versus engineering strain of the DP980 and HSLA as-received materials, as well as similar and dissimilar combination fiber laser welds (welding power and speed of 6.0 kW, 16 m/min)

In contrast to DP980 steel, the joint efficiency and elongation of the HSLA welds were not influenced by the welding speed (Table 4-1), these welds consistently fractured in the

BM, which suggested that strain localization occurred in the BM because the weld area had a higher hardness than the unaffected BM. This can be inferred from the hardness distribution pattern (Figure 4-6); in contrast to the DP980 steel welds, there is no softened zone found in the HSLA steel welds; the hardness values throughout the HAZ were much higher than those of the BM. Fracture occurred in the BM away from the center of the FZ in similar HSLA welds (Figure 4-8(b)). Prior to fracture, extensive necking and elongation was observed, eventually fracture occurred at one side of the weldment.

Table 4-1 Mechanical properties of fiber laser welded DP980, and HSLA steels of different welding speeds. The tolerance limit represents the 95% confidence interval.

Steel	Weld Type	Welding Speed (m/min)	YS (MPa)	UTS (MPa)	Elongation (%)	Joint Efficiency (%)
DP980	BM	-	719 ± 5	1097 ± 11	12.9 ± 0.37	-
	Welded	16	725 ± 15	1041 ± 16	4.7 ± 0.5	95
		14	721 ± 17	1085 ± 25	4.8 ± 0.7	99
		12	736 ± 4	1081 ± 3	3.9 ± 0.3	99
HSLA	BM	-	401 ± 1	548 ± 4	20.0 ± 0.5	-
	Welded	16	404 ± 1	530 ± 2	20.0 ± 0.8	98
		14	414 ± 13	538 ± 4	20.2 ± 2.5	98
		12	412 ± 0.4	534 ± 9	20.0 ± 0.4	98

For the dissimilar welds, tensile samples fractured in the HSLA BM (Figure 4-8(c)), as in the case of the similar HSLA weld (Figure 4-8(b)). This was attributed to the lower BM strength of HSLA, which was the weakest area of the dissimilar weld, and exhibited lower hardness values than the SCHAZ on the DP980 side of the joint (Figure 4-6). The DP980 steel similar weld exhibited a greater YS and UTS compared to the similar HSLA and dissimilar welds; however, the dissimilar welds demonstrated slightly higher YS and achieved the material UTS at lower elongation values as half of the joints were yielded, with a reduction in the elongation compared to the HSLA similar welds. However, the UTS of the dissimilar weld was close to that of the HSLA welds; because the DP980 steel side of the weld did not yield and so the plastic deformation only occurred in the HSLA side of

the weld, resulting in the decrease in the elongation when compared to the HSLA-HSLA welds. The minimum concavity of the joint was estimated to be within the industrial acceptable range (below 20%). It was reported that the moderate level (≤20%) of welds concavity (reduction of the thickness of the FZ) and misalignments of the sheets has insignificant effect on the tensile and fatigue properties of the laser beam welded joints as investigated by Westerbaan et al. [109].

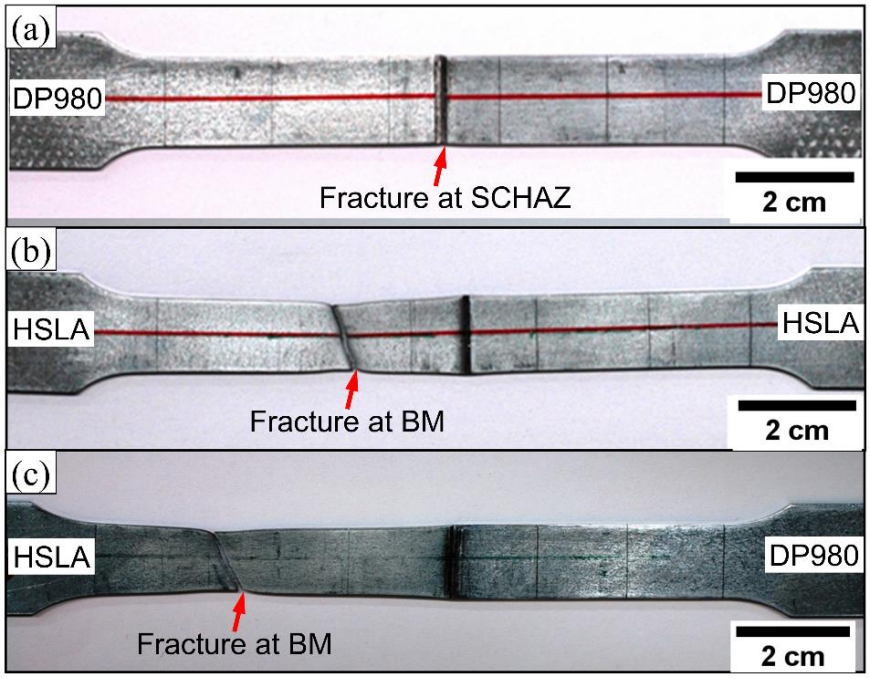

Figure 4-8 Typical tensile fractured locations of the fiber laser welded joints: (a) DP980-DP980, (b) HSLA-HSLA, and (c) dissimilar weld (HSLA-DP980), all of the samples are produced using power: 6 kW and speed: 16 m/min [98]

4.5 Discussion

4.5.1 Effect of chemistry on the FZ microstructure

As discussed earlier, the FZ of the dissimilar weld was composed predominantly of martensite with a bainitic structure; the distribution of structures within the FZ depends on the cooling rate associated with the FLW process. Nd:YAG laser welds (very similar to FLW) have high cooling rates; the normal cooling rates range is about 10^3 to 10^5°C/s [100]. The Rosenthal equation (4-1) was used to estimate the cooling rate within the FZ [110]:

$$\frac{\partial \Theta}{\partial t} = -\frac{2\pi {k_s}^2}{\alpha}\left(\frac{\upsilon \Delta x}{Q}\right)^2 (\Theta - \Theta_0)^3 \qquad (4\text{-}1)$$

where $\partial\Theta/\partial t$ is the cooling rate, k_s is the thermal conductivity of the carbon steel (30 W/m/K), α is the thermal diffusivity of the carbon steel (5.613×10^{-6} m^2/s), υ is the welding speed (m/s), Δx is the sheet thickness (mm), Q is the power input (J/mm^2), Θ, and Θ_0 are temperature (K) of the weldment (1798 K) and the ambient temperature (298 K), respectively. The corresponding values and constants of the parameters indicated in equation (4-1) were taken from reference [100]. Using equation (4-1), the cooling rate in the FZ was estimated to be about 10,000 K/s; which is consistent with the values reported in the literature [100, 110]. This cooling rate was sufficient to form fully martensitic structure in the FZ. In addition, the DP980 steel used in this study contained high C and Mn percentage (Table 3-1), leading to high hardenability by delaying the ferrite and bainite formation thus increasing the critical cooling rate [110]. Therefore, it is reported that the rapid cooling rate (about 10,000 K/s) in the FLW coupled with higher hardenability of the DP980 steel formed a FZ with fully martensitic structure.

In contrast to DP980 steel, HSLA steel formed a FZ microstructure with a mixed microstructure containing bainite and martensite, which is attributed to the lower hardenability of the steel because of the lower alloying additions compared to the DP980 steel (Table 3-1). Mn is an austenite stabilizer and thus lowering Mn content prompts ferrite formation at lower cooling rate; however, the cooling rate in the FLW was rapid for ferrite nucleation resulting in the observed bainitic or martensitic microstructure. This can be better explained by referring to the calculated continuous cooling transformation (CCT) curve (note that the calculated CCT curve for dissimilar weld was done based on the 50:50 fraction mixed in the FZ) of the investigated steels (Figure 4-9), the bainite nose shifts to the right of the curve when more alloying additions are added to the steel. Therefore, due to a lower alloying addition and rapid cooling (about 10,000K/s), the cooling curve can intersect the bainite nose to form a small fraction of bainite along with the predominantly martensite matrix in the HSLA-HSLA and HSLA-DP980 welds [111].

The microstructure containing martensite and bainite microconstituents were detected along the centerline of the dissimilar welds. As discussed in the earlier sections, the HSLA side of the FZ consisted of bainite and martensite phase; whereas the DP980 side of the FZ

was expected to form a similar microstructure due to the mixing of molten steels in the weld pool. The chemistry within the FZ of a dissimilar weld is theoretically considered as the average of those of the corresponding BM considering that the metal was not lost from the weld pool [112]. Furthermore, the cooling rate was same in all the welds as similar welding parameters were used. Accordingly, it was expected that the CCT curve of the steel with chemistry that of the dissimilar weld would lie between the individual curve of the HSLA and DP980 steel (Figure 4-9). Therefore, bainite was expected to form in the FZ of the dissimilar weld; however, the bainite volume fraction would be lower than that formed in the FZ of the HSLA-HSLA weld (Figure 4-6). This was reflected in the hardness profiles as well. For example, the dissimilar weld FZ possessed an average hardness of 425 HV, which was close to the average hardness of the FZ of HSLA weld (415 HV). Therefore, it can be anticipated that identical FZ microstructure i.e. bainite and martensite were formed in both dissimilar and similar HSLA steel welds with slight high hardness in dissimilar FZ because of the richer chemistry. On the other hand, the fully martensitic microstructure in the DP980 steel FZ resulted in higher average hardness (480 HV).

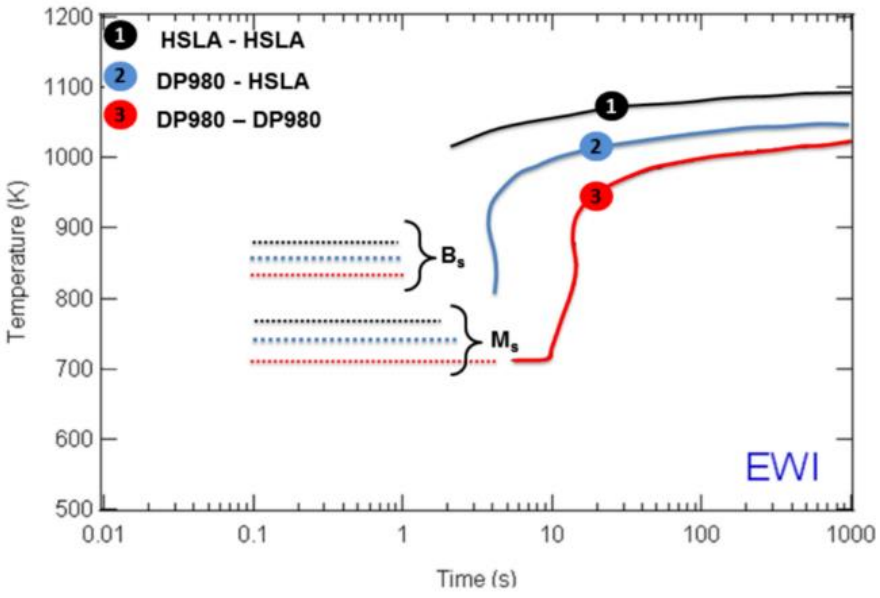

Figure 4-9 Calculated CCT diagram for a representative DP980, HSLA steels, and their dissimilar combination based on the model developed by Bhadeshia and Sevensson [113]

4.5.2 TEM and nanoindentation study of bainite structure

The formation of bainite was confirmed by TEM analysis, the representative TEM micrographs of the dissimilar weld FZ are shown in Figure 4-10. The microstructure well resembled the typical lower bainite sheaf (Figure 4-10(a)) containing multiple variants of carbide precipitates (Figure 4-10(b) and (c)) within bainitic ferrite laths [38, 61]. The average lath width of bainitic ferrite was measured from images of 3-4 different regions to be about 1.5 ± 0.5 μm. Apart from dispersion multi variant carbides precipitate within the bainitic ferrite laths (Figure 4-10(c)); plate-like carbides were formed at the bainitic ferrite lath boundaries (marked as interlath cementite in Figure 4-10(b)). The selected area diffraction pattern (SADP) taken from the bainitic ferrite laths was indexed to be the $[\bar{1}11]_{\alpha}$ zone axis of ferrite (α) (inset of Figure 4-10(c)); the lattice parameter (a) was measured to be 2.87 Å. The dark field image (Figure 4-10(d)), taken using the diffraction spot close to the $(101)_{\alpha}$ diffraction spot (indicated by the arrow) of α revealed the carbides precipitated in a single crystallographic variant within the bainitic ferrite sheaves. The d-spacing measured for this spot was indexed to be the (013) reflection of cementite.

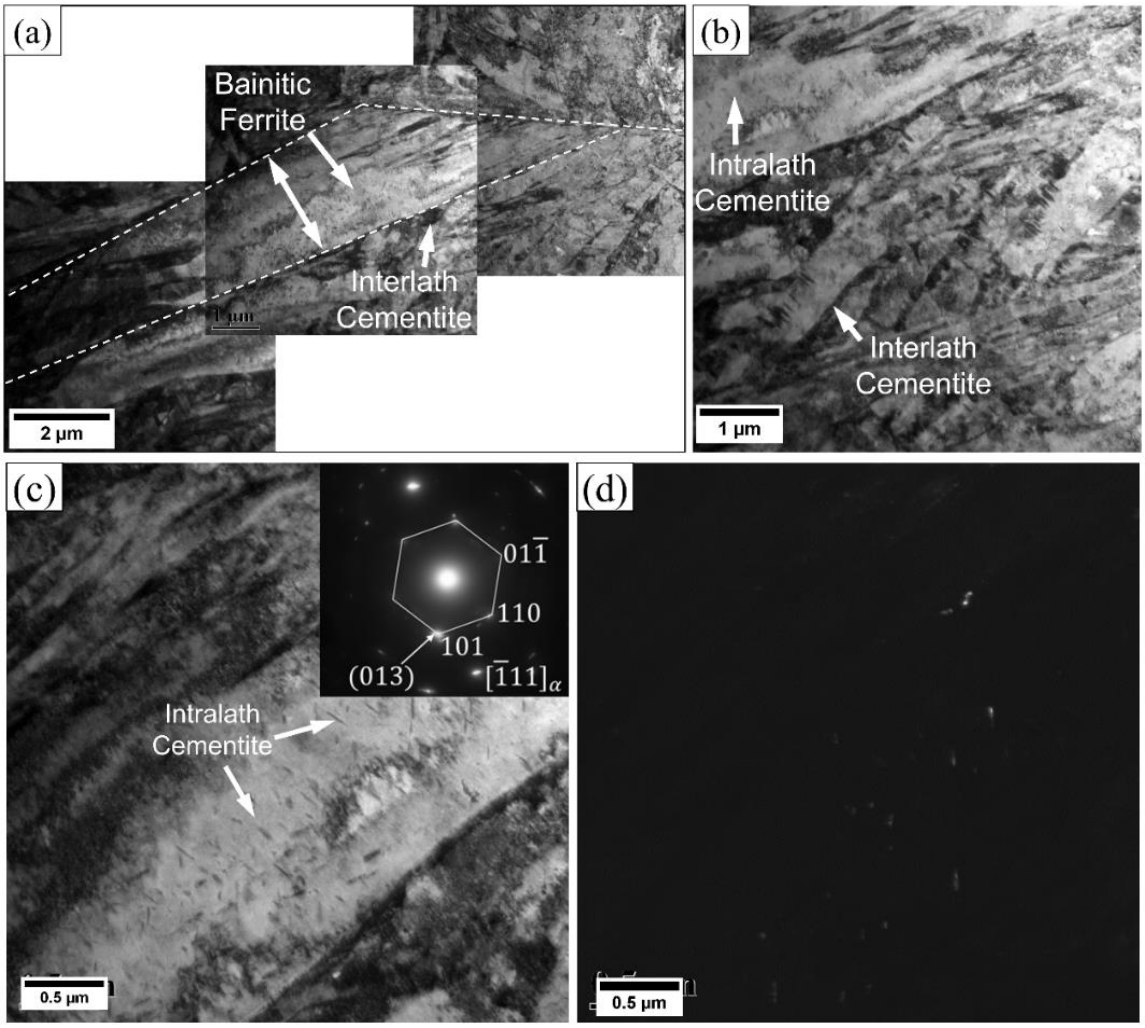

Figure 4-10 Microstructure of dissimilar DP980-HSLA FZ showing: (a) a lower bainite; bainitic ferrite lath (bright region) with interlath cementite plates (dark areas), (b) another view of bainite showing inter and intralath cementite, (c) bright images of bainitic ferrite lath with intralath cementite and corresponding indexed SAD inset, (d) dark field image of (c) taken using θ-Fe_3C (013) spot confirming the cementite

The typical martensite microstructure observed in the FZ (Figure 4-11) showed blocks, which were composed of several parallel martensite laths separated by thin films of retained austenite. The martensite laths showed typical feature of lath martensite phase i.e. a high density of dislocations (Figure 4-11(b)). TEM analysis clearly differentiated the microstructural constituent i.e. lower bainite and martensite in Figure 4-10 and Figure 4-11, respectively, which were seen within the dissimilar FZ.

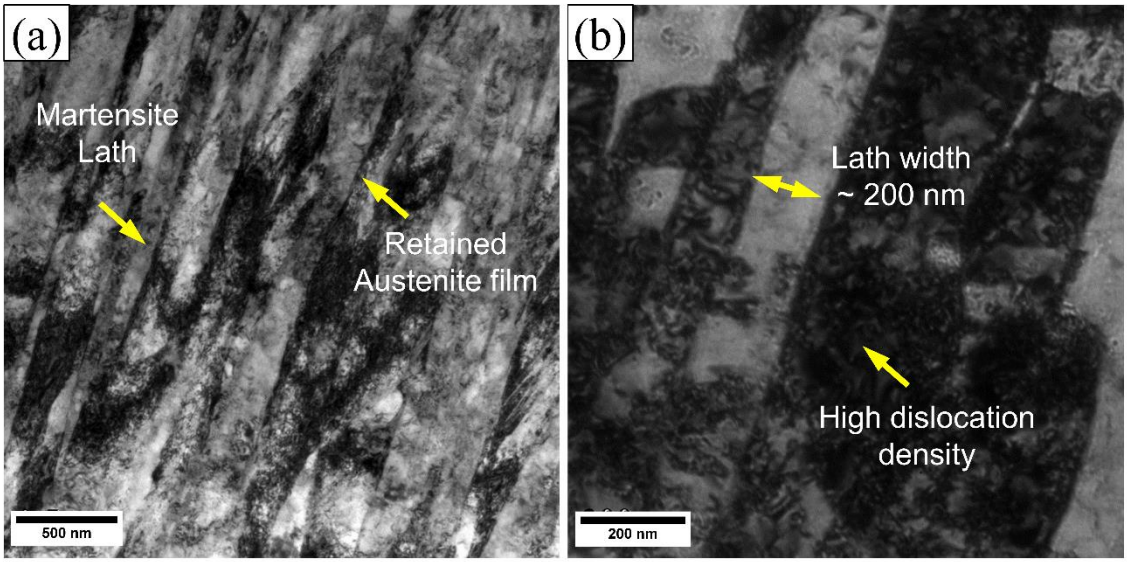

Figure 4-11 Representative TEM images delineating martensite structure in the dissimilar DP980 and HSLA FZ: (a) martensite laths embedded with interlaths retained austenite films, and (b) a magnified view of laths showing high dislocation density

Further confirmation of the bainite structure observed in TEM analysis of the FZ was obtained by nanoindentation. As expected, the martensite and bainite phases showed different nano-hardness within the FZ. The load-displacement curves for indents impression of the lowest (4.11 GPa, for bainite) and highest (6.57 GPa, for martensite) are presented in Figure 4-12(a); and their corresponding SEM micrographs are shown in Figure 4-12(b) and (c), respectively. It should be noted that SEM study indicated that the indents which spanned across both microconstituents had intermediate hardness values. The indent in Figure 4-12(b) clearly indicated that the nano-hardness of the lower bainitic ferrite lath structure. The bainitic ferrite lath width in Figure 4-12(b) was found to be identical (about 1.5 ± 0.5 μm) to that observed in TEM (Figure 4-10(a)). On the other hand, the impression shown in Figure 4-12(c) corresponds to the martensite laths; without any contribution of boundaries between phases to nano-hardness. The SEM image of bainite (Figure 4-12(b)) suggested that the indent on a bainitic ferrite phase shows significant plastic flow of the materials at the periphery of the indent; and also a high indentation depth can be detected in this case. In contrast to bainitic ferrite structure, indentation on finer martensite laths can resist deformation resulting in less pile-up or excursion [114], which was consistent with the load-displacement curves for both the indents (Figure 4-12(a)). The indent on

martensite laths possesses the highest nano-hardness (6.57 GPa) and shows lower indent depth (136 nm) compared to the bainitic ferrite counterpart (170 nm). The measured nano-hardness value of the martensite structure was close to those obtained by Hernandez et al. [115]. The nano-hardness of bainite structure is reported to be 3.8 to 4.9 GPa [116] with the variation in the nano-hardness being strongly correlated to the intrinsic characteristics of the bainite, such as, the fraction of precipitated cementite, crystallographic orientation and the non-uniformity of the dislocation density. In the present study, nano-hardness of bainite was measured in the range of 4.11 GPa to 4.53 GPa and was determined by the locations of the indents i.e. at center of the bainite or in the vicinity of the lath boundaries. Therefore, it was concluded that reduction of hardness detected near the weld centerline of dissimilar weld (Figure 4-6) was due to the formation of lower bainite structure as a result of chemistry dilution.

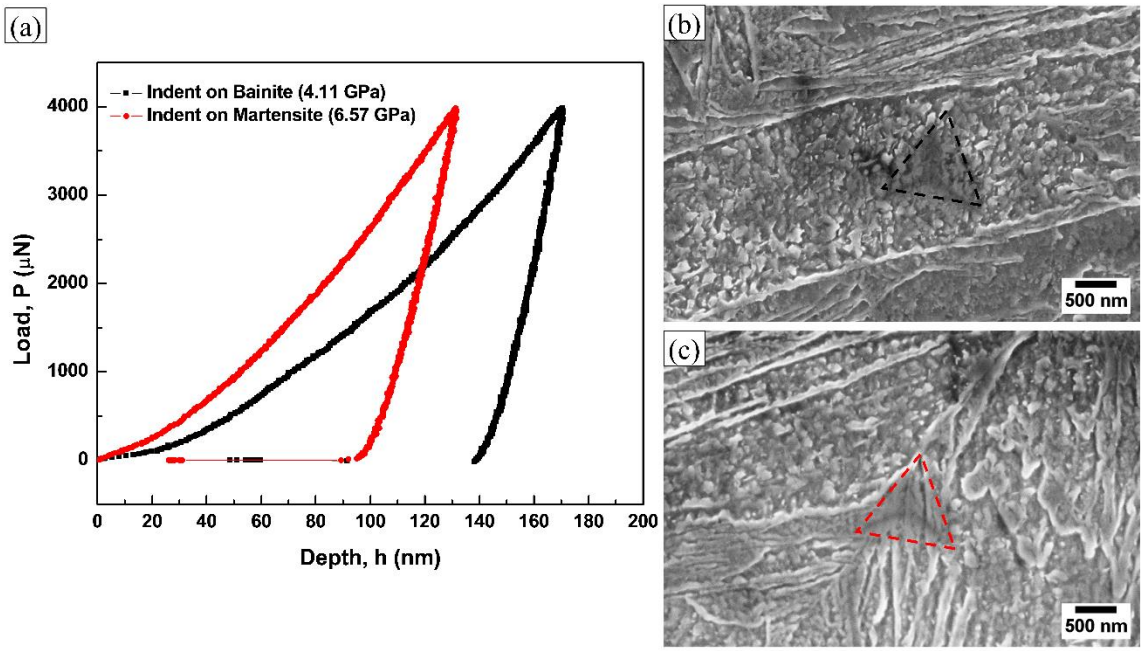

Figure 4-12 Nanoindentation test results on the FZ showing, (a) load-displacement curves (*P-h*) corresponding to indent on bainite and martensite and (b) and (c) showing impressions for bainite and martensite, respectively

4.5.3 Fracture location during tensile testing

The fracture occurred at the SCHAZ for similar DP980 (Figure 4-8(a)) where the microstructure consists of ferrite and tempered martensite (Figure 4-3(b)); therefore, the fracture surface shows dimpled cup-like fracture (Figure 4-13(a)). The tempered martensite structure and HSLA BM microstructure were identical, having a ferrite matrix and precipitated carbides; therefore, the deformation behaviour of these structures was identical leading to typical dimple morphology of the ductile fracture (Figure 4-13(b)). This can also be attributed to the identical strength i.e. hardness of these two structures [115]. Hernandez et al. [115] reported that the nano-hardness of the tempered martensite and ferrite phase are close; therefore indistinguishable fracture morphologies is expected. On the other hand, the fracture in the HSLA and dissimilar welds consistently occurred in the HSLA BM. Figure 4-8(b) and (c) indicated that substantial plastic deformation (necking) of the BM had occurred in the HSLA BM before it fractured at a certain angle to the loading direction (Figure 4-8(c)).

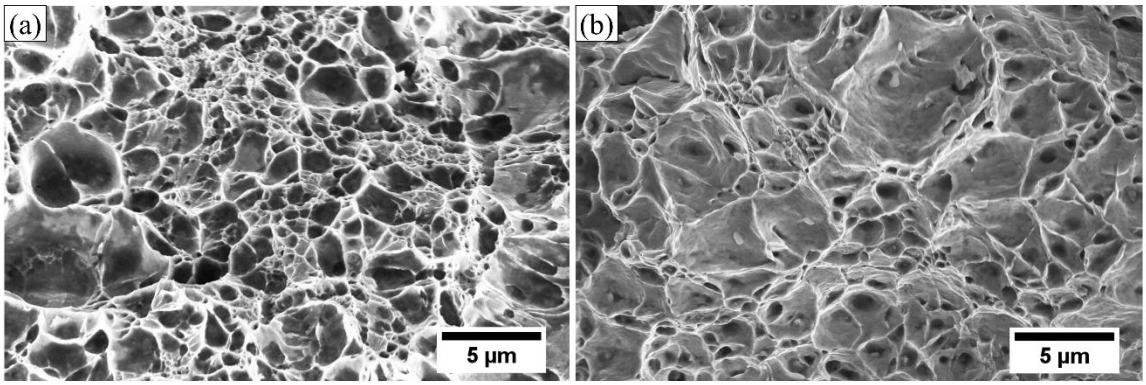

Figure 4-13 SEM micrographs of the tensile fractured surface of a welded joint (a) SCHAZ of DP980, and (b) HSLA BM

4.6 Summary

Fiber laser welded DP980 steel, HSLA steel, and their dissimilar combination were evaluated with respect to microstructure, hardness, and tensile properties. Following conclusions were drawn from this study.

1. Lean chemistry was formed in the fusion zone due to mixing of the two materials which resulting CCT diagram to be shifted to the left side. However, the hardness trend of the dissimilar weld implies that the mixing was not completed which reduces the hardenability due to inhomogeneity.

2. Hardness distributions exhibited a significant variation within the dissimilar weld, implying that the mixing of elements within the FZ was not homogeneous.

3. TEM study revealed that the bainite phase observed in the dissimilar FZ comprised of bainitic ferrite embedded with both intra-lath and interlath cementite precipitates. The bainite structure exhibited a lower nano-hardness (4.5 GPa), with a significant plastic flow of the materials at the periphery of the indents, compared to martensite phase which was harder (6.57 GPa) with little evidence of plastic flow.

4. Tensile strength of the dissimilar welds was close to the HSLA welds, but lower than the DP980 steel welds, with fracture consistently in the HSLA BM as observed in HSLA welds. DP980 welds fractured at the tempered region of the HAZ where softening was observed.

5 Effects of Steel Chemistry and Microstructure on the Tempering Kinetics of Martensite

5.1 Introduction

It has been demonstrated in Chapter 4 that softening in the SCHAZ deteriorated weld performance as joints consistently fractured at the softened zone where martensite is severely tempered. It was also reported that martensite tempering is directly influenced by volume fraction of martensite and alloying addition in the untempered BM. Chapter 5 deals with the two major factors which have a prominent effect on the tempering kinetics of martensite these are steel chemistry, and microstructure. To investigate these two issues, this Chapter is subdivided into two parts. In the first part, a DP780 steel containing minor secondary hardening evoked elements such as Cr, Mo, V, and Nb which were added in the steel in order to obtain a good combination of strength and ductility, was selected for the tempering kinetics analysis. This section shows that the presence of these elements produces secondary carbides which provides a secondary hardening peak when subjected to the rapid thermal cycle. The content presented in this part has been previously published by Saha et al. [117].

In the second part, microstructure of DP980 steel was optimized with additional alloying elements; therefore, DP980 steel was produced with a combination of a predominant ferrite, martensite, a little fraction of bainite, and blocky retained austenite. A comparative analysis of two commercially produced DP980 steels showed that the severity of martensite tempering can be avoided by modifying the microstructure of the steels; the DP980 steel produced with a combination of martensite, ferrite, bainite, and blocky retained austenite phase promotes high tensile strengths of the laser welded joints similar to the un-welded material.

5.2 Effects of steel chemistry

Although hardness is expected to decrease when martensite containing steels are tempered [72, 100, 103, 105, 118-122], it has shown that the lower temperature (below the

Ac_1 line) areas of the HAZ of the diode laser welds in bainite (α_b) containing DP780 steel (referred as DP780 (FMB) in Table 3-1) will sometimes show an increased in hardness, although softening would be expected [123]. This hardness increase has been determined to be secondary hardening [123], which has been observed in martensitic steels containing carbide formers such as Mo and Cr after prolonged (over 1 hr) tempering at about 500°C [61-63, 124]. Secondary hardening occurs because cementite dissolves within the structure, being replaced with alloy carbides such as Mo_2C and VC, which are reported to be the cause of secondary hardening. In previous studies, it was observed that α′ was transformed into α-ferrite and cementite (Fe_3C). As tempering time increases, the cementite dissolved and carbon went into solid solution before forming Mo_2C and VC [62].

5.2.1 Experimental

The present study examined a 1.35 mm thick DP780 steel with a ferrite-martensite-bainite microstructure. The chemical composition of the steel is listed in Table 3-1 and its mechanical properties are shown in Table 3-3. Fiber laser welding was carried out at a welding power of 6 kW and a speed of 14 m/min. Rapid tempering of the steel was performed using a Gleeble 3500 thermomechanical simulator. Heating rates between 1,500°C/s and 2,000°C/s were used to temper the specimens between 400°C and 650°C for 0.2, 0.5, 1, 2, and 10 s, which were then quenched in water with cooling rates of 5,000 to 10,000°C/s. Microstructural observations were carried out using SEM, TEM, and HAADF-STEM analysis; both thin foil and carbon replica methods were used to prepare the TEM samples. Two samples were observed under TEM for each sample condition.

To study the effect of steel microstructure on tempering kinetics, two different commercially produced 1.2 mm thick DP980 steels were used in the present work whose chemical compositions are reported in Table 3-1; alloying elements such as Cr, Mo, Ti, and Nb were added in Steel B. Steel A contains ferrite (α), martensite (α′), and a small fraction (<1%) of slender retained austenite (RA); on the other hand, Steel B composed of additional blocky retained austenite (RA) and bainite (α_b) phase. The volume fractions of phases are provided in Table 3-2. The sheets were welded in a butt joint configuration using fiber laser system with two different sets of power and speed. FIB method [92] was used

to extract the samples lamella from the SCHAZ (Ac_1 isotherm line which is about 500 μm away from the center of the welds) for TEM analysis.

5.2.2 Characterization of as-received DP780 (FMB)

The SEM micrograph of the steel used in this study is illustrated in Figure 5-1. The DP780 steel contains 63% α (the dark phase) and 24% α′ islands (the white phase) with an additional 13% α_b microconstituents (Table 3-2). The typical lath structure can be observed inside of each α′ island. The α_b phase contains bainitic ferrite plates separated by cementite. The volume fraction of each phase was estimated using SEM imaging at 2,000X magnification and manually outlining each representative phase, which was identified by its contrast and morphology. To obtain an accurate volume fraction, approximately 500 grains were used. Each image was able to capture up to approximately 35 grains; 15 SEM images were used to estimate the volume fraction.

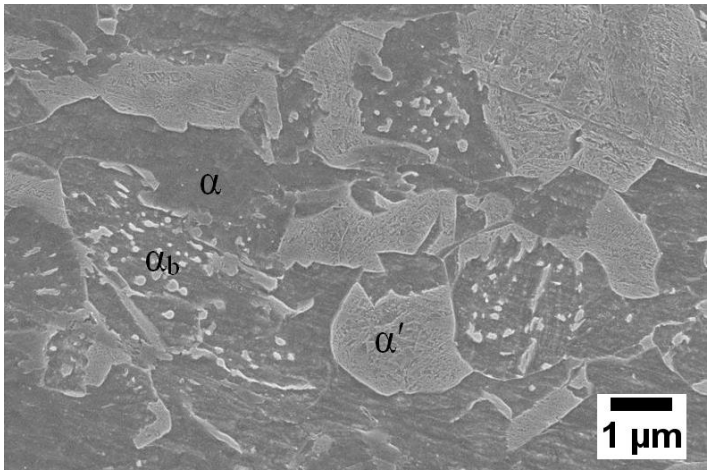

Figure 5-1 SEM micrograph of the as-received DP780 (FMB) steel showing a ferrite (α) matrix with combination of martensite (α′) and bainite (α_b) microconsituents

5.2.3 Microhardness and tempering parameter

Figure 5-2 illustrates the microhardness profile across the fiber laser weld zone in the DP780 steel. The different areas of the weld are marked as: FZ, HAZ, and BM. An increase in hardness was measured close to the BM on multiple welds. The hardness increase was significantly higher than both the BM and the minimum HAZ hardness measured closer to the fusion boundary. This increased hardness is referred to as secondary hardening. This

phenomenon was also observed in diode laser welds [123]. As similar secondary hardening trends were observed for both fiber and diode laser welding; therefore, it suggests that the secondary hardening phenomenon was dependent on the material chemistry, rather than the specific laser welding process (fiber or diode). Secondary hardening in the fiber laser welded samples was not expected, as due to the high power density ($\geq 10^5$ W/cm^2), and travel speed of this process, the material underwent rapid tempering. Typically secondary hardening is not seen in the samples tempered for short time; it has been observed only in martensitic steel tempered for long (more than 1 hr) time at temperature at or above 500°C [125]. The steel investigated in this study contains minor alloying additions of Cr, Mo, V, and Nb. Therefore, it is interesting to investigate the mechanism responsible for the secondary hardening observed during rapid tempering in this DP780 (FMB) steel.

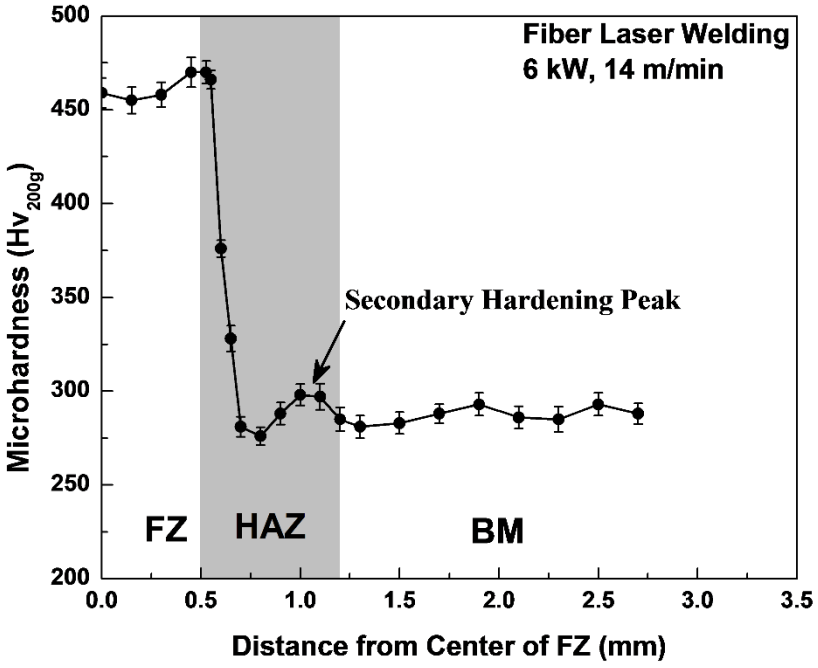

Figure 5-2 Vickers microhardness profile of DP780 steel fiber laser weld. The error bars represent 95% confidence interval of 6 individual indents

To reproduce the HAZ microstructure, the steel was tempered in a Gleeble with wide range of conditions. As the tempering process is influenced by both temperature and time, the tempering cycle was generalized using the Hollomon-Jaffe (H-J) [78] tempering parameter, which has been used extensively to investigate the correlation between hardness and tempering conditions. The H-J parameter is calculated using equation (2-8).

The calculated tempering parameters of Gleeble samples were plotted against their microhardness in Figure 5-3. When plotted, it was seen that the increase of the hardness of the tempered DP780 was a function of tempering parameter, regardless of the tempering temperature. Secondary hardening was observed at all tempering temperature, however, it was most pronounced at shorter durations (<1 s). The maximum hardening was measured at a tempering temperature of 500°C and 0.5 s duration where the hardness increased by 8% with respect to the BM. This secondary hardening trend was consistent with the results of fiber laser welded sample (Figure 5-2) where hardness increased by 3.5% of the BM hardness. Figure 5-3 also shows the effect of tempering temperature and time on hardness. It can be observed that the tempered hardness was not affected by tempering duration when tempered at 400°C. However, when the sample was tempered at 500°C the highest secondary hardening peak was observed at short tempering time (0.5 s) and hardness decreased with increasing tempering duration. It was also found that with increasing tempering time, the hardness values tend to decrease, which was due to coarsening of cementite particles, increasing the effective free length of dislocations and decreasing the flow stresses [126].

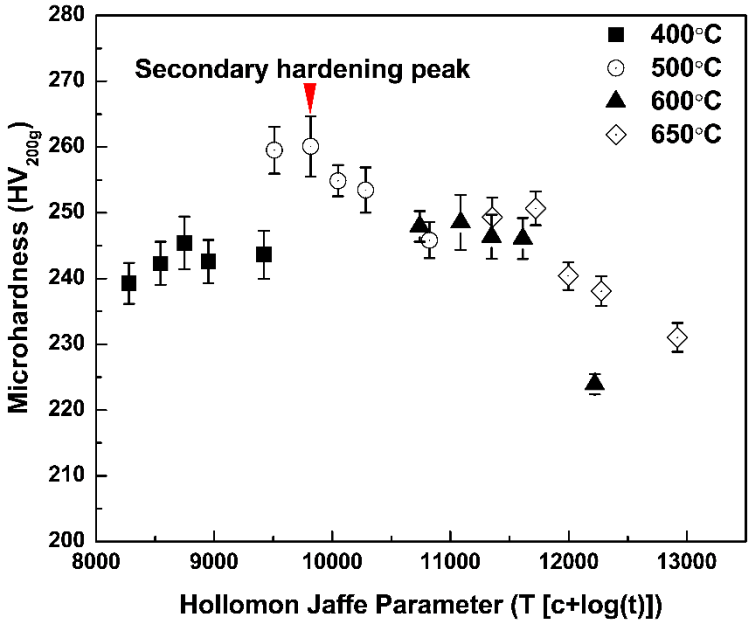

Figure 5-3 Vickers microhardness plot as a function of Hollomon-Jaffe tempering parameter of Gleeble heat-treated samples for DP780 steel [123]. The error bars represent 95% confidence interval of 12 individual indents.

5.2.4 TEM investigation of untempered DP780 (FMB)

The TEM micrographs of α, α′, and α_b structures of the as-received steel are shown in Figure 5-4(a). Twinned structure was seen inside the martensite block (marked by the dotted lines in Figure 5-4(b)) having packets, with unidirectional twins, oriented in a different angle. Bright-field images of α′ and α_b structures with the corresponding selected area diffraction (SAD) patterns are illustrated in Figure 5-4(c) and (e), respectively. The indexed SAD pattern shows the $[011]_{\alpha'}$ zone axis, and the twinned substructures are visible inside the α′ structure. Twinned structure is typically only observed in high carbon containing steel. The presence of twins in the α′indicates that C was portioned from the matrix to the α′ when the DP structure was formed, increasing the C content of the α′ above that of the bulk amount. The α′ carbon content was calculated using equation (5-1).

$$\%C_m = \frac{(\%C_s - 0.02)}{f_m + f_b} + 0.02 \qquad (5\text{-}1)$$

where, C_s is carbon content of the bulk steel, C_m is carbon content of martensite, f_m is volume fraction of α′ and f_b is volume fraction of α_b. The C content of α′ of the DP780 was calculated to be 0.52 wt.%, justifying the twinned structure observed within the α′phase [127]. Nayak et al. [103] also reported the twinned α′ for similar carbon and manganese containing DP780 steel. The SAD pattern presented in Figure 5-4(c) also shows the double reflection of the α′ twin plates which confirmed the existence of twin plates as expected from the calculated carbon content.

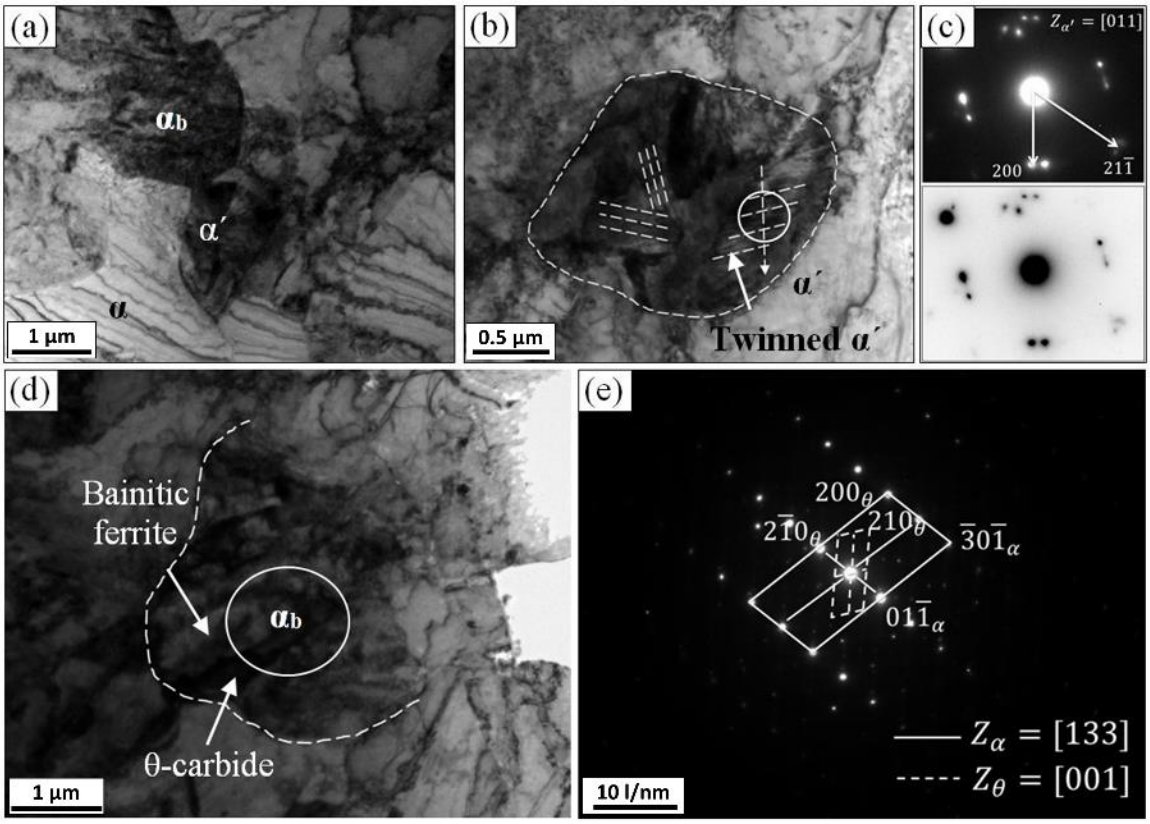

Figure 5-4 The TEM micrographs of the as-received DP780 (FMB) steel: (a) bright field image delineating the α, α´, and α_b microconstituents, (b) the α´ phase showing twinned martensite plates, (c) the SAD pattern taken from the area marked with a circle in (b) illustrates the martensite twins reflections, (d) the α_b microconstituents with bainitic ferrite plates and θ-carbides between the plates, and (e) indexed SAD of the bainitic ferrite and θ-carbide

The α_b structure was also observed in the steel structure, having cementite at the boundaries of the bainitic ferrite laths (Figure 5-4(d)) following $[001]_\theta \| [133]_{\alpha_b}$ orientation relationship. Bright field micrographs (Figure 5-5(a) and (b)) and HAADF image (Figure 5-5(c)) of the extracted carbon replica depicted different morphologies of the carbide precipitates: irregular spherical (no. 1, and 4), faceted (no. 2 and 3), and cuboids (no. 5, and 6) shape. The size of the faceted shape precipitates (no. 2, and 3) were in the range of 30-90 nm, whereas precipitate no. 5 exhibited cubic shaped carbide, was about 145 nm. The SAD patterns of particles 2, 4, 5 and 6 were indexed to have a face centered cubic (FCC) crystal structure, showing [011], $[\bar{1}23]$, [013], [001] zone axis and lattice

parameter (*a*) of 4.27 Å, 4.41 Å, 4.40 Å, and 4.31 Å, respectively. The crystal structure and lattice parameter of the particles confirmed the precipitates to be TiC, Ti(C,N), and TiN, which are known to precipitate within the α grains during thermomechanical processing of low alloy steels [128-130]. For instance, the precipitates 5 and 2, identified to be Ti(N) and Ti(C,N), had an FCC structure with the lattice parameter of 4.40 Å and 4.27 Å, respectively, also matched the literature [128, 131, 132]. The cubic Ti(C,N) precipitates (no. 5) exhibited a larger lattice parameter compared to the faceted shape precipitates TiC (no. 2), which is attributed to an increase in the lattice parameter when a N atom enters the TiC lattice to form Ti(C,N) [133, 134]. Additionally, TiC (no. 6) precipitates observed with an average size of 40 nm and a lattice parameter of 4.31 Å were in agreement with the size (2 to 30 nm) and lattice parameter (4.32 Å) of the TiC particles reported in the literature [128, 135]. Apart from cubic and faceted TiC, TiN, and Ti(C,N) precipitates, spherical shape precipitates were also observed (marked as 7 in Figure 5-5(c)), which produced a SAD pattern showing the $[\bar{1}12]$ zone axis (SAD 7) of orthorhombic crystal structure with lattice parameters of a = 4.85, b = 4.89, and c = 6.73 Å; which was close to those of orthorhombic cementite (a = 4.52, b = 5.08, and c = 6.74 Å) [61]. The current observation was corroborated with that of Schissler et al. [136] reporting the formation of orthorhombic carbides in a steel rich in silicon. The difference between the measured lattice parameters of the observed precipitates and the typical lattice parameters for cementite suggests that the observed precipitates are $(Fe,M)_3C$ type cementite, where M is Mn and Cr. The electron energy loss spectroscopy (EELS) and EDX analysis (Figure 5-6(a)) of the θ-carbides (inset of Figure 5-6(a)) confirmed the presence of peaks of the substitutional elements of Mn and Cr along with the parent Fe peak, which has also been reported by Nayak et al. [103]. Recently, Jang et al. [137] have reported the changes in the lattice parameters and total volume of the cementite lattice when the Fe atoms are substituted by Mn, Si, Al. For example, Si_3C, and Al_3C enlarge volume by approximately 34% due to elongation in the *b*-axis compared to Fe_3C, whereas Mn_3C showed 3% volume reduction [137]. The α and α′ phases are free from θ-carbides [61], the θ-carbides found in the extracted replicas were confirmed to be from the bainite phase in the studied DP780 steel (Figure 5-4(d)). The EELS spectrum for cuboid shape precipitates (no. 5 in Figure 5-5(c)) is confirmed to be Ti(CN) as shown in Figure 5-6(b) (no. 5 is also shown in the inset).

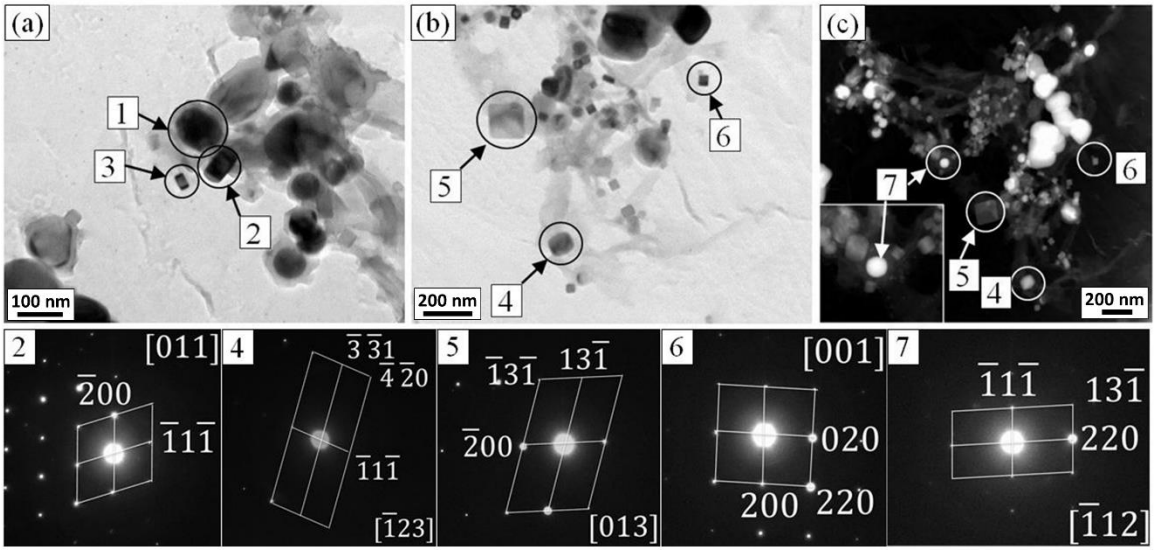

Figure 5-5 The microstructure of the carbides from the as-received DP780 (FMB) steel: (a) and (b) carbon-replica sample showing spherical, and faceted carbides (marked with circles), and (c) HAADF-STEM image of the spherical and cuboid carbides. The indexed SAD patterns taken from the particles are also included

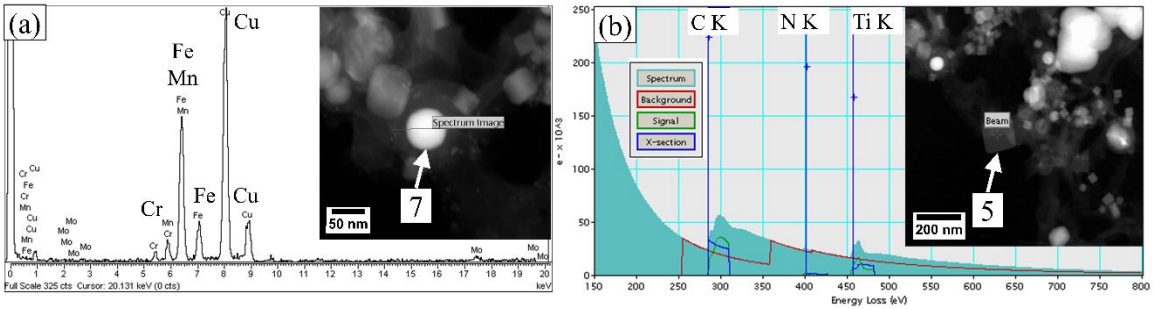

Figure 5-6 EELS analysis of extracted carbides from DP780 (FMB) steel: (a) EELS spectrum indicating peaks of Fe, Mn, and Cr (inset HAADF-STEM image of cementite); and (b) EELS profile obtained from one of the square shaped carbonitride which showing peaks of Ti, C, and N (inset HAADF image of the carbonitride).

TEM and STEM images of the sample heat treated at 500°C for 0.5 s showed the products of the decomposed α′ and α_b structure (Figure 5-7), where the decomposed martensite was marked as DM, and the decomposed bainite was marked as DB. The martensite structure decomposed into α and θ (Figure 5-7(a)); the spherical θ (having an average diameter of 50 ± 3 nm) are indicated by the arrows. The θ-carbides were confirmed

by the SAD pattern (marked with the circle), which showed a $[\bar{1}13]_\theta$ zone axis parallel to $[\bar{1}12]_\alpha$ of α-matrix. The EDX analysis of the circled θ-carbides in Figure 5-7(a) and (b) confirmed that Cr and Mn was present within the carbide (Figure 5-8), indicated that the θ-carbide had the stoichiometric form $(Fe_{0.87}Mn_{0.11}Cr_{0.02})_3C$. The θ-carbides were predominately located at the prior-γ grain boundaries and block boundaries, as is common in tempered martensite [28, 72]. Elongated carbides were also seen at the interlath regions of the DM structure (Figure 5-7(c)). The elongated carbides were formed from decomposition of the retained austenite films originally found in the interlath boundaries of martensite laths. This observation agrees with those by Hernandez et al. [72]. Partial decomposed martensite (PDM) was also observed; the presence of the PDM indicates that there was insufficient time to complete the tempering reaction. Unlike the spherical carbides seen in the DM, the carbides formed in the decomposed α_b were predominantly needle-shaped and uniformly distributed throughout the DB structure (Figure 5-7(d), (e) and (f)). In addition to needle-shape carbides, irregular θ-carbides (marked with the circle in Figure 5-7(d)). The irregular θ-carbides had $[\bar{1}11]_\alpha \| [2\bar{2}0]_\theta$ orientation relationship with the α-matrix. The α-phase observed in the DB structure (Figure 5-7(d), (e) and (f)) was free from carbides as in the as-received α phase (Figure 5-4(a)). When the DB was imaged using HAADF (Figure 5-7(f)), the needle-shaped carbides had brighter contrast, indicating that they were composed of higher atomic weight elements. This was confirmed by EDX analysis, which indicated that these were M_2C type carbides, where M corresponds to Fe, Mn, and or Mo. The M_2C carbides (Figure 5-9) in the DM precipitated at the expense of the orthorhombic θ-carbide particles presents in the as-received steel (Figure 5-5(c)). During tempering, the Fe atoms within the cementite (Fe_3C) were substituted by strong carbide forming elements (Cr and Mo in the examined steel), eventually forming M_2C carbides [61, 138, 139]. The formation of M_2C carbides within the material structure lead to an increase in the hardness i.e. secondary hardening peak (Figure 5-2 and Figure 5-3). Fine M_2C-type carbides are precipitated by the dissolution of M_3C-type cementite when the material is aged at 500°C. M_2C-type carbides have needle-shape morphology with a HCP crystal structure [138, 140], which is consistent with Figure 5-9.

Once identified, the distribution, size, and structure of the needle-shaped precipitates were measured by analyzing images from carbon replicas. The area fraction of needle-

shaped precipitates was measured (using ImageJ software) to be 25-30% (Figure 5-9(a) and (b)). HAADF was used to image individual precipitates as shown in Figure 5-9(c), which were measured. Figure 5-9(d) shows a single elongated needle shape precipitates having a length and width of 525 and 25 nm, respectively. The aspect ratio of the observed needles was estimated to be in the range of 10-25. The SAD pattern taken from one of the needles (Figure 5-9(e)) indicates that it has an HCP crystal structure with the lattice parameters of a = 2.88 Å, and c = 4.76 Å. The measured lattice parameter was in good agreement with the lattice parameters of Mo_2C (a = 3.0 Å, and c = 4.72 Å) as reported by Yamasaki and Bhadeshia [138]. It should be noted that the lattice parameters measured by electron diffraction is only accurate to 0.1% (as calibrated with standard Au sample). This analysis definitively indicates that Mo_2C is distributed throughout the DB structure. It is well known that the precipitation of the Mo_2C provides secondary hardening peak tempered high-speed steels [141]. The secondary hardening is due to the coherent precipitation of these carbides [142], which increases the initial flow stress, resulting in the observed hardness increase [143].

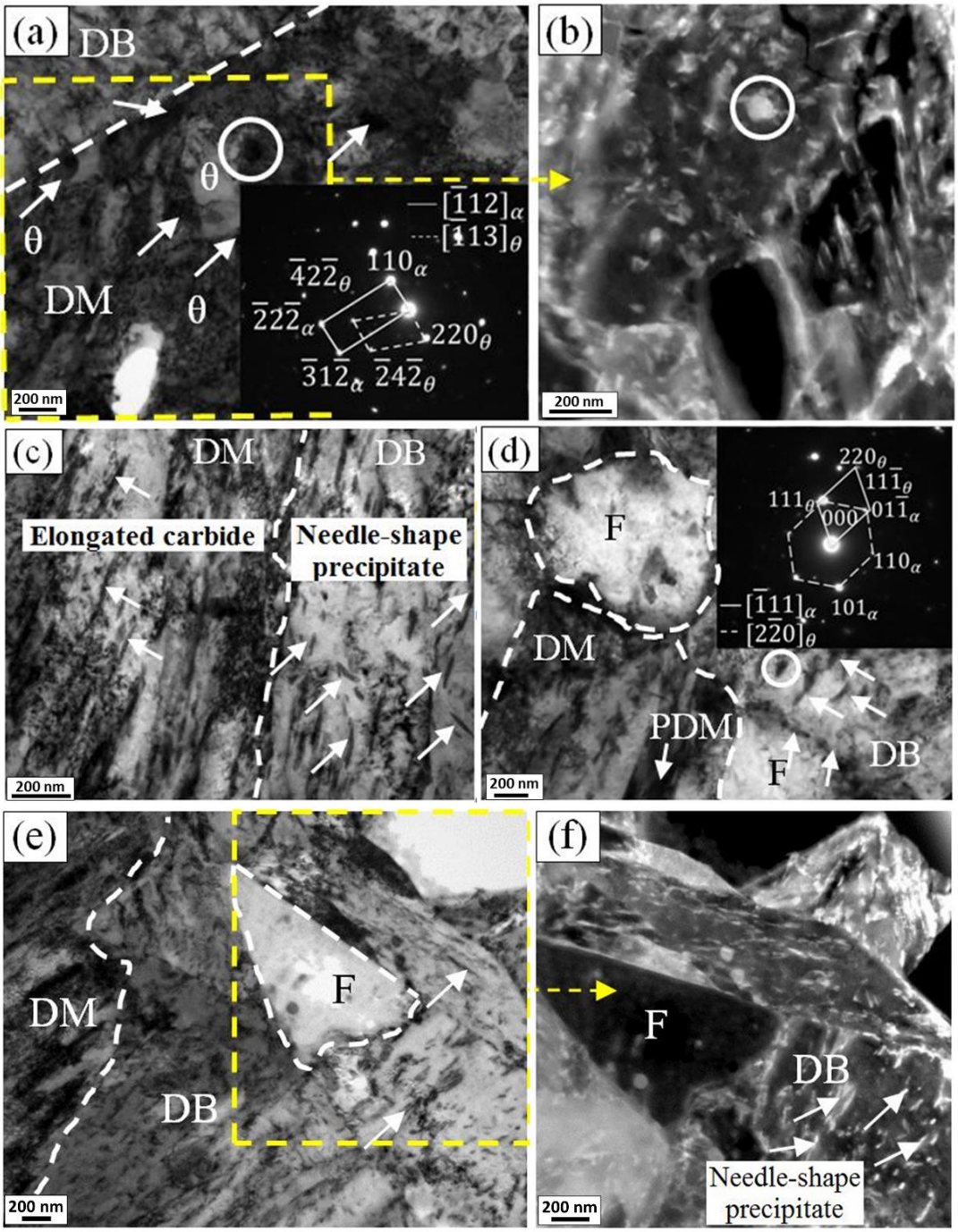

Figure 5-7 DP780 steel isothermally tempered at 500°C for 0.5 s showing (a) spheroidized precipitates in the DM, (b) STEM image of selected rectangle in (a), (c) and (d) interlath elongated cementite in the DM, and needle-shape precipitates in the DB, (e) bright field micrograph of the DM, DB, and F structure, and (f) HAADF-STEM image of the DB structure showing needle-shape carbides (bright contrast, higher atomic level)

In the high magnification images of the replicas seen in Figure 5-9(a) and (b), additional plate-shaped precipitates are observed that could not be resolved in the bulk specimens (Figure 5-7(d)). A SAD pattern taken from these precipitates (Figure 5-9(f)) was indexed as the [012] zone axis of a FCC structure having a lattice parameter of 4.30 Å. The plate-shaped precipitates exhibited a lattice parameter close to that of M_4C_3 (for V_4C_3, a = 4.20 Å) type carbides, where M implies the alloying elements such as V, Fe, and Mn. The difference between the measured and standard values for the lattice parameter was again due to the replacement of V by other elements in this particular material. Pearson [144] observed that the lattice parameter decreases as the V:C ratio increases. As with the M_2C, the observed M_4C_3 precipitated at the expense of θ-carbides, so it may therefore be predicted that the θ-carbides present in the untempered materials transformed into the plate-shaped M_4C_3 carbide during the tempering. Again, V is a strong carbide forming element, so during tempering at 500°C, the Fe atoms in the θ-carbide are substituted by the V atoms and formed stable alloy carbides, which were also responsible for the secondary hardening (Figure 5-2 and Figure 5-3).

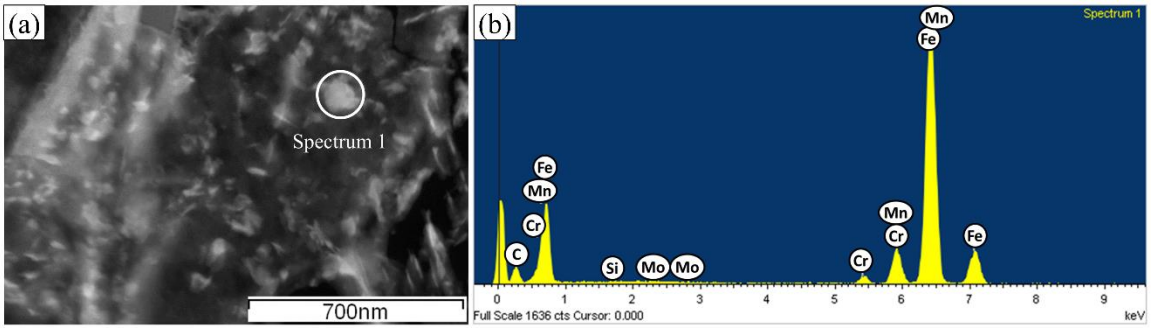

Figure 5-8 (a) HAADF image illustrating a spheroidized cementite precipitate in the DM and (b) corresponding EDX spectrum of the confirming Fe, Mn, Cr content of it. The EDX analysis indicated that cementite has a stoichiometric of $(Fe_{0.87}Mn_{0.11}Cr_{0.02})_3C$

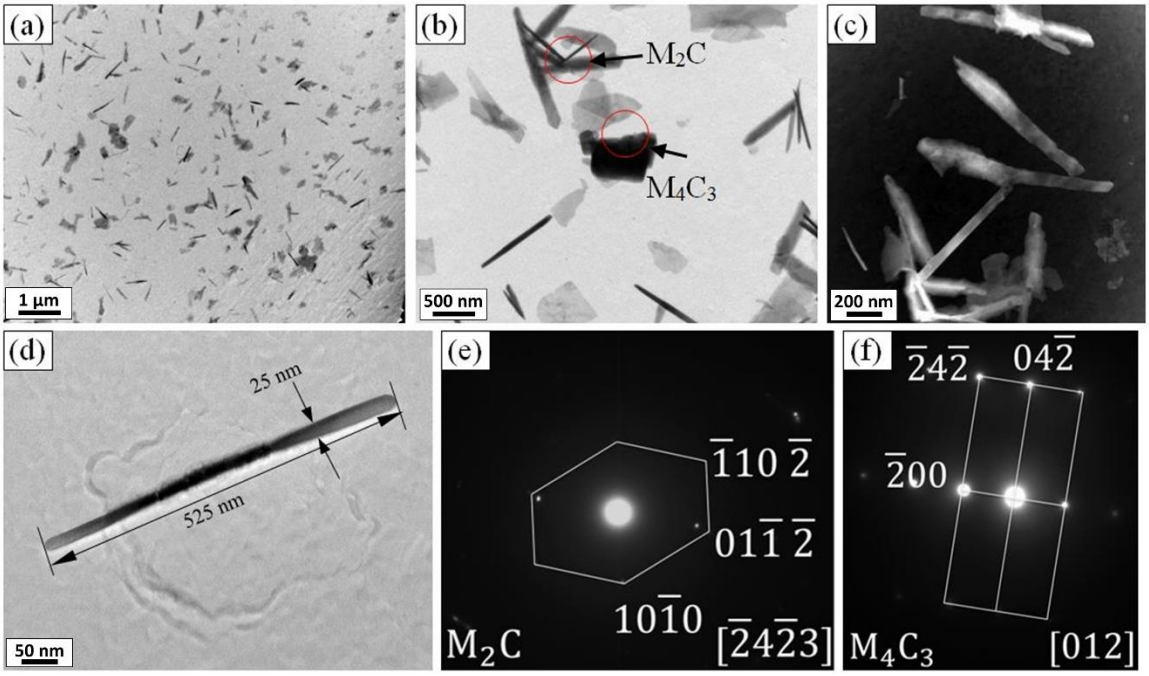

Figure 5-9 TEM images (carbon replica) of the alloy carbide particles found in the isothermally tempered DP780 steel samples at 500°C for 0.5 s showing (a) and (b) bright field image with dispersedly distributed alloy carbides M_2C, and M_4C_3 (c) HAADF-STEM images of the alloy carbides showing higher atomic resolution (bright contrast), (d) a single needle-shape M_2C carbide, and (e) and (f) showing corresponding indexed SAD for M_2C and M_4C_3 marked on (b)

It can be stated that Mo_2C were formed at the expense of θ-carbides present in the α_b structure of the DP780 steel, which resulted in secondary hardening. The TiC, and M_3C present in the as-received DP780 steel which were enriched with Mo and V, transformed to form M_4C_3 first and then dissolve *in situ* to provide free carbon to form molybdenum-rich M_2C precipitates [61]. Bhadeshia [61] reported that M_2C type carbides form within the bainite plates in contrast to a mixture of carbides at the bainite plate boundaries. Since, high-angle boundaries are strong heterogeneous nucleation sites; these locations are preferred for nucleation of the alloy carbides. In the present study, the location of the needle-shaped M_2C precipitates were also identified within the bainitic ferrite plates as shown in Figure 5-7(d) and (f).

During tempering, the Fe atoms in the metastable cementite were replaced by the substitutional solute atoms to form the alloy carbides. Once the alloy carbide precipitated,

the secondary hardening peak was observed. It is reported that softening in steels can be reduced by precipitation of ε-copper and other carbides, nitrides, and or carbonitrides of V, Nb, and Mo [145]. However, further tempering of the steels coarsened the carbides, and they lost coherency with the matrix, decreasing hardness [61]. This trend in hardness was seen in Figure 5-2 and Figure 5-3 where a hardness peak was seen at moderate levels of tempering, then as tempering progressed (either by tempering at higher peak temperatures or longer durations), the hardness decreased as the carbides continued to coarsen. It must be noted that secondary hardening was observed only in bainite containing steel because time necessary for hardening was too short for M_2C and M_4C_3 to form in the tempered martensite. The orthorhombic θ-carbides present in the bainite structure meant that fewer transformations needed to occur to precipitate coherent M_2C carbides, effectively accelerating the onset of secondary hardening. Without pre-existing θ-carbides in the structure longer tempering times are needed before secondary hardening can be observed [138]. The current study confirmed that DP780 steel containing 13% bainite exhibited some secondary hardening phenomenon; however, further study may require to confirm the relationship between the fraction of bainite microconstituents and the percentage of the secondary hardening response.

5.3 Effects of steel microstructure

The objective of this section is to optimize the steel microstructure to obtain a high UTS of the welded joints similar to the un-welded material. For this purpose, two grades of DP980 steels were produced with varying alloying elements and microstructures (referred as steel A and steel B in Table 3-1). This study has shown that the influences of the HAZ softening can be avoided by modifying the steel microstructure which shifted the fracture location from the SCHAZ to the unaffected BM i.e., the identical location where the un-welded BM fractured during tensile loading.

5.3.1 Microstructural evolution of as-received materials

SEM micrographs reveal a predominant ferrite (α) and martensite (α′) phase on the as-received BM of Steel A (Figure 5-10(a)); in addition, a negligible fraction (<1%) of the

slender retained austenite (RA) also found on the massive ferritic grains as marked with the circles in Figure 5-10(a). Conversely, beside these, Steel B contains additional 7% bainite (α_b) and 9% of blocky RA phase (Figure 5-10(b) and (c)). Two kinds of RA phase can be identified in the Steel B, the first one is slender-like phase inside large α grain (marked with dotted circles) which is identical to the RA phase observed in Steel A (Figure 5-10(a)); the second kind is a blocky RA phase which is surrounded by proeutectoid ferrite [146]. The blocky RA forms at ferrite grain boundary thus appeared to be identical to the α′ phase (Figure 5-10(b)). However, the α′ and RA phase can be distinguished by their specific features where α′ phase contains several lath-like structure; on the other hand, the blocky RA phase is featureless (Figure 5-10(c)). It has been reported that proeutectoid ferrite surrounded the blocky RA phase forms during intercritical annealing between Ac_1 and Ac_3 temperature line [146]. During proeutectoid ferrite formation, diffusion of carbon occurred from ferrite to austenite thus the carbon content of austenite increased which leads to decrease the martensite starts temperature significantly. Therefore, high carbon containing austenite remained its blocky morphology covered with a proeutectoid ferrite phase. The α′ grain size in Steel B was smaller compared to the α′ phase in Steel A; moreover, RA and α′ phase were found to be identical grain size in Steel B. A typical lath-like martensite was observed on Steel A with a few nanoscale autotempered carbides (Figure 5-10(a)) [31]; on the other hand, these carbides are rarely visible on the α′ phase of Steel B (Figure 5-10(c)).

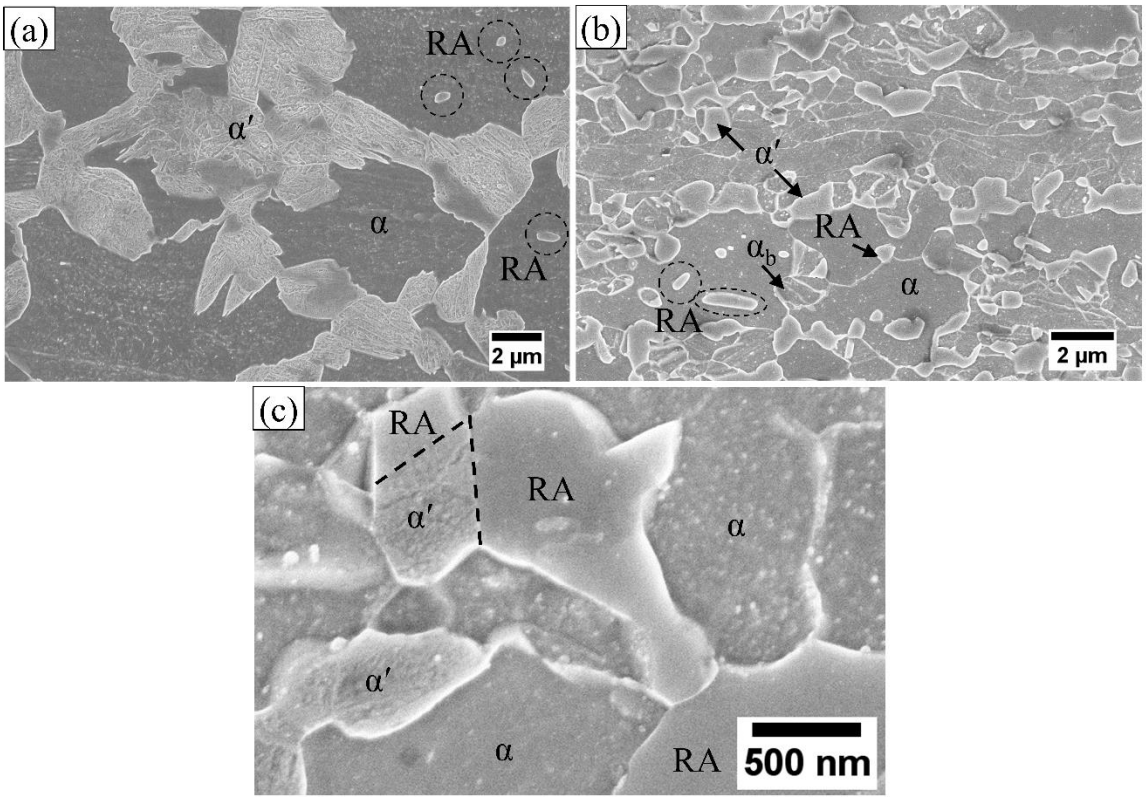

Figure 5-10 SEM images of as-received materials showing the microstructure of (a) Steel A, (b) Steel B, and (c) a magnified view of α′ and blocky RA and the interfaces between the phases observed in Steel B

5.3.2 SCHAZ microstructure evolution

Both the steels were welded using the welding parameters as shown in Table 5-1. The microstructures of the tempered regions at SCHAZ of Steel A and Steel B are shown in Figure 5-11(a) and (c), and (b) and (d), respectively. The SCHAZ microstructure of Steel A shows tempered martensite (TM); a fine dispersion of nanoscale carbides was found at various boundaries such as prior-γ grain, packets, blocks, and lath boundaries as well as intralath (inside the lath) locations (Figure 5-11(c)) [9-11]. On the other hand, the slender RA located on a α grain was not influenced by the thermal cycle as they are appeared to be identical to the un-welded material (Figure 5-10(a)). The SCHAZ of Steel B revealed a combination of α, blocky RA, and TM; it can be noted that α_b, and α′ shows similar features (carbides and α) after tempering; therefore, any distinction between the tempered α_b and tempered α′ cannot be made. However, according to Bhadeshia [61] both the phases

followed the same tempering process while subjected to a tempering process. As expected, the blocky RA phase is remained untempered due to higher thermal stability [147].

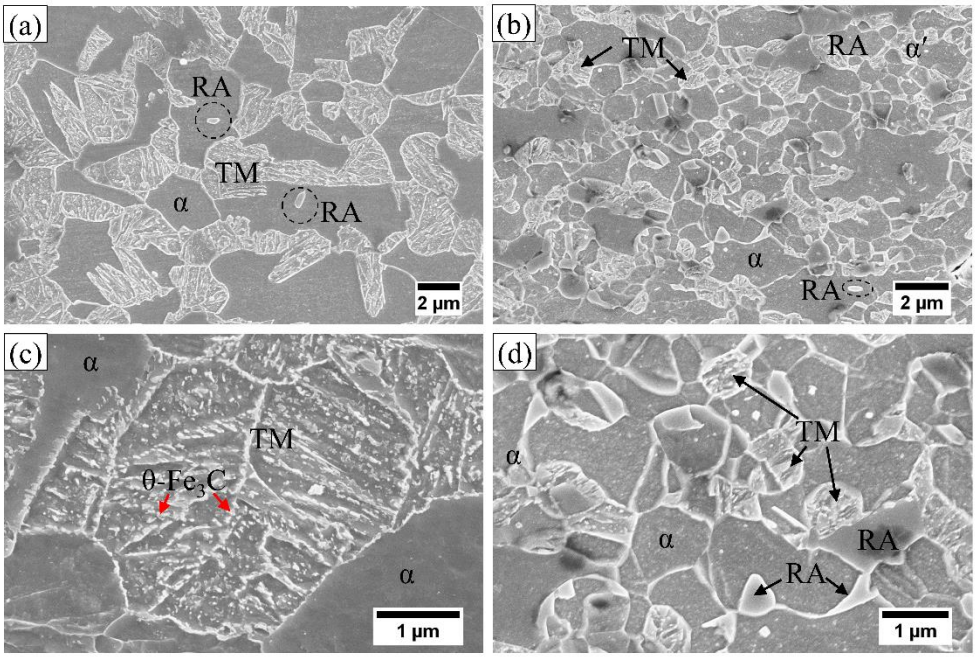

Figure 5-11 SEM micrographs of the SCHAZ illustrating the microstructure of (a) tempered martensite (TM), slender-like RA, and α phase in Steel A, (b) TM, blocky RA, α_b, and α phase in Steel B, (c) a magnified view of the TM in Steel A, and (d) a magnified view of the TM and blocky RA phase in steel B

The FIB samples extracted from the SCHAZ of two laser welded samples were observed under TEM as shown in Figure 5-12 and Figure 5-13. Figure 5-12(a) reveals the tempered α′ (TM) and α phase; the TM phase is outlined with a dotted line. In addition, slender RA phase observed in α grain as shown in Figure 5-12(b). Several carbides like particles were found on the TM phase which were precipitated at various boundaries during tempering. A high density of dislocation also observed on the TM phase implying partial recovery of the α′ laths. The selected area diffraction (SAD) pattern was taken from the TM phase showing the projection plane of ferrite $[011]_\alpha$; the diffraction spots corresponding to nanoscale cementite (θ) also identified with a *d*-spacing of 2.210 Å and 1.712 Å corresponding to the diffraction spots of $d(120)_\theta$ and $d(030)_\theta$, respectively. Interestingly, in addition to the spots from α and θ, two extra diffraction spots can be found at $\frac{1}{3}(\overline{211})_\alpha$ and $\frac{2}{3}(\overline{211})_\alpha$ positions (as indicated by red arrows in Figure 5-12(d)). The

origin of these spots was reported to be the presence of the ultra-fine nanoscale ω phase which usually exists at twin martensite lath boundaries [148-150]. The ω phase is coherent with the α matrix and obeyed a well-defined orientation relationship of $[011]_\alpha||[01\bar{1}0]_\omega$ (Figure 5-12(c)). The indexed spots of ω phase confirmed the hexagonal closed packed (HCP) crystal structure (P6/mmm) with a lattice relationship of $a_\omega = \sqrt{2} \times a_\alpha$, and $c_\omega = \frac{\sqrt{3}}{2} \times a_\alpha$, where a_α is the ferrite lattice parameter [148-150]. In the present study, the influences of the ω phase on the properties of the tempered martensite is still unknown.

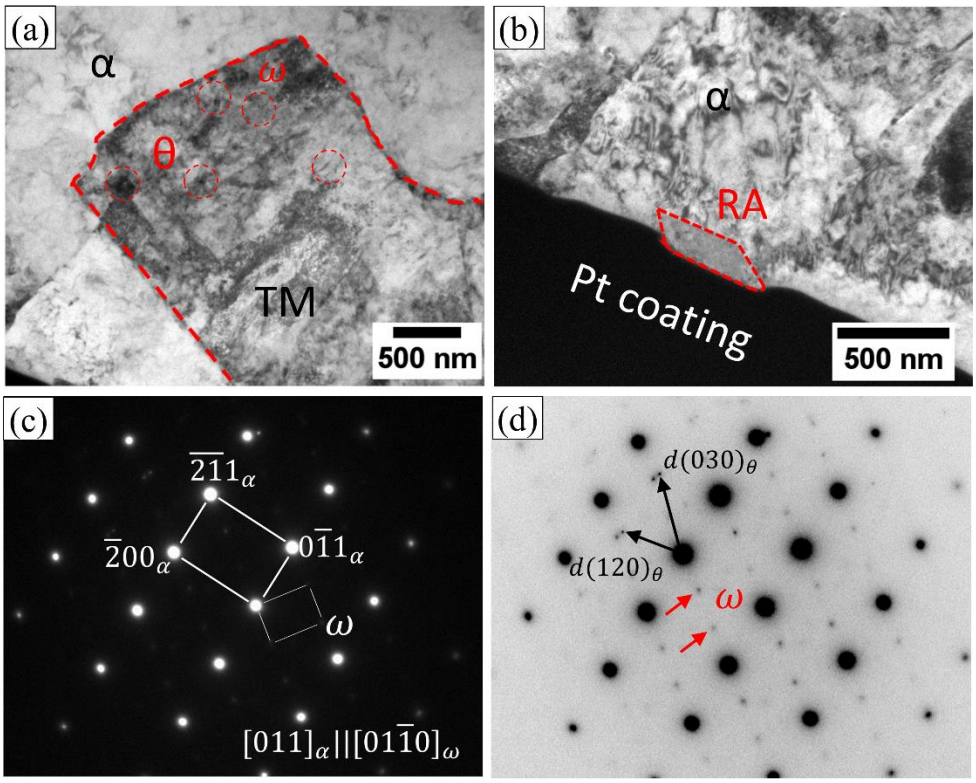

Figure 5-12 Bright-field TEM micrographs of the SCHAZ in Steel A; (a) α and TM phase; nanoscale carbides on the TM phase are marked with circles, (b) slender-like RA on a α grain, (c) the indexed SAD pattern of the area taken from the TM phase showing the orientation relationship of $[011]_\alpha||[01\bar{1}0]_\omega$ between BCC α and HCP ω phase, (d) inverted image of the SAD pattern of (c) illustrating the spots corresponding to orthorhombic θ phase with a *d*-spacing of 2.210 Å and 1.712 Å corresponding to the diffraction spots of $d(120)_\theta$ and $d(030)_\theta$, respectively; the spots representing the ω phase also shown with red arrows in (d)

Figure 5-13 shows the microstructure of the SCHAZ of Steel B, in accordance to the SEM images presented in Figure 5-11(b) and (d), identical microstructure with a combination of the TM, blocky RA, and α phase is observed. A predominant fraction of blocky RA phase is found which appeared to be in darker contrast compared to the TM and α phase. Some of the TM and blocky RA share the common interfaces as shown in Figure 5-13(b) and (d); however, the precipitates carbide was only observed on the α′ phase. Conversely, the blocky RA phase was found to be highly dislocated; the SAD pattern taken from the circled area of Figure 5-13(b) was indexed as FCC structure of RA with a projection plane of $[\bar{1}11]_{RA}$ (Figure 5-13(c)). The slender-like RA phase on a larger α grain also identified at SCHAZ as can be found in Figure 5-13(e) and the corresponding SAD pattern with an indexed zone axis of $[011]_{RA}$ in Figure 5-13(f).

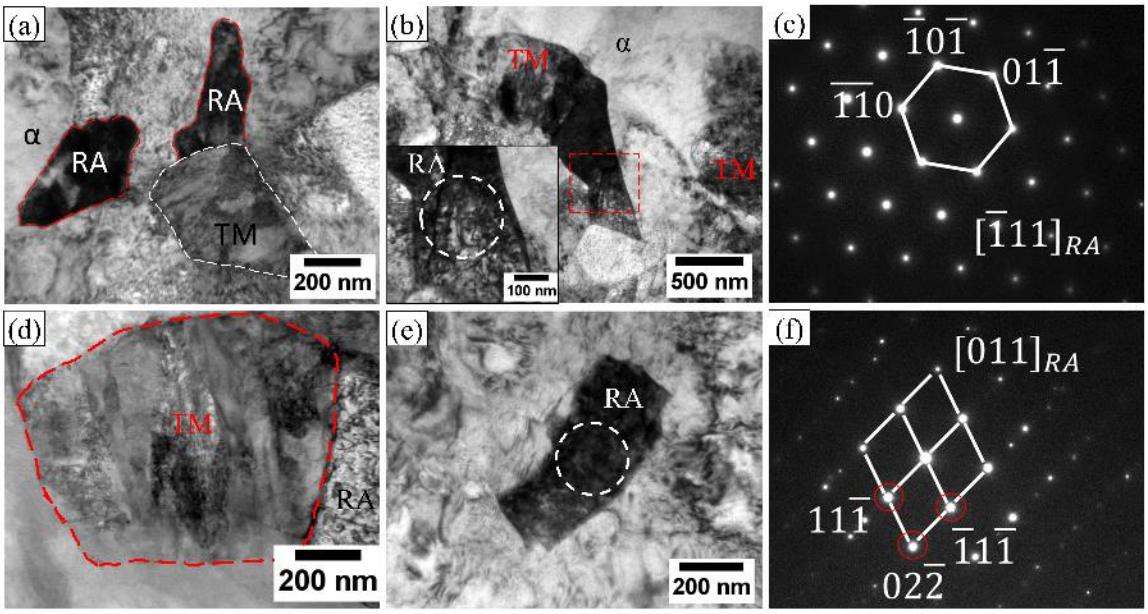

Figure 5-13 Bright-field TEM micrographs of the SCHAZ obtained from Steel B; (a) a combined microstructure of α, blocky RA, and TM, (b) an interface between TM, and blocky RA, the carbides on the TM phase also shown; a magnified view of the blocky RA is shown in inset, (c) indexed SAD patterns of blocky RA phase taken from the circled area of inset image of (b) showing the zone axis of $[\bar{1}11]_{RA}$, (d) HAADF-STEM image of the interface between TM and blocky RA phase, (e) a slender RA phase on a ferritic grain, and (f) indexed SAD patterns of FCC RA phase shown in (e) with a projection plane of $[011]_{RA}$

5.3.3 Microhardness and tensile performance

Vickers microhardness profile across the welds cross-section of Steel A and B are presented in Figure 5-14. The microhardness distributions represent the average of 4-5 individual hardness profile across the weld cross-section. Steel A has a BM microhardness value of about 349 ± 2.95 HV, which is about 16 HV higher than the BM microhardness of Steel B (333 ± 2.66 HV). The differences in BM microhardness is due to the differences of the α′ fraction where Steel A contains 56% α′ phase compared to 38% in Steel B although the sum of α′, α_b, and RA is similar (54%) to that of the α′ fraction in Steel A. However, the matrix strength of α′ is superior to all other phases found in the studied steels. Figure 5-14 also shows the variation of microhardness measurement at FZ, where the FZ of Steel B possesses lower microhardness resulted from the lesser carbon percentage compared to Steel A (Table 3-1). Most importantly, a significant hardness differences were obtained in the SCHAZ of two different welded joint. The microhardness in the SCHAZ was found to be softened less in Steel B which shows a reduction of microhardness from 333 HV to 315 HV due to lower fraction of TM and existence of an untempered blocky RA phase. The thermal stability of the blocky RA phase was demonstrated by Podder et al. [147, 151], they found that the blocky RA phase is very stable due to carbon enrichment. The volume fraction of the blocky RA phase decreased while subjected to the prolong tempering duration at 400°C [147, 151]; however, during high-speed fiber laser welding process, the steel is exposed to Ac_1 temperature for a very short duration (<1 s) due to rapid heating and cooling rate [97]. As a result, the thermal effect on the blocky RA phase decomposition can be disregarded. Unlike steel B, the SCHAZ of Steel A shows a severe softening which exhibits about 17% reduction of microhardness from 349 HV to 289 HV. Table 5-1 indicates that the soft zone width in Steel B is also significantly decreased compared to that of Steel A.

Table 5-1 Welding parameters and properties of the SCHAZ of the investigated steels. The tolerance limit represents the 95% confidence interval.

Material	Power (kW)	Speed (m/min)	BM Hardness (HV)	SCHAZ Hardness (HV)	Softening (HV)	Soft Zone Width (μm)
Steel A	4	20.5	349 ± 2.95	289 ± 4	60	400
	2	10		283 ± 5	66	650
Steel B	4	20.5	333 ± 2.66	315 ± 3	18	100
	2	10		305 ± 8	20	200

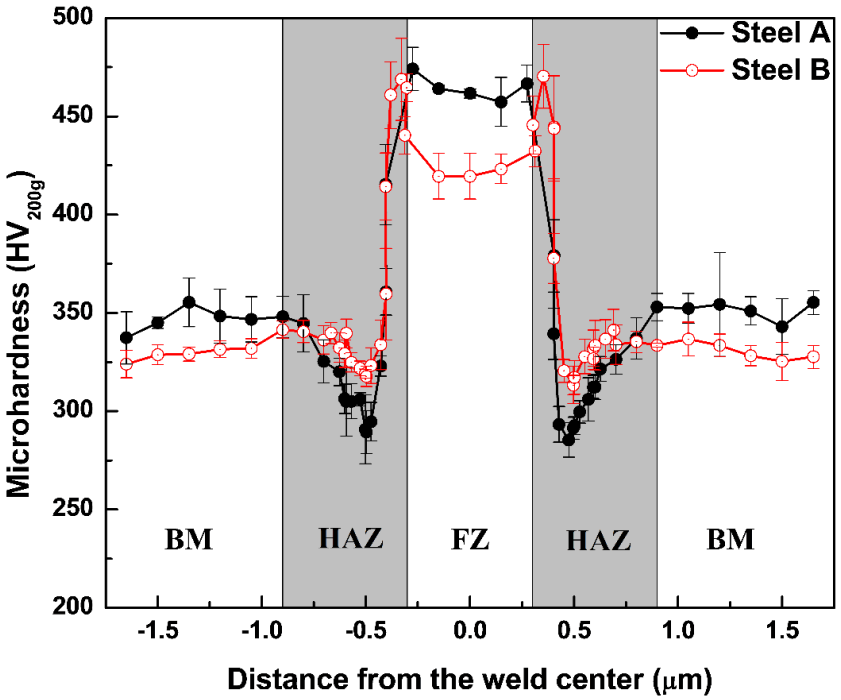

Figure 5-14 Vickers microhardness profile across the weld cross-sections of Steel A and Steel B (reproduced from reference [94]). The error bars represent the 95% confidence interval.

Figure 5-15 represents the engineering stress versus engineering strain curves of Steel A and B as-received (BM) and as-welded condition. Three samples were tested for each condition. Steel A possesses higher YS and UTS resulting from higher carbon percentage and greater α′ fraction; however, the uniform elongation in Steel B was higher than the one

in Steel A indicating more energy absorption capacity due to higher fraction of the blocky RA phase [146, 152, 153] (Table 3-2). The tensile curves of the welded joints indicated different scenario, the welded joint of Steel A fractured very quickly due to the stress localization resulted from the α′ tempering at SCHAZ. This can be predicted from the microhardness distribution as hardness values were significantly lower in the SCHAZ zone (Figure 5-14). The engineering strain significantly reduced from 12.2% to only 2.5% although UTS was above 1000 MPa which shows a joint efficiency of 93.4%. On the other hand, a highest joint efficiency (100%) was obtained to the welded joint of Steel B. It can be concluded that the HAZ softening (martensite tempering) has insignificant effect on weld properties of Steel B as the welded joint consistently fractured at BM. Both YS and UTS of the welded joint of Steel B was found to be identical to that of the BM of Steel B although joint elongation little bit decreased (from 14.4% to 13.5%) due to the presences of hard weld metal at the middle of the tensile gauge length [97].

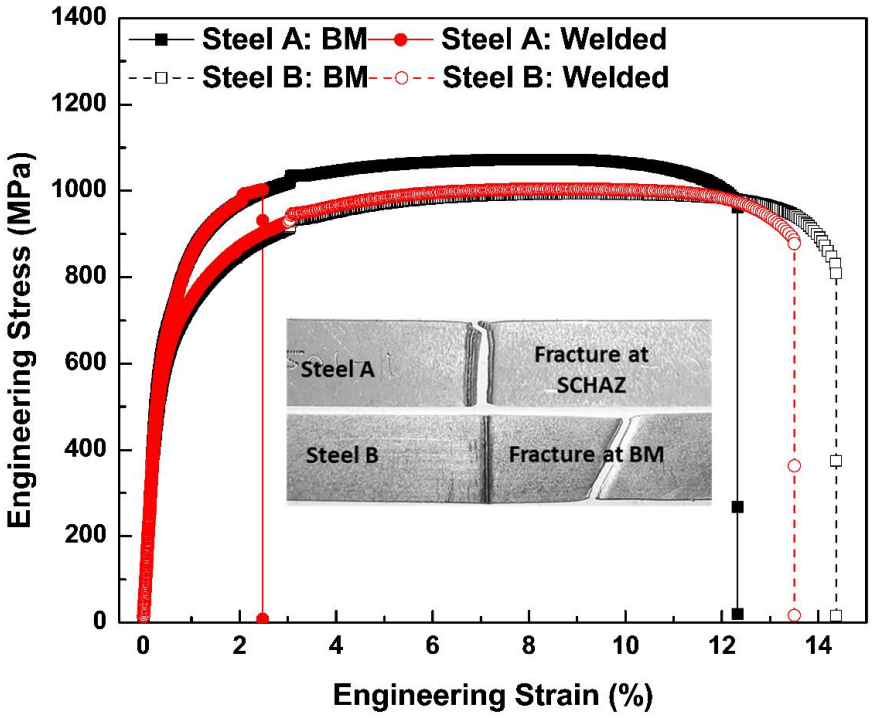

Figure 5-15 Representative engineering stress versus engineering strain curves of the welded joints of Steel A and Steel B with inset fractured macrographs showing the fracture locations (reproduced from reference [94])

Table 5-2 Mechanical properties of Steel A and Steel B as-received and welded conditions. The tolerance limit represents the 95% confidence interval.

Material	Conditions	YS (MPa)	UTS (MPa)	Elongation (%)	Joint efficiency (%)	Fractured location
Steel A	BM	697 ± 5	1072 ± 12	12.3 ± 0.4	-	BM
	Welded	695 ± 8	1002 ± 6	2.5 ± 0.8	93.5	SCHAZ
Steel B	BM	618 ± 18	996 ± 14	14.4 ± 0.7	-	BM
	Welded	621 ± 15	1004 ± 21	13.5 ± 0.6	100	BM

5.4 Summary

1. In the first part of this Chapter, the secondary hardening identified in rapid tempering i.e. Gleeble tempering and laser welding of microalloyed DP780 steel with a ferrite, martensite, and bainite microstructure. The hardness profile in the laser welds agreed well with hardness versus H-J tempering parameter, suggesting that secondary hardening occurred in the steel when tempered at 500°C for a very short duration (< 1 s). Secondary hardening was due to the transformations of the pre-existing carbides found within the bainite structure. The pre-existing cementite Fe_3C, and TiC were dissolved at high temperature, providing a carbon source to form the plate-shaped M_4C_3 and needle-shape M_2C carbides, which led to secondary hardening in the Gleeble specimen tempered at 500°C for 0.5 s. The isothermal tempering products strongly correlate with the hardening peak observed in the HAZ of the DP780 steel laser welds. However, this phenomenon is not likely occur in bainite-free DP780 steels where no such θ-carbides are available to transform into secondary hardening carbides during rapid tempering and welding.
2. The experimental evidences presented in the second part of this Chapter suggested that the HAZ softening can be mitigated by modifying the steel microstructure without compromising the UTS of the steel. The laser welded joints of the steel composed of ferrite, martensite, bainite, and blocky retained austenite performs better than ferrite and martensite containing DP980 steel. The presence of 7% bainite and 9% blocky

retained austenite in a steel significantly improves the welded joints properties which exhibits identical tensile behavior as the un-welded material.

6 Effects of Tempering Mode on the Structural Changes of Martensite

6.1 Introduction

Martensite is considered as a composite structure which can be comprised of several microstructural units such as laths, blocks, packets, and prior-γ grains [30, 154-159]. During tempering, softening of these units may occur and be influenced by several tempering factors such as mode of tempering, heat input, temperature, and time. In order to model and design an alloy system, an in-depth understanding of the microstructural parameters of martensite is desirable. For the as-quenched martensite, the strength contributions include grain size, solid solution, and the forest dislocation density; however, in the case of the tempered martensite, the contribution from the nanoscale carbides, coarsening of laths, and martensite recovery needs to be accounted for. Most importantly, a dynamic change that occurs during tempering where carbides grow and become coarser, along with recovery and annihilation of the forest dislocation occurs with increasing tempering temperature. However, the combination of these factors leads to a decreased in the overall strength of the structure [80, 82, 160].

Hernandez et al. [72] studied the influences of isothermal and nonisothermal tempering process on DP steel and reported that the nonisothermal process employed using a resistance spot welder produces finer cementite and less recovery in the ferrite structure compared to the sample obtained in a furnace heat treatment (isothermal tempering) process. Chapter 6 deals with the influences of tempering modes on the subtle changes of microstructural units during martensite tempering. In addition, the strength contribution from dislocation densities and precipitates are evaluated. The work demonstrated in this Chapter has been recently published by Saha et al. [161].

6.2 Experimental

A 1.20 mm thick 0.23 wt.% C containing fully martensitic steel (M220) were used; the chemical compositions of the investigated steel is shown in Table 3-1. In order to obtain

various tempered structures, different tempering methods were employed with different heating and cooling rates, temperatures, and times (Figure 6-1, and Table 6-1). To produce a furnace heat treated (FHT) sample, tempering was carried out in a muffle furnace at 500°C for 1 hr, followed by cooling to 25°C within 10 s. For comparison, a sample was Gleeble heat treated (GHT) in a thermal simulator by resistively heating the sample at 100°C/s, to 495°C, and holding for 1 s, followed by cooling to 25°C within 70 s (Figure 6-1). Two other samples were prepared from the SCHAZ (Ac_1 isotherm line) of the diode and fiber laser welded samples, which are henceforth referred to as DLW, and FLW sample, respectively (Figure 6-1). It can be noted that the thermal profiles presented in Figure 6-1 were measured (using a thermocouple welded to the sheet surface) directly from the HAZ during diode laser and fiber laser welding. Due to the narrow HAZ width (about 400 μm) of the FLW, it was not possible to record the temperature close to the Ac_1 isotherm line; however, the heating and cooling sections of the measured thermal profile was successfully predicted (using suitable curve fitting method) and extended to Ac_1 line (725°C) as shown in Figure 6-1. The cooling rate in the SCHAZ of the laser welded samples were estimated using the Rosenthal model (4-1) [88]; where Θ, and Θ_0 temperature (K) are considered as 725°C and 25°C, respectively [97]. The parameters used to temper the samples such as heating rates, cooling rates, temperatures, and times are presented in Table 6-1. Two samples were used for the FHT, FLW, and DLW conditions whereas one sample was considered for the GHT condition. In this work, the FHT and DLW processes are categorized as slow tempering modes, and the FLW and GHT are regarded as fast tempering modes due to the differences in heat input, and heating rates.

Table 6-1 Parameters used for tempering the samples

Sample ID	Heating Rate (°C/s)	Temperature (°C)	Time (s)	Cooling Rate (°C/s)	Tempering Parameter
FHT	Isothermal	500	3600	Air cooled	15,460
DLW	115	725	Nonisothermal	1,248	18,740
GHT	100	495	1	50	13,000
FLW	517	725	Nonisothermal	10,856	13,550

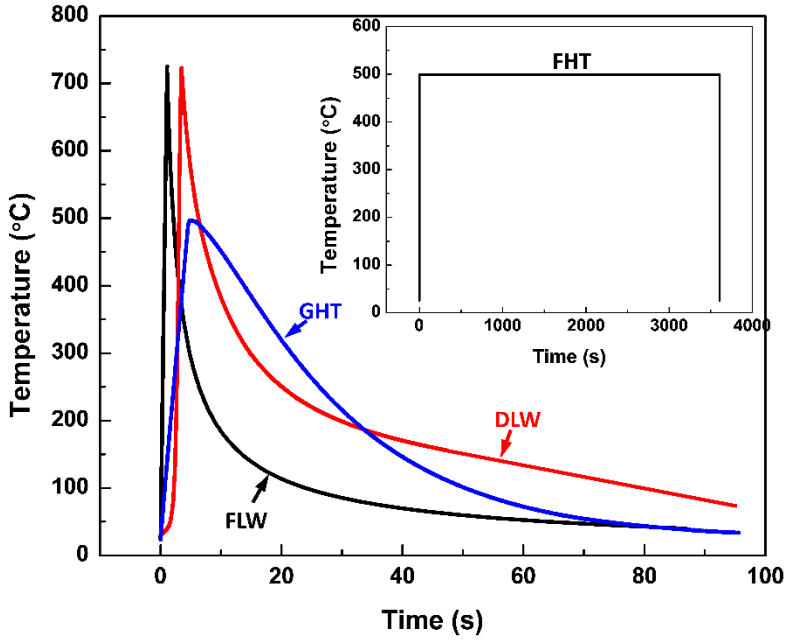

Figure 6-1 Thermal cycles imposed on martensitic steels during tempering using a Gleeble heat treatment (GHT), fiber (FLW), diode laser welder (DLW), and furnace heat treatment (FHT)

6.3 As-received martensitic microstructure

Figure 6-2 shows the microstructure of as-received material which contains fully autotempered [31] typical lath-like martensite with an estimated prior-γ grain size (measured using a linear intercept method [127]) of about 6.3 ± 0.72 μm (marked with arrows in Figure 6-2(a)). Each prior-γ grain is divided into four packets as outlined with dotted lines. Two kinds of laths were developed during martensitic transformation due to

the differences in transformation sequences and temperatures [39]. The coarse laths were formed at the beginning of the martensite formation with relatively high temperature and exhibited reasonably low dislocation density due to greater recovery of dislocations throughout the extended period of transformation [39, 40]. On the other hand, thin martensite laths formed at a later stage of martensite transformation which maintained a high dislocation density (Figure 6-2(b)). The intralath carbides associated with the autotempered martensite are also delineated in Figure 6-2(a), where it was observed that the autotempered carbide likely to be precipitated on the coarse martensite laths (thickness: > 500 nm) whereas the thin laths with an approximate width of 200 nm were free of autotempered carbides (Figure 6-2(b)). TEM micrograph of the lath martensite (Figure 6-2(b)) indicated different contrast of martensite variants (bright and dark) under certain incident directions of the electron beam. SAD patterns taken from the martensite laths were indexed by following the BCT structure of α′ showing the projection plane of $[013]_{\alpha'}$. The faint diffraction spots (marked with red circles on the inset SAD) were also observed illustrating the presence of the autotempered carbides as identified on the FE-SEM micrograph (Figure 6-2(a)). The carbide spots were indexed to be orthorhombic crystal structure of cementite (Pnma) with a *d*-spacing of 2.102 Å corresponding to $< 211 >_{\theta}$ cementite reflection as marked on the inset SAD pattern in Figure 6-2(b).

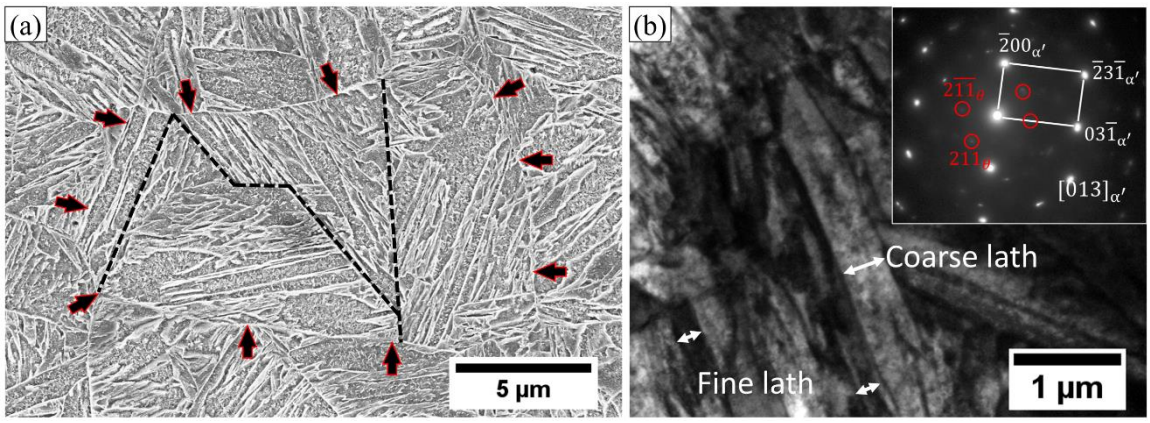

Figure 6-2 Typical martensitic microstructure of as-received material; (a) FE-SEM micrograph of a prior-austenite grain of martensite with four packets and several blocks, (b) TEM image with indexed SAD pattern (inset) of lath martensite showing the zone axis of $[013]_{\alpha'}$; the faint diffraction spots corresponding to the nanoscale autotempered carbides are marked with circles

6.4 Characterization of tempered martensite

The sheet was tempered using various tempering methods and parameters as described in section 6.2 (Table 6-1) and the resulting high-resolution FE-SEM micrographs are shown in Figure 6-3. The micrograph from the DLW sample (Figure 6-3(a)), indicates a severely tempered structure, and the GHT sample (Figure 6-3(d)) exhibits a comparatively less tempered structure. The DLW sample shows highly decomposed martensite with spheroidized carbides at laths boundaries (particle diameters: 45 ± 1.23 nm, marked with smaller arrows) and prior-γ grain boundaries (particle diameters: 170 ± 3.51 nm, marked with bigger arrows); the intra-lath carbides are almost dissolved (less particle density: 1.6×10^{-5} nm^{-2} compared to other conditions (Table 6-2)) representing a greater reduction of dislocation density as intra-lath carbides mainly precipitate at dislocation cell structures.

In addition, the inter-particle distance (245 nm) was also larger on the DLW sample compared to the other conditions (Table 6-2) suggesting less Orowan looping effect [162, 163]. While the sample was tempered in a furnace at 500°C for 1 hr (FHT sample, Figure 6-3(b)), similar morphologies of the spheroidized carbides were identified; however, some of the smaller intra-lath carbides (marked with small arrows) were also observed indicating the presence of the low dislocation density, which was further observed via TEM and HAADF-STEM imaging as will be discussed in section 6.5. The FLW (Figure 6-3(c)) and GHT (Figure 6-3(d)) showed more dispersedly distributed finer carbides; however, the carbides in the GHT sample had an elongated shape with an aspect ratio of about 3.85 ± 0.47. On the other hand, many small quasi-spherical carbides were observed in the FLW sample with a diameter of about 35 ± 1.05 nm; the morphological differences of the carbides among these two samples were solely due to differences in heating rates (Table 6-1), where the heating rate in the FLW process was about five times higher than the one applied in the GHT process (100°C/s).

The spherical shape of carbides on the FLW sample representing a short range carbon diffusion due to higher particle density and shorter inter-particle spacing. It is well-known that the maximum number of precipitates is directly proportional to the density of nucleation sites [164]; therefore, it can be presumed that the precipitates nucleated at dislocation sites maintain an identical size and shape distributions (Figure 6-3(c)). As per

Perrard et al. [164], when there is a high dislocation density, the nucleation process is accelerated due to greater solute consumption; as a result, the growth period decreases and the particles directly go from nucleation to coarsening. Conversely, directional diffusion of carbon may occur along the length axis of carbides found on a GHT sample; therefore, an elongated shape of carbides was precipitated (Figure 6-3(d)).

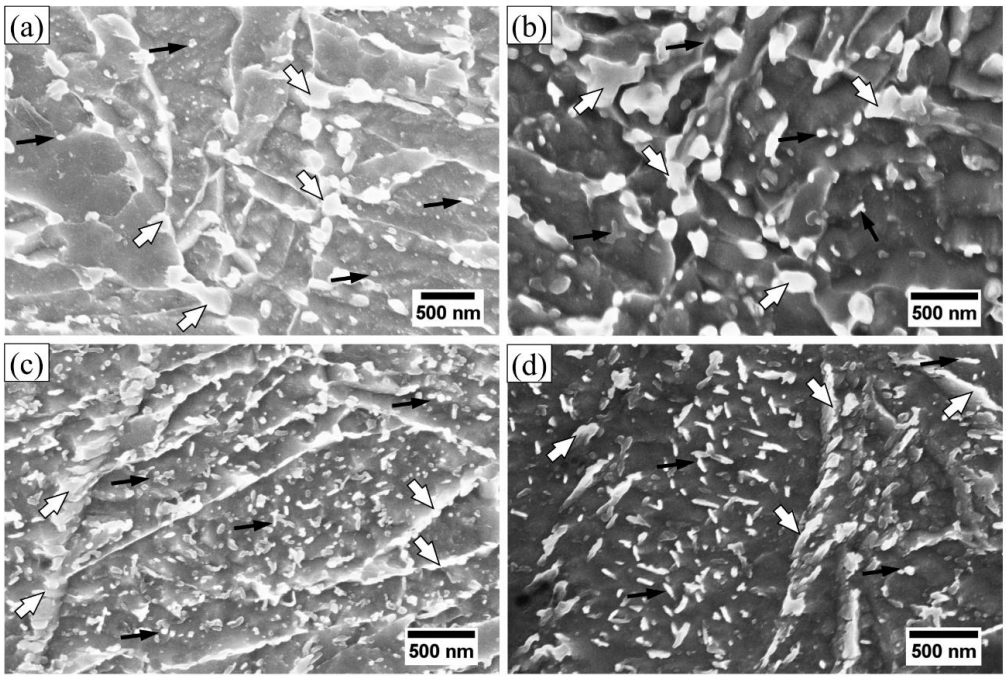

Figure 6-3 Representative high-resolution FE-SEM micrographs of the tempered martensite obtained via various tempering modes; (a) DLW, (b) FHT, (c) FLW, and (d) GHT

Table 6-2 Carbide size measurements at different samples obtained with different tempering modes. The tolerance limit represents the 95% confidence interval.

Tempering mode	Sample Conditions	Low-angle boundaries (nm)	High-angle boundaries (nm)	Inter-particle distance (nm)	Particle density (nm^{-2})
Slow heating	DLW	45 ± 1.23	170 ± 3.51	245	1.6E-5
	FHT	58 ± 2.10	145 ± 3.68	201	2.5E-5
Fast heating	FLW	35 ± 1.05	95 ± 1.58	100	10.0E-5
	GHT	39 ± 0.61	56 ± 1.49	134	5.6E-5

6.5 TEM and HAADF-STEM analysis of matrix and precipitates

In order to investigate the influences of tempering modes on subtle microstructural changes of martensite, TEM and HAADF-STEM imaging were performed and the results are presented in Figure 6-4 and Figure 6-5. TEM study revealed disc-shaped, and spherical carbides at high- and low-angle boundaries, in the DLW and FHT samples, respectively. In the HAADF-STEM images (Figure 6-4(b) and (e)), the precipitated carbides appeared to be brighter in contrast resulting from very high-angle, incoherently scattered electrons. The carbides observed on the DLW sample are well-developed, coarser, and randomly distributed. Similar coarser carbides at high-angle boundaries were identified on the FHT sample (Figure 6-4(d) and (e)); in addition, spherical intralath carbides with a diameter of 58 ± 2.10 nm are observed. The presence of these intralath carbides may be attributed to: (i) precipitate at the final stage of carbide precipitation or (ii) dissolution state (as per classical nucleation theory) due to smaller than the critical carbide size [165, 166]. On the other hand, the high-angle boundary carbides are interconnected (Figure 6-4(e)) illustrating a short-circuit diffusion path [166]. The carbides observed in the tempered martensite structures were indexed to be orthorhombic crystal structure of cementite (θ-Fe_3C) whereas the matrix phase was identified as BCC structure of ferrite. The orientation relationships (OR) between ferrite (α) and cementite (θ) were determined to be $[023]_\alpha||[110]_\theta$, and $[1\bar{1}1]_\alpha||[3\bar{1}1]_\theta$ for the DLW, and FHT sample, respectively. The ferrite and cementite OR in the FHT sample was matched with Isaichev OR [68, 69] (or close to it) with $[3\bar{1}1]_\theta$ at an angle of 0.91° from $[1\bar{1}1]_\alpha$.

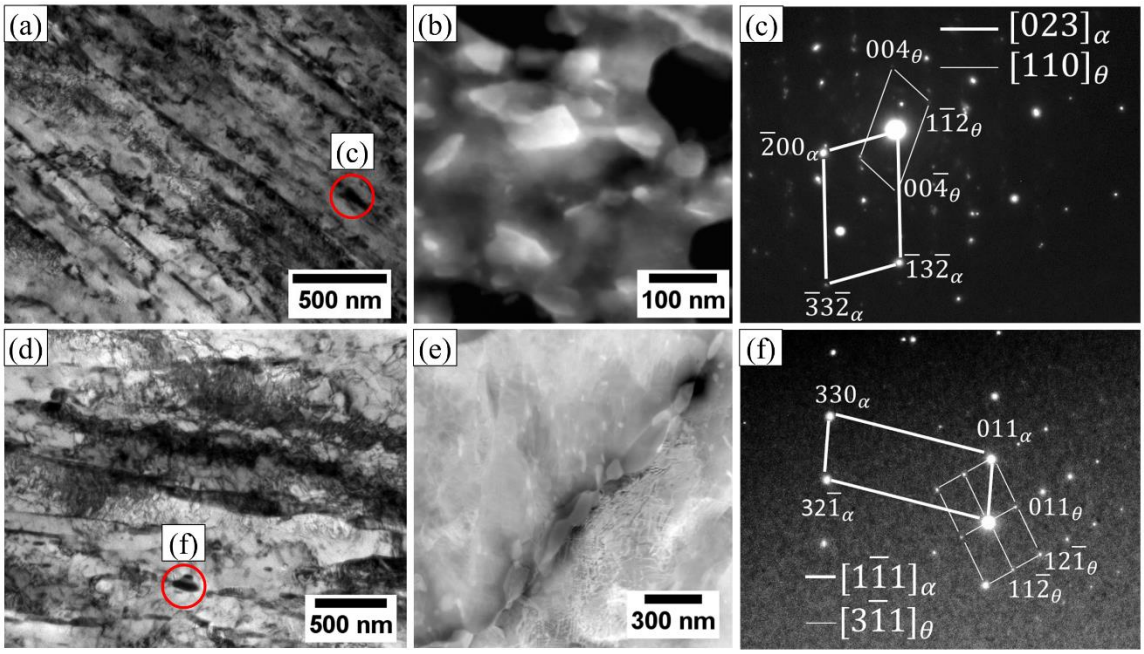

Figure 6-4 Bright-field TEM micrographs, HAADF-STEM images, and their corresponding indexed matrix-precipitates SAD patterns; (a) (b) and (c) DLW sample, and (d), (e) and (f) FHT sample

Conversely, intra- and inter-lath carbides became extremely finer and denser when rapid thermal cycles were employed using a fiber laser and Gleeble thermal cycle (Figure 6-5(a) and (d)). It was noticeable that the size distribution of carbides at low-angle boundaries were similar for both the FLW and GHT samples; however, the size of the high-angle boundary carbides in the FLW was about three times larger than those from the GHT sample (Table 6-1). Interestingly, the intra-lath carbides found on the FLW sample were randomly distributed and spherical in shape (Figure 6-5(b)); however, the carbides in the intra-lath position of the GHT sample maintained a specific orientation relation with the adjacent laths. It was observed that the multivariate carbides were oriented along $< 112 >_\alpha$ direction of the ferrite matrix with an approximate angular position of 33° to the lath boundary (inset of Figure 6-5(d)). The indexed SAD patterns presented in Figure 6-5(c) and (f) confirmed the OR of $[012]_\alpha||[2\bar{4}1]_\theta$, and $[\bar{1}12]_\alpha||[001]_\theta$ for FLW, and GHT sample, respectively. It is noted that the cementite precipitated on the GHT sample maintained a well-defined Bagaryatsky orientation relationship [66, 67].

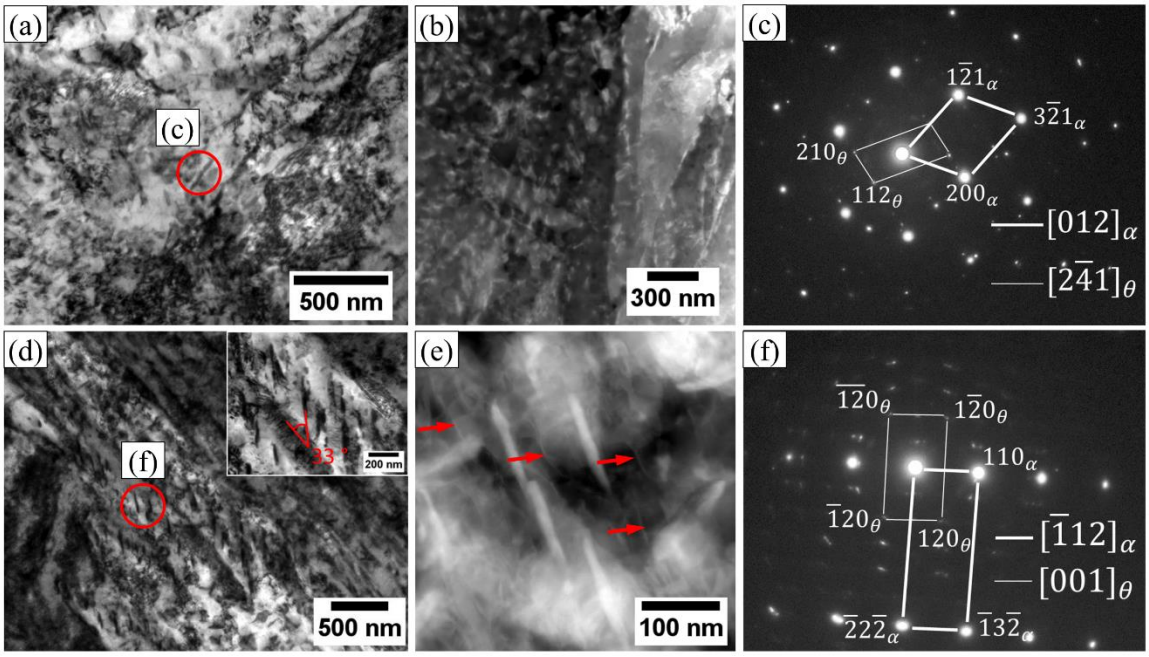

Figure 6-5 Bright-field TEM micrographs, HAADF-STEM images, and their corresponding indexed matrix-precipitates SAD patterns; (a) (b) and (c) FLW sample, and (d) (e) and (f) GHT sample

TEM study of the slowly tempered structures (Figure 6-4) revealed a low dislocation density on the ferrite structure, suggesting that the recovery of dislocation substructure was more pronounced in the case of slowly heated samples [72]. Conversely, faster thermal cycles provided less tempering time, retained more dislocation cell structures (Figure 6-5) [28]; with some of the dislocation lines marked with arrows for example in Figure 6-5(e). In addition, the dislocation lines observed on the GHT sample are almost parallel to the length axis of the cementite platelets attributing the growth of the plate-like cementite occurred along the dislocation line.

6.6 Dislocation density and tempering parameters

The dislocation density is an important parameter which impedes the lattice movement, thus increases the strength of the steels. To estimate the dislocation density, several experimental methods are usually employed such as X-ray diffraction line-broadening method [167], TEM [37], electron backscattered diffraction (EBSD) [73, 168]. In the present investigation, the dislocation density of the untempered martensite was estimated

using a synchrotron X-ray measurement at the 33-ID-D beamline of the Advanced Photon Source (APS) at the Argonne National Laboratory. One sample was tested for each condition to measure the dislocations density. The dislocation density of the used steel was estimated to be in the order of $4.90 \pm 0.5 \times 10^{15}$ m^{-2}, which is about three times compared to other studies (about 1.6×10^{15} m^{-2} [37, 169]) for the identical martensitic steel carbon content (0.2 wt.%). It is well-known that dislocation density is not uniform throughout the sample; therefore, the values measured using TEM and EBSD technique may provide local dislocation density whereas the synchrotron measurement is considered a bulk area analysis which provides more representative values of the average through the thickness.

Figure 6-6(a) shows a relationship between dislocation density and the carbon content of steels [21, 28, 37, 73, 170], which indicates that dislocation density increases with carbon content due to local distortion induced by the interstitial carbon atoms. Aside from carbon content, dislocation density is also influenced by cooling rate, and martensite start temperature during transformation [37]. However, when a highly dislocated martensite phase is exposed to the higher temperature, then dislocation density decreases due to annihilation and recovery process [57, 163]. Dislocation density is expected to decrease with tempering temperature and holding time; however, a slow heating cycle results in more annihilation and recovery rate than the rapidly heated cycle as observed in Figure 6-4 and Figure 6-5 which is also supported by other studies [28, 73].

In the present study, the tempering processes considered have different heating rate, temperature, and time (Table 6-1); therefore, the influences of these factors were combined in the form of tempering parameter as proposed by Tsuchiyama [171]. The proposed model applies the additivity rule for time in order to consider heating and cooling time during tempering. In this method, the heating and cooling cycles are divided into several small isothermal time (t_n) segments at T_n temperature. After n isothermal steps, the tempering parameter (TP_n) can be presented as:

$$TP_n = T_n(20 + logt_n) \tag{6-1}$$

$$t_n = 10^{\{\frac{T_{n-1}}{T_n}(20+logt_{n-1})-20\}} + \Delta t \tag{6-2}$$

$$T_n = T_{n-1} + \alpha\Delta t \tag{6-3}$$

where α and Δt are the heating or cooling rate and the isothermal time step at T_{n-1} temperature, respectively. By plotting dislocation density as a function of tempering parameters of fully martensitic steels [28, 73], it is found that the dislocation density of the tempered martensite varied as a cubic function (fitting coefficient, R^2 = 0.96) of the tempering parameter (Figure 6-6(b)). Using the fitted function, the dislocation densities of the studied samples are predicted based on their tempering parameter as shown in Figure 6-6(b); the highest recovery of dislocations is predicted for the DLW sample which is due to greater heat input and higher tempering parameter [100]. Conversely, the GHT sample experiences less recovery and a high amount of dislocation density is retained as observed experimentally via TEM as shown in Figure 6-5(d) and (e).

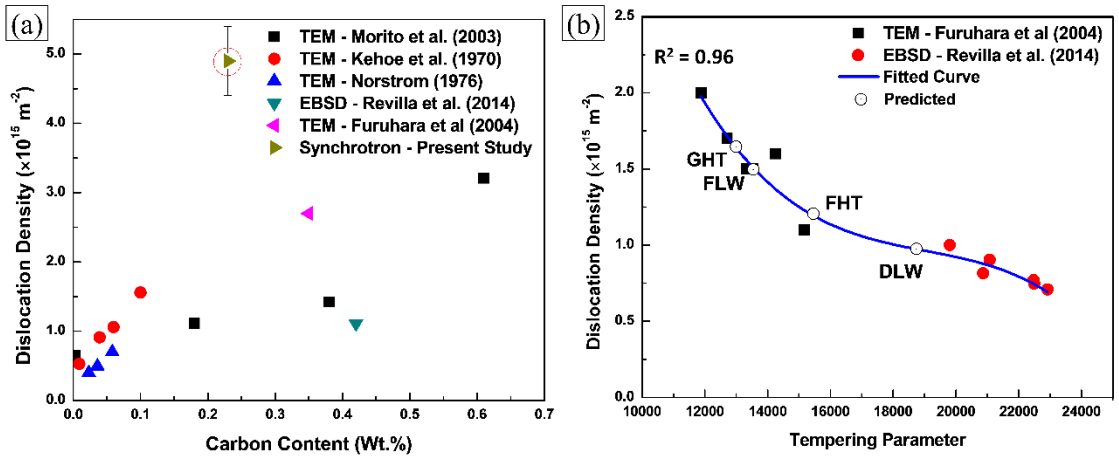

Figure 6-6 Relationship between dislocation density and the carbon content of martensite, and (b) a plot of dislocation density as a function of tempering parameter

6.7 Micro- and nano-scale properties

Micro- and nano-scale properties of the tempered martensite were further assessed using Vickers microhardness and nanoindentation tests as shown in Figure 6-7. Microhardness were performed across the thickness of the samples. Nanohardness of the samples were measured at similar locations as the microhardness indented area; however, the nanohardness indented area was about 100 μm away from the Vickers microhardness indented area to avoid strain field induced by microhardness indent. Two prior-γ grains were selected for nanohardness measurements; nanoindents were performed by randomly indenting on each prior-γ grain and the average hardness values are reported in this study.

There are four microstructural units in a low carbon lath martensite, prior-γ grains, packets, blocks, and laths. The prior-γ grain is typically divided into four packets (Figure 6-2(a)), which is composed of six blocks with identical crystal orientation, and each block is subdivided into several parallel laths (Figure 6-2(b)) with a high density of lattice defects [29, 30, 154, 155]. The lath boundaries are considered to be the low-angle grain boundaries (θ_{min}= 2.8-2.9°) and do not provide effective dislocation barriers. On the other hand, the block boundaries effectively impede dislocation propagation; therefore, these are considered as major boundaries in lath martensite [80]. The hardness measured using Vickers indentation combines all of the microstructural units including high- and low-angle boundaries, dislocation, solid solution, precipitation. On the other hand, using a nanoindenter (Berkovich type) with a smaller tip size (about 50 nm tip diameter) which is less than the lath width (about 200 nm); therefore, the effects of the high-angle boundaries ($\theta_{min} \geq 15°$) on the nanohardness may be disregarded [157, 159].

Figure 6-7(a) illustrates the Vickers micro- and nanohardness of four tempered martensite structures considered; in which the microhardness values are converted to GPa for comparison. Both hardness measures decrease as heat input increase (signifying a higher tempering parameter), due to a minor decomposition of lath structures. Nanohardness measured on the samples are higher than adjacent microhardness tests which is due to the differences of the projected areas consider for hardness measurements. Hardness values determined with a nanoindenter are based on the ratio of load to projected contact area whereas indenter's contact area is used in the Vickers microhardness. Therefore, for a perfect Berkovich indenter, the projected area is corrected to contact area by multiplying with a factor of 0.927 [172]. The structure containing a large amount of boundaries has a higher microhardness compared to the structure with a fewer boundaries. Therefore, the greater reduction of microhardness on the DLW sample implying higher softening of the boundary regions. On the other hand, nanohardness on the samples marginally decreased with increased of the heat input. As the nanoindenter mainly measures the block martensite matrix strength which mainly accounted the effect of dislocations density; therefore, as dislocations density decreased with heat input, nanohardness decreased as well. Conversely, both the boundary softening and the dislocations density reduction influenced on the microhardness values; as a result,

microhardness on the DLW exhibited lower hardness compared to the adjacent nanohardness indent. However, the deviation between microhardness and nanohardness values decreases as it approaches to rapidly heated condition; it is notable that for the GHT sample, both hardness values are similar due to less softening of the boundary areas. It may be concluded that when the structure is heated slowly, the boundary regions softened more as carbon diffusion occurred much faster in the boundaries during tempering [11, 28, 61]. One should also consider the indenter penetration depth of the Vickers indenter using a 1 kg load would be drastically higher than the Berkovich nanoindenter, thus interrogating a larger volume which may include multiple boundary areas with lower dislocation density.

Figure 6-7(b) shows a plot of hardness ratio (H_n/H_v) as a function of Vickers microhardness; the hardness ratio represents the contribution of matrix strength on the total macroscopic hardness of the structure as can be approximated by the following relationship.

$$\frac{H_n}{H_V} = 1 - \frac{k' d^{-\frac{1}{2}}}{H_V} \tag{6-4}$$

where the locking parameter k' is a constant, and d is the grain size. Ohmura et al. [156, 157, 159] reported that the higher the H_n/H_v ratio, the greater the reduction of the grain boundary effect on macroscopic strength; therefore, from Figure 6-7(b), it may be concluded that the DLW sample has higher destruction of the boundary regions (greater recovery) so in this sample, grain boundary strengthening will have less contribution to overall strength as compared to the FLW and GHT samples.

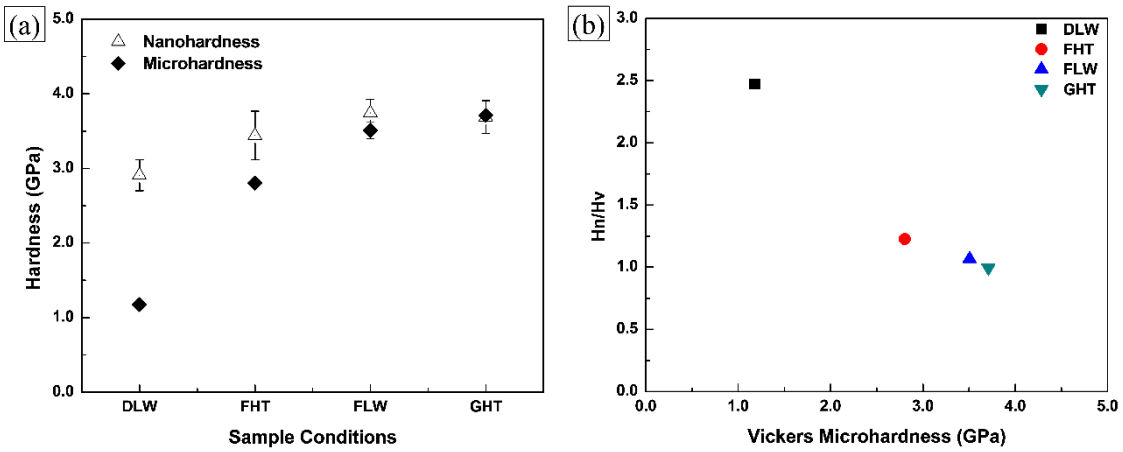

Figure 6-7 (a) Vickers microhardness and nanohardness of the tempered martensite plotted as a function of the tempering conditions, and (b) a plot of hardness ratio (H_n/H_V) with respect to the measured Vickers microhardness. The error bars represent the 95% confidence interval.

6.8 Contribution of dislocations and precipitations

Typically, the yield strength of the lath martensite is correlated from the contributions of lattice friction stress of pure iron (σ_0), the solid solution strengthening (σ_{ss}), the precipitation strengthening (σ_{pct}), grain boundary strengthening, and forest dislocation density strengthening (σ_ρ) at lath and sub-block boundaries. However, considering the tempering effect on the martensite strength, in this study, only dislocation density and precipitation strengthening are evaluated. In addition, the solid solution hardening effects on the tensile strength also disregarded as the same steel chemistry was used and negligible carbon remained in solid solution after tempering. Dilatometric analysis (Chapter 8) shows that the carbide precipitation was completed when the sample was tempered with a tempering parameter of 13,000 (GHT sample) which was the lowest tempering parameter among the four types of sample considered. Therefore, it can be presumed that all of the carbon atoms already diffused and combined with the iron atoms to form stable cementite, thus solid solution hardening effect can be omitted. The strength contribution in relation to the dislocation density is estimated using Taylor formula [173]:

$$\Delta\sigma_\rho = M\alpha Gb\sqrt{\rho} \tag{6-5}$$

where M = 3 is the Taylor factor, α = 0.25 is a fitting constant related to the interaction between forest dislocations [174], G = 76 GPa is the elastic isotropic shear modulus of the lath martensite [175], b is the Burgers vector, and ρ is the dislocation density. The ferrite lattice constant of the investigated steel was estimated from the TEM selected area diffraction patterns to be a = 2.915 ± 0.015 Å. The value of b is considered to be 2.52 Å along <111> slip direction.

The strength of lath martensite can be correlated from the contributions of the carbide precipitation which may increase the strength by impeding dislocation glide [162, 176]. The contribution of precipitation strengthening is predicted using the Orowan-Ashby model [162, 163] as presented in equation (6-6).

$$\sigma_{pct} = 10.8\frac{\sqrt{f}}{d}\ln(1630d) \tag{6-6}$$

where, f and d are the volume fraction of precipitate and mean particle diameter (μm), respectively. The volume fraction and the mean particle diameter are estimated from the high-resolution FE-SEM and TEM micrographs by following the formulas as described in reference [162]. The strength contribution due to a high density of forest dislocations and precipitation are plotted in Figure 6-8 with respect to the tempering parameter. The relationship in this figure indicates that the dislocation density has prominent contribution over that of the carbide precipitation, and the observation is consistent with other researchers [80].

The structure heated with rapid nonisothermal process (FLW sample) possessed the highest precipitation hardening effect due to the highest particle density (10×10^{-5} nm^{-2}) resulting from a short carbon diffusion and shorter growth period, although the high-angle boundary carbides were larger than the one on the GHT sample (Table 6-2). In overall, rapidly tempered GHT and FLW samples have higher precipitation strength contributions compared to the slowly tempered FHT and DLW samples; a similar phenomenon was observed by Biro et al. [177]. As expected, dislocation density strength contribution declined as a function of the tempering parameter (Figure 6-8), which was reported by other researchers [80, 82, 160] as a function of the tempering temperature.

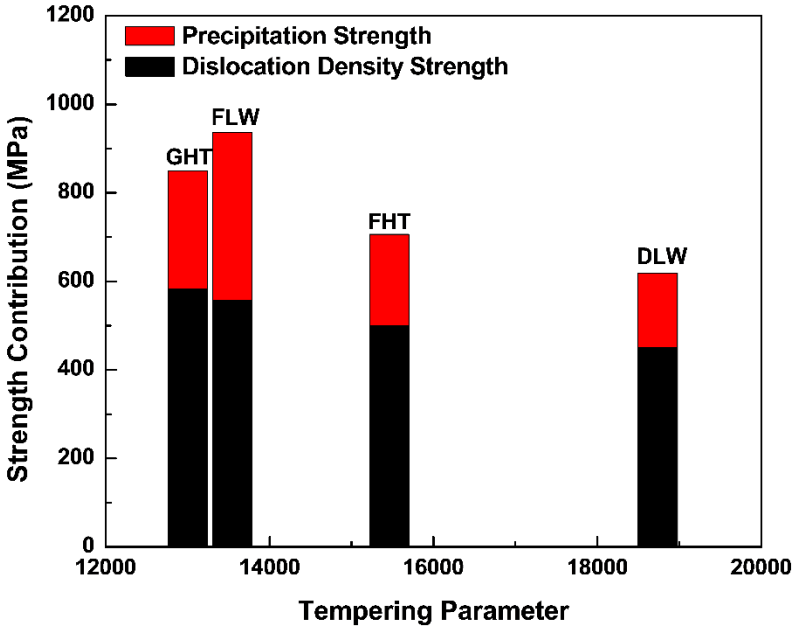

Figure 6-8 Dislocation density and precipitation strength predictions as a function of the tempering parameter for four different tempered martensite samples

6.9 Summary

In-depth characterization of the tempered martensite obtained from various thermo-mechanical processing methods were characterized using TEM and nanoindentation study. The major findings are summarized as follows:

1. Crystallographic analysis of the tempered martensite confirmed that a Bagaryatsky and near Isaichev orientation relationships exist between ferrite and cementite in the sample produced via Gleeble thermomechanical simulation and isothermal furnace heat treatment, respectively. On the other hand, ferrite and cementite observed on the non-isothermally produced laser welded samples do not obey a strict OR.
2. The growth kinetics of the precipitated carbides suppressed when the sample was subjected to the rapid thermal cycle employed via fiber laser welding system. In addition, a rapidly tempered structure maintains a high density of dislocation and less destruction of the boundary regions.

3. Micro-scale softening was more pronounced on the sample subjected to the slowly heated cycle; conversely, microscopic and nanoscale hardness was found to be in the same level when rapid thermal cycle was applied.
4. The strength contribution due to dislocation density was higher than that of precipitation strengthening for the tempered martensite. The rapidly tempered samples have higher precipitation strength contributions compared to the slowly tempered samples.

7 Carbide Precipitation Kinetics under Influences of Plastic Deformation and Rapid Thermal Cycles

7.1 Introduction

In Chapter 6, it was discussed that dislocation density has a dominant effect on the macroscopic strength of the tempered martensite over all other strength contributors such as precipitation, solid solution, and lattice friction stress of the pure iron. It was also observed that the sample heated with a rapid thermal cycle retained a high density of dislocations after tempering thus improving the tempered martensite strength. In addition, Chapter 6 shows that the rapidly tempered samples had higher precipitation strength contributions due to the higher precipitate number density resulting from of the high retained dislocation density.

Dislocation density of the martensite structure was increased by the application of plastic deformation (cold-rolling); a higher dislocation density provides more nucleation sites for carbide precipitation [178-184]. As carbides precipitate preferentially on the dislocation sites during martensite tempering [185-187], tempering of cold-rolled material would result in an increase in the precipitate density and a decrease in the precipitate size due to a smaller inter-particle spacing compared to the tempered strain-free materials. Smaller and more numerous precipitated cementite also inhibits annihilation of dislocations during recovery [28]. Plastic deformation prior to tempering accelerates the recrystallization process [76, 188]; for example, it has been reported that complete recrystallization occurred when a sheet was rolled to 80% prior to tempering at 650°C for 1 hr, whereas a lath martensite morphology of packets and blocks was still maintained when tempered at 700°C for 90 hrs without the cold-rolling [188]. Therefore, it is worth analyzing the tempering phenomenon in the rapidly heated structure that experienced prior plastic deformation, as many sheet metal products are commonly manufactured by rolling or forming prior to welding. The combined effect of the rapid heating and plastic deformation may lead to improved joint integrity by reducing the severity of the martensite tempering effect. Chapter 7 will focus on the effects of dislocation density coupled with

the rapid thermal cycle on the precipitation kinetics during tempering of the fully martensitic steel.

7.2 Experimental methodology

All experiments were performed on 1.2 mm thick 0.23 wt.% C containing fully martensitic steel; the nominal composition of the investigated steel is presented in Table 3-1. The sheet was used in the undeformed as well as in the cold-rolled conditions, where samples were cold-rolled between 10% and 25% of the thickness of the sheet. From this point onwards, strain designations of 0% refer to the undeformed sheet and 25% corresponds to a 25% reduction of the sheet thickness and so on. Sheets were tempered in a muffle furnace at temperature between 200 and 725°C for a duration of 1 hr. In order to obtain a rapid thermal cycle, samples were welded using a fiber laser welding system (heating and cooling rate about 500°C/s and 10,000°C/s [97], respectively as estimated using the Rosenthal equation [88]), the tempered structures corresponding to the SCHAZ, where the peak temperature is about the Ac_1 line, was taken into account for this investigation. Two samples were considered for Vickers microhardness, nanoindentation, and TEM analysis whereas one sample was used for Synchrotron, XRD, and DSC analysis for each condition.

7.3 Results

7.3.1 As-received and as-deformed martensitic microstructure

The representative FE-SEM and TEM micrographs illustrated a typical aligned lath martensite structures in the 0% BM, which were arranged as a parallel group (Figure 7-1(a) and (b)). In addition, evenly distributed intralath carbides usually associated with autotempered martensite [38] were also delineated in the coarser laths as marked with arrows in Figure 7-1(b). The microstructures obtained after 25% deformation (Figure 7-1(c), and (d)) also show a similar autotempered martensitic structure; however, the prior-γ grains, packets, blocks, and laths are substantially deformed with increasing deformation percentage, in accordance with other studies [75].

TEM micrographs and the corresponding selected area diffraction (SAD) patterns (inset) of 0% and 25% samples are presented in Figure 7-1(b) and (d), respectively. The SAD pattern of 0% sample was indexed with a BCC, and orthorhombic crystal structure of martensite (α′), and cementite (θ-Fe_3C), respectively. The weak diffraction spots associated with the nanoscale precipitates confirmed the existence of θ phase with derived orientation relationship (OR) of $[\bar{1}12]_{\alpha'}||[111]_{\theta}$ with the α′ phase. Unlike, the SAD pattern of the 0% sample, a double twins spot was observed in the 25% sample (Figure 7-1(d)) suggesting the presence of a few fine micro deformation twins. The matrix and twin spots were indexed based on the BCC crystal structure representing the projection plane of $[\bar{1}13]_{\alpha'}$. In addition to martensite matrix and twin spots, extra double spots also appeared at $\frac{1}{3}[2\bar{1}1]_{\alpha'}$, and $\frac{2}{3}[2\bar{1}1]_{\alpha'}$ positions as indicated by small arrows in Figure 7-1(d) (inset). This kind of double diffractions has also been observed in a martensitic steel and was reported to be due to the presence of twin structure along the $[112] < 111 >$ direction [150, 189-191]. The lattice parameter of martensite was estimated from the synchrotron experiments to be 2.863 Å, and 2.887 Å, for the 0% and 25% sample, respectively. The measured value indicated about a 6.87% increased of the lattice parameter when the sheet was deformed by 25%. Although both the micrographs showed similar lath martensite structure; however, the laths structure on the 25% sample was found to be highly dislocated (Figure 7-1(d)).

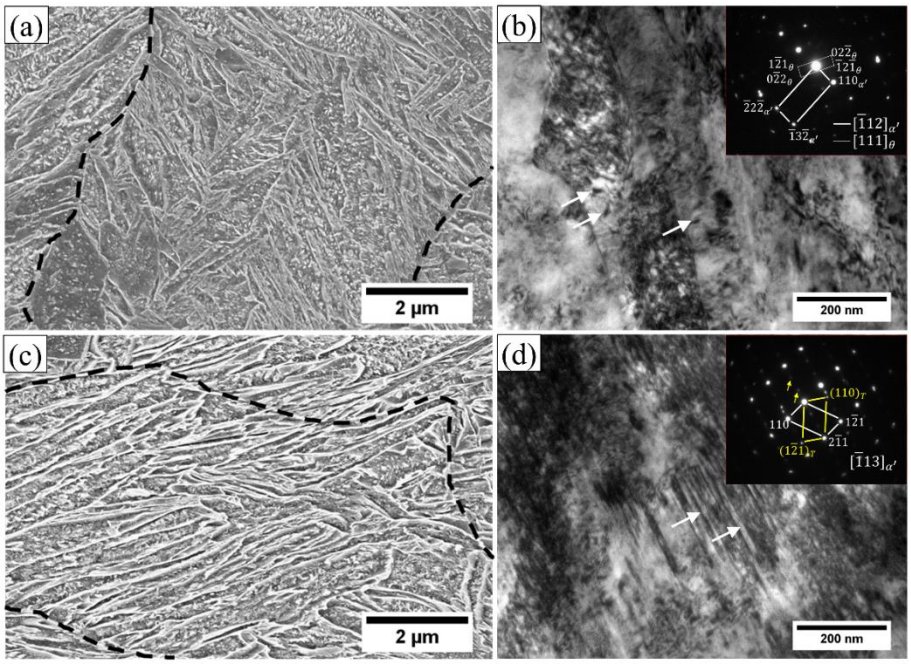

Figure 7-1 SEM and TEM micrographs and the corresponding selected area diffraction patterns of martensite at (a) and (b) undeformed (0%) condition; and (c) and (d) 25% cold-rolled condition, respectively

7.3.2 Dislocation density evolution

As-received material (0%) displayed an approximate dislocation density of 4.90 ± 0.5 × 10^{15} m^{-2} (the tolerance limit represents one standard deviation). Synchrotron experiments illustrated an increase of dislocation density when sheets were deformed to different levels (Figure 7-2); this observation was also confirmed by other researchers [75]. It is interesting to report that when the structure was plastically deformed, some grains were deformed more severely compared to others. Therefore, it seems like the deformed sample behaves similar to a composite structure having a combination of the hard and soft phase. Synchrotron measurement shows asymmetric peak shapes which was correlated by using two component system (A, and B) where structures with relatively lower and higher dislocation density were observed (Table 7-1). The peak of the softer phase shifts to a lower 2θ angle indicating an increase in lattice spacing, which corresponds to a tensile elastic residual strain. On the other hand, the peak of the harder phase shifts to a higher 2θ angle meaning a decrease in lattice spacing, attributed to a compressive elastic residual strain. It

was estimated that dislocation density of the soft phase was close to an identical value as the undeformed (0%) sample; however, this value on the hard phase increased to about $29.7 \pm 3 \times 10^{15}$ m^{-2} when the sheet was deformed by 25% (Table 7-1).

Table 7-1 The microstructural parameters for the samples cold rolled at different levels. The tolerance limit represents the standard deviation.

Sample conditions	$\langle X \rangle_A$ (nm)		ρ ($\times 10^{15}$ m^{-2})		Ratio of screw dislocations (%)		Dislocation arrangement parameter	
	A	B	A	B	A	B	A	B
0%	45±5		4.9±0.5		45±5		7±1	
25%	32.5±6	60±10	3.4±0.4	29.7±3	45±5	35±5	4.1±0.5	2.1±0.2

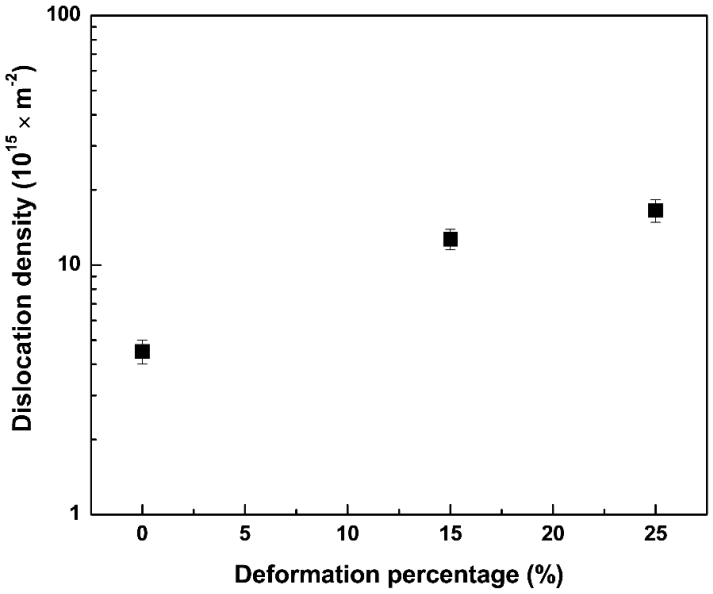

Figure 7-2 A plot of dislocation density as a function of deformation percentage. The error bars represent the standard deviation.

7.3.3 Isothermal tempering

Figure 7-3 shows the trend of microhardness while samples were tempered isothermally at temperatures between 200 and 725°C for 1 hr. The microhardness plot can

be divided into two (for 0% sample) or three (for 25% sample) distinct zones based on the microstructural evidence as marked in Figure 7-3. The hardness trend of the 0% sample shows a small reduction of hardness up to 200°C (Zone 1) which is attributed to the segregation of carbon atoms at lattice defect sites and reorganization of dislocations. However, in the case of 25% sample, the temperature of Zone 1 is extended to 300°C suggesting a longer carbon segregation temperature range due to the high density of dislocations (Figure 7-2). At temperatures between 200 and 500°C the material softened significantly as noted by the large hardness drop; however, sheets with greater plastic deformation had a higher hardness due to a large amount of retained dislocations and pinning of dislocations by the redistributed carbon atoms as will be discussed in section 7.4. The reduction of hardness at 500°C was measured to be about 45%, and 41% for 0%, and 25% sample, respectively; regardless of deformation conditions, similar softening was detected. It can be seen that the hardness trend of 25% sample shows a severe softening above 500°C tempering temperature (referred as Zone 3) due to greater recovery, polygonalization, and recrystallization in ferrite phase.

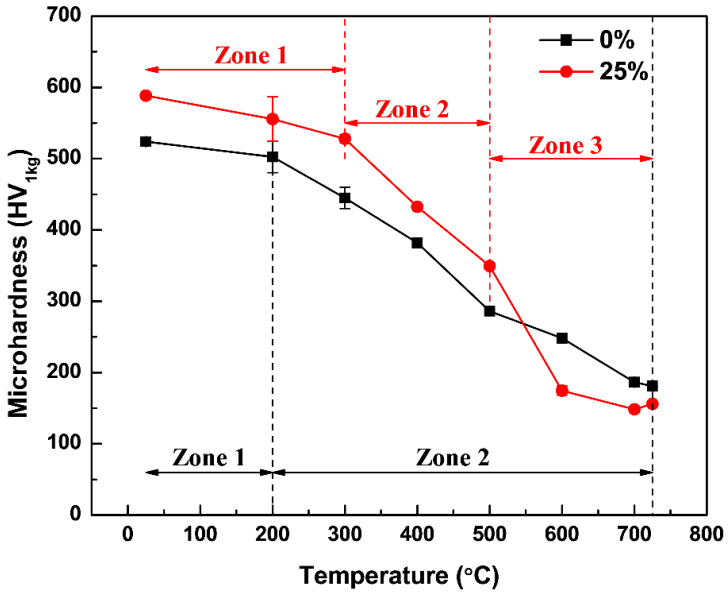

Figure 7-3 Hardness responses during isothermal tempering between 200-725°C for 1 hr with respect to the tempering temperature for 0% and 25% sample. The error bars represent the 95% confidence interval.

The tempered structures were characterized using a high-resolution FE-SEM, TEM, HAADF-STEM imaging as presented in Figure 7-4 and Figure 7-5. The precipitated carbides may be regarded as intra- and interlath types, the former nucleates in the vicinity of dislocations inside the martensite lath and the later in the lath boundaries. At 300°C which is the temperature at which the precipitation began, the carbides appeared elongated in shape at various boundaries on the 0% sample (Figure 7-4(a)); however, when 25% deformation was imposed, the carbides remained more or less identical (Figure 7-4(b)) as in the 0% condition. When tempered at higher temperature (500°C) the intralath carbide became extremely fine (diameter: 9 ± 0.42 nm, Figure 7-4(d)) compared to particle diameter: 57 ± 3.46 nm on the 0% sample (Figure 7-4(c)) suggesting that the carbide growth and coarsening kinetics was slower due to the high dislocation density [164, 192, 193]. However, the energy stored in the deformed sheets provided the driving force for cementite precipitation at dislocation cell structures; therefore, precipitates identified in the 25% sample were more densely dispersed which may be identified as strain induced precipitates (Figure 7-4(d)). The intralath carbides in the 0% sample maintained nearly elongated morphologies until 500°C; however, the particle number density decreased with increasing temperature. Above 500°C tempering temperature, deformation enhanced dislocation annihilation and recovery processes within the martensite laths; therefore, more recovered and recrystallized structure was found in the 25% sample (Figure 7-4(f)) when tempered at 600°C for 1 hr as noted by the large hardness drop (Figure 7-3). The bigger and spheroidized cementite (diameter: 140 ± 11.64 nm) was observed on the tempered 25% condition compared to the ones (diameter: 63 ± 4.71 nm) on the 0% sample (Figure 7-4(e) and (f), Table 7-2).

Table 7-2 Carbide size distribution at various locations of the tempered martensite subjected to various temperature. The tolerance limit represents the 95% confidence interval.

Temper-ature (°C)	Low angle grain boundary (nm)			High-angle grain boundary (nm)		
	0%	15%	25%	0%	15%	25%
300	52 ± 2.91	40 ± 2.22	41 ± 2.49	91 ± 3.19	79 ± 3.19	73 ± 2.63
400	54 ± 3.46	39 ± 2.36	37 ± 2.22	97 ± 4.02	81 ± 3.74	75 ± 3.74
500	57 ± 3.46	45 ± 2.77	9 ± 0.42	135 ± 5.27	110 ± 4.85	33 ± 1.39
600	63 ± 4.71	112 ± 8.59	140 ± 11.6	168 ± 9.70	239 ± 8.87	274 ± 10.2
SCHAZ	35 ± 1.66	33 ± 1.66	38 ± 2.08	79 ± 2.49	66 ± 2.22	68 ± 2.63

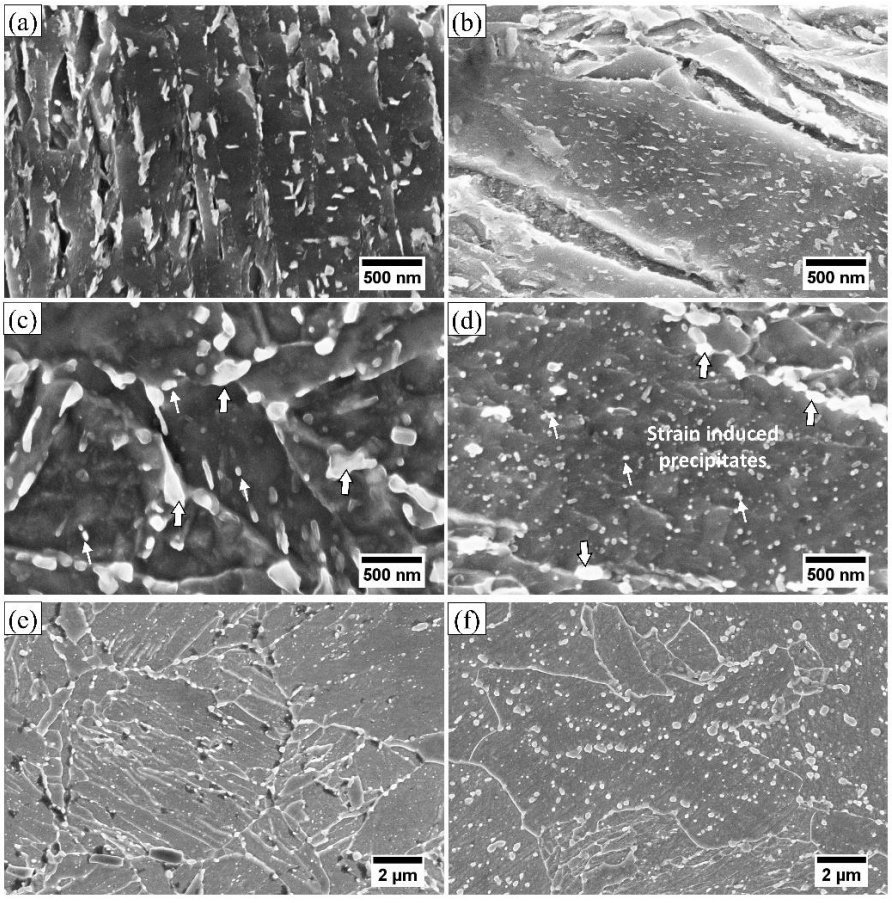

Figure 7-4 SEM micrographs of the furnace heat treated 0% and 25% deformed martensite at a temperature of 300, 500°C, and 600°C: (a) 0% at 300°C, (b) 25% at 300°C, (c) 0% at 500°C, (d) 25% at 500°C, (e) 0% at 600°C, and (f) 25% at 600°C

The samples tempered at 500°C for 1 hr were observed via TEM and HAADF-STEM imaging as shown in Figure 7-5. Bright-field TEM micrographs and the indexed selected area diffraction (SAD) patterns taken from the circled area marked in Figure 7-5(a) and (d); some of the high- and low-angle boundary carbides are marked with large and small arrows, respectively. SAD patterns were indexed by following BCC and orthorhombic crystal structures of ferrite (α) and cementite (θ-Fe_3C), respectively. It was found that an OR between cementite and ferrite on the 0% tempered at 500°C sample obeyed the Isaichev OR with $[\bar{3}1\bar{1}]_\theta$ 0.91° from $[1\bar{1}1]_\alpha$ [68, 69]; on the other hand, the OR between matrix and precipitates ($[\bar{1}12]_\alpha||[1\bar{1}\bar{1}]_\theta$) in the 25% tempered sample deviated from the Bagaryatsky OR due to the crystal rotation.

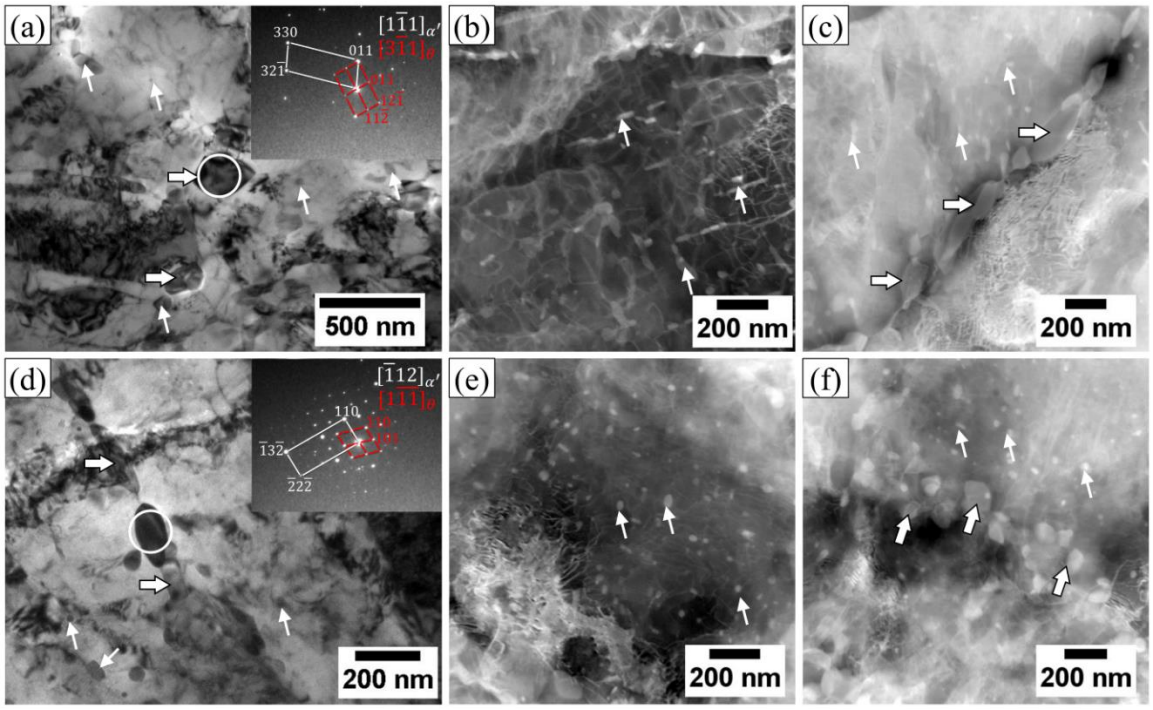

Figure 7-5 TEM and HAADF-STEM images of tempered martensite obtained via furnace tempering at 500°C for 1 hr, (a) to (c) 0% sample, and (d) to (f) 25% sample

HAADF-STEM images presented in Figure 7-5(b) and (c) illustrates finer and elongated shape, and film-like interconnected carbides (short-circuit diffusion path [166]) at low- and high-angle boundaries, respectively. The intralath carbides were effectively pinned by dislocations; a high dislocation density was retained even after tempering of the 0% sample at 500°C for 1 hr (Figure 7-5(b)). In contrast to the 0% sample, a spherical and

highly dense carbides were found at low-angle boundaries of the 25% tempered sample (Figure 7-5(e)); tangled dislocation networks were pinned with the carbides. Unlike the observation in the 0% deformation sample, the high-angle boundary carbides become spherical and smaller in size (Figure 7-5(f)) compared to that of 0% sample (Figure 7-5(c))) which implies that short-range carbon diffusion occurred.

7.3.4 Rapid tempering

The effects of the plastic deformation on the microhardness of the tempered structure within the weld SCHAZ and the BM is shown in Figure 7-6. The SCHAZ hardness increases with increasing deformation percentage, implying that the hardness of the SCHAZ and the BM was mostly dependent on the microstructural parameters such as the dislocation density of the sheets. The BM hardness increased from 524 ± 4.53 HV to 588 ± 4.53 HV, i.e. about 64 HV increase, when the sheet was deformed by 25% of its original thickness; similarly, the SCHAZ increased from 357 ± 10.75 HV to 453 ± 11.32 HV. In overall, the SCHAZ hardness was calculated to be softened less by about 96 HV when sheets were deformed by 25%. The 0% BM sample had hardness of 524 ± 4.53 HV, which dropped down to 357 ± 10.75 HV in the SCHAZ region of the laser welded sample representing 32% reduction of microhardness. The SCHAZ hardness increased to 453 ± 11.32 HV on the 25% deformed sample, which accounted about 27% improvement of the hardness of the SCHAZ compared to the SCHAZ hardness of the 0% sample. The hardness differences between the BM and SCHAZ were found to be decreased with increasing deformation percentage implies that higher plastic deformation retards the softening kinetics while sheets were subjected to the rapid thermal cycle.

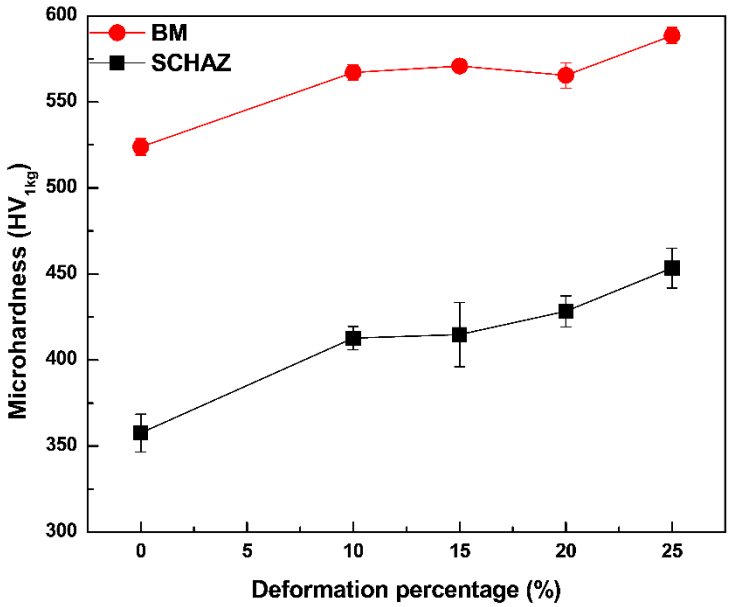

Figure 7-6 Microhardness of the BM and SCHAZ of the welded joints as a function of deformation percentage. The error bars represent the 95% confidence interval.

High-resolution FE-SEM micrographs of the tempered zone in the HAZ obtained during fiber laser welding process are illustrated in Figure 7-7. The locations of the SCHAZ were measured from the FE-SEM images to be about 470 μm away from the center of the FZ. The micrographs presented in Figure 7-7(a) and (b) were taken from about 100 μm away from the SCHAZ towards the BM i.e. 570 μm from the weld centerline and Figure 7-7(c) and (d) from the SCHAZ of the two samples. Figure 7-7(a) and (b) depicts the influences of the dislocation density on carbide dispersion; high populations of tiny spherical carbide were identified on the 25% sample compared to the carbides in the 0% sample (Figure 7-7(a)). The particles at low- and high-angle boundaries were measured from the SCHAZ for three different (i.e., 0%, 15%, and 25% deformation) sample conditions as shown in Table 7-2. At the SCHAZ, the carbides in the 0% sample remained as elongated shape but well decorated at lath and prior-γ grain boundaries. Intralath carbides mostly had an elongated morphology with an aspect ratio of 1.7-3.0, while spherical carbides were of about 34 ± 1.11 nm diameter. In the tempered 0% sample (Figure 7-7(c)), multi variate carbides were well-aligned along the lath boundaries, which suggests that the elongated carbide were preferentially precipitated in the lath boundaries. In addition, intralath smaller spherical carbides were also observed in the deformed samples,

and the general trend was that the morphology of the carbide transitioned from an elongated shape to small spherical shapes (35 ± 1.25 nm) when 25% deformation was imposed. It was noted that the number density of carbides was significantly higher at 100 μm away from the SCHAZ, and was decreased at the SCHAZ. As per classical nucleation theory [165], the particle lower than the critical size will dissolve and the bigger particle will growth by the expense of the smaller one.

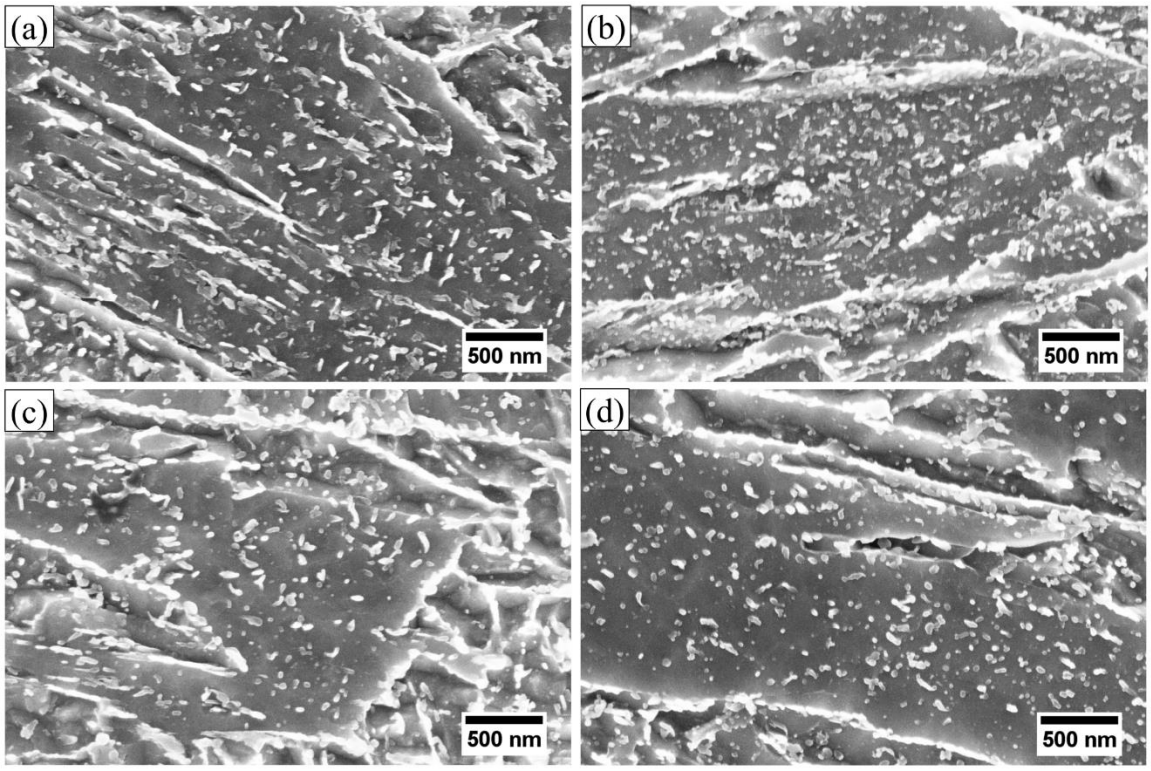

Figure 7-7 The SEM micrographs of the HAZ obtained at different locations of the laser welded sample (a) 0% at 570 μm from the weld centre, (b) 25% at 570 μm from the weld centre, (c) 0% at 470 μm (SCHAZ) from the weld centre, and (d) 25% at 470 μm (SCHAZ) from the weld centre

The TEM and HAADF-STEM image in Figure 7-8 reveals the carbide morphologies in the tempered martensite obtained from the SCHAZ of the 0% sample. Well decorated arrays of carbide were precipitated along the interlath boundaries (marked with larger arrows in Figure 7-8(a)), which exhibited interconnected film-like morphology [166]. The intralath carbide (marked with smaller arrows) was mostly elongated (Figure 7-8(b) and (c)), although small spherical carbide particles were also observed. The sample prepared

by using a carbon replica method was examined as well to confirm the precipitated carbide's crystal structure as presented in Figure 7-8(b) and (d). Elongated carbides located in the intralath regions were not possible to extract on the carbon replica; however, a trace of the elongated carbides was identified in the TEM bright field image as indicated by arrows in Figure 7-8(b). The corresponding selected area diffraction pattern of spherical carbides was indexed to be an orthorhombic crystal structure of cementite (θ-Fe_3C) showing the projection plane of $[010]_\theta$ (Figure 7-8(d)).

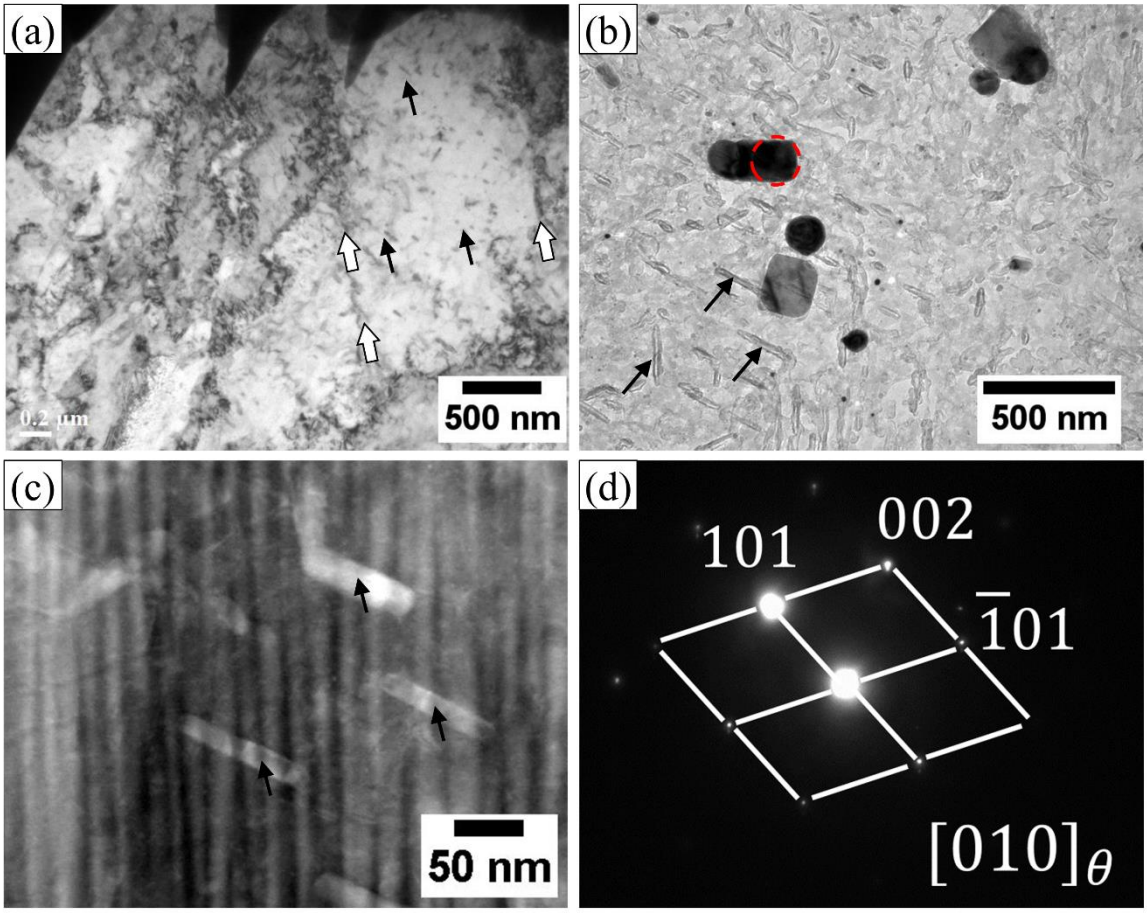

Figure 7-8 TEM study of the SCHAZ of 0% sample showing, (a) bright-field images of matrix and carbides at intra and interlath locations, (b) carbides on an extracted carbon replica, (c) HAADF-STEM image of the elongated carbides, and (d) indexed SAD pattern of cementite with a projection plane of $[010]_\theta$

The FIB sample extracted from the SCHAZ of 25% sample was also observed by TEM and HAADF-STEM imaging as presented in Figure 7-9. The morphologies of the

cementite on the 25% sample were quasi-spherical compared to the elongated one as observed on the 0% sample. In addition, tiny spherical cementite was observed (Figure 7-9(f)), which was believed to be strain induced precipitates. Furthermore, an untempered or partially tempered martensite (UTM or PTM, Figure 7-9(c)), retained dislocation cells, and tangled dislocations (Figure 7-9(e)) were visible in the SCHAZ of the 25% sample. It was observed that the martensite grains with slender shape (aspect ratio: 6.90 ± 2) were not tempered completely due to insufficient reaction time resulting from the highly dislocated structure as higher density of dislocations retards the tempering kinetics. Some of the slender shape martensite grains are marked with dotted elliptical lines in Figure 7-9(a), (b) and (c) which were not affected by the tempering process or only partially tempered. HAADF-STEM image of the large rectangular area in Figure 7-9(a) is shown in Figure 7-9(b) which depicts the UTM or PTM structure with brighter contrast resulting from very high-angle, incoherently scattered electrons representing the presence of the heavier atomic elements and a high density of defects (dislocations). Figure 7-9(c) illustrates a magnified view of a UTM or PTM phase connected to a prior-γ grain boundary (PAGB) which confirmed the BCT crystal structure of martensite with a derived zone axis of $[011]_{\alpha'}$ martensite (Figure 7-9(d)). The dark-field image taken with a $(\overline{2}00)_{\alpha'}$ martensite reflection is shown in Figure 7-9(d). The lattice parameters of the UTM or PTM was measured to be a = 2.870 Å, and c = 2.937 Å with a tetragonality of c/a = 1.023 implies that the tetragonality of the UTM or PTM martensite was maintained at the SCHAZ when the structure was highly dislocated.

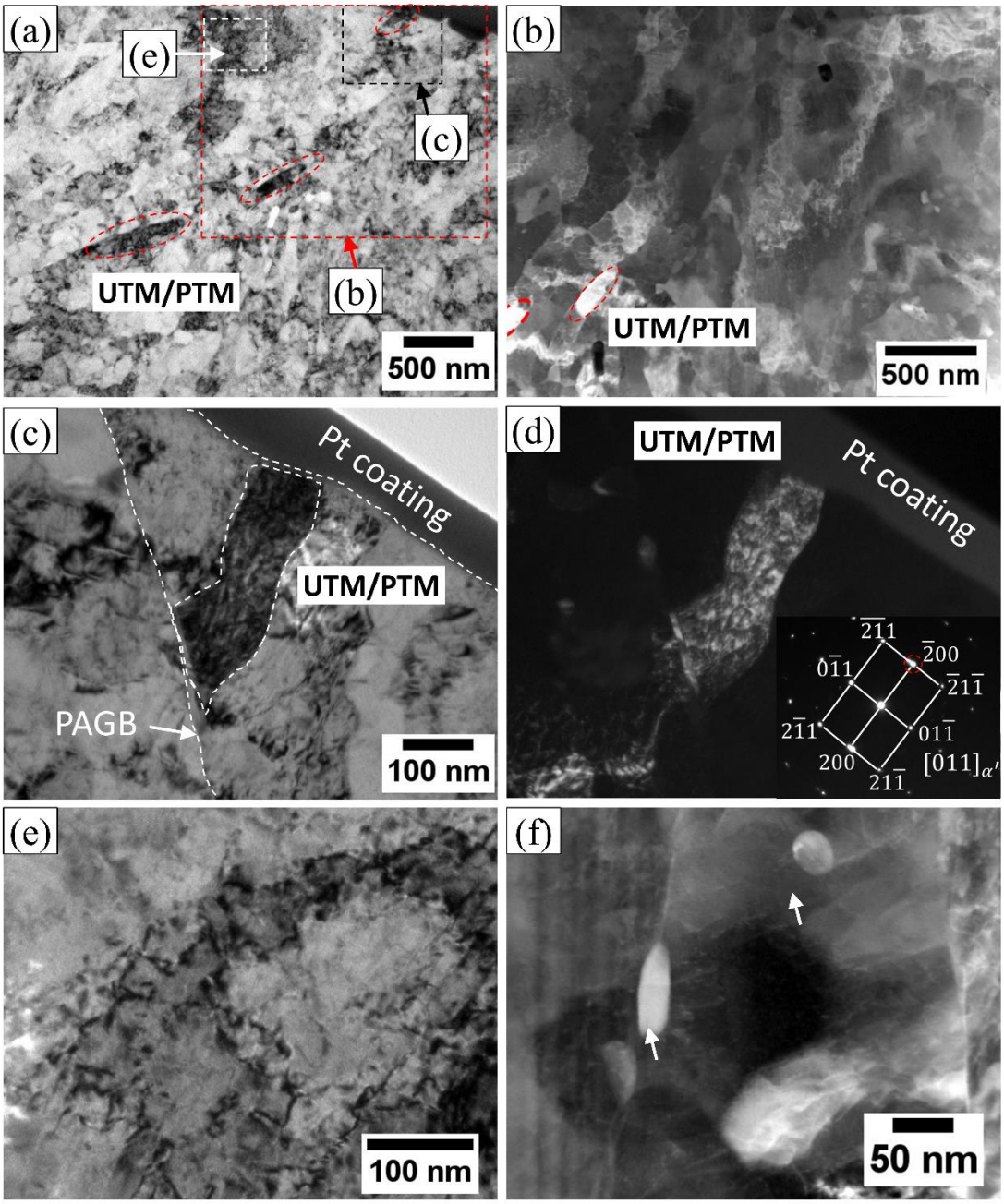

Figure 7-9 TEM study of the SCHAZ of 25% sample showing, (a) bright-field image of tempered martensite with precipitates and untempered or partially tempered martensite, (b) HAADF-STEM image of the large rectangular area marked in (a), (c) enlarged view of the UTM or PTM marked on (a), (d) dark-field image of the UTM or PTM taken with a martensite diffraction spot of $(\bar{2}00)_{\alpha'}$ with indexed SAD, (e) the area with tangled dislocation and pinned precipitates as marked in (a), and (f) HAADF-STEM image of the precipitates

7.3.5 Thermal analysis of tempering kinetics

The influences of defect density on the martensite tempering kinetics was further investigated using a differential scanning calorimetry (DSC) analysis by heating two differently dislocated samples from room temperature to 700°C with a heating rate of 100 K/min. Figure 7-10 shows the kinetics study for the various stages of tempering such as carbon segregation and formation of carbon clusters (*sg*), precipitation of cementite (θ), and the decomposition of interlath retained austenite (γ). Three inflection points were detected on each heat flow vs. temperature curve; however, the inflection points corresponding to the precipitation of cementite and retained austenite overlapped each other (Figure 7-10(a)). It is noticeable that both the inflection points were shifted to a higher temperature when sheet was deformed by 25%; however, due to smaller precipitate volume fraction the amount of heat generated was significantly lower (0.813 J/g) than the 0% sample one (6.906 J/g). The first inflection point that occurred at 132°C, and 229°C (Figure 7-10(b)) was due to the segregation of carbon in the lattice defects for the 0%, and 25% sample, respectively. It has been reported that plastic deformation can retard the ε-carbide precipitation by lowering the carbon atoms into dislocations in medium and high carbon containing steels [194]. In the current investigation, it was found that the temperature for the carbon segregation increased by about 100°C (from 132°C to 229°C) when the average defect (dislocation) density increased by three times (from $4.90 \pm 0.5 \times 10^{15}$ m^{-2} to $16.55 \pm 1.7 \times 10^{15}$ m^{-2}, Figure 7-2). It was also experimentally observed that when a sample was tempered at 300°C for 1 hr, the carbide precipitation did not occur in the 25% sample (Figure 7-4(b)), rather autotempered carbides were more or less identical to that of the untempered 25% sample (Figure 7-1(c)). Figure 7-10(c) represents the heat flow curve corresponding to the cementite precipitation, which indicates the reduction of the transformation temperature range from 215-550°C to 317-488°C. Therefore, it can be concluded that a high density of dislocation can effectively delay the precipitation growth kinetics by lowering the carbon available for precipitation which was also reported by Perrard et al. [164]. The kinetics of the retained austenite decomposition were also influenced by the plastic deformation as shown in Figure 7-10(a) and (d). It was found that the volume fraction of retained austenite significantly decreased when sheet was plastically

deformed (decomposition of the retained austenite was further investigated using synchrotron characterization as discussed in section 7.4.1); therefore, during heating, it produced very negligible heat flow. In addition to cementite, plastic deformation also delayed the retained austenite decomposition kinetics as shown in Figure 7-10(d). A further study is required to validate the mechanisms explained in this section. Some of the issues may need to be accounted for in future investigation such as dynamic tempering effect while cold-rolling. It may be possible to have different carbide (such as ε-carbide) forming during deformation.

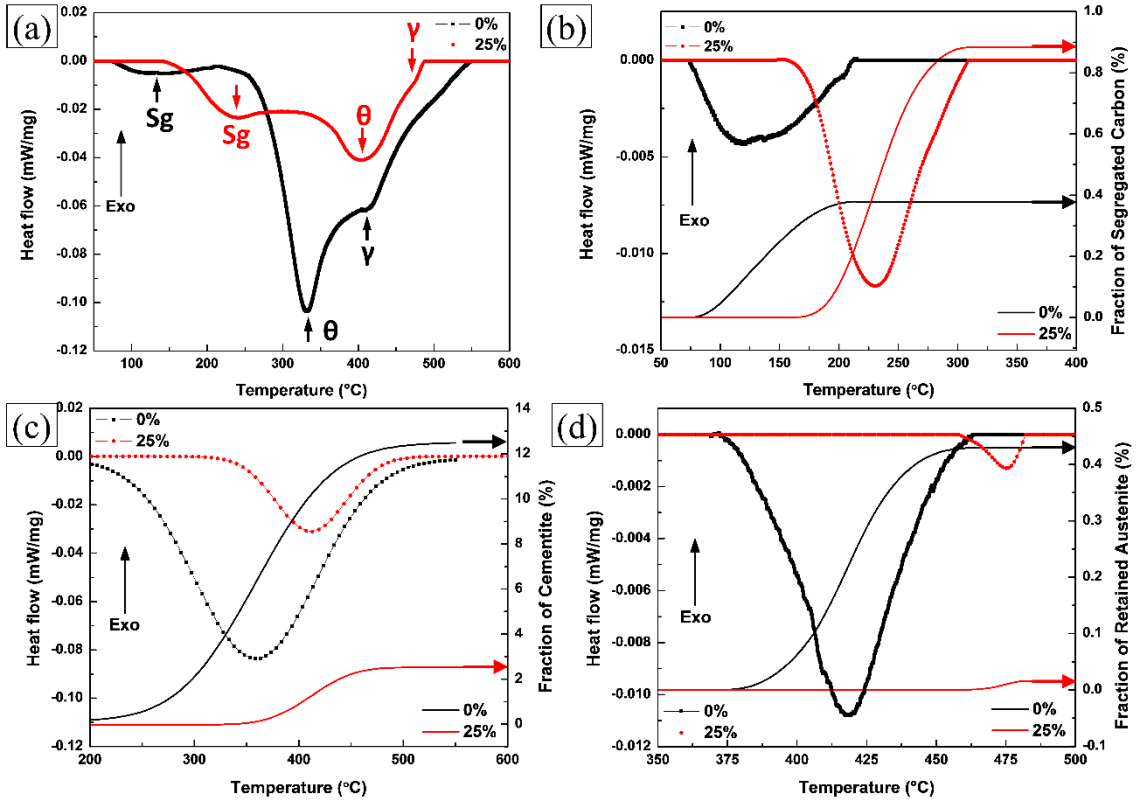

Figure 7-10 Typical DSC curves obtained during heating the undeformed (0%) and 25% deformed martensitic steels with a heating rate of 100 K/min; (a) full DSC curves of both the samples, (b) carbon segregation part of the curves and fraction of segregated carbon, (c) cementite precipitation part of the curves and fraction of cementite, and (d) retained austenite decomposition part of the curves and fraction of retained austenite

7.4 Discussion

7.4.1 Carbide and retained austenite decomposition during cold-rolling

Figure 7-11 shows the diffraction peaks obtained from the synchrotron characterization of 0% and 25% deformed samples in the untempered condition. In order to identify the diffraction peaks, martensite($I4/mmm$), ferrite($Im\bar{3}m$), austenite($Fm\bar{3}m$), and cementite ($Pnma$) phases were considered in accordance with Inorganic Crystal Structure Database (ICSD). The considered lattice parameters are: a_α = 2.8664 Å, a_γ = 3.5852 Å, a_θ = 4.5241 Å, b_θ = 5.0883 Å, c_θ = 6.7416 Å [195]. It is well documented that carbides (cementite) existing in the tempered martensite [196] or pearlite [197, 198] may decompose during cold drawing of the sheets; however, the cementite decomposition rate is higher at higher true strain. As the studied martensitic steel contains autotempered carbides (Figure 7-1(a) and (b)), therefore, they are likely to decompose when plastic deformation is applied. On the 0% sample, the cementite peaks were identified with a relatively larger intensity, the $(012)_\theta$ and $(021)_\theta$ peaks were indexed in Figure 7-11. It can be stated that the observed peaks positions were slightly shifted to the higher angles due to straining during sample preparation. The 25% sample showed decreases in intensities of these peaks due to the reduction of volume fraction of cementite as a result of diffusion and decomposition. Decomposition of cementite was also observed during cold drawing of tempered martensite via 3D atom probe analysis [196] and it was reported that cementite completely decomposed when sheet was cold drawn at 3.6% true strain. Their study also confirmed the strong evidence of carbon rich atmospheres around dislocation lines in the deformed martensite structure. It has also been found that during cementite decomposition, carbon atoms migrated to dislocations near the interface due to a higher binding enthalpy between carbon atoms and dislocations in ferrite [198].

As-received material (0%) contains a small amount of film-like retained austenite between martensite laths due to partitioning of carbon atoms during martensitic transformation [199]. The volume fraction of retained austenite was estimated from the integrated peaks intensity of ferrite (α) and austenite (γ) by following the method as demonstrated by van Dijk et al. [93] (see section 3.4.4.1). The estimated value shows that

the as-received material contained approximately 0.157% of retained austenite which is almost completely decomposed while sheet was deformed by 25%. On the 25% sample, the austenite peaks corresponding to $(002)_\gamma$, $(022)_\gamma$, and $(113)_\gamma$ almost disappeared as shown in Figure 7-11. The mean lattice parameter of retained austenite in the 0% undeformed sample was estimated from synchrotron X-ray peaks to be 3.616 Å.

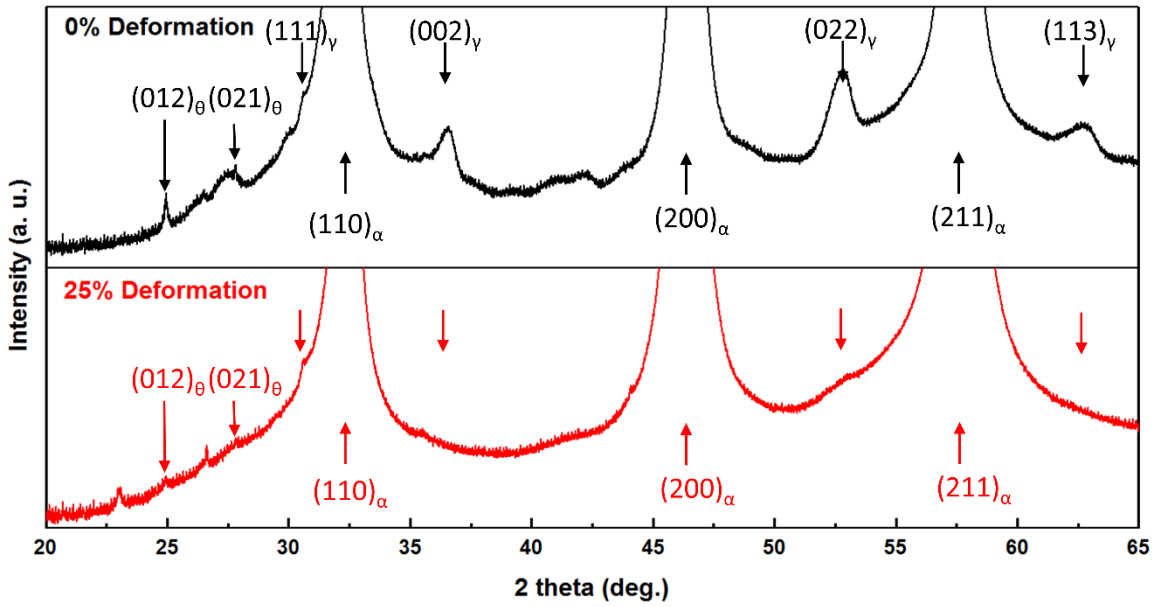

Figure 7-11 Synchrotron characterization of the carbides and retained austenite decomposition during cold-rolling

7.4.2 Dislocation - precipitation interaction

The 0% and 25% structures tempered at different temperatures exhibited significant changes of the morphologies of the precipitates, which appeared to be due to the nucleation of carbides at dislocation-trapped carbon sites. As plastic deformation induced high dislocation populations into the material (Figure 7-2), carbon segregation took place at dislocation lines due to rearrangement and migration of carbon atoms. It has been demonstrated that dislocations introduced by plastic deformation can act as effective carbon trapping sites thus decreasing the chemical driving force for the carbide precipitation [185, 192]. Thermodynamic calculation showed that the phase fraction of cementite and the driving force both decreased with increasing dislocation density [192, 200]; these phenomena provide evidence of finer carbides in the deformed martensite

structure (Figure 7-4(b)). Kalish and Cohen [185] demonstrated that the driving force for the carbon segregation at dislocations is two-fold compared to the driving force of the cementite precipitation. Therefore, the increase of dislocation density retarded the growth kinetics of precipitates by lowering the amount of carbon remaining in solid solution to feed the carbides to grow. The amount of carbon available for precipitation (C_0) is dependent on dislocation density and can be approximated as [201]:

$$C_{seg} = (\frac{\rho}{a_{seg}})v_{at} \quad (7\text{-}1)$$

$$C_0 = C_{nom} - (\frac{\rho}{a_{seg}})v_{at} \quad (7\text{-}2)$$

where, C_{seg}, C_{nom}, v_{at}, ρ, and a_{seg} are the segregated carbon atoms, nominal carbon composition of the steel, atomic volume of iron, dislocation density, and average distance between the carbon atoms segregated to dislocation, respectively. The amount of carbon segregated to dislocation density of the 0% sample (ρ = 4.90 ± 0.5 × 10^{15} m^{-2}) was calculated to be about 0.04 wt.% which increased to a level of 0.14 wt.% with 25% deformation of the sample (ρ = 16.55 ± 1.7 × 10^{15} m^{-2}). Therefore, the available carbon to feed carbides to grow would be 0.19 wt.% and 0.09 wt.% for the 0% and 25% sample, respectively. Therefore, the decreased available carbon content will reduce the thermodynamic driving force for growth kinetics of precipitates under paraequilibrium condition [201].

7.4.3 Evolution of chemical composition of precipitates

During tempering, carbide spheroidization is controlled by the diffusion of carbon and alloying elements. It has been reported that the growth rate of cementite is substantially suppressed by the addition of Mn, Cr, and Si [202, 203]. In the present study, the Mn and Si content of ferrite and cementite were estimated using EDX analysis in the HAADF-STEM mode and reported in Table 7-3. The samples tempered at 500°C for 1 hr shows identical Mn content in the ferrite matrix of both the deformed and undeformed condition; however, Si content of ferrite in the 25% sample appeared to be higher which implies greater ejection of Si from the cementite. On the other hand, the percentage of Mn was

reduced (from 0.94 wt.% to 0.75 wt.%) in cementite obtained on the 25% sample. The reduction of Mn content in the cementite was attributed to the reduction of local Mn content due to higher number density of cementite particles. Conversely, the Mn concentration in cementite decreased in the structure obtained from the SCHAZ due to the shorter tempering time resulting from the rapid tempering process. Miyamoto et al. [203] reported that the partitioning of Mn in cementite increased with tempering time; therefore, higher tempering time will allow more segregation of Mn in cementite. The Mn partitioning in to cementite is affected by the deformation; lesser partitioning of Mn is detected on the samples deformed by 25% regardless of thermal cycles.

Table 7-3 EDX analysis of matrix and precipitates found in the various tempering conditions. The tolerance limit represents the 95% confidence interval.

Phase	Tempering Condition	0% Sample		25% Sample	
		Mn	Si	Mn	Si
Ferrite	500°C	0.43 ± 0.07	0.12 ± 0.03	0.49 ± 0.05	0.32 ± 0.02
Cementite		0.94 ± 0.30	0.11 ± 0.05	0.75 ± 0.18	0.19 ± 0.04
Ferrite	SCHAZ	0.38 ± 0.11	0.27 ± 0.09	0.56 ± 0.06	0.58 ± 0.13
Cementite		0.44 ± 0.06	0.23 ± 0.07	0.24 ±0.06	0.22 ± 0.08

7.4.4 HRTEM study of matrix and precipitates

Figure 7-12 shows HRTEM lattice fringe images of cementite and ferrite matrix found in the SCHAZ of the 0% sample. The FFT (Fast Fourier Transformation) was performed in two regions ((b) and (c)) where zone (b) and (c) are located at the center of the cementite platelet and at cementite-ferrite interface, respectively. The inverse Fourier filtered transformation (IFFT) lattice image obtained from the diffraction spot of $[121]_\theta$ confirmed the cementite with a *d*-spacing of 2.116 Å. Center of the cementite showed a nearly perfect single crystal with no visible lattice mismatch; however, at the vicinity of cementite and ferrite interface, several lattice distortions and edge dislocations were observed which may be attributed to the partitioning or rejection of the other alloying elements such as Mn and Si. The chemical analysis confirmed the presence of Mn and Si in the cementite phase (Table 7-3). The atomic radius of Fe, Mn, and Si are 1.24 Å, 1.29 Å, and 1.14 Å [204];

therefore, when the Fe atoms of cementite are replaced by Mn or Si atoms then it causes the lattice strain or contraction by severe lattice distortion and partial dislocations. The cementite and ferrite interface was found to be very incoherent with high lattice mismatch (Figure 7-12(c)) which did not follow any periodic crystal disorder. The incoherent cementite-ferrite interface may be attributed to the ejection of elements such as Si from the cementite and build up a Si-rich layer at the interface as reported in the literature [202, 205].

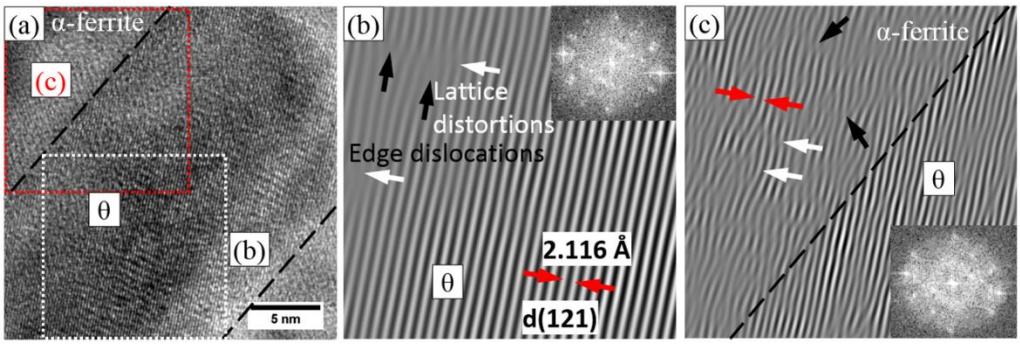

Figure 7-12 HRTEM micrographs of cementite and ferrite matrix extracted from the SCHAZ of 0% sample. (a) lattice fringe image of cementite platelet and the interface between cementite and ferrite matrix, (b) IFFT image of the cementite with inset FFT pattern, and (c) IFFT image of interface between cementite and ferrite matrix, FFT pattern is presented in inset

Similar HRTEM analysis of cementite and ferrite observed in the SCHAZ of 25% sample is shown in Figure 7-13. The FFT diffraction patterns and the corresponding IFFT lattice image of the cementite (zone (I)) is shown in Figure 7-13(b) and (c), respectively. The atomic arrangement of cementite is highly ordered with no lattice mismatch; in addition, the lattice image is free of edge dislocations and lattice distortions implying less influences of substitutional elements on lattice strain. A reduction of lattice spacing of cementite was observed from 2.116 Å to 2.068 Å on the 25% sample. The FFT and IFFT lattice image of ferrite-cementite interface (zone (II) in Figure 7-13(a)) is shown in Figure 7-13(d) and (e), respectively. The interface was found to be flat with a single mismatch occurring every 4 to 5 $(210)_\theta$ crystal planes (marked with $\perp$); the interface, therefore, referred to as a semicoherent interface with lattice strain. The relative strain due to the

lattice misfit is estimated using ferrite as a reference: $\varepsilon = |\frac{d_{\alpha-Fe}-d_{\theta}}{d_{\alpha-Fe}}|$, shows about 19.25% elastic strain which implies that every 5 continuous planes of cementite phase there will be a dislocation to accommodate the misfit of the two lattices. Figure 7-13(e) confirms the presence of an edge dislocation in every 4-5 lattice planes of cementite along $(210)_{\theta}$ direction.

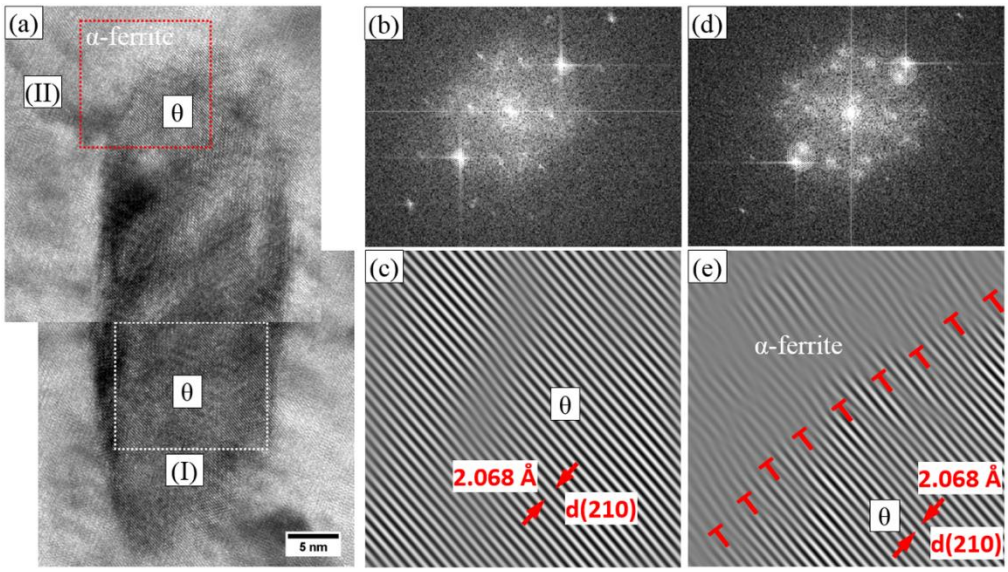

Figure 7-13 HRTEM lattice image of cementite and ferrite observed in the SCHAZ of 25% sample, (a) lattice fringe of cementite platelet and ferrite matrix, (b) FFT pattern of cementite taken from region (I) in (a), (c) IFFT image of the cementite taken from region (I), (d) FFT pattern of cementite-ferrite interface taken from region (II), and (e) IFFT image of interface between cementite and ferrite taken from region (II)

7.4.5 Microstructure and hardness correlation of tempered martensite

Figure 7-14 shows $(200)\alpha$ ferrite diffraction peaks of 0% and 25% sample at untempered BM and tempered at 400°C for 1 hr. As it can be seen that high intensity and sharpening of the ferrite peak occurred after tempering at 400°C, which is attributed to the reduction of defect density (i.e. dislocation density) by recovery and annihilation. However, more sharpening of the peak was detected in the case of tempered 0% sample (0%-400°C) compared to the 25%-400°C sample indicating greater reduction of dislocation density on the former one. Therefore, it may be concluded that 25% sample

yielded a high density of dislocation even after tempering at 400°C for 1 hr in contrast to the 0%-400°C sample.

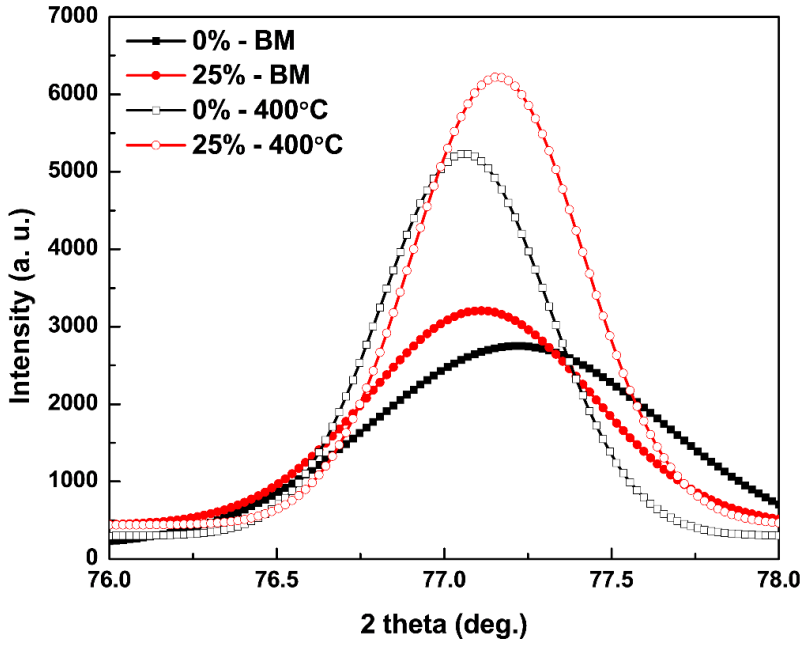

Figure 7-14 The positions of $(200)_\alpha$ ferrite diffraction peaks of 0% and 25% sample at untempered BM (0%-BM, and 25%-BM) and tempered at 400°C for 1 hr (0%-400°C, and 25%-400°C)

The strength of martensite blocks tempered at 500°C for 1 hr was further assessed using instrumentation nanoindentation study; the plot of load-depth (*P*-*h*) curves during nanoindentation is presented in Figure 7-15. The Hertzian elastic contact solution which represent the transition between elastic and plastic zone is also plotted in Figure 7-15. The Hertzian elastic deformations of the block matrix of lath martensite were plotted according to equations (7-3) and (7-4) [206].

$$P = \frac{4}{3} E_r R_i^{\frac{1}{2}} h^{\frac{3}{2}} \tag{7-3}$$

$$E_r = \frac{1 - v_i^2}{E_i^2} + \frac{1 - v_s^2}{E_s^2} \tag{7-4}$$

where, P, E_r, R_i, h, E, v is the applied load, effective indentation modulus, indenter tip radius, contact depth, Young's modulus, and Poisson's ratio, respectively. The subscripts

i and *s* represent the parameters corresponding to indenter and specimen, respectively. The values used to plot the Hertzian elastic contact solution can be found in Table 7-4.

Table 7-4 The parameters for the Hertzian elastic contact solution calculation

Parameters	R_i	ν_i	ν_s	E_i	E_s
Values (Unit) [41, 206-209]	200 nm	0.07	0.3	1141 GPa	220 GPa

Both the curves show deviation from the Hertzian solution representing plastically deformed; however, more plastic deformation was observed on the martensite block of the 0% tempered sample illustrating greater recovery of dislocations. The average nanohardness on the martensite block of the tempered 0% and 25% sample was measured to be 3.77 ± 0.16 GPa and 4.76 ± 0.26 GPa, respectively; it can be seen that the average block nanohardness increased by 1 GPa while sheet was 25% deformed prior to tempering at 500°C for 1 hr. In addition, more plastic deformation of the block matrix was observed which shows about contact depth of 174.6 ± 5.06 nm compared to 148.6 ± 5.46 nm on the 25% tempered sample. It can be concluded that a high density of retained dislocations in the deformed and tempered martensite increases the block matrix strength; in addition, the smaller size of carbides on the deformed and tempered samples provided higher hardness compared to that of the 0% tempered sample.

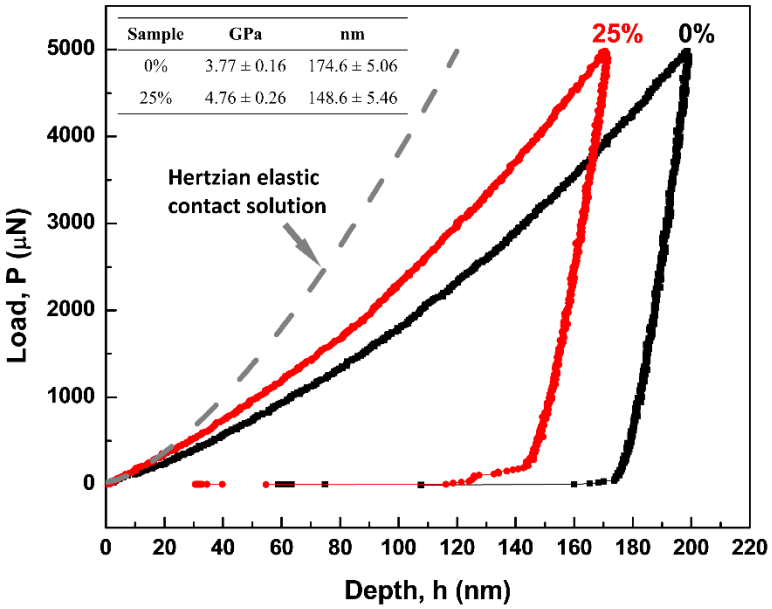

Figure 7-15 The plot of load-depth (*P-h*) curve of the martensite block of 0% and 25% sample tempered at 500°C for 1 hr (inset average hardness and indent depth). The Hertzian elastic contact solution curve for the martensite matrix is also shown

7.5 Summary

The effect of heating rate on the tempering of plastically deformed martensite and the properties of the lath martensite structure was reported by considering the dislocation density effect on the tempering kinetics. The outcomes of this study are listed as follows:

1. Dislocation density of the lath martensite increases with plastic deformation which shortens the cementite transformation temperature range and provides a longer carbon segregation period thus carbon segregation temperature range increases with dislocation density.

2. The higher dislocation density of the deformed material resulted in more nucleation sites for cementite precipitation, short-range diffusion of carbon and lower growth period for cementite. The morphologies of the cementite were changed from the elongated to small quasi-spherical with plastic deformation when lath structure of the

initial martensite was damaged and more nucleation sites were created by the process of cold-rolling.

3. Prior plastically deformed and tempered lath martensite structure yielded a higher structural strength due to a higher retained dislocation density, finer and semicoherent precipitates, and large fraction of the untempered and partially tempered martensite blocks.

8 Carbide Precipitation Kinetics and Strength Prediction of Martensitic Steel Subjected to Short Term Tempering

8.1 Introduction

Throughout the Chapters 4, 5, 6 and 7, it was experimentally observed that various factors affect the strength of complex lath martensite. One of the major contributors is the amount of carbon dissolved into the solid solution. In the as-quenched condition, the carbon atoms segregate at lath boundaries and form a Cottrell atmosphere [25, 55, 207], which tends to diffuse during tempering and coarsen the lath boundaries by forming carbides. The diffusion of carbon depends on the tempering temperature and time which are related to the other factors such as heat input, and heating rate. It has been reported that the rapid heating cycle improves the strength and toughness of the martensitic steel by fine cementite dispersion [28, 73, 208]. In addition, it has also been demonstrated that the tempered structure maintains a larger dislocation density when subjected to a rapid thermal cycle and thus provides a larger dislocation density strengthening contribution compared to the other factors as reported in section 6.8 also supported by Kim et al. [80]. The estimation of dislocation density of the tempered lath martensite is an expensive and laborious process; dislocation density of as-quenched lath martensite may be related to the carbon content; however, the existing model cannot be applied to the tempered martensite structure because during tempering, a transient change of dislocation occurs. Recently, Galindo-Nava and Rivera-Díaz-del-Castillo [82, 160], proposed a model by which the dislocation density of lath martensite can be predicted by linking carbon content of steel and the lath width after tempering. The model was successfully applied to the martensitic and DP steels to predict the strength of the steels both in the untempered and tempered conditions [82, 160]. The rapid thermal cycles that are applied in some processing applications such as during laser beam welding and induction heating, provides a dynamic change of dislocation density and carbide precipitation where the heating rate of the tempering cycle has a major influence. The model proposed by Galindo-Nava and Rivera-Díaz-del-Castillo [82, 160] did not consider the individual effects of each tempering parameter such as heating rate, temperature, and duration of heating. Therefore, the proposed model cannot be applied in

the process where samples are tempered non-isothermally (such as welding, and induction heating processes). Chapter 8 incorporated all the parameters associated with the tempering process and combined them together in order to predict the microstructural units and strengths of the tempered martensite subjected to the rapid tempering process. The model was generalized for a wide range of heating rates, temperatures, and times and validated with the experimental observation carried out using dilatometer, Gleeble, SEM, TEM, and EBSD analysis.

8.2 Experimental

The carbide precipitation kinetics studies during continuous heating and isothermal holding were investigated using a dilatometer (model: DSI Gleeble 3800). The dilatometric specimens with a dimension of $20 \times 100 \times 1.8$ mm^3 were heated above the Ac_1 line with heating rates of 0.5°C/s to 500°C/s; samples were cooled down to room temperature by constant cooling rate of 25°C/s. The dimensional changes (width of the samples) were measured along with the recorded temperature. Afterward recorded data were filtered to reduce noise in the data sets. For metallographic analysis, interrupted quenching was performed in the Gleeble thermomechanical simulator by employing identical thermal profile (Figure 3-4, and Table 3-5) as applied in the dilatometry tests.

8.3 Carbide precipitation kinetics

Figure 8-1 represents a comparative analysis of the DSC and dilatometer study while heating the sample from room temperature to 550°C with a heating rate of 100 K/min and 60 K/min, respectively. It can be seen that the reactions corresponding to the carbon clustering, and retained austenite decomposition produced stronger signals in the DSC curve; however, no detectable slope changes were observed on the dilatometer response, only a single slope change was identified due to the carbide (θ-Fe_3C) precipitation. In the current investigation, the dilatometer was used in order to construct a full continuous heating transformation (CHT) diagram as well as to study the microstructure and mechanical responses. Both studies confirmed the cementite start temperature to be about

265°C (DSC) and 240°C (dilatometer). The deviation of cementite start temperature between the testing methods maybe attributed to the slight differences in the heating rate.

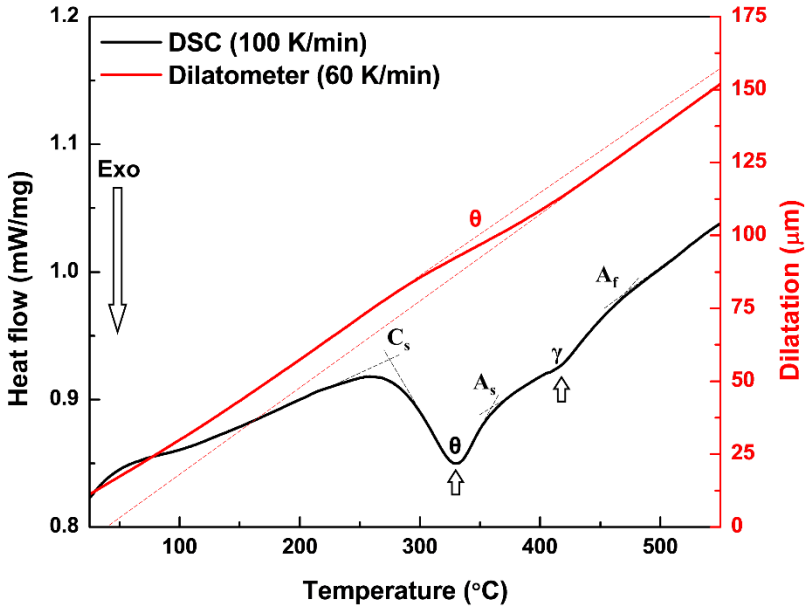

Figure 8-1 A comparative analysis of DSC and dilatometry of the sample heating from room temperature to 550°C with a heating rate of 100 K/min and 60 K/min, respectively

Figure 8-2(a) shows dilatation curves of the material during heating from room temperature to Ac_1 line (725°C) with heating rates between 0.5°C/s to 500°C/s. Only the heating part of the dilatation curves were plotted as a function of temperature; for better visualization, each curve was offset to different level. The initiation of tempering is manifested by the hump in the curves; the transformation temperature range was identified to be between 240°C and 527°C for all of the considered heating rates. As the investigated material contains 0.23 wt.% C, therefore, no observable slope changes corresponding to the ε-carbide ($Fe_{2.4}C$) was detected. However, the segregation of carbon atoms and the formation of carbon clusters can be expected to be taken place at its lattice defects (such as dislocations) while tempering at low temperature (below 200°C) (Figure 8-1). Nevertheless, the dimensional change of the material is not influenced by carbon atom segregation; therefore, the dilatation of the material corresponding to the carbon segregation is disregarded. While the sample was slowly heated with a heating rate of 0.5°C/s, the carbide precipitation occurred between 240-420°C which shifted to 340-527°C when a rapid heating cycle (500°C/s) was applied. It is noticeable that both the precipitation

start and finish temperatures shifted to the higher temperature by keeping the transformation temperature difference nearly constant (about 180°C). However, the time required to complete the reaction kinetics is significantly decreased with increasing heating rate.

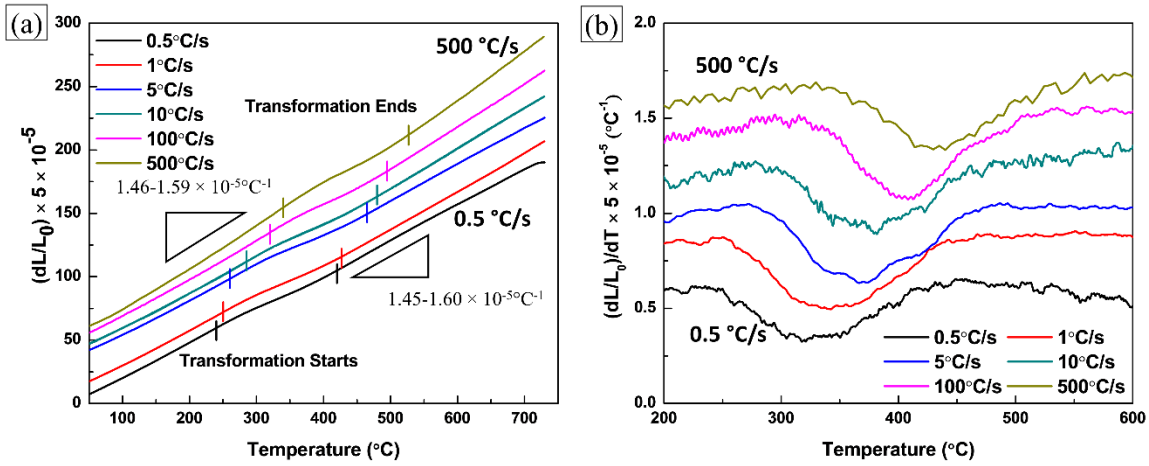

Figure 8-2 (a) Dilatometric curves of 0.23 wt.% C martensitic steel recorded during continuous heating with different heating rates (0.5°C/s to 500°C/s), and (b) the first derivatives of the curves presented in (a)

To improve the visualization of the dimensional changes associated with the martensite tempering kinetics, the first derivate of the dilatation curve was plotted in Figure 8-2(b). The duration of carbide precipitation decreases with increases of the heating rate implying short-range carbon diffusion and the precipitation ended up quickly; this phenomenon was reported to be due to the shorter carbides growth period at a higher heating rate as was observed in Chapter 6. During heating, a single maximum point was observed which is the so-called normal transformation and the phase fraction of carbide was estimated from the recorded relative length change by applying the lever rule [209] as presented in Figure 8-3. The plot represents the influences of heating rate on the transformed fraction of tempered products which showed that the carbide precipitation occurred earlier (at 240°C) when lower heating rate (0.5°C/s) is considered. At lower heating rate, there was sufficient time to nucleate and precipitate carbides at much lower temperature. With the progression of tempering temperature, the matrix carbon content depleted allowing carbide precipitation to finish earlier. Conversely, due to inadequate time

carbide precipitation occurred at much higher temperature (340°C) while the sample was subjected to rapid heating rate (500°C/s). It can be seen that the cementite precipitation start temperature increased by about 100°C while the heating rate was increased from 0.5°C/s to 500°C/s, which suggested that the carbide precipitation kinetics were delayed with increasing heating rates; therefore, the volume fraction of carbides decreases with increases of heating rate in a particular tempering temperature.

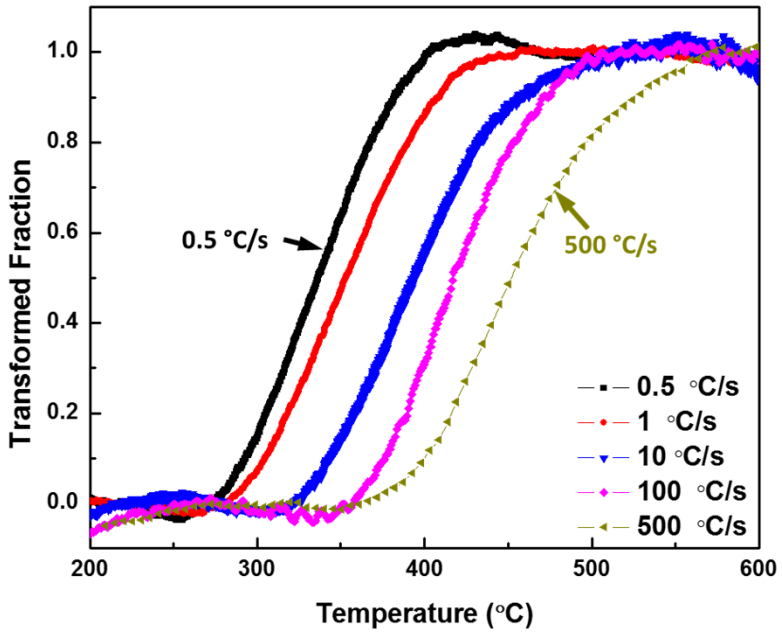

Figure 8-3 The kinetics of martensite tempering as a function of tempering temperature showing the transformed fraction of the tempered martensite

The CHT diagram of the used steel was constructed using heating rates between 0.5°C/s to 500°C/s as presented in Figure 8-4. Two large transformation zones were marked in the CHT diagram which correspond to the carbide precipitation, and austenite transformation. Carbide precipitation occurred in the temperature ranges of 240°C to 527°C. As aforementioned, transformation temperature ranges increased to the higher temperature with increase of heating rate; however, time to complete carbide precipitation was decreased which implies that precipitated carbide would be finer leading to the higher tempered structure strength.

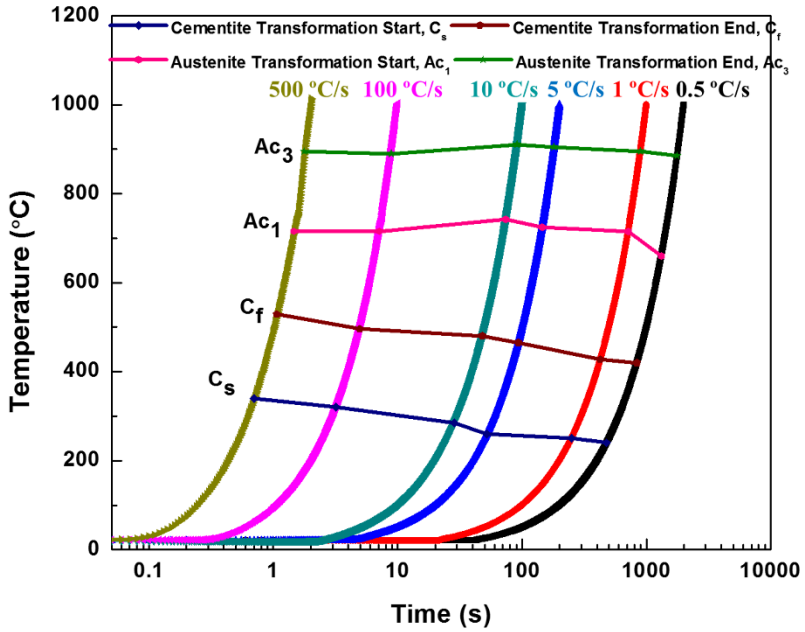

Figure 8-4 The CHT diagram of the used martensitic steel constructed using the heating rates of 0.5°C/s to 500°C/s

In addition to temperature, the tempering time also influences the tempering kinetics; therefore, the effect of the isothermal holding time at 0%, 50%, and 100% cementite precipitation temperatures was investigated. Figure 8-5(a) represents the strain associated with isothermal tempering, at 1°C/s heating rate strain corresponding to 100 s holding time increased from 0.00172 to 0.0147 when temperature increased from 240°C to 330°C. However, the strain was again found to be decreased to 0.0054 at 420°C which implies that there was insufficient amount of carbon in solid solution; therefore, the kinetics of carbide precipitation are retarded. This scenario is different when 100°C/s heating rate is considered, the largest strain (0.0444) was detected at the start of the precipitation temperature (330°C) when holds for 100 s (Figure 8-5); as temperature increased to 495°C, the strain decreased to 0.0403. When the identical tempering temperatures and times were considered, it was found that a higher strain is associated with a higher heating rate; the amount of strain obtained with 100°C/s heating rate is about three times that seen with 1°C/s heating rate. At above 400°C, the strain was measured to be about eight times with higher heating rate (100°C/s). One distinguishable feature is that at higher temperature and rapid heating rate, a rapid contraction of the sample occurred at much shorter time which

implies that there is a relatively larger driving force for carbide precipitation. While comparing Figure 8-5(a) and (b) for 100°C/s heating rate, a sharp reduction of the rate of change occurred at about 20 s holding time which implies that carbide precipitation was almost completed within this short tempering time. It should be noted that the experimental results revealed a largest strain at the middle of the transformation temperature except 100°C/s and 100 s tempering condition which shows the greatest strain at the beginning of the transformation temperature (320°C).

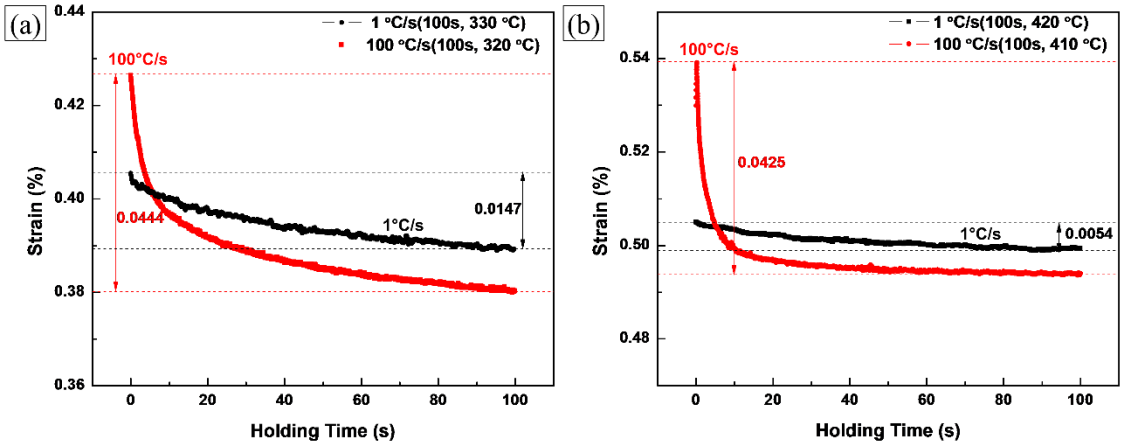

Figure 8-5 Dilatometric curves obtained during tempering with 1°C/s and 100°C/s heating rate and 100 s holding times at (a) 1°C/s at 330°C and 100°C/s at 320°C, and (b) 1°C/s at 420°C and 100°C/s at 410°C

The influences of heating rates on isothermal martensite tempering kinetics is presented as a function of logarithmic time in Figure 8-6(a) by following Johnson-Mehl-Avrami-Kolmgorov (JMAK) equation. The slope of the curves represents the Avrami exponent (reaction rate exponent) of martensite tempering process and is plotted with respect to heating rate in Figure 8-6(b). The reaction rate exponent was found to have a decreasing trend with increasing heating rates. Higher reaction rate at slow heating rate implies that there is a greater tendency of martensite to be tempered; however, as heating rate increases the reaction became slower resulting in a smaller precipitation reaction.

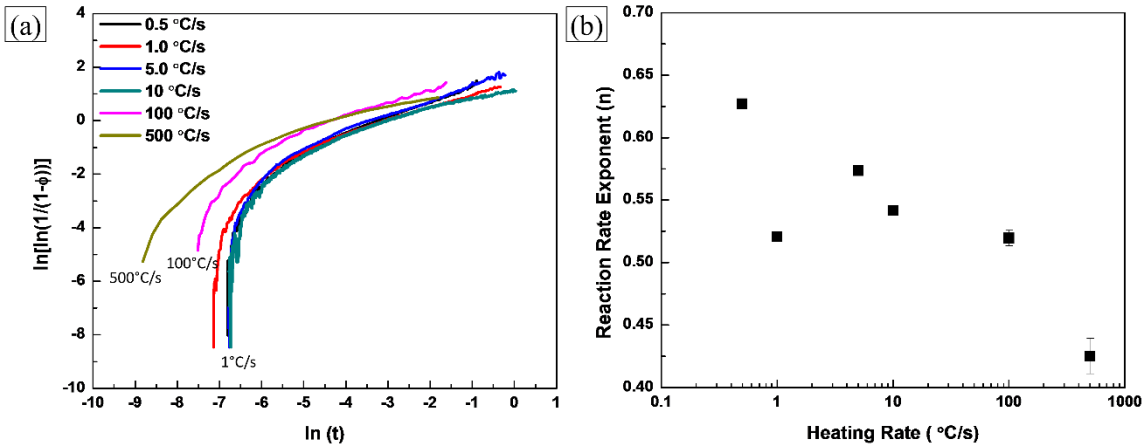

Figure 8-6 (a) The fraction of cementite isothermally transformed plotted as a function of time, and (b) JMAK reaction rate exponent as a function of heating rate

8.4 Microhardness and tempering parameters

The measured Vickers microhardness of the samples obtained at various tempering conditions are presented in Figure 8-7(a) as a function of tempering temperature. As expected, microhardness declined with increasing temperature, and holding time due to the ejection of carbon atoms and formation of stable carbides i.e. cementite; in addition, dislocation density also decreased by annihilation and recovery while samples were exposed to the higher temperature. Figure 8-7(a) illustrates the influences of two major parameters: tempering time and heating rate, which directly relate to the tempering process. It can be seen that the sample tempered using 100°C/s heating rate had a higher microhardness compared to the sample heated with 1°C/s. The smaller reduction of microhardness on the rapidly tempered samples attributed to less decomposition of the martensite structure, formation of finer, denser and dispersed carbides, and a higher amount of retained dislocation density as described in Chapters 6 and 7. However, when the sample was tempered for a longer duration, then the effects of heating rate diminished; the microhardness trends obtained using the two different heating rates are overlapped representing insignificant effect of heating rate in the longer duration tempering process. It can be concluded that there is a significant effect of heating rates under short time

tempering process; a higher microhardness is achieved when rapid heating rate and short tempering time is considered (Figure 8-7(a)).

Generally, the effects of tempering temperature and time on hardness response of the tempered martensite is determined by following H-J parameter (equation (2-4)) [78]. It can be noted that equation (2-4) is only valid for isothermal tempering cycles; in the present study, the samples were heated isochronally with a constant heating rate; therefore, temperature and time both varies simultaneously. In order to include the heating and cooling part of the thermal cycle, an additivity rule is taken into account as proposed by Tsuchiyama [210]. The tempering parameters are calculated by following equations (6-1 to 6-3). Figure 8-7(b) shows a plot of microhardness data as a function of tempering parameter indicating a linear relationship as expected; a greater reduction of microhardness is associated with the larger tempering parameter.

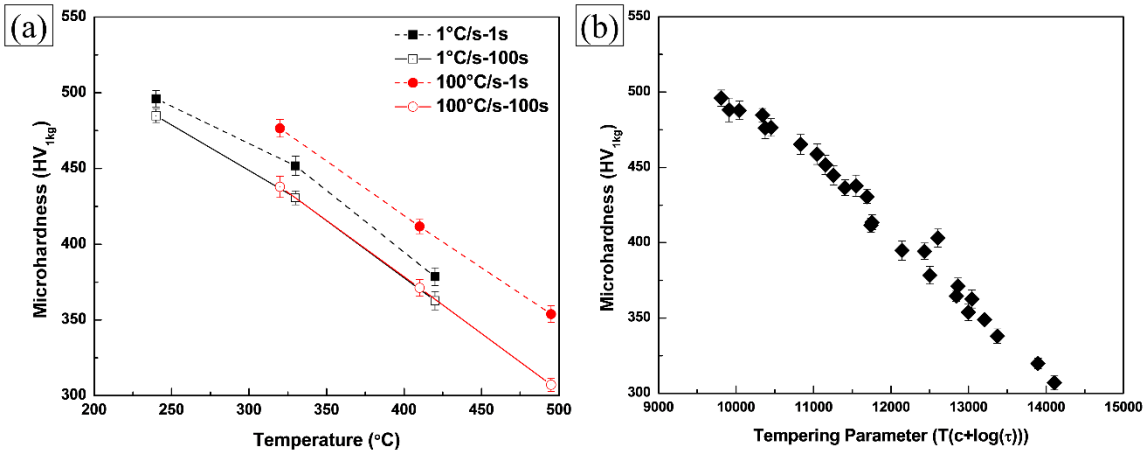

Figure 8-7 (a) the plot of microhardness as a function of tempering temperature, and (b) as a function of tempering parameter. The error bars represent the 95% confidence interval.

8.5 Carbon diffusion and carbide precipitation

Diffusion distance (x) of carbon in ferrite during tempering was calculated using the following equations.

$$x = \sqrt{D_{diff} t} \tag{8-1}$$

$$D_{diff} = 6.2 \times 10^{-7} \exp(-\frac{80000}{RT}) \quad (8\text{-}2)$$

The calculated result shows a longer diffusion distance while a slower heating rate is considered due to the longer time required to achieve a certain temperature compared to the rapidly heated condition (Figure 8-8). The carbon diffusion distance is about two orders of magnitude higher in the case of 1°C/s compared to 100°C/s while considering the same tempering temperature.

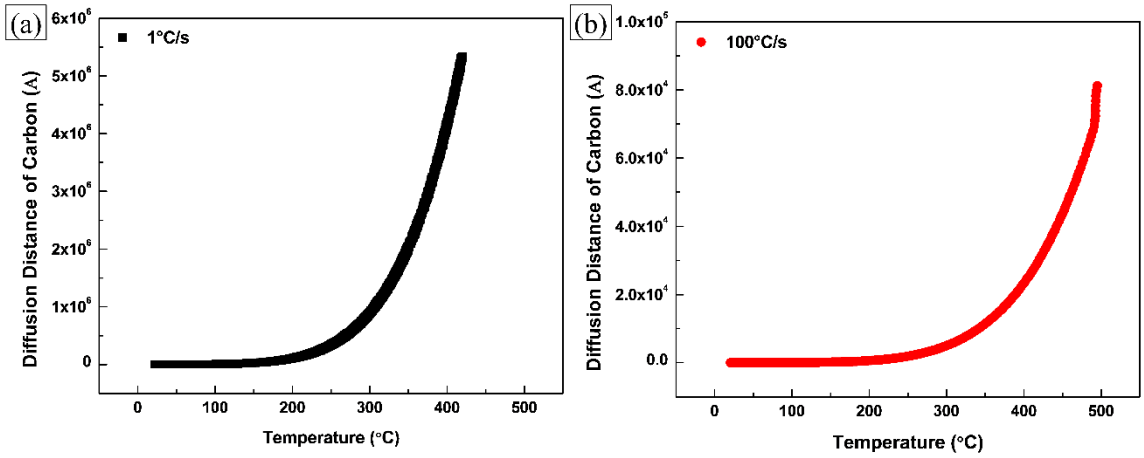

Figure 8-8 Calculated diffusion distance of carbon in ferrite during continuous heating with heating rate of (a) 1°C/s, and (b) 100°C/s

8.6 Modelling of yield strength of tempered martensite

Typically, the yield strength of lath martensite can be correlated with the contributions of lattice friction stress (σ_0 = 50 MPa [211]) of pure iron, the solid solution strengthening (σ_{ss}), the precipitation strengthening (σ_{pct}), the grain boundary strengthening (σ_{gb}), and the forest dislocation density strengthening (σ_ρ) at lath and sub-block boundaries.

8.6.1 Solid solution strengthening, σ_{ss}

In order to estimate the contribution of solid solution strengthening from the alloying elements, empirical data obtained from reference [163] were used. The solid solution constants presented in Table 8-1 are calculated by using equations (8-3 to 8-7) [212, 213].

$$\eta_i' = \frac{\eta_i}{(1 + 0.5\eta_i)} \tag{8-3}$$

$$\eta_i = \frac{|\mu_i - \mu_{Fe}|}{\mu_{Fe}} \tag{8-4}$$

$$\delta_i = \frac{|r_i - r_{Fe}|}{r_{Fe}} \tag{8-5}$$

$$\beta_i = k\mu(\eta_i' + 16\delta_i)^{3/2} \tag{8-6}$$

$$\sigma_{ss} = \sum_i (\beta_i^2 x_i)^{1/2} \tag{8-7}$$

where, k, η, δ, r, μ are the fitting parameter (k = 0.0045), modulus, lattice distortion, atomic radius, and shear modulus of elements. It was estimated that the solid solution strengthening (σ_{ss} = 81.18 MPa) has only marginal effect on the total yield strength of martensite.

Table 8-1 Solid solution constants of the studied M220 martensitic steel

Elements	r_i (nm)	μ_i (GPa)	δ_i (nm/nm)	η_i (GPa/GPa)	β_i (MPa/at.)
Fe	0.124	82	-	-	-
Mn	0.129	75	0.04	0.09	223.17
Si	0.114	50	0.08	0.39	740.13
S	0.088	7.7	0.29	0.91	4353.75
P	0.098	11	0.21	0.87	2835.93
Cr	0.13	115	0.05	0.40	420.56
Mo	0.146	126	0.18	0.54	2120.73

8.6.2 Grain boundary strengthening, σ_{gb}

During martensitic transformation, the austenite grains are divided into several packets which consist of various blocks; the blocks are subdivided into several laths. It has been reported that a low carbon containing martensite (< 0.6 wt.% C) shows a lath kind of structure [214]. The studied material contained 0.23 wt.% C; therefore, a typical lath kind of martensite structure can be expected also experimentally observed as reported in section 6.3. Several researchers investigated the orientation relationship (OR) between parent austenite (γ) and martensite (α′) phase [29, 37, 154, 169, 215, 216]; it was shown that a low

and medium carbon containing lath martensite maintain a Kurdjumov-Sachs (K-S) OR of $\{111\}_\gamma||\{011\}_{\alpha'}$ and $< 110 >_\gamma \,||\, < 111 >_{\alpha'}$. A typical martensite prior-γ grain is divided into 4 packets (as packets share common $\{111\}_\gamma$ habit plane) which are sub-divided to 6 blocks with several parallel ruler type laths. Therefore, a martensite grain contains 24 crystallographic variants [155]. A relationship between a packet, and block with prior-γ grain are presented by several authors [82, 160, 169] as:

$$d_p = \sqrt{\frac{3\sqrt{3}}{32} D_\gamma} = 0.40 D_\gamma \tag{8-8}$$

$$d_b = \frac{1}{6}\, d_p = 0.067 D_\gamma \tag{8-9}$$

where, d_p, d_b, D_γ are the packet, block, and prior-γ grain size, respectively.

The D_γ size of the studied steel was estimated to be 6.3 ± 0.72 μm; the subsequent packet and block size were measured to be about 3.5 μm and 0.67 μm, respectively; which are similar compared to the calculated one (packet: 2.52 μm, and block: 0.42 μm). It has been reported that the high-angle boundaries arrest dislocation motion whereas the low-angle boundaries with a misorientation angle 2.8-2.9° allow dislocation propagation. In the case of lath martensite, a majority of the block boundaries are considered as high-angle boundaries which is accounted as an effective grain boundary for the low carbon lath martensite [80, 156-159]. The contributions of grain boundary strengthening on the overall yield strength can be approximated by the following Hall-Petch relationship:

$$\sigma_{gb} = \frac{k_{HP}}{\sqrt{d_b}} \tag{8-10}$$

where, k_{HP} is the Hall-Petch constant (300 MPaμm$^{1/2}$), and d_b is the block size. The grain boundary component on the total yield strength was estimated to be 463 MPa.

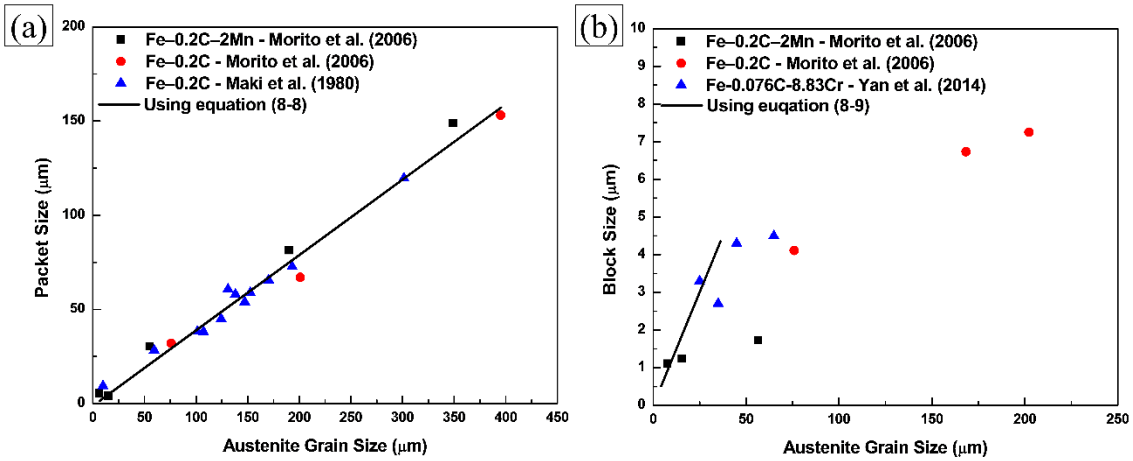

Figure 8-9 A relationship between prior-γ grain size and (a) packet size, and (b) block size for the fully martensitic steels

8.6.3 Forest dislocation density strengthening, σ_ρ

The strengthening contribution in relation to the dislocation density can be estimated using Taylor formula [173] equation (6-5). The estimation of the dislocation density is important in order to evaluate the contribution of forest dislocation density which is reported to be major contributor on the total yield strength of the tempered martensite. Recently, Galindo-Nava and Rivera-Díaz-del-Castillo [82, 160] proposed a model estimating the dislocation density by equating the lattice strain energy and dislocation strain energy at the lath boundaries [82, 160]. They have concluded that dislocation density of lath martensite can be estimated solely from the carbon content of steel by the following equation (8-11):

$$\rho_{lath,0} = \frac{3E}{(1+2v^2)\mu}\frac{4\varepsilon^2 d_{Cottrell}}{d_{lath,0}^2 b} \tag{8-11}$$

where $\rho_{lath,0}$, E, v, μ, and ε are the dislocation density as-quenched condition, Young's modulus (211 GPa), Poisson ratio (0.3), shear modulus (80 GPa), and lattice strain associated with the carbon redistribution, respectively.

8.6.4 Precipitation strengthening, σ_{pct}

The contribution from the precipitated carbides which may increase the yield strength by impeding dislocation glide was approximated by using Orowan-Ashby model [162, 163].

$$\sigma_{pct} = 0.26\frac{\mu b}{r_p} f_p^{1/2} \ln\left(\frac{r_p}{b}\right) \quad (8\text{-}12)$$

where r_p, and f_p are the mean radius and the volume fraction of carbides, respectively.

8.7 Modelling of microstructural units of tempered martensite

In order to model microstructural units of tempered martensite two major factors are taken into account which are (i) diffusion of carbon at lath boundaries which coarsen the laths and the reduction of dislocation density by migration of carbon atoms; and (ii) carbide precipitation due to carbon segregation and migration.

8.7.1 Lath width

8.7.1.1 As-quenched condition

The average lath width of the as-received quenched martensite was estimated from several TEM bright-field images to be varied between 180 to 220 nm. However, a coarse lath (thickness > 500 nm) was also observed; however, more than 80% of the laths of the investigated material were found to be fine lath with an average width of 200 nm. Figure 8-10 shows a plot of martensite lath width with respect to the steel carbon content (in wt.%); as expected lath width decreases with increases of steel carbon content. However, the laths become very coarse below the carbon level of 0.2 wt.%, as the carbon content increased over 0.2 wt.% the lath width decreased slowly. The experimental data presented in Figure 8-10 were obtained from references [79, 80, 199, 217, 218] along with the measured value of the present study as marked with a dotted circle.

Galindo-Nava and Rivera-Díaz-del-Castillo [82, 160] reported that the amount of carbon existing at austenite lath prior to the martensitic transformation segregated and partitioned into the lath boundaries which is also controlled by the thickness of the Cottrell

atmosphere (see Figure 2-5) [207]. Thus, the width of the lath at as-quenched condition ($d_{lath,0}$) can be estimated as:

$$d_{lath,0} = d_{Cottrell}\frac{l_c^2}{b^2} \tag{8-13}$$

where, $d_{Cottrell}$, l_c, and b are the width of the Cottrell atmosphere (7 nm [25]), mean carbon spacing [219], and Burgers vector. $\frac{l_c^2}{b^2}$ in equation (8-13) represents the available effective carbon atoms for segregation (carbon content in the autotempered precipitates was disregarded owing to their smaller volume fraction). The calculated lath width as a function of carbon content of steel is presented in Figure 8-10 which shows a very good agreement between the experimental and calculated result for a wide range of steels carbon content (0.05 to 0.6 wt.% C).

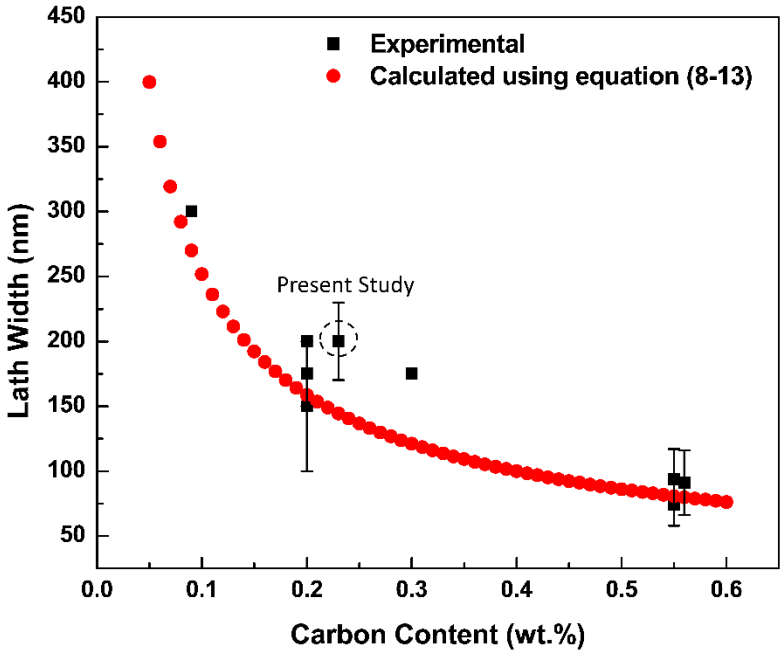

Figure 8-10 Relationship between the martensite lath width and the carbon content of steels

During tempering, carbon which diffused out from the lath boundary widened or coarsened the laths; therefore, the coarsening of martensite laths was estimated using the relationship as proposed by Cottrell and Bilby [220] where the lath thickness was reported to be increased by the decrease of carbon atoms diffused out from the dislocation lines.

$$d_{lath} = d_{lath,0} + \lambda_0 x_c^{\alpha'} \sqrt{D_{diff} t} \quad (8\text{-}14)$$

$$D_{diff} = 6.2 \times 10^{-7} \exp(-\frac{80000}{RT}) \quad (8\text{-}15)$$

where $\sqrt{D_{diff} t}$ is the mean diffusion length, λ_0 is the constant accounting for the diffusion barrier for carbon segregation. *R*, *T*, and *t* are molar gas constant (8.31 $Jk^{-1}mol^{-1}$), absolute temperature (K), and tempering time (s), respectively.

8.7.1.2 As tempered condition

Lath widths of the tempered martensite during heating with two different heating rates were calculated using equation (8-14) as shown in Figure 8-11. As expected, the tempered martensite lath width increased with temperature; however, lath width increased more in the case of slower heating rate due to a longer carbon diffusion period. The predicted lath width also agrees with the experimental observation as reported by Kim et al. [80].

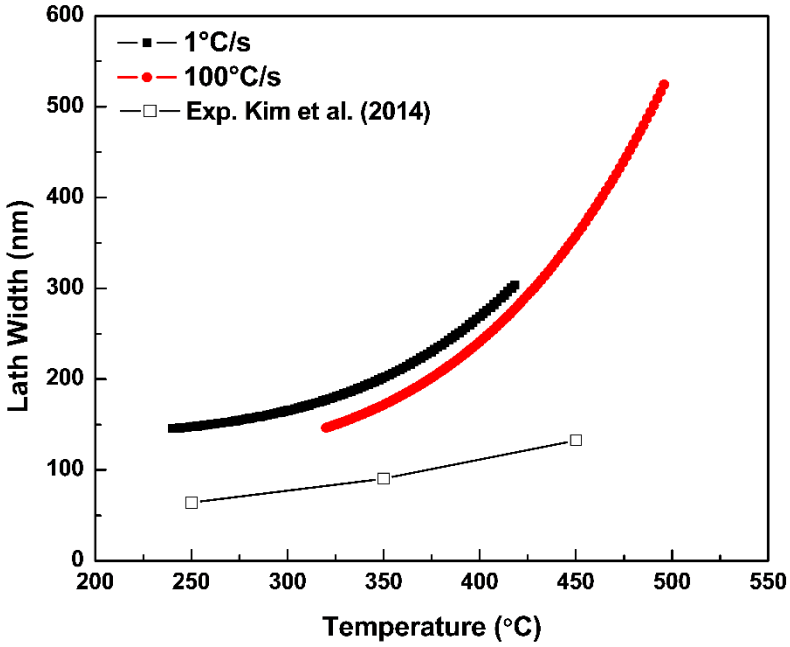

Figure 8-11 Predicted lath width during tempering with 1°C/s and 100°C/s heating rate plotted as a function of tempering temperature

Figure 8-12 shows the predicted lath width as a function of tempering parameter (the tempering parameters are calculated using equations 6-1 to 6-3). The sample heated using

100°C/s heating rate possessed lower lath width; however, the lath width increased with the tempering time. It was also found that the heating rate had a prominent effect on the martensite laths coarsening during short periods of tempering; on the other hand, the effects of heating rate became insignificant in the course of the longer tempering period (in this study, 100 s).

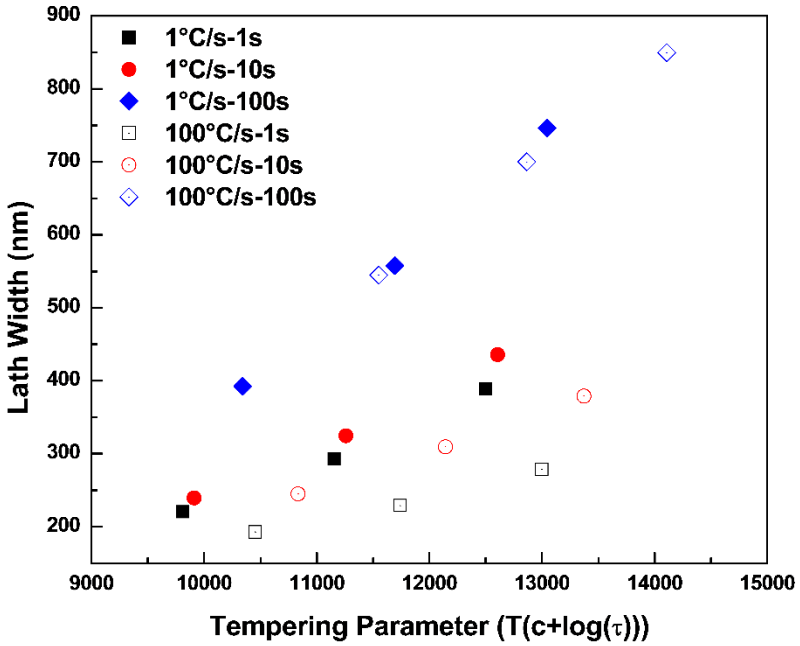

Figure 8-12 Predicted lath width plotted as a function of tempering parameter

8.7.2 Dislocation density

Dislocation density of the tempered martensite was predicted by equating the dislocation energy and the lattice strain energy generated by carbon redistribution at the lath boundaries as proposed by Galindo-Nava and Rivera-Díaz-del-Castillo [82, 160].

$$\rho_{lath} = \frac{3E}{(1+2v^2)\mu}\frac{4\varepsilon^2 d_{Cottrell}}{d_{lath}^2 b} \tag{8-16}$$

$$\varepsilon = \sqrt{\varepsilon_x^2 + \varepsilon_y^2 + \varepsilon_z^2} \tag{8-17}$$

$$\varepsilon_x = \varepsilon_x = \varepsilon_x = \frac{\frac{\sqrt{2}}{2}a_\gamma - a'_\alpha}{\frac{\sqrt{2}}{2}a_\gamma} \tag{8-18}$$

where, ε_x, ε_y, and ε_z are the lattice strain from FCC to the martensitic structure along *x*, *y*, and *z* direction. a_γ, and $a_{\alpha'}$ are the lattice parameter of austenite and martensite, respectively.

The reduction of dislocation density of lath martensite during tempering was calculated using equations 8-16 to 8-18. Figure 8-13 and Figure 8-14 show the decreasing trend of dislocation density as a function of temperature and tempering parameter due to annihilation and recovery; a similar trend was reported by other researchers [28, 80]. The calculated dislocation density suggests that the tempered sample retained a high density of dislocation when a rapid thermal cycle is applied which is also demonstrated by Furuhara et al. [28] and Revilla et al. [73]. The calculated results were also supported by experimental investigation carried out using TEM and EBSD analysis as will be discussed in sections 8.8 and 8.9.

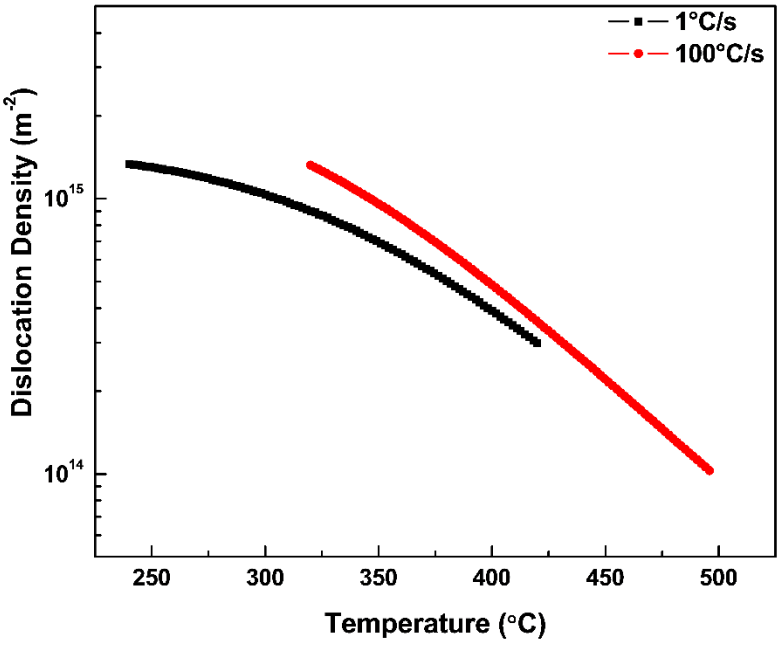

Figure 8-13 Predicted trend of dislocation density during tempering with 1°C/s and 100°C/s heating rate plotted as a function of tempering temperature

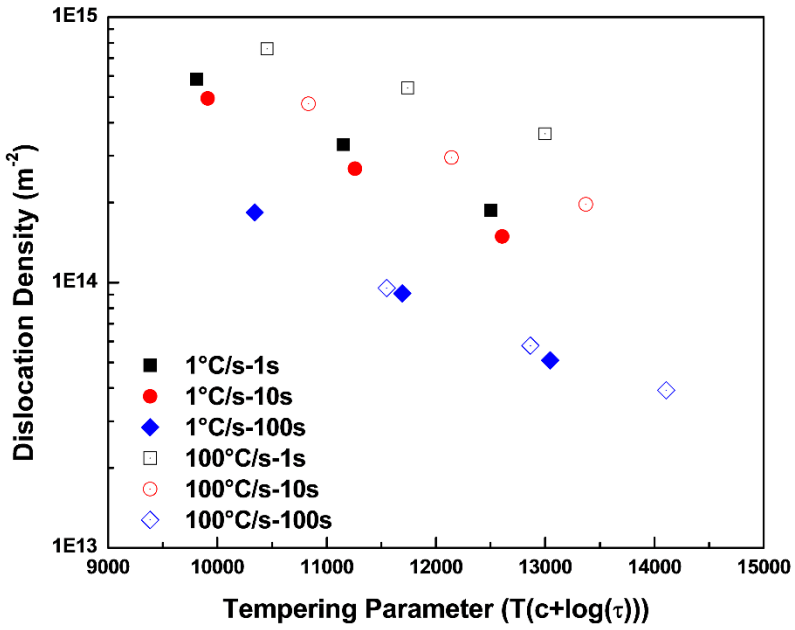

Figure 8-14 Predicted dislocation density plotted as a function of tempering parameter for two different heating rates

8.8 TEM investigation of tempered martensite

In order to understand the effects of tempering temperature, heating rate, and isothermal holding time on the microstructural changes of lath martensite, 5 samples were selected for the TEM and EBSD study as shown in Table 8-2. In addition to the tempered martensite, the as-received BM was also examined as a reference. Two samples were used for TEM study whereas one sample was considered for the EBSD analysis, for each sample condition.

Table 8-2 Samples selected for the microstructural study using TEM and EBSD analysis

Sample ID	Heating Rate (°C/s)	Temperature (°C)	Time (s)
BM	-	-	-
1°C/s-420°C-1s	1	420	1
100°C/s-410°C-1s	100	410	1
100°C/s-495°C-1s	100	495	1
100°C/s-495°C-100s	100	495	100

8.8.1 Influence of heating rate on tempering kinetics

In order to examine the effects of heating rate on the lath martensite tempering, 1°C/s -420°C-1s and 100°C/s-410°C-1s were chosen which shows only differences in heating rate (1°C/s and 100°C/s) and the temperatures (nearly identical) and holding times are same.

Figure 8-15 shows the TEM micrographs of the tempered structure obtained by slowly (1°C/s) heating the sample at a temperature of 420°C and holding for a very short period of time, 1 s. The micrograph shows an interconnected carbide-film at lath boundaries due to the highest diffusion energy at this location [166]. However, quasi-spherical (equivalent diameter about 50 nm) carbides were also identified at intralath locations with a very small density (Figure 8-15(b)) suggesting that the spherical carbides at this location went through the Ostwald ripening process due to a longer diffusion period resulting from the slower heating rate. The dark-field TEM micrograph presented in Figure 8-15(c) was obtained with the $< 211 >_{\theta}$ cementite diffraction spots which highlighted the quasi-spherical particles. The OR between the ferrite matrix and cementite particles was determined to be $[010]_{\alpha} \,||\, [011]_{\theta}$. Previously, dilatometric analysis revealed (section 8.3) that when the sample was tempered using a 1°C/s heating rate the carbide precipitation finished at 420°C; therefore, a complete carbide coarsening was expected as observed via TEM in Figure 8-15. It was also found that the majority of the intralath carbides were dissolved and provided carbon to grow the interlath carbides.

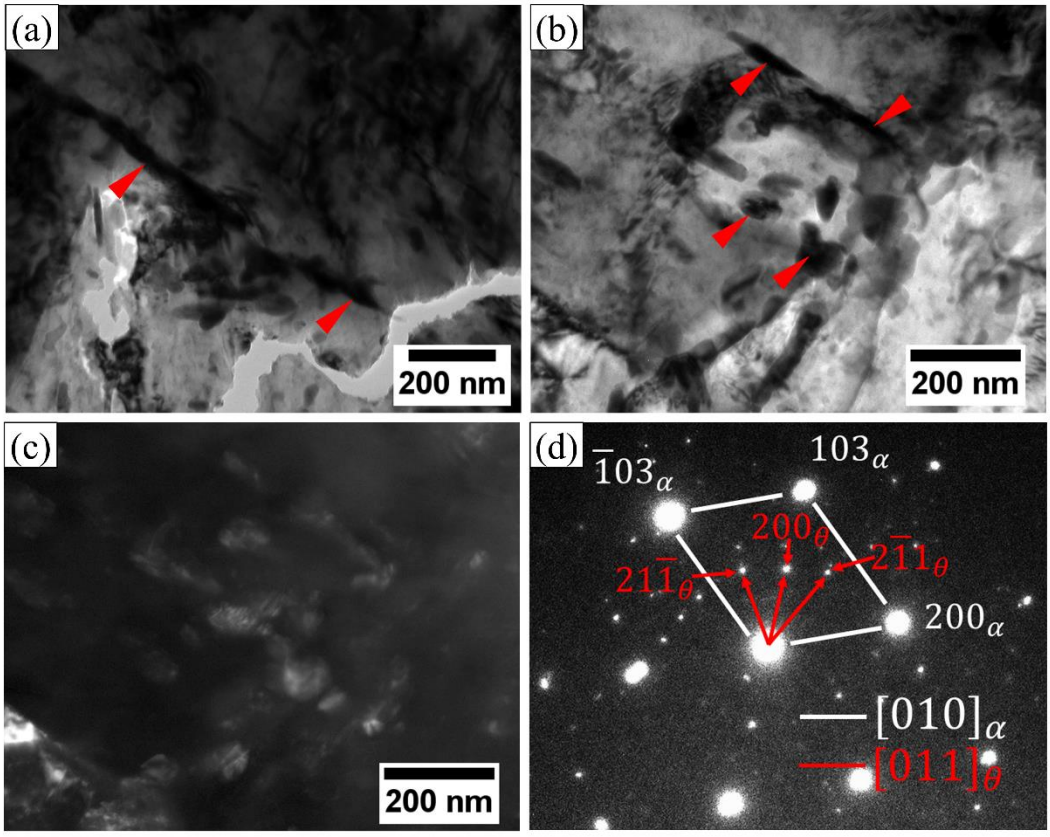

Figure 8-15 (a) and (b) TEM bright-field micrographs of the 1°C/s-420°C-1s sample showing the carbide precipitates in a ferrite matrix (some of the intralath and interlath carbides are marked with arrows), (c) dark-field image of (b) taken with a $< 211 >_\theta$ cementite reflection highlighted the carbides, and (d) the indexed SAD showing the OR of $[010]_\alpha \,||\, [011]_\theta$ between ferrite and cementite

On the other hand, when the rapid thermal cycle (100°C/s) was applied carbides became elongated, coherent and highly dense as depicted in Figure 8-16. The micrograph of 100°C/s-410°C-1s sample displays multivariate elongated shape (aspect ratio about 3.5) carbides oriented in different directions as highlighted with arrows in Figure 8-16(b); in addition, a few spherical particles with a diameter of about 40 nm were also observed (marked with circles) which are the cross-sectioned view of the elongated particles grown normal to the observed plane direction. Furthermore, the tangled dislocations at the vicinity of the lath boundaries were identified where densely populated carbides were pinned (Figure 8-16(a) and (c)). The dark-field TEM micrograph presented in Figure 8-16(c) was obtained by considering the $< 120 >_\theta$ cementite reflection confirms the presence of the

carbides along the tangled dislocations around the lath boundaries. A high density of dislocations was also observed via HAADF-STEM imaging as shown in Figure 8-17(b). The indexed SAD patterns show the orientation relationship between the matrix and precipitate as $[012]_\alpha \,||\, [001]_\theta$ which obeyed the well-defined Bagaryatsky orientation relationship [66, 67]. It was noticeable that the rapid thermal cycle provided the driving force for the effective carbide nucleation in the dislocation sites and carbide became more dispersed. In addition, due to the shorter diffusion period, carbide precipitates at various locations whether lath boundaries or intralath regions and defect sites maintained equal particle size and distribution (Figure 8-16(c)).

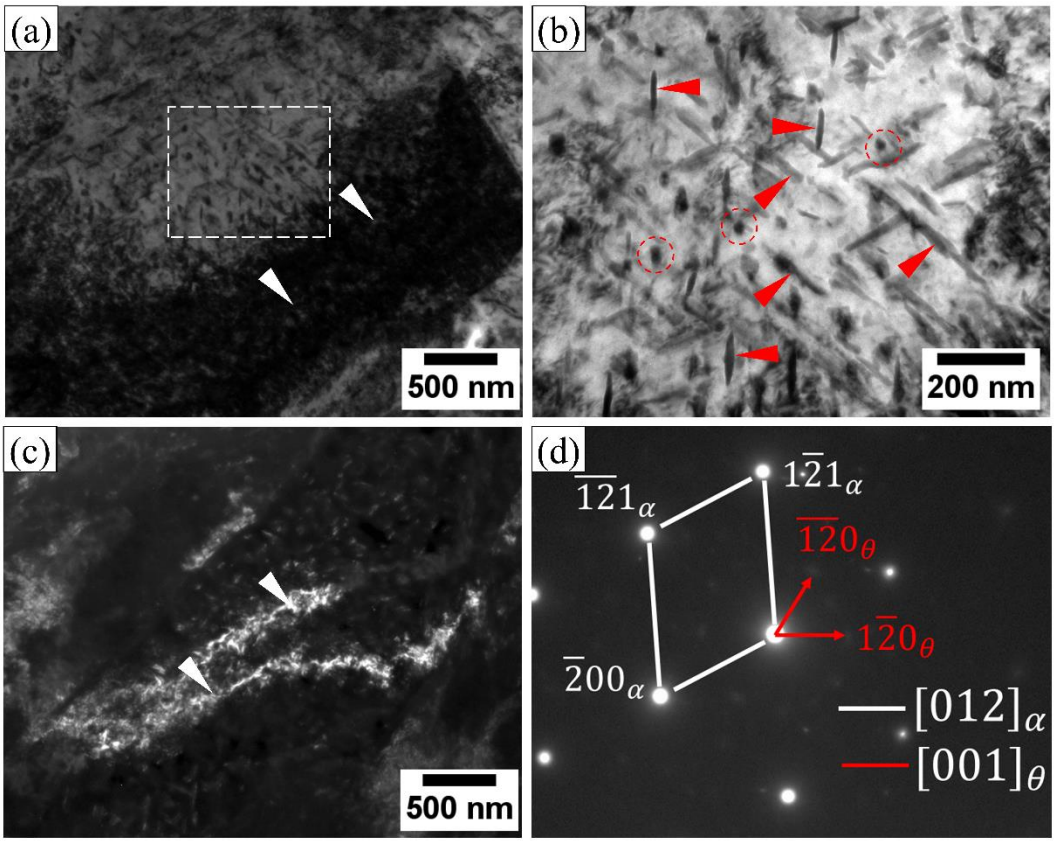

Figure 8-16 (a) TEM bright-field micrographs of the 100°C/s-410°C-1s sample showing the elongated multivariate carbide precipitates in a ferrite matrix, (b) enlarged view of the rectangular area marked in (a) (some of the intralath carbides are indicated with arrows), (c) dark-field image of (b) taken with a $< 120 >_\theta$ cementite reflection highlighted the carbides only, and (d) indexed SAD showing the OR of $[012]_\alpha \,||\, [001]_\theta$between ferrite and cementite

General findings indicate that when the rapid thermal cycle was used, the carbides became finer, denser, elongated and highly coherent with the matrix thus improving the structural strength by precipitation strengthening. In addition, a high density of dislocations (Figure 8-17(b) and (c)) was observed on the rapidly heated samples resulting from insufficient reaction time needed to complete annihilation and recovery of highly dislocated martensite laths.

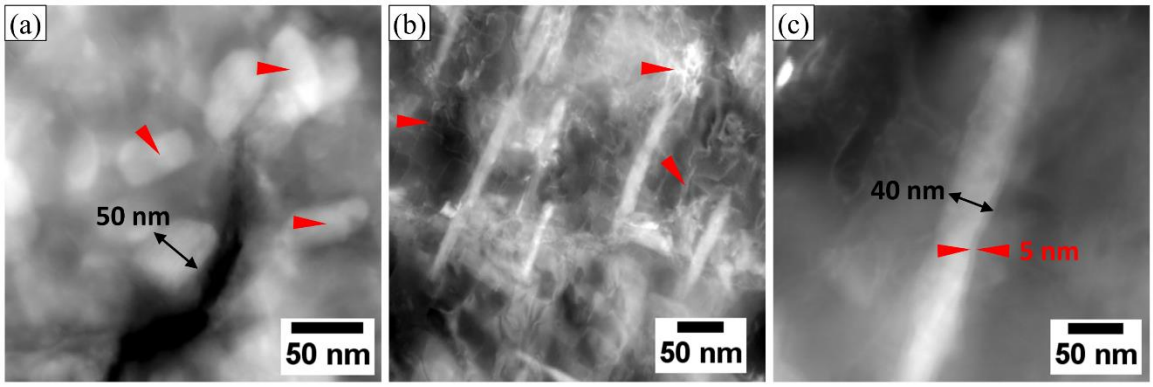

Figure 8-17 HAADF-STEM images of cementite precipitated on a ferrite matrix, (a) 1°C/s-420°C-1s sample, (b) 100°C/s-410°C-1s, (c) a single elongated shape of carbides in the 1°C/s-420°C-1s sample

8.8.2 Influence of holding time on tempering kinetics

The influence of tempering time was investigated by taking into account two samples tempered using the same heating rate at same temperature with different tempering durations. One sample was held for 1 s after heating with a heating rate of 100°C/s at 495°C while the other sample was tempered for 100 s at the same heating rate and temperature condition. The TEM micrographs of the samples (100°C/s-495°C-1s and 100°C/s-495°C-100s) are shown in Figure 8-18 and Figure 8-19, respectively. Distinguishable microstructural differences were observed among the samples. Carbides precipitated on the 100°C/s-495°C-1s sample remained with elongated shape and orientated in a direction with a OR $[\bar{1}12]_\alpha||[001]_\theta$ which obeyed a well-defined Bagaryatsky orientation relationship [66, 67]. It was found that due to limited tempering reaction time the high and low-angle carbides showed similar morphologies and dimension as can be found in the dark-field image (Figure 8-18(c)) taken with $< 120 >_\theta$ cementite reflection.

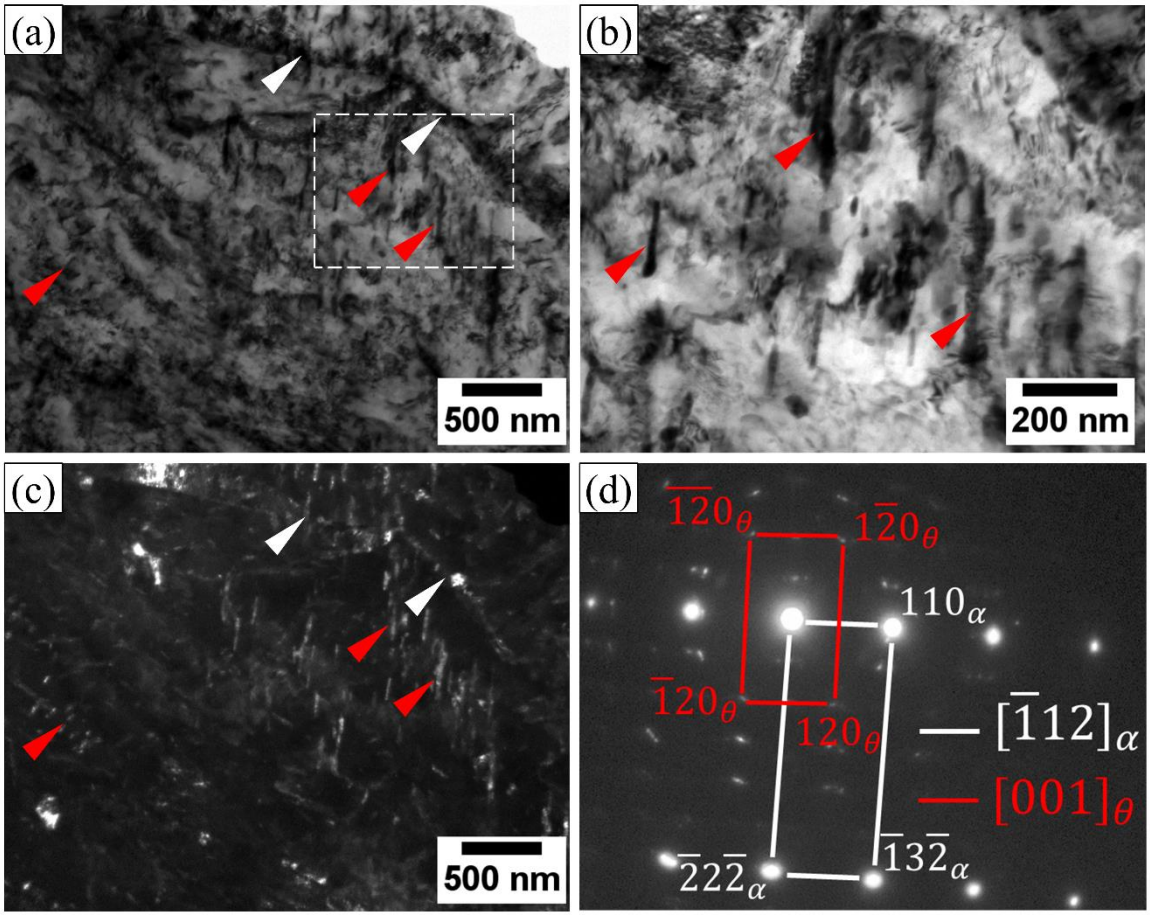

Figure 8-18 (a) TEM bright-field micrographs of the 100°C/s-495°C-1s sample showing the elongated multivariate carbide precipitates in a ferrite matrix, (b) enlarged view of the rectangular area marked in (a) (some of the intralath carbides are marked with arrows), (c) dark-field image of (b) taken with a $< 120 >_\theta$ cementite reflection highlighted the carbides, and (d) indexed SAD showing the OR of $[\bar{1}12]_\alpha \,||\, [001]_\theta$ between ferrite and cementite

While the sample was tempered for a longer duration (100 s), the cementite morphology changed from elongated needle-shape to quasi-spherical and the number of intralath carbides decreased significantly (Figure 8-19). In addition, more recovery of dislocations and loss of coherency between the ferrite matrix and the precipitates were observed (Figure 8-20).

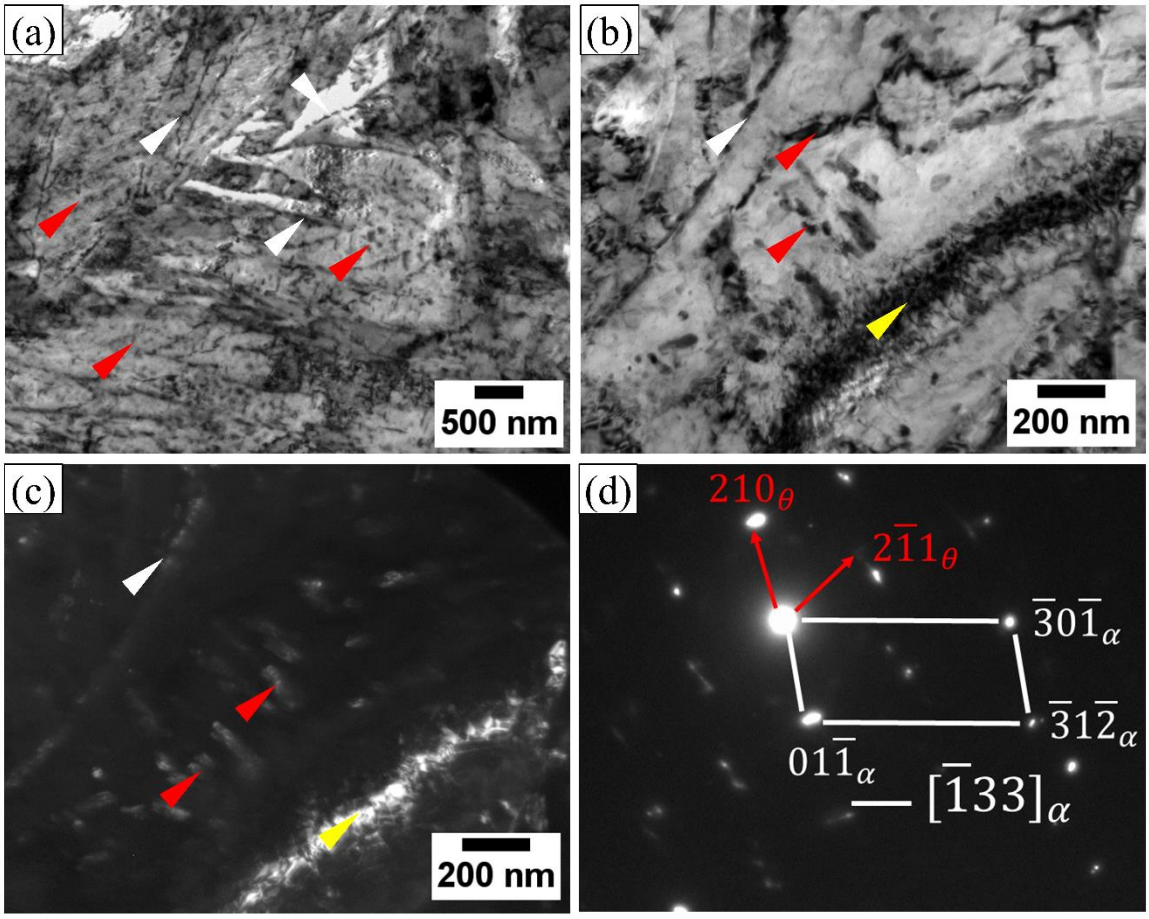

Figure 8-19 (a) TEM bright-field micrographs of the 100°C/s-495°C-100s sample showing the quasi-spherical carbide precipitates in a ferrite matrix, (b) enlarged view of the matrix and precipitates (some of the intralath carbides are marked with arrows), (c) dark-field image of (b) taken with a $< 2\bar{1}1 >_\theta$ cementite reflection highlighted the carbides, and (d) indexed SAD patterns of ferrite and cementite

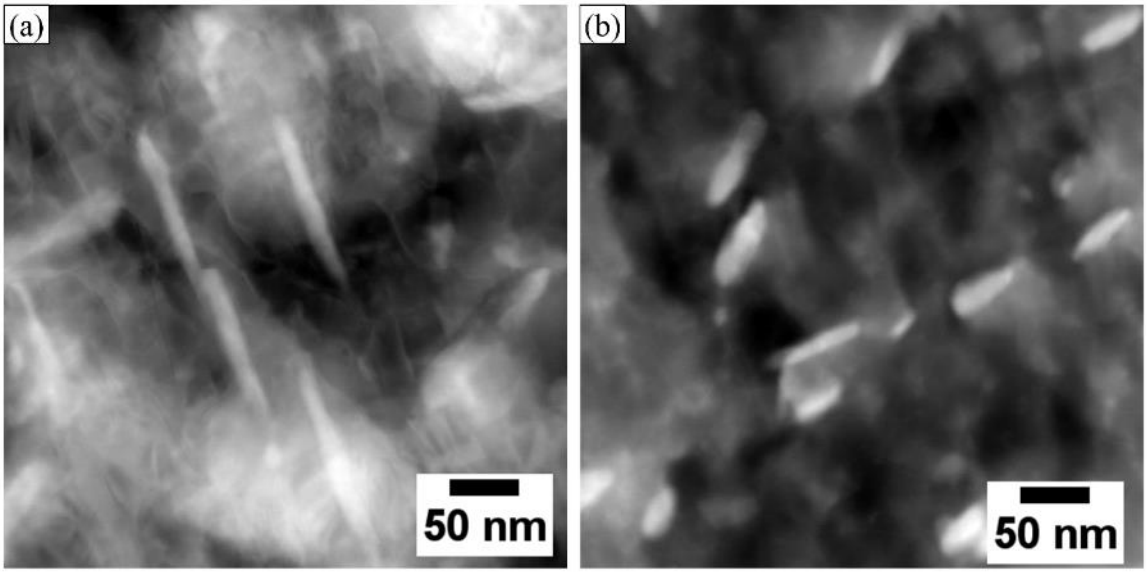

Figure 8-20 HAADF-STEM images of sample (a) 100°C/s-495°C-1s, and (b) 100°C/s-495°C-100s

8.9 Crystallographic analysis of tempered martensite

EBSD data were post-processed using Tango and Mambo (HKL Channel 5) software. The inverse pole figure (IPF) maps and band contrast (BC) of the samples 1°C/s-420°C-1s, and 100°C/s-410°C-1s obtained after noise reduction are shown in Figure 8-21. In the IPF color maps, the boundaries corresponding to less than 3° misorientation angle between the adjacent points and larger than 10° are outlined with yellow and red lines, respectively. On the other hand, similar boundaries are marked with the red and black line in the BC maps in Figure 8-21. The misorientation criteria larger than 10° between the adjacent points was chosen in order to identify the packets and block boundaries because according to misorientation calculations reported by Kitahara et al. [29], all the packets and block boundaries should have misorientation angle larger than 10°. The misorientation angle $\leq 3°$ between adjacent points represents the lath boundaries [155]. It was found that most of the laths were oriented in the lower misorientation angle (below 0.5°) representing very fine laths in the investigated martensitic steel. When the samples were heated with two different heating rates, the reduction of the lath boundaries were detected; however, the lath

boundaries were found to be more decreased in the sample subjected to the slower tempering cycle (1°C/s, 1°C/s-420°C-1s sample).

Grain distribution functions of the samples are presented in Figure 8-22; the grain area frequency of each samples are also shown in inset. The distribution function shows a very fine grain structure with a grain diameter of about 225 nm; more than 80% of the grains have an area between 0-2 μm^2. However, it was noticeable that 100°C/s-410°C-1s sample and untempered BM had identical grain distribution; on the other hand, the grain area was slightly increased in the 1°C/s-420°C-1s sample due to the lath coarsening resulting from the longer carbon diffusion period (slower heating rate) as also predicted in section 8.7.1.

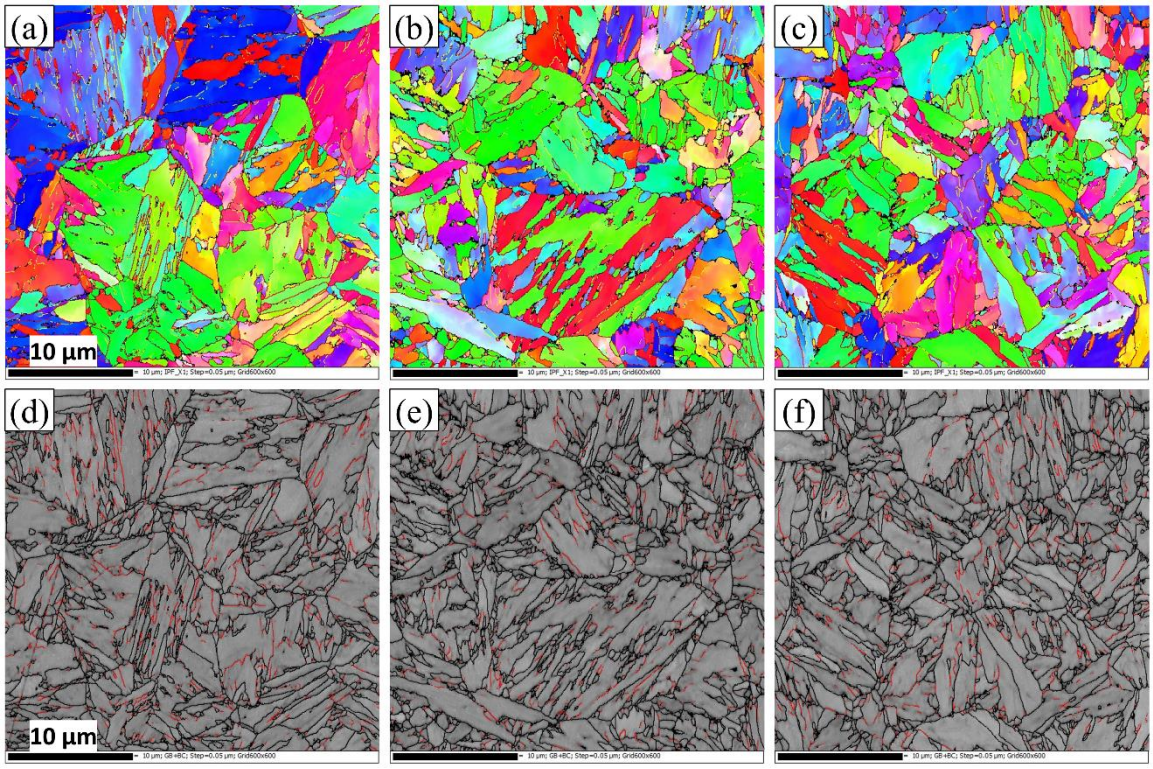

Figure 8-21 EBSD analysis showing IPF map of (a) BM, (b) 1°C/s-420°C-1s sample, (c) 100°C/s-410°C-1s sample, and BC map of (d) BM, (e) 1°C/s-420°C-1s sample, and (f) 100°C/s-410°C-1s sample

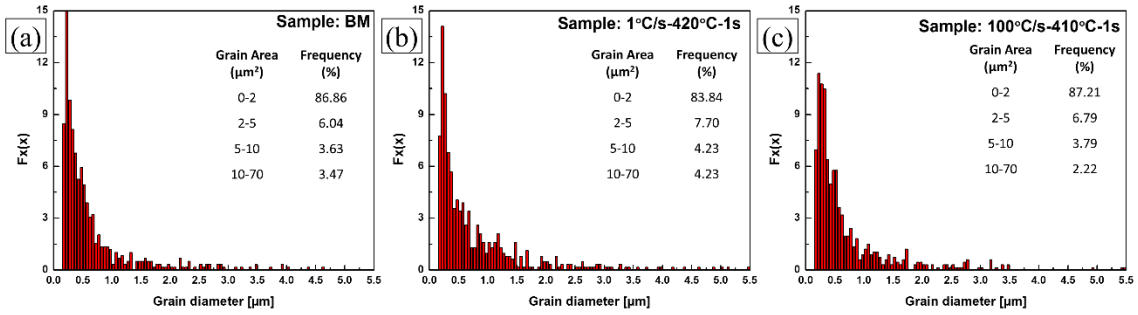

Figure 8-22 Grain distribution function of the samples (a) untempered BM, (b) 1°C/s-420°C-1s, and (c) 100°C/s-410°C-1s. Grain area frequency of each sample is presented in inset

The kernel average misorientations (KAM) maps corresponding to the untempered BM, 1°C/s-420°C-1s, and 100°C/s-410°C-1s samples are shown in Figure 8-23. The blue color is referred to the areas with the lower misorientation angle and yellow colored regions with the high misorientation angle; the boundaries outlined with the red lines corresponding to misorientation angle ≥10°. The KAM maps indicate the reduction of the local misorientation when samples were exposed to the tempering process. However, it was found that the tempering cycle had an insignificant effect on the areas with the low misorientation angles; while the high local misorientation regions were decreased significantly when the lower heating rate was applied.

Figure 8-23(d) to (f) shows the boundary maps constructed using the three different misorientation angle criteria where the red lines indicate misorientation angle ≤2°, the green lines that between 2° and 5°, and the black lines are larger than 10° misorientation angle. It can be seen that the grain boundaries were significantly affected by the tempering process; the boundary lines were decreased after tempering. However, the boundary lines corresponding to less than 5° misorientation which represents the lath boundaries [155] were recovered more compared to the boundary lines with larger than 10° misorientation. It was also observed that the black boundary lines in the tempered structures were not continuous, they appeared to be broken indicating the presence of other phases with different crystal structures such as orthorhombic cementite (Fe_3C), which was disregarded during data processing. In the slowly heated sample (1°C/s-420°C-1s), the boundary regions were recovered more compared to the rapidly heated one (100°C/s-410°C-1s).

Kernel average misorientation (KAM) plots as a function of heating rate are presented in Figure 8-24. A shift of the distributions towards the lower misorientation was detected in the case of the tempered martensite; however, distribution shifts were more pronounced in the case of 1°C/s-420°C-1s sample. It was also observed that the relative frequency distribution at 59.5° of misorientation which represents Kurdjumov-Sachs (K-S) and Nishiyama-Wassermann (N-W) OR is decreased on the tempered samples; however, the sample with 100°C/s heating rate retained a large amount of grains with K-S and N-W OR compared to the 1°C/s-420°C-1s sample.

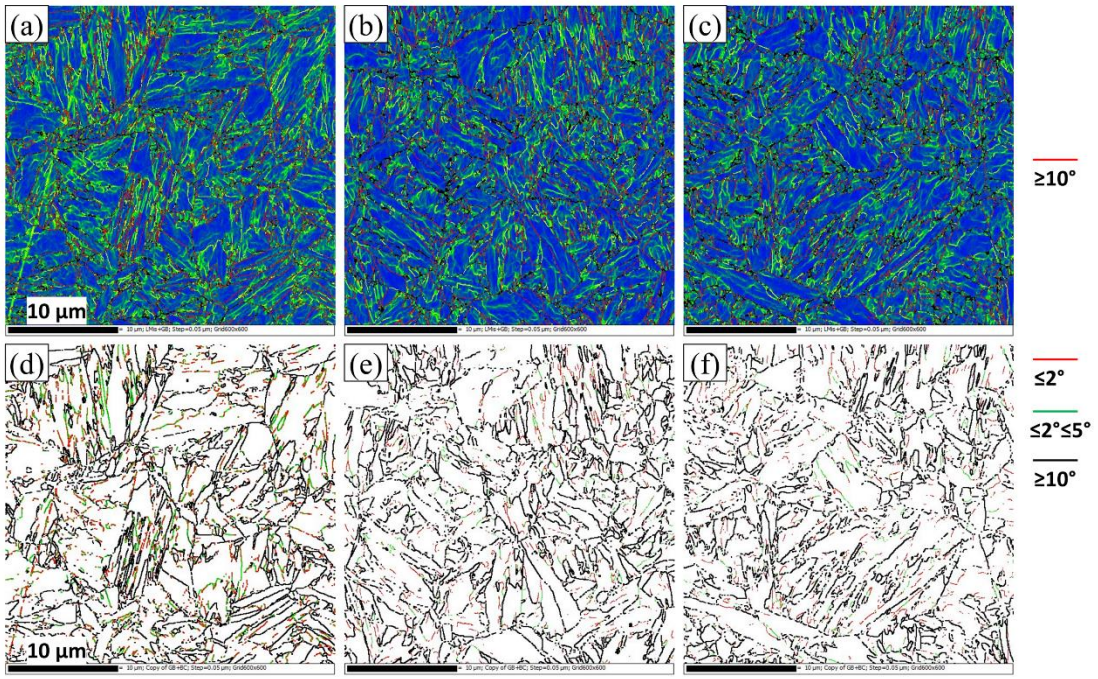

Figure 8-23 (a) to (c) Kernel average misorientation maps for first neighbours and (d) to (f) boundary maps using different misorientation angle criteria. (a) and (d) untempered BM, (b) and (e) 1°C/s-420°C-1s sample, and (c) and (f) 100°C/s-410°C-1s sample

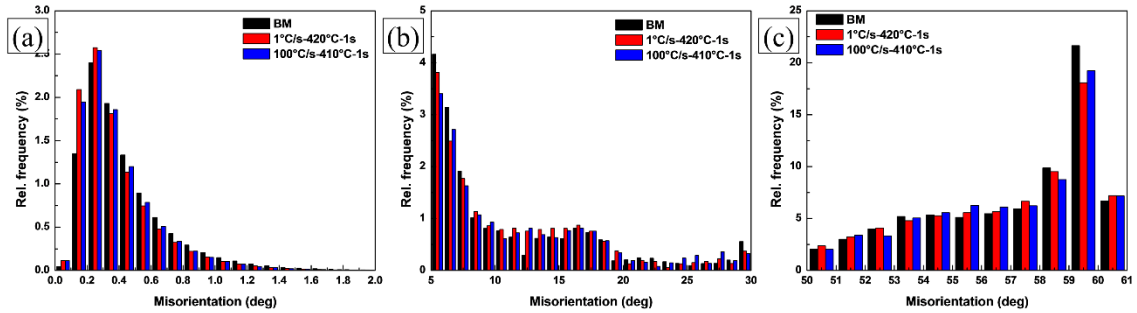

Figure 8-24 Kernel average misorientation angle distribution as a function of heating rate

In order to understand the influences of holding time on the structural changes of martensite, similar crystallographic analysis was performed on the 100°C/s-495°C-1s, and 100°C/s-495°C-100s sample as presented in Figure 8-25 to Figure 8-28. Throughout the study, it was found that the holding time considered in this investigation had an insignificant effect on the grain diameter and grain area; identical frequency of grain area was observed in both the samples similar to the untempered BM as shown in Figure 8-26. The KAM maps in Figure 8-27 shows less recovery of the regions with high misorientation (yellow colored region) suggesting the holding time has less prominent effects on grain recovery. Conversely, the region with the low misorientation angle significantly recovered illustrating a larger reduction of dislocation density which is also supported by the dislocation density prediction presented in section 8.7.2.

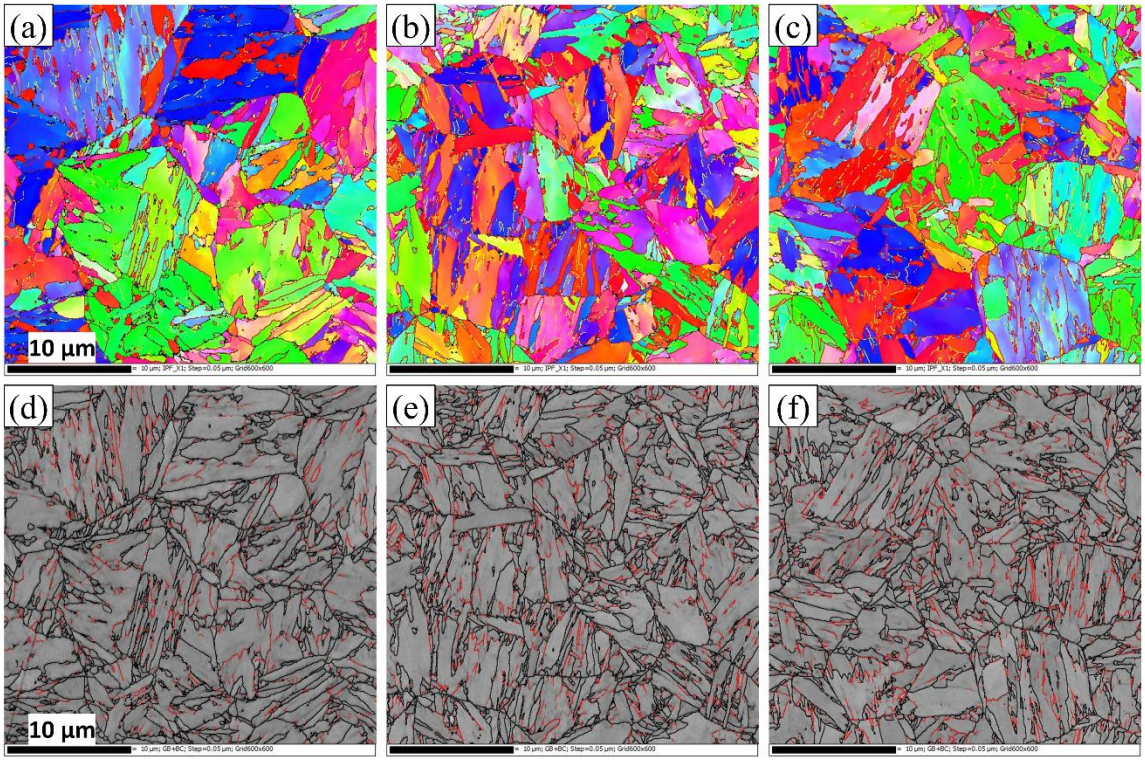

Figure 8-25 EBSD analysis showing IPF map of (a) BM, (b) 100°C/s-495°C-1s sample, (c) 100°C/s-495°C-100s sample, and BC map of (d) BM, (e) 100°C/s-495°C-1s sample, and (f) 100°C/s-495°C-100s

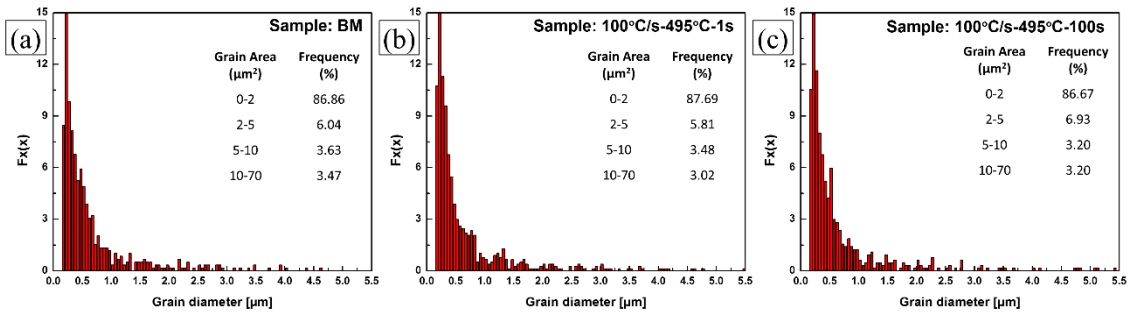

Figure 8-26 Grain distribution function of the samples (a) untempered BM, (b) 100°C/s-495°C-1s, and (c) 100°C/s-495°C-100s. Grain area frequency of each sample is presented in inset

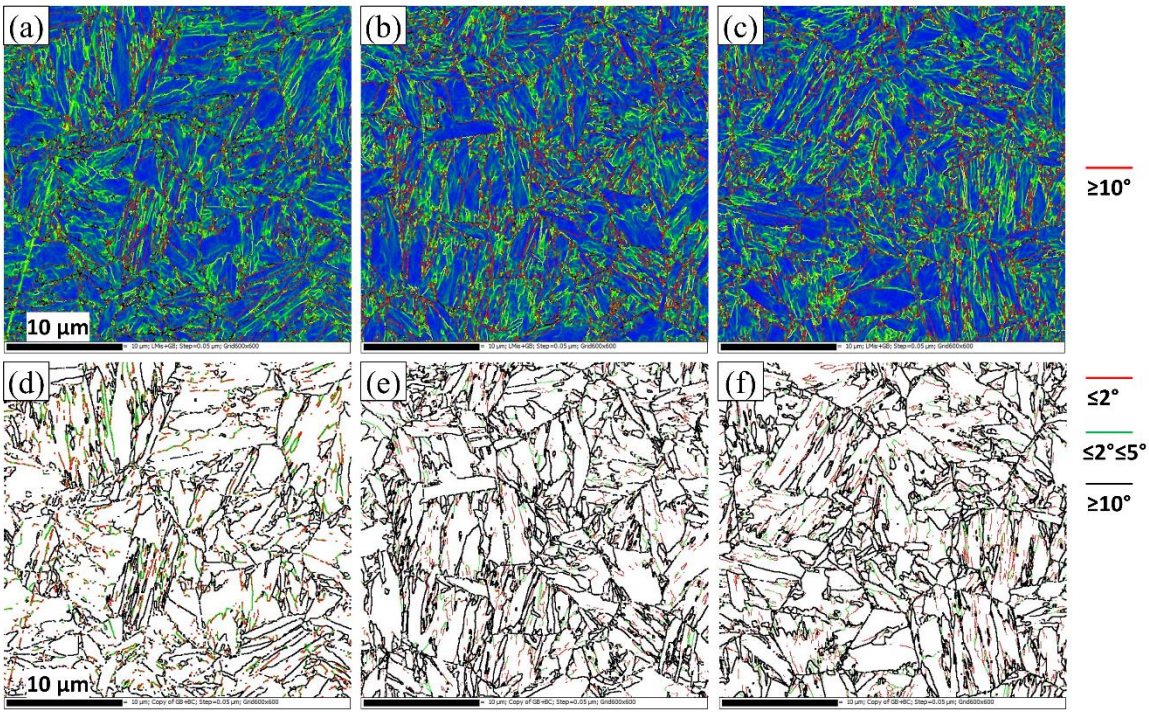

Figure 8-27 (a) to (c) Kernel average misorientation maps for first neighbours and (d) to (f) boundary maps using different misorientation angle criteria. (a) and (d) untempered BM, (b) and (e) 100°C/s-495°C-1s sample, and (c) and (f) 100°C/s-495°C-100s sample

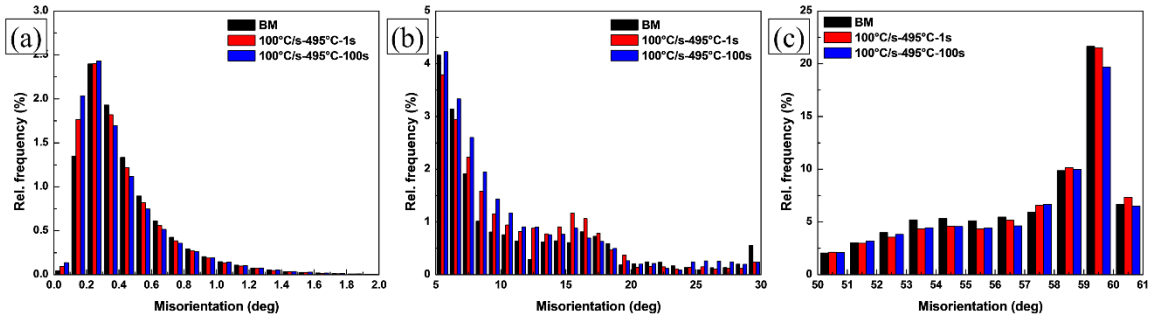

Figure 8-28 Kernel average misorientation angle distribution as a function of holding time

8.10 Validation of the modeling results

8.10.1 Yield strength

Yield strength of the tempered martensite subjected to the short term tempering were calculated using equations 8-19 and 8-20. Figure 8-29 shows the predicted yield strength as a function of temperature and tempering parameter. As expected, the yield strength continuously decreased with the tempering temperature and holding time (Figure 8-29(a)). However, the result shows that the heating rate had significant effects on the yield strength in the case of short period of time (1 s and 10 s); as the holding time increased from 10 s to 100 s, the influence of the heating rates became insignificant as both the samples showed the identical yield strength.

$$\sigma_Y = \sigma_0 + \sigma_{ss} + (\sigma_{Mart}^2 + \sigma_{pct}^2)^{1/2} \tag{8-19}$$

$$\sigma_{Mart} = \frac{300}{\sqrt{d_{block}}} + 0.25M\mu b\sqrt{\rho} \tag{8-20}$$

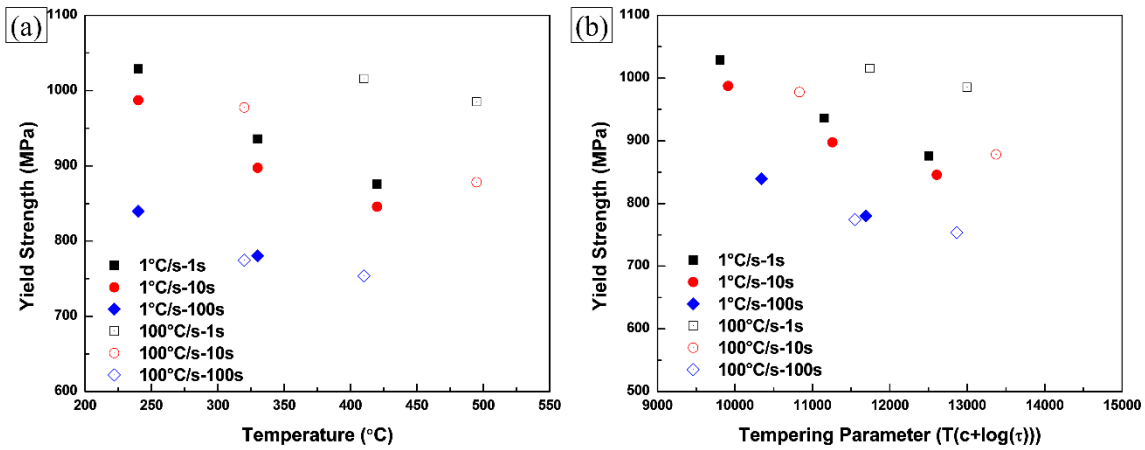

Figure 8-29 Predicted yield strengths are plotted as a function of (a) temperature, and (b) tempering parameter

8.10.2 Hardness

The predicted yield strengths were converted to Vickers microhardness (H_v) using the relationship as shown in equation (8-21), which is commonly applied to the martensitic steel [221]. The predicted hardness values were validated with the experimental data as plotted in Figure 8-30. The predicted results showed a very good agreement with the experimental data with some discrepancies; however, more than 80% of the predicted results follow the same trend as of the experimental results. The red dotted line drawn in Figure 8-30(b) shows the relationship between the measured and predicted microhardness where predicted microhardness is 20 HV lower than the measured value. As can be seen, most of the predicted results shows a very good agreement with the measured data. However, some of the predicted results (open filed points in Figure 8-30(b)) are not aligned with the experimental ones due to inaccurate carbide size and volume fraction measurements. For example, in this investigation, the elongated needle-like carbides are considered to be a sphere with the same equivalent surface area which may lead to inaccurate carbide size measurement. A further study is recommended to measure carbide sizes and volume fractions more accurately.

$$H_v = 0.4(\sigma_Y + 110) \tag{8-21}$$

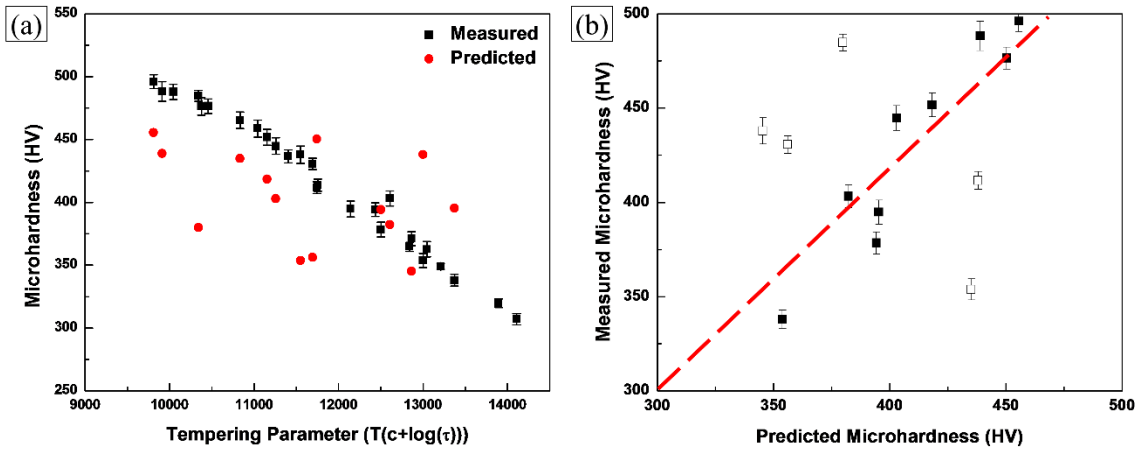

Figure 8-30 Comparison between the predicted and experimental microhardness. The open filed points in (b) represent the data corresponding to 100 s hold time.

The yield strength and microhardness prediction method developed in this work will be particularly useful to study the time and temperature effects on the martensite tempering when sheet is subjected to the rapid thermal cycle such as involve during induction heating of automotive parts. For example, the induction heating is used to temper the B-pillar produced from the hot-formed martensitic boron steel [222]. During mechanical loading, the cracks initiate at the HAZ of the resistance spot welded area due to strain localization. To distribute the strain more uniformly and avoid crack localization around welds, the B-pillar can be rapidly tempered using induction heating prior to welding. In addition, the developed method would be helpful to predict the yield strength and the microhardness of the tempered zone of the laser beam welded martensite containing steels.

8.11 Summary

Martensite tempering kinetics under influences of rapid thermal cycles were investigated by thermal and microstructural analysis. In addition, a model was applied for the strength (yield strength and microhardness) prediction of the tempered martensite by incorporating the effects of heating rate, tempering temperature, and time. The major findings of this work are listed below:

1. Heating rate has significant effect on the carbide precipitate transformation temperature; the transformation temperature range increases to the higher temperature

when heating rate becomes rapid. In the case of the rapid thermal cycle, both the precipitation start and finish temperatures shifted to higher temperature by keeping the transformation temperature span nearly constant.

2. The reaction rate exponent was found to be decreased with increasing of heating rates. Higher reaction rate at slow heating rate implies that there is a greater tendency of martensite to be tempered; however, as the heating rate increases the reaction became slower resulting in a smaller precipitation fraction. Thus the faster heating rate provides lower precipitate volume fraction at a certain tempering temperature.
3. The rapidly heated samples possessed the higher microhardness values resulting from the lesser decomposed laths, formation of finer, denser and dispersed carbides, and a higher amount of the retained dislocation density compared to the slowly heated samples. However, when the sample was tempered for a longer duration, then the minor effects of the heating rate could be observed. The microhardness trends obtained using the two different heating rates were overlapped representing an insignificant effect of heating rate in the longer duration of tempering process.
4. The holding time considered in this investigation had a very insignificant effect on the grain diameter and grain area; however, it had pronounced effect on the carbide precipitation and dislocation density recovery. A high density of dislocations was observed on the rapidly heated samples resulting from insufficient reaction time needed to complete annihilation and recovery of the highly dislocated martensite laths.
5. The predicted yield strength showed a continuous decreasing trend as a function of temperature and tempering parameter; however, the heating rate has prominent effect on the strength at a short period of tempering time. Faster heating rate coupled with a very short duration of time provided the highest tempered martensite strength.

9 General Conclusions and Recommendations for Future Work

9.1 Microstructure-properties correlation of tempered martensite during fiber laser welding

A reduction of microhardness in the SCHAZ of the DP980 steel was detected due to the tempering of martensite and formation of fine carbides. Hardness distributions exhibited a significant variation within dissimilar welds, implying that the mixing of elements within the FZ was inhomogeneous thus leading to the formation of the soft bainite microconstituents along with the predominant martensite phase. Tensile strength of the dissimilar welds was close to the HSLA welds, but lower than the DP980 steel welds, with fracture consistently in the HSLA base metal as observed in the similar HSLA welds. DP980 welds fractured at the tempered region of the HAZ where softening was observed.

9.2 Effects of steel chemistry and microstructure on the tempering kinetics of martensite

The secondary hardening was identified in rapid tempering i.e. Gleeble tempering and laser welding of microalloyed DP780 steel with a ferrite, martensite, and bainite microstructure. The hardness profile in the laser welds agreed well with hardness versus H-J tempering parameter, suggesting that secondary hardening occurred in the steel when tempered at 500°C for a very short duration (< 1 s). Secondary hardening was due to the transformations of the pre-existing carbides found within the bainite structure. The pre-existing cementite Fe_3C, and TiC were dissolved at high temperature, providing a carbon source to form the plate-shaped M_4C_3 and needle-shape M_2C carbides, which led to secondary hardening in the Gleeble specimens tempered at 500°C for 0.5 s. The isothermal tempering products strongly correlated with the hardening peak observed in the HAZ of the DP780 steel laser welds. However, this phenomenon is not likely to occur in bainite-free DP780 steels where no such θ-carbides are available to transform into secondary hardening carbides during rapid tempering and welding.

The experimental evidence suggested that the HAZ softening can be mitigated by modifying the steel microstructure without compromising the UTS of the steel. The laser welded joints of the steel composed of ferrite, martensite, bainite, and blocky retained austenite performed better than ferrite and martensite containing DP980 steel. The presence of 7% bainite and 9% blocky retained austenite in a DP980 steel significantly improved the welded joint properties, which exhibited identical tensile behaviour to the un-welded material.

9.3 Effects of tempering mode on the structural changes of martensite

Crystallographic analysis of the tempered martensite confirmed that a Bagaryatsky and near Isaichev orientation relationships existed between ferrite and cementite in the sample produced via Gleeble thermomechanical simulation and isothermal furnace heat treatment, respectively. On the other hand, ferrite and cementite observed on the non-isothermally produced laser welded samples did not obey a strict OR, which is believe to be the effect of the higher interfacial energy and the larger lattice misfit. The growth kinetics of the precipitated carbides were suppressed when the sample was subjected to the rapid thermal cycle employed via fiber laser welding system. In addition, a rapidly tempered structure maintains a high density of dislocations and less destruction of boundary regions. Micro-scale softening was more pronounced on the samples subjected to a slow heating cycle; conversely, microscopic and nanoscale hardness was found to be in the same level when rapid thermal cycle was employed. The strength contribution due to dislocation density was higher than that of precipitation strengthening for the tempered martensite. The rapidly tempered samples had higher precipitation strength contributions compared to the slowly tempered samples.

9.4 Carbide precipitation kinetics under influences of plastic deformation and rapid thermal cycles

The higher dislocation density of the deformed material resulted in more nucleation sites for cementite precipitation, short-range diffusion of carbon and lower growth period for cementite. The morphologies of the cementite were changed from elongated to small

quasi-spherical with plastic deformation when lath structure of the initial martensite was damaged and more nucleation sites were created by the process of cold-rolling. Prior plastically deformed tempered lath martensite structures yielded a higher structural strength due to a higher retained dislocation density, finer and semicoherent precipitates, and higher fraction of untempered and partially tempered martensite blocks.

9.5 Carbide precipitation kinetics and strength prediction of martensitic steel subjected to short term tempering

Heating rate has significant effect on the carbide precipitation transformation temperature; the transformation temperature range increases to higher temperature when heating rate becomes rapid. In the case of rapid thermal cycle, both the precipitation start and finish temperature shifted to the higher temperature, keeping the transformation temperature span nearly constant. The reaction rate exponent was found to be decreasing with increasing heating rates. Higher reaction rate at slow heating rate implies that there is a greater tendency of martensite to be tempered; however, as heating rate increases the reaction became slower resulting in a smaller precipitation fraction. Thus the faster heating rate provides a lower precipitate volume fraction in a certain tempering temperature. The rapidly heated samples possessed higher microhardness values resulting from the less lath martensite decomposition, formation of finer, denser and dispersed carbides, and a higher amount of retained dislocation density compared to the slowly heated sample. However, when the sample was tempered for a longer duration (> 10 s), then the negligible effects of the heating rate were observed. The microhardness trends obtained using the two different heating rates were overlapped representing an insignificant effect of heating rate in the longer duration tempering process. A high density of dislocations was observed on the rapidly heated samples resulting from insufficient reaction time needed to complete annihilation and recovery of the highly dislocated martensite laths. The predicted yield strength shows a continuous decreasing trend as a function of temperature and tempering parameter; however, heating rate has prominent effect on the strength under short period of tempering time. Faster heating rate coupled with a very short duration of time provides the highest tempered martensite strength.

9.6 Recommendations for future work

The present investigation addressed some of the major issues associated with the martensite tempering kinetics under rapid thermal cycles. However, this work also revealed several interesting aspects for further consideration:

1. This work shows that 13% bainite containing DP780 steel produces some secondary hardening effect when steel contains the secondary hardening promoting elements. However, it was not clear whether the bainite fraction considered in this investigation is the optimized fraction to have the optimized secondary hardening response. In addition, the DP780 steel used in this study has only secondary hardening effect while tempered for a short duration (< 1 s). Therefore, it would be interesting to see whether similar secondary hardening effects can be obtained when tempered for a long period by further optimizing the alloying elements and bainite volume fraction.
2. Throughout this study, it was found that steel chemistry plays an important role on the martensite tempering kinetics. Not only the carbon which has significant effect on tempering kinetics but also the other substitutional elements such as Mn, Cr, Mo have prominent effects on the growth kinetics of carbides. Therefore, the steel produced with varying these alloying elements would be a point of interest where the effects of major alloying elements can be generalized in the form of an equation to predict the tempering response on a wide range of steel compositions.
3. The influences of martensite grain size on the tempering kinetics of martensite were not considered in the current study. To investigate the grain size effect, steels can be produced with various martensite grain size by intercritically annealing with different temperature and time. Different martensite grain size and volume fraction would provide different carbon partitioning into the martensite phase. Therefore, it would be of great interest to study the effect of grain size and the martensite carbon content on the tempering kinetics under isothermal and nonisothermal process.
4. In Chapter 5, Section 5.3, it was observed that about 9% blocky retained austenite can effectively suppress the severity of martensite tempering due to the higher thermal stability of retained austenite. However, FLW process provides a very low heat input thus blocky retained austenite was not influenced by the thermal cycle and remained

untempered. Further investigation may be required to evaluate the thermal stability of this blocky retained austenite under isothermal or nonisothermal process such as using the furnace heat treatment, diode laser welding, and gas metal arc welding where these processes provide higher heat input.

5. The current study leaves aside the issue of whether martensite tempering kinetics are influenced by the externally applied stress (either tensile or compressive). Therefore, the tempering cycles can be programmed in a Gleeble simulator where the external stress can be controlled during nonisothermal tempering of martensite.
6. *In-situ* real-time carbide precipitation observation during martensite tempering in a TEM heating stage will provide further understanding on the interaction of the various factors such as boundaries, dislocation density, location of carbide precipitation, carbides dissolution, and coarsening.

References

[1] D. Shindell, G. Faluvegi, M. Walsh, S. C. Anenberg, R. Van Dingenen, N. Z. Muller, J. Austin, D. Koch, and G. Milly, "Climate, health, agricultural and economic impacts of tighter vehicle-emission standards," *Nat. Clim. Chang.*, vol. 1, pp. 59-66, 2011.

[2] H. J. Kim, C. McMillan, G. A. Keoleian, and S. J. Skerlos, "Greenhouse gas emissions payback for lightweighted vehicles using aluminum and high-strength steel," *J. Ind. Ecol.*, vol. 14, pp. 929-946, 2010.

[3] A. S. P. Program, *Tailor welded blank design and manufacturing manual*: Auto/Steel Partnership, 1995.

[4] M. Uchihara and K. Fukui, "Formability of tailor welded blanks fabricated by different welding processes. Study of tailor welded blanks using automotive high-strength steel sheets (1st report)," *Welding International*, vol. 20, pp. 612-621, 2006.

[5] H. Kusuda, T. Takasago, and F. Natsumi, "Formability of tailored blanks," *J. Mater. Process. Technol.*, vol. 71, pp. 134-140, 1997.

[6] M. F. Shi, G. H. Thomas, M. X. Chen, and J. R. Fekete, "Formability performance comparison between dual phase and HSLA steels," *Iron and Steelmaker (I and SM)*, vol. 29, pp. 27-32, 2002.

[7] W. Xu, D. Westerbaan, S. Nayak, D. Chen, F. Goodwin, E. Biro, and Y. Zhou, "Microstructure and fatigue performance of single and multiple linear fiber laser welded DP980 dual-phase steel," *Mater. Sci. Eng. A*, vol. 553, pp. 51-58, 2012.

[8] W. Xu, D. Westerbaan, S. S. Nayak, D. L. Chen, F. Goodwin, and Y. Zhou, "Tensile and fatigue properties of fiber laser welded high strength low alloy and DP980 dual-phase steel joints," *Mater. Des.*, vol. 43, pp. 373-383, 2013.

[9] R. C. Thomson and M. K. Miller, "Carbide precipitation in martensite during the early stages of tempering Cr- andMo-containing low alloy steels," *Acta. Mater.*, vol. 46, pp. 2203-2213, 1998.

[10] M. Jung, S. J. Lee, and Y. K. Lee, "Microstructural and dilatational changes during tempering and tempering kinetics in martensitic medium-carbon steel," *Metall. Mater. Trans. A*, vol. 40A, pp. 551-559, 2009.

[11] G. B. Olson and W. S. Owen, "Martensite," in *Martensitic Nucleation*, ed Materials Park, OH, USA: ASM International, 1992, p. 261.

[12] H. D. Sherman, M. S. Cross, S. Kim, F. Grandjean, J. G. Long, and K. M. Miller, "Characterization of the carbon and retained austenite distributions in martensitic medium carbon, high silicon steel," *Metall. Mater. Trans. A*, vol. 38, pp. 1698-1711, 2007.

[13] R. G. Davies and C. L. Magee, "Physical metallurgy of automotive high-strength steels," *JOM*, vol. 31, pp. 17-23, 1979.

[14] R. G. Davies, "Influence of martensite composition and content on the properties of dual phase steels," *Metall. Trans. A*, vol. 9, pp. 671-679, 1978.

[15] R. Kot and B. Bramfitt, *Fundamentals of dual-phase steels: proceedings of a symposium*: Metallurgical Society of AIME, 1981.

[16] W. Steel, "Advanced high strength steel (AHSS) application guidelines," International Iron & Steel Institute2014.

[17] J. H. Sung, J. H. Kim, and R. H. Wagoner, "A plastic constitutive equation incorporating strain, strain-rate, and temperature," *International Journal of Plasticity*, vol. 26, pp. 1746-1771, 2010.

[18] H.-C. Chen and G.-H. Cheng, "Effect of martensite strength on the tensile strength of dual phase steels," *Journal of Materials Science*, vol. 24, pp. 1991-1994, 1989.

[19] E. C. Bain and H. W. Paxton, *Alloying elements in steel*. Metals Park, Ohio: American Society of Metals, 1966.

[20] K. Andrews, "Empirical formulae for the calculation of some transformation temperatures," *J. Iron Steel Inst*, vol. 203, pp. 721-727, 1965.

[21] M. Kehoe and P. M. Kelly, "The role of carbon in the strength of ferrous martensite," *Scripta. Metall.*, vol. 4, pp. 473-476, 1970.

[22] S. C. Kennett, "Strengthening and toughening mechanisms in low-C microalloyed martensitic steel as influenced by austenite conditioning," Doctor of Philosophy, Metallurgical and Materials Engineering, Colorado School of Mines, Golden, Colorado, 2014.

[23] L. Cheng, A. Böttger, T. H. de Keijser, and E. J. Mittemeijer, "Lattice parameters of iron-carbon and iron-nitrogen martensites and austenites," *Scripta. Metall. Mater.*, vol. 24, pp. 509-514, 1990.

[24] A. W. Cochardt, G. Schoek, and H. Wiedersich, "Interaction between dislocations and interstitial atoms in body-centered cubic metals," *Acta. Metall. Mater.*, vol. 3, pp. 533-537, 1955.

[25] J. Wilde, A. Cerezo, and G. D. W. Smith, "Three-dimensional atomic-scale mapping of a cottrell atmosphere around a dislocation in iron," *Scripta. Mater.*, vol. 43, pp. 39-48, 2000.

[26] G. Krauss and A. R. Marder, "The morphology of martensite in iron alloys," *Metall. Trans.*, vol. 2, pp. 2343-2357, 1971.

[27] T. Maki, K. Tsuzaki, and I. Tamura, "The morphology of microstructure composed of lath martensite in steels," *Trans. ISIJ*, vol. 20, pp. 207-214, 1980.

[28] T. Furuhara, K. Kobayashi, and T. Maki, "Control of cementite precipitation in lath martensite by rapid heating and tempering," *ISIJ Int.*, vol. 44, pp. 1937-1944, 2004.

[29] H. Kitahara, R. Ueji, N. Tsuji, and Y. Minamino, "Crystallographic features of lath martensite in low-carbon steel," *Acta. Mater.*, vol. 54, pp. 1279-1288, 2006.

[30] S. Morito, H. Tanaka, R. Konishi, T. Furuhara, and T. Maki, "The morphology and crystallography of lath martensite in Fe-C alloys," *Acta. Mater.*, vol. 51, pp. 1789-1799, 2003.

[31] H. K. D. H. Bhadeshia and R. W. K. Honeycombe, *Steels - Microstructure and Properties*, 3rd ed. Oxford, UK: Butterworth-Heinemann, 2006.

[32] R. Aborn, "Low carbon martensites," *Transactions of the ASM,* vol. 48, pp. 51-85, 1956.

[33] G. R. Speich, "Tempering of low-carbon martensite," *Trans. TMS-AIME.*, vol. 245, pp. 2552-2564, 1969.

[34] R. P. Foley, R. K. Weiss, S. W. Thompson, and G. Krauss, "Tempering behavior of martensitic plate steels produced by direct-quench and reaustenitize-and-quench processing," in *International Symposium on Low-Carbon Steels for the 90's*, Warrendale, PA, 1993, pp. 243-256.

[35] G. Krauss, "Tempering of martensite in carbon steels," in *Phase Transformations in Steels*. vol. 2, E. Pereloma and D. V. Edmonds, Eds., ed: Woodhead Publishing, 2012, pp. 126-150.

[36] G. Krauss, *Steels: processing, structure, and performance*: ASM International, 2005.

[37] S. Morito, J. Nishikawa, and T. Maki, "Dislocation density within lath martensite in Fe-C and Fe-Ni alloys," *ISIJ Int.*, vol. 43, pp. 1475-1477, 2003.

[38] R. W. K. Honeycombe and H. K. D. H. Bhadeshia, *Steels: microstructure and properties*: E. Arnold, 1981.

[39] L. Morsdorf, C. C. Tasan, D. Ponge, and D. Raabe, "3D structural and atomic-scale analysis of lath martensite: Effect of the transformation sequence," *Acta. Mater.*, vol. 95, pp. 366-377, 2015.

[40] B. B. He and M. X. Huang, "Revealing the intrinsic nanohardness of lath martensite in low carbon steel," *Metall. Mater. Trans. A,* vol. 46, pp. 688-694, 2015.

[41] A. M. Sherman, G. T. Eldis, and M. Cohen, "The aging and tempering of iron-nickel-carbon martensites," *Metall. Trans. A,* vol. 14A, pp. 995-1005, 1983.

[42] P. C. Chen and P. G. Winchell, "Martensite lattice changes during tempering," *Metall. Trans. A,* vol. 11A, pp. 1333-1339, 1980.

[43] G. B. Olson and M. Cohen, "Early stages of aging and tempering of ferrous martensites," *Metall. Trans. A,* vol. 14A, pp. 1057-1065, 1983.

[44] P. C. Chen, B. O. Hall, and P. G. Winchell, "Atomic displacements due to C in Fe Ni C martensite," *Metall. Trans. A,* vol. 11A, pp. 1323-1331, 1980.

[45] M. L. Bernshtein, L. M. Kaputkina, and S. D. Prokoshkin, "Studies of the quenched and tempered martensite crystal lattice," *Scripta. Metall.*, vol. 18, pp. 863-868, 1984.

[46] H. Hayakawa, M. Tanigami, and M. Oka, "Low temperature aging of the freshly formed martensite in an Fe-Ni-C alloy," *Metall. Trans. A,* vol. 16A, pp. 1745-1750, 1985.

[47] J. R. Genin and P. A. Flinn, "Mössbauer effect evidence for the clustering of carbon atoms in iron-carbon martensite during aging at room temperature," *Transactions of TMS-AIME,* vol. 242, pp. 1419-1430, 1968.

[48] W. K. Choo and R. Kaplow, "Mössbauer measurements on the aging of iron-carbon martensite," *Acta. Mater.,* vol. 21, pp. 725-732, 1973.

[49] N. DeCristofaro and R. Kaplow, "Interstitial atom configurations in stable and metastable Fe-N and Fe-C solid solutions," *Metall. Trans. A,* vol. 8A, pp. 35-44, 1977.

[50] N. DeCristofaro, R. Kaplow, and W. S. Owen, "The kinetics of carbon clustering in martensite," *Metall. Trans. A,* vol. 9A, pp. 821-825, 1978.

[51] V. I. Izotov and L. M. Utevskiy, *Mhys. Met. Metallogr.,* vol. 25, pp. 86-96, 1968.

[52] S. Nagakura, Y. Hirotsu, M. Kusunoki, T. Suzuki, and Y. Nakamura, "Crystallographic study of the tempering of martensitic carbon steel by electron microscopy and diffraction," *Metall. Trans. A,* vol. 14A, pp. 1025-1031, 1983.

[53] M. Kusunoki and S. Nagakura, "Modulated structure of iron-carbon martensite studied by electron microscopy and diffraction," *J. Appl. Cryst.,* vol. 14, pp. 329-336, 1981.

[54] M. K. Miller, P. A. Beaven, and G. D. W. Smith, "A study of the early stages of tempering of iron-carbon martensites by atom probe field ion microscopy," *Metall. Trans. A,* vol. 12A, pp. 1197-1204, 1981.

[55] M. K. Miller, P. A. Beaven, S. S. Brenner, and G. D. W. Smith, "An atom probe study of the aging of iron-nickel-carbon martensite," *Metall. Trans. A,* vol. 14A, pp. 1021-1024, 1983.

[56] Y. Ohmori and I. Tamura, "Epsilon carbide precipitation during tempering of plain carbon martensite," *Metall. Trans. A,* vol. 23, pp. 2737-2751, 1992.

[57] G. R. Speich and W. C. Leslie, "Tempering of steel," *Metall. Trans.,* vol. 3, pp. 1043-1054, 1972.

[58] S. Matas and R. F. Hehemann, "Retained austenite and the tempering of martensite," *Nature,* vol. 187, pp. 685-686, 1960.

[59] C. Roberts, B. Averbach, and M. Cohen, "The mechanism and kinetics of the first stage of tempering," *Trans. ASM,* vol. 45, pp. 576-604, 1953.

[60] C. R. Brooks, *Principles of the heat treatment of plain carbon and low alloy steels*: ASM international, 1996.

[61] H. K. D. H. Bhadeshia, *Bainite in Steels - Transformations, Microstructure and Properties*. London, United Kingdom: IOM Communications Ltd, 2001.

[62] A. D. B. Gingell, H. K. D. H. Bhadeshia, D. G. Jones, and K. J. A. Mawella, "Carbide precipitation in some secondary hardened steels," *Journal of Materials Science,* vol. 32, pp. 4815-4820, 1997.

[63] D. Delagnes, P. Lamesle, M. H. Mathon, N. Mebarki, and C. Levaillant, "Influence of silicon content on the precipitation of secondary carbides and fatigue properties of a 5%Cr tempered martensitic steel," *Mater. Sci. Eng. A,* vol. 394, pp. 435-444, 2005.

[64] C. Yoo, H. Lee, J. Chan, and J. Morris, Jr., "M2C precipitates in isothermal tempering of high Co-Ni secondary hardening steel," *Metall. Mater. Trans. A,* vol. 27, pp. 3466-3472, 1996.

[65] G. A. Roberts and R. Kennedy, *Tool steels*: ASM International, 1998.

[66] Y. A. Bagaryatskii and H. E. Brutcher, *The probable mechanism of the martensite decomposition*: H. Brutcher Technical Translations, 1950.

[67] D. S. Zhou and G. J. Shiflet, "Ferrite: Cementite crystallography in pearlite," *Metall. Trans. A,* vol. 23, pp. 1259-1269, 2013.

[68] M. X. Zhang and P. M. Kelly, "Accurate orientation relationships between ferrite and cementite in pearlite," *Scripta. Mater.,* vol. 37, pp. 2009-2015, 1997.

[69] M. X. Zhang and P. M. Kelly, "Crystallography of spheroidite and tempered martensite," *Acta. Mater.,* vol. 46, pp. 4081-4091, 1998.

[70] K. H. Jack, "Structural transformations in the tempering of high carbon martensitic steels," *Journal of Iron and Steel Institute,* vol. 169, pp. 26-36, 1951.

[71] H. Bhadeshia, "Geometry of crystals," *Institute of Materials, London,* 2001.

[72] V. H. B. Hernandez, S. S. Nayak, and Y. Zhou, "Tempering of martensite in dual-phase steels and its effects on softening behavior," *Metall. Mater. Trans. A,* vol. 42, pp. 3115-3129, 2011.

[73] C. Revilla, B. López, and J. M. Rodriguez-Ibabe, "Carbide size refinement by controlling the heating rate during induction tempering in a low alloy steel," *Mater. Des.,* vol. 62, pp. 296-304, 2014.

[74] Y. I. Son, Y. K. Lee, K.-T. Park, C. S. Lee, and D. H. Shin, "Ultrafine grained ferrite–martensite dual phase steels fabricated via equal channel angular pressing: Microstructure and tensile properties," *Acta. Mater.,* vol. 53, pp. 3125-3134, 2005.

[75] S. Takaki, S. Iizuka, K. Tomimura, and Y. Tokunaga, "Influence of cold working on recovery and recrystallization of lath martensite in 0.2%C steel," *Mater. Trans.,* vol. 33, pp. 577-584, 1992.

[76] S. Takaki, S. Iizuka, K. Tomimura, and Y. Tokunaga, "Role of Carbide in the Recovery Process of 0.2% Carbon Lath Martensitic Structure," *Mater. Trans.,* vol. 32, pp. 207-213, 1991.

[77] L. M. Kaputkina and D. Kaputkin, "Structure and phase transformation under quenching and tempering during heat and thermomechanical treatment of steels," in *Mater. Sci. Forum.*, 2003, pp. 1119-1126.

[78] J. H. Hollomon and L. D. Jaffe, "Time-temperature relations in tempering steel," *Trans. TMS-AIME,* vol. 162, pp. 223-249, 1945.

[79] T. Swarr and G. Krauss, "The effect of structure on the deformation of as-quenched and tempered martensite in an Fe-0.2 pct C alloy," *Metall. Trans. A,* vol. 7, pp. 41-48, 1976.

[80] B. Kim, E. Boucard, T. Sourmail, D. San Martín, N. Gey, and P. E. J. Rivera-Díaz-del-Castillo, "The influence of silicon in tempered martensite: Understanding the microstructure–properties relationship in 0.5–0.6 wt.% C steels," *Acta. Mater.,* vol. 68, pp. 169-178, 2014.

[81] C. Zhang, Q. Wang, J. Ren, R. Li, M. Wang, F. Zhang, and Z. Yan, "Effect of microstructure on the strength of 25CrMo48V martensitic steel tempered at different temperature and time," *Materials & Design (1980-2015),* vol. 36, pp. 220-226, 2012.

[82] E. I. Galindo-Nava and P. E. J. Rivera-Díaz-del-Castillo, "A model for the microstructure behaviour and strength evolution in lath martensite," *Acta. Mater.,* vol. 98, pp. 81-93, 2015.

[83] T. Ohmura, A. Minor, E. Stach, and J. Morris, "Dislocation–grain boundary interactions in martensitic steel observed through in situ nanoindentation in a transmission electron microscope," *J. Mater. Res.,* vol. 19, pp. 3626-3632, 2004.

[84] T. Ohmura, A. Minor, K. Tsuzaki, and J. Morris, "Indentation-induced deformation behavior in martensitic steel observed through in situ nanoindentation in a transmission electron microscopy," in *Mater. Sci. Forum.*, 2006, pp. 239-244.

[85] M. Natori, Y. Futamura, T. Tsuchiyama, and S. Takaki, "Difference in recrystallization behavior between lath martensite and deformed ferrite in ultralow carbon steel," *Scripta. Mater.,* vol. 53, pp. 603-608, 2005.

[86] C. T. Dawes, *Laser welding: A practical guide*: Elsevier Science, 1992.

[87] G. Shannon, "Laser welding modes: conduction, transition, & keyhole welding," in *Amada Miyachi Blog* vol. 2016, ed: Amada Miyachi America, 2016.

[88] D. Rosenthal, "The theory of moving sources of heat and its application to metal treatments," 1946.

[89] K. E. Easterling, *Introduction to the physical metallurgy of welding*: Butterworth Heinemann, 1992.

[90] T. Kasuya and N. Yurioka, "Carbon Equivalent and Multiplying Factor for Hardenability of Steel," *Weld. J.*, vol. 72, pp. S263-S268, 1993.

[91] S. J. Lee, M. T. Lusk, and Y. K. Lee, "Conversional model of transformation strain to phase fraction in low alloy steels," *Acta. Mater.*, vol. 55, pp. 875-882, 2007.

[92] D. B. Williams and C. B. Carter, *The transmission electron microscope*: Springer, 1996.

[93] N. H. van Dijk, A. M. Butt, L. Zhao, J. Sietsma, S. E. Offerman, J. P. Wright, and S. van der Zwaag, "Thermal stability of retained austenite in TRIP steels studied by

synchrotron X-ray diffraction during cooling," *Acta. Mater.*, vol. 53, pp. 5439-5447, 2005.

[94] D. Westerbaan, "Fiber laser welding of advanced high strength steels," Master of Applied Science, Department of Mechanical Engineering, University of Waterloo, 2013.

[95] N. Barbakadze, S. Enders, S. Gorb, and E. Arzt, "Local mechanical properties of the head articulation cuticle in the beetle Pachnoda marginata (Coleoptera, Scarabaeidae)," *Journal of Experimental Biology*, vol. 209, pp. 722-730, 2006.

[96] A. International, "Standard test methods for tension testing of metallic materials," in *ASTM Standard E8, 2011*, ed. West Conshohocken, PA: Annual Book of ASTM Standards, ASTM, 2011.

[97] D. C. Saha, D. Westerbaan, S. S. Nayak, E. Biro, A. P. Gerlich, and Y. Zhou, "Microstructure-properties correlation in fiber laser welding of dual-phase and HSLA steels," *Mater. Sci. Eng. A*, vol. 607, pp. 445-453, 2014.

[98] D. Westerbaan, S. S. Nayak, D. Parkes, W. Xu, D. L. Chen, S. D. Bhole, F. Goodwin, E. Biro, and Y. Zhou, "Microstructure and mechanical properties of fiber laser welded DP980 and HSLA steels," in *Sheet Metal Welding Conference XV*, Michigan, USA, 2012.

[99] N. Farabi, D. Chen, and Y. Zhou, "Tensile properties and work hardening behavior of laser-welded dual-phase steel joints," *Journal of Materials Engineering and Performance*, vol. 21, pp. 222-230, 2012.

[100] M. S. Xia, E. Biro, Z. L. Tian, and Y. N. Zhou, "Effects of heat input and martensite on HAZ softening in laser welding of dual phase steels," *ISIJ Int.*, vol. 48, pp. 809-814, 2008.

[101] N. Farabi, D. L. Chen, and Y. Zhou, "Fatigue properties of laser welded dual-phase steel joints," *Procedia Eng.*, vol. 2, pp. 835-843, 2010.

[102] N. Sreenivasan, S. Lawson, Y. Zhou, and Z. Tian, "A comparative study of formability of diode laser welds in DP980 and HSLA steels," *Journal of engineering materials and technology*, vol. 129, p. 447, 2007.

[103] S. S. Nayak, V. H. B. Hernandez, and Y. Zhou, "Effect of chemistry on nonisothermal tempering and softening of dual-phase steels," *Metall. Mater. Trans. A*, vol. 42A, pp. 3242-3248, 2011.

[104] A. Kumar, S. B. Singh, and K. K. Ray, "Influence of bainite/martensite-content on the tensile properties of low carbon dual-phase steels," *Mat Sci Eng a-Struct*, vol. 474, pp. 270-282, 2008.

[105] E. Biro and A. Lee, "Welded properties of various DP600 chemistries," in *Proc. Sheet Metal Welding Conference XI*, 2004.

[106] V. H. Baltazar Hernandez, S. K. Panda, Y. Okita, and N. Y. Zhou, "A study on heat affected zone softening in resistance spot welded dual phase steel by nanoindentation," *Journal of Materials Science*, vol. 45, pp. 1638-1647, 2010.

[107] E. Biro and A. Lee, "Tensile Properties of Gleeble-Simulated HAZ from Various Dual-Phase Steels," in *Sheet Metal Welding Conference XII*, Livonia, MI, 2006, pp. 1-13.

[108] M. Mukherjee and T. K. Pal, "Influence of Heat Input on Martensite Formation and Impact Property of Ferritic-Austenitic Dissimilar Weld Metals," *J. Mater. Sci. Technol.,* vol. 28, pp. 343-352, 2012.

[109] D. Westerbaan, D. Parkes, S. S. Nayak, D. L. Chen, E. Biro, F. Goodwin, and Y. Zhou, "Effects of concavity on tensile and fatigue properties in fibre laser welding of automotive steels," *Sci. Technol. Weld. Joi.,* vol. 19, pp. 60-68, 2014.

[110] J. E. Gould, S. P. Khurana, and T. Li, "Predictions of microstructures when welding automotive advanced high-strength steels - A combination of thermal and microstructural modeling can be used to estimate performance of welds in advanced high-strength steels," *Weld. J.,* vol. 85, pp. 111s-116s, 2006.

[111] S. Kou, *Welding Metallurgy*. Hoboken, NJ: Wiley & Sons, Inc., 2003.

[112] A. Santillan Esquivel, S. Nayak, M. Xia, and Y. Zhou, "Microstructure, hardness and tensile properties of fusion zone in laser welding of advanced high strength steels," *Canadian Metallurgical Quarterly,* vol. 51, pp. 328-335, 2012.

[113] H. K. D. H. Bhadeshia and L. E. Svensson, "Modelling the Evolution of Microstructure in Steel Weld Metal," in *Mathematical Modeling of Weld Phenomena*, ed London: Institute of Materials, Minerals and Mining, 1993, pp. 109-180.

[114] K. O. Kese, Z. C. Li, and B. Bergman, "Method to account for true contact area in soda-lime glass during nanoindentation with the Berkovich tip," *Mater. Sci. Eng. A,* vol. 404, pp. 1-8, 2005.

[115] V. H. Baltazar Hernandez, S. K. Panda, M. I. Kuntz, and Y. Zhou, "Nanoindentation and Microstructure Analysis of Resistance Spot Welded Dual Phase Steel," *Mater. Lett.,* vol. 64, pp. 207-210, 2010.

[116] B. W. Choi, D. H. Seo, and J. I. Jang, "A nanoindentation study on the micromechanical characteristics of API X100 pipeline steel," *Metals and Materials International,* vol. 15, pp. 373-378, 2009.

[117] D. C. Saha, S. S. Nayak, E. Biro, A. P. Gerlich, and Y. Zhou, "Mechanism of secondary hardening in rapid tempering of dual-phase steel," *Metall. Mater. Trans. A,* vol. 45, pp. 6153-6162, 2014.

[118] C. W. Yao, B. S. Xu, J. Huang, P. L. Zhang, and Y. X. Wu, "Study on the softening in overlapping zone by laser-overlapping scanning surface hardening for carbon and alloyed steel," *Optics and Lasers in Engineering,* vol. 48, pp. 20-26, 2010.

[119] T. Burns, "Weldability of a dual-phase sheet steel by the gas metal arc welding process," Master Thesis, Mechanical and Mechatronics Engineering, University of Waterloo, 2009.

[120] P. Ghosh, "Thermal cycle and microstructure of heat affected zone (HAZ) of flash butt welded Mn-Cr-Mo dual phase steel," *ISIJ Int.*, vol. 30, pp. 317-324, 1990.

[121] V. H. B. Hernandez, S. K. Panda, Y. Okita, and N. Y. Zhou, "A study on heat affected zone softening in resistance spot welded dual phase steel by nanoindentation," *Journal of Materials Science*, vol. 45, pp. 1638-1647, 2010.

[122] H. Tanabe, A. Miyasaka, I. Anai, and S. Tanioka, "HAZ softening-resistant high-strength steel tubes for automobile propeller shafts," *Nippon Steel. Tech. Rep.*, pp. 62-68, 1995.

[123] D. Huang, S. S. Nayak, M. A. Wells, Y. Zhou, and E. Biro, "Comparison of isothermal Gleeble treatment and HAZ of dual-phase steels," in *Sheet Metal Welding Conference XV*, Livonia, MI, 2012, pp. 1-11.

[124] C. H. Yoo, H. M. Lee, J. W. Chan, and J. W. Morris Jr., "M2C precipitates in isothermal tempering of high Co-Ni secondary hardening steel," *Metall. Mater. Trans. A*, vol. 27A, pp. 3466-3472, 1996.

[125] F. Danoix, R. Danoix, J. Akre, A. Grellier, and D. Delagnes, "Atom probe tomography investigation of assisted precipitation of secondary hardening carbides in a medium carbon martensitic steels," *Journal of Microscopy*, vol. 244, pp. 305-310, 2011.

[126] D. Kuhlmann-Wilsdorf, "Theory of workhardening 1934-1984," *Metall. Trans. A*, vol. 16, pp. 2091-2108, 1985.

[127] in *ASTM E. Standard test methods for determining average grain size. West Conshohocken, PA: ASTM International; 2014*, ed.

[128] W. Saikaly, X. Bano, C. Issartel, G. Rigaut, L. Charrin, and A. Charai, "The effects of thermomechanical processing on the precipitation in an industrial dual-phase steel microalloyed with titanium," *Metall. Mater. Trans. A*, vol. 32A, pp. 1939-1947, 2001.

[129] J. H. Jang, C.-H. Lee, H. N. Han, H. K. D. H. Bhadeshia, and D.-W. Suh, "Modelling coarsening behaviour of TiC precipitates in high strength, low alloy steels," *Mater. Sci. Technol.*, pp. 1-6, 2013.

[130] K. Nishioka and K. Ichikawa, "Progress in thermomechanical control of steel plates and their commercialization," *Science and Technology of Advanced Materials*, vol. 13, pp. 1-20, 2012.

[131] G. K. Tirumalasetty, C. M. Fang, Q. Xu, J. Jansen, J. Sietsma, M. A. van Huis, and H. W. Zandbergen, "Novel ultrafine Fe(C) precipitates strengthen transformation-induced-plasticity steel," *Acta. Mater.*, vol. 60, pp. 7160-7168, 2012.

[132] K. Aigner, W. Lengauer, D. Rafaja, and P. Ettmayer, "Lattice parameters and thermal expansion of Ti(C/sub x/N/sub 1-x/), Zr(C/sub x/N/sub 1-x/), Hf(C/sub x/N/sub 1-x/) and TiN/sub 1-x/ from 298 to 1473 K as investigated by high-temperature X-ray diffraction," *Journal of Alloys and Compounds*, vol. 215, pp. 121-126, 1994.

[133] W. Kim, J. S. Park, C. Y. Suh, S. W. Cho, S. Lee, and I. J. Shon, "Synthesis of TiN nanoparticles by explosion of Ti wire in nitrogen gas," *Mater. Trans.*, vol. 50, pp. 2897-2899, 2009.

[134] H. A. Wriedt and J. L. Murray, "The N-Ti (Nitrogen-Titanium) System," *Bulletin of Alloy Phase Diagrams*, vol. 8, pp. 378-388, 1987.

[135] Y.-l. Kang, Q.-h. Han, X.-m. Zhao, and M.-h. Cai, "Influence of nanoparticle reinforcements on the strengthening mechanisms of an ultrafine-grained dual phase steel containing titanium," *Mater. Des.*, vol. 44, pp. 331-339, 2013.

[136] J. M. Schissler, J. Arnould, and G. Metauer, "Study of decomposition of post-bainitic austenite in Fe-C-Si alloys with 1 percent C and 4 percent Si during isothermal holding," *Mem. Sci. Rev. Metallurgie*, vol. 6, pp. 779-793, 1975.

[137] J. H. Jang, I. G. Kim, and H. K. D. H. Bhadeshia, "Substitutional solution of silicon in cementite: A first-principles study," *Computational Materials Science*, vol. 44, pp. 1319-1326, 2009.

[138] S. Yamasaki and H. K. D. H. Bhadeshia, "Modelling and characterisation of Mo2C precipitation and cementite dissolution during tempering of Fe-C-Mo martensitic steel," *Mater. Sci. Technol.*, vol. 19, pp. 723-731, 2003.

[139] D. Delagnes, F. Pettinari-Sturmel, M. H. Mathon, R. Danoix, F. Danoix, C. Bellot, P. Lamesle, and A. Grellier, "Cementite-free martensitic steels: A new route to develop high strength/high toughness grades by modifying the conventional precipitation sequence during tempering," *Acta. Mater.*, vol. 60, pp. 5877-5888, 2012.

[140] T. P. Hou, Y. Li, Y. D. Zhang, and K. M. Wu, "Magnetic field-induced precipitation behaviors of alloy carbides M2C, M3C, and M6C in a molybdenum-containing steel," *Metall. Mater. Trans. A*, vol. 45, pp. 2553-2561, 2014.

[141] A.-M. E. Rakayby and B. Mills, "Tempering and Secondary Hardening of M 42 high-speed steel," *Mater. Sci. Technol.*, vol. 2, pp. 175-180, 1986.

[142] Z. Hu, X. Wu, and C. Wang, "HRTEM study on precipitates in high Co-Ni steel," *Journal of Material Science and Technology*, vol. 20, pp. 425-428, 2004.

[143] M. S. Bhat, J. Garrison, W.M., and V. F. Zackay, "Relations between microstructure and mechanical properties in secondary hardening steels," *Mater. Sci. Eng.*, vol. 41, pp. 1-15, 1979.

[144] W. B. Pearson, "Alphabetical index of work on borides, Carbides, Hydrides, Nitridies, and Binary Oxides," in *Lattice Spacings and Structures of Metals and Alloys*, G. V. Raynor, Ed., ed New York, USA: Pergarom Press, Inc., 1958, pp. 895-1037.

[145] K. S. Cho, J. H. Choi, H. S. Kang, S. H. Kim, K. B. Lee, H. R. Yang, and H. Kwon, "Influence of rolling temperature on the microstructure and mechanical properties of secondary hardening high Co-Ni steel bearing 0.28 wt% C," *Mat Sci Eng a-Struct*, vol. 527, pp. 7286-7293, 2010.

[146] X. C. Xiong, B. Chen, M. X. Huang, J. F. Wang, and L. Wang, "The effect of morphology on the stability of retained austenite in a quenched and partitioned steel," *Scripta. Mater.,* vol. 68, pp. 321-324, 2013.

[147] A. S. Podder, I. Lonardelli, A. Molinari, and H. K. D. H. Bhadeshia, "Thermal stability of retained austenite in bainitic steel: an in situ study," *Proceedings of the Royal Society of London A: Mathematical, Physical and Engineering Sciences,* vol. 467, pp. 3141-3156, 2011.

[148] Y. Song, J. Cui, and L. Rong, "Microstructure and mechanical properties of 06Cr13Ni4Mo steel treated by quenching–tempering–partitioning process," *J. Mater. Sci. Technol.,* vol. 32, pp. 189-193, 2016.

[149] P. Zhang, Y. Chen, W. Xiao, D. Ping, and X. Zhao, "Twin structure of the lath martensite in low carbon steel," *Progress in Natural Science: Materials International,* vol. 26, pp. 169-172, 2016.

[150] T. Liu, D. Zhang, Q. Liu, Y. Zheng, Y. Su, X. Zhao, J. Yin, M. Song, and D. Ping, "A new nanoscale metastable iron phase in carbon steels," *Scientific Reports,* vol. 5, p. 15331, 2015.

[151] A. S. Podder, "Tempering of a mixture of bainite and retained austenite," Doctor of Philosophy, Department of Materials Science and Metallurgy, University of Cambridge, 2011.

[152] B. C. De Cooman, "Structure–properties relationship in TRIP steels containing carbide-free bainite," *Current Opinion in Solid State and Materials Science,* vol. 8, pp. 285-303, 2004.

[153] P. J. Jacques, "Transformation-induced plasticity for high strength formable steels," *Current Opinion in Solid State and Materials Science,* vol. 8, pp. 259-265, 2004.

[154] S. Morito, Y. Adachi, and T. Ohba, "Morphology and crystallography of sub-blocks in ultra-low carbon lath martensite steel," *Mater. Trans.,* vol. 50, pp. 1919-1923, 2009.

[155] S. Morito, X. Huang, T. Furuhara, T. Maki, and N. Hansen, "The morphology and crystallography of lath martensite in alloy steels," *Acta. Mater.,* vol. 54, pp. 5323-5331, 2006.

[156] T. Ohmura, T. Hara, and K. Tsuzaki, "Mechanical characterization of secondary-hardening martensitic steel using nanoindentation," *J. Mater. Res.,* vol. 19, pp. 79-84, 2004.

[157] T. Ohmura, T. Hara, and K. Tsuzaki, "Evaluation of temper softening behavior of Fe–C binary martensitic steels by nanoindentation," *Scripta. Mater.,* vol. 49, pp. 1157-1162, 2003.

[158] T. Ohmura, K. Tsuzaki, and S. Matsuoka, "Evaluation of the matrix strength of Fe-0.4 wt% C tempered martensite using nanoindentation techniques," *Philosophical Magazine A,* vol. 82, pp. 1903-1910, 2002.

[159] T. Ohmura, K. Tsuzaki, and S. Matsuoka, "Nanohardness measurement of high-purity Fe–C martensite," *Scripta. Mater.*, vol. 45, pp. 889-894, 2001.

[160] E. I. Galindo-Nava and P. E. J. Rivera-Díaz-del-Castillo, "Understanding the factors controlling the hardness in martensitic steels," *Scripta. Mater.*, vol. 110, pp. 96-100, 2016.

[161] D. C. Saha, E. Biro, A. P. Gerlich, and Y. Zhou, "Effects of tempering mode on the structural changes of martensite," *Mater. Sci. Eng. A*, vol. 673, pp. 467-475, 2016.

[162] T. Gladman, "Precipitation hardening in metals," *Mater. Sci. Technol.*, vol. 15, pp. 30-36, 1999.

[163] T. Gladman, *The physical metallurgy of microalloyed steels* vol. 615: Maney Pub, 1997.

[164] F. Perrard, A. Deschamps, and P. Maugis, "Modelling the precipitation of NbC on dislocations in alpha-Fe," *Acta. Mater.*, vol. 55, pp. 1255-1266, 2007.

[165] H. I. Aaronson, M. Enomoto, and J. K. Lee, *Mechanisms of diffusional phase transformations in metals and alloys*: CRC Press, 2010.

[166] E. Kozeschnik, C. Bataille, and K. Janssens, *Modeling solid-state precipitation*: Momentum Press, 2012.

[167] W. H. Hall and G. K. Williamson, "The diffraction pattern of cold worked metals: II changes in integrated intensity," *Proceedings of the Physical Society. Section B*, vol. 64, p. 946, 1951.

[168] Q. Liu, D. Juul Jensen, and N. Hansen, "Effect of grain orientation on deformation structure in cold-rolled polycrystalline aluminium," *Acta. Mater.*, vol. 46, pp. 5819-5838, 1998.

[169] S. Morito, H. Yoshida, T. Maki, and X. Huang, "Effect of block size on the strength of lath martensite in low carbon steels," *Mater. Sci. Eng. A*, vol. 438–440, pp. 237-240, 2006.

[170] L. Norstrom, "Yield strength of quenched low-C lath martensite," *Scandinavian Journal of Metallurgy*, vol. 5, pp. 159-165, 1976.

[171] T. Tsuchiyama, "Physical meaning of tempering parameter and its application for continuous heating or cooling heat treatment process," *Netsu Shori (Journal of the Japan Society for Heat Treatment) (Japan)*, vol. 42, pp. 163-168, 2002.

[172] R. M. P. and S. R. E., "Correlation of nanoindentation and conventional mechanical property measurements," in *Symposium on Fundamentals of Nanoindentation and Nanotribology II*, 2002.

[173] U. F. Kocks and H. Mecking, "Physics and phenomenology of strain hardening: the FCC case," *Prog. Mater. Sci.*, vol. 48, pp. 171-273, 2003.

[174] M. Huang, P. E. J. Rivera-Díaz-del-Castillo, O. Bouaziz, and S. van der Zwaag, "Modelling strength and ductility of ultrafine grained BCC and FCC alloys using irreversible thermodynamics," *Mater. Sci. Technol.*, vol. 25, pp. 833-839, 2009.

[175] G. Ghosh and G. B. Olson, "The isotropic shear modulus of multicomponent Fe-base solid solutions," *Acta. Mater.*, vol. 50, pp. 2655-2675, 2002.

[176] A. S. Argon, *Strengthening mechanisms in crystal plasticity*: Oxford University Press Oxford, 2008.

[177] E. Biro, J. R. McDermid, S. Vignier, and Y. N. Zhou, "Decoupling of the softening processes during rapid tempering of a martensitic steel," *Mater. Sci. Eng. A*, vol. 615, pp. 395-404, 2014.

[178] B. Dutta, E. Valdes, and C. M. Sellars, "Mechanism and kinetics of strain induced precipitation of Nb(C,N) in austenite," *Acta Metall. Mater.*, vol. 40, pp. 653-662, 1992.

[179] B. Dutta and C. M. Sellars, "Effect of composition and process variables on Nb(C, N) precipitation in niobium microalloyed austenite," *Mater. Sci. Technol.*, vol. 3, pp. 197-206, 1987.

[180] B. Dutta, E. J. Palmiere, and C. M. Sellars, "Modelling the kinetics of strain induced precipitation in Nb microalloyed steels," *Acta. Mater.*, vol. 49, pp. 785-794, 2001.

[181] W. J. Liu, "A new theory and kinetic modeling of strain-induced precipitation of Nb(CN) in microalloyed austenite," *Metall. Mater. Trans. A*, vol. 26, pp. 1641-1657, 1995.

[182] O. Kwon and A. J. DeArdo, "Interactions between recrystallization and precipitation in hot-deformed microalloyed steels," *Acta Metall. Mater.*, vol. 39, pp. 529-538, 1991.

[183] E. V. Pereloma, B. R. Crawford, and P. D. Hodgson, "Strain-induced precipitation behaviour in hot rolled strip steel," *Mater. Sci. Eng. A*, vol. 299, pp. 27-37, 2001.

[184] Z. Q. Wang, X. P. Mao, Z. G. Yang, X. J. Sun, Q. L. Yong, Z. D. Li, and Y. Q. Weng, "Strain-induced precipitation in a Ti micro-alloyed HSLA steel," *Mat Sci Eng a-Struct*, vol. 529, pp. 459-467, 2011.

[185] D. Kalish and M. Cohen, "Structural changes and strengthening in the strain tempering of martensite," *Mater. Sci. Eng.*, vol. 6, pp. 156-166, 1970.

[186] E. Kozeschnik and H. K. D. H. Bhadeshia, "Influence of silicon on cementite precipitation in steels," *Mater. Sci. Technol.*, vol. 24, pp. 343-347, 2008.

[187] Y. Kang, H. Yu, J. Fu, K. Wang, and Z. Wang, "Morphology and precipitation kinetics of AlN in hot strip of low carbon steel produced by compact strip production," *Mater. Sci. Eng. A*, vol. 351, pp. 265-271, 2003.

[188] M. Tokizane, N. Matsumura, K. Tsuzaki, T. Maki, and I. Tamura, "Recrystallization and formation of austenite in deformed lath martensitic structure of low carbon steels," *Metall. Trans. A*, vol. 13, pp. 1379-1388, 1982.

[189] A. Stormvinter, P. Hedström, and A. Borgenstam, "A Transmission electron microscopy study of plate martensite formation in high-carbon low alloy steels," *J. Mater. Sci. Technol.*, vol. 29, pp. 373-379, 2013.

[190] P. Zhang, Y. Chen, W. Xiao, D. Ping, and X. Zhao, "Twin structure of the lath martensite in low carbon steel," *Progress in Natural Science: Materials International*.

[191] A. J. Clarke, M. K. Miller, R. D. Field, D. R. Coughlin, P. J. Gibbs, K. D. Clarke, D. J. Alexander, K. A. Powers, P. A. Papin, *et al.*, "Atomic and nanoscale chemical and structural changes in quenched and tempered 4340 steel," *Acta. Mater.*, vol. 77, pp. 17-27, 2014.

[192] M. Maalekian and E. Kozeschnik, "A thermodynamic model for carbon trapping in lattice defects," *Calphad-Computer Coupling of Phase Diagrams and Thermochemistry*, vol. 32, pp. 650-654, 2008.

[193] H. F. Lan, W. J. Liu, and X. H. Liu, "Ultrafine ferrite grains produced by tempering cold-rolled martensite in low carbon and microalloyed steels," *ISIJ Int.*, vol. 47, pp. 1652-1657, 2007.

[194] D. V. Wilson, "Effects of plastic deformation on carbide precipitation in steel," *Acta. Metall. Mater.*, vol. 5, pp. 293-302, 1957.

[195] K. W. Andrews, D. J. Dyson, and S. R. Keown, *Interpretation of electron diffraction patterns*, 1971.

[196] X. Sauvage, X. Quelennec, J. J. Malandain, and P. Pareige, "Nanostructure of a cold drawn tempered martensitic steel," *Scripta. Mater.*, vol. 54, pp. 1099-1103, 2006.

[197] J. Chakraborty, M. Ghosh, R. Ranjan, G. Das, D. Das, and S. Chandra, "X-ray diffraction and Mössbauer spectroscopy studies of cementite dissolution in cold-drawn pearlitic steel," *Philosophical Magazine*, vol. 93, pp. 4598-4616, 2013.

[198] V. G. Gavriljuk, "Decomposition of cementite in pearlitic steel due to plastic deformation," *Mater. Sci. Eng. A*, vol. 345, pp. 81-89, 2003.

[199] S. Morito, K. Oh-ishi, K. Hono, and T. Ohba, "Carbon enrichment in retained austenite films in low carbon lath martensite steel," *ISIJ Int.*, vol. 51, pp. 1200-1202, 2011.

[200] W. Mayer, S. Sackl, Y. V. Shan, S. Primig, and E. Kozeschnik, "Evolution of precipitates and martensite substructure during continuous heat treatment," *Materials Today: Proceedings*, vol. 2, pp. S619-S622, 2015.

[201] G. Badinier, C. W. Sinclair, X. Sauvage, X. Wang, V. Bylik, M. Gouné, and F. Danoix, "Microstructural heterogeneity and its relationship to the strength of martensite," *Mater. Sci. Eng. A*, vol. 638, pp. 329-339, 2015.

[202] B. Kim, C. Celada, D. San Martín, T. Sourmail, and P. E. J. Rivera-Díaz-del-Castillo, "The effect of silicon on the nanoprecipitation of cementite," *Acta. Mater.*, vol. 61, pp. 6983-6992, 2013.

[203] G. Miyamoto, J. C. Oh, K. Hono, T. Furuhara, and T. Maki, "Effect of partitioning of Mn and Si on the growth kinetics of cementite in tempered Fe–0.6 mass% C martensite," *Acta. Mater.*, vol. 55, pp. 5027-5038, 2007.

[204] D. W. H. Rankin, "CRC handbook of chemistry and physics, 89th edition, edited by David R. Lide," *Crystallography Reviews,* vol. 15, pp. 223-224, 2009.

[205] C. Zhu, X. Y. Xiong, A. Cerezo, R. Hardwicke, G. Krauss, and G. D. W. Smith, "Three-dimensional atom probe characterization of alloy element partitioning in cementite during tempering of alloy steel," *Ultramicroscopy,* vol. 107, pp. 808-812, 2007.

[206] K. L. Johnson, *Contact mechanics*: Cambridge University Press, 1985.

[207] B. Hutchinson, J. Hagstrom, O. Karlsson, D. Lindell, M. Tornberg, F. Lindberg, and M. Thuvander, "Microstructures and hardness of as-quenched martensites (0.1-0.5%C)," *Acta. Mater.,* vol. 59, pp. 5845-5858, 2011.

[208] M. Hayakawa, S. Matsuoka, K. Tsuzaki, H. Hanada, and M. Sugisaki, "Atomic force microscopy of induction- and furnace-heating-tempered prestressed steels with different delayed fracture properties," *Scripta. Mater.,* vol. 47, pp. 655-661, 2002.

[209] E. Mittemeijer, "Fundamentals of materials science: The microstructure–property relationship using metals as model systems, Chap. 9: Phase transformations," ed: Heidelberg: Springer-Verlag, 2010.

[210] T. Tsuchiyama, "Physical meaning of tempering parameter and its application for continuous heating or cooling heat treatment process," *J. Jpn. Soc. Heat Treat.,* vol. 42, pp. 163-168, 2002.

[211] A. Akhtar and E. Teghtsoonian, "Substitutional solution hardening of magnesium single crystals," *Philosophical Magazine,* vol. 25, pp. 897-916, 1972.

[212] R. L. Fleischer, "Substitutional solution hardening," *Acta. Metall. Mater.,* vol. 11, pp. 203-209, 1963.

[213] I. Toda-Caraballo, E. I. Galindo-Nava, and P. E. J. Rivera-Díaz-del-Castillo, "Understanding the factors influencing yield strength on Mg alloys," *Acta. Mater.,* vol. 75, pp. 287-296, 2014.

[214] G. Krauss, *Steels: Heat treatment and processing principles*. Materials Park (OH): ASM International, 1990.

[215] C. C. Kinney, K. R. Pytlewski, A. G. Khachaturyan, and J. W. Morris, "The microstructure of lath martensite in quenched 9Ni steel," *Acta. Mater.,* vol. 69, pp. 372-385, 2014.

[216] T. Furuhara, H. Kawata, S. Morito, and T. Maki, "Crystallography of upper bainite in Fe–Ni–C alloys," *Mater. Sci. Eng. A,* vol. 431, pp. 228-236, 2006.

[217] H. Yoshida, S. Takagi, S. Sakai, S. Morito, and T. Ohba, "Crystallographic analysis of lath martensite in ferrite-martensite dual phase steel sheet annealed after cold-rolling," *ISIJ Int.,* vol. 55, pp. 2198-2205, 2015.

[218] S. Morito, H. Saito, T. Ogawa, T. Furuhara, and T. Maki, "Effect of austenite grain size on the morphology and crystallography of lath martensite in low carbon steels," *ISIJ Int.,* vol. 45, pp. 91-94, 2005.

[219] D. Hull and D. J. Bacon, *Introduction to dislocations* vol. 257: Pergamon Press Oxford, 1984.

[220] A. H. Cottrell and B. A. Bilby, "Dislocation theory of yielding and strain ageing of iron," *Proceedings of the Physical Society. Section A,* vol. 62, p. 49, 1949.

[221] E. J. Pavlina and C. J. Van Tyne, "Correlation of yield strength and tensile strength with hardness for steels," *Journal of Materials Engineering and Performance*, vol. 17, pp. 888-893, 2008.

[222] H. O.P. and A. M.A., "Tempering of hot-formed steel using induction heating," Master of Science, Department of Materials and Manufacturing Technology, Chalmers University of Technology, 2011.